Landscape and climate evolution in arid to hyperarid climates with special focus on the Atacama Desert

I n a u g u r a l - D i s s e r t a t i o n

Zur

Erlangung des Doktorgrades
der Mathematisch-Naturwissenschaftlichen Fakultät
der Universität zu Köln

vorgelegt von
M.Sc. Benedikt Ritter
aus Neuss

Köln 2019

Berichterstatter:	Prof. Dr. Tibor J. Dunai (Universität zu Köln)
(Gutachter)	Prof. Dr. Martin Melles (Universität zu Köln)
	Prof. Dr. Eduardo Campos
	(Universidad Catolica del Norte, Chile)

Tag der mündlichen Prüfung: 23.01.2019

Abstract

The Atacama Desert of northern Chile and Peru is one of the driest places on Earth, with a modern hyperarid core, receiving less than 2 mm/yr of precipitation. The persistent arid climate in the Atacama Desert preserves evidences of earlier 'wetter' periods in the geological record. These evidences indicate that even during prolonged aridity, active geomorphological and biological processes existed. Arid conditions are controlled by several interconnected processes, such as atmospheric circulation, oceanic currents, and tectonic activity. Although the main factors forcing aridity have been identified, their timing and succession is still being debated. Most paleoclimate studies in the Atacama Desert have been carried out on the fringes of the extreme hyperarid zone (here, hyperarid regions are considered to be those displaying <2 mm/yr modern precipitation), in regions that still receive noticeable amounts of precipitation and/or runoff from the high Andes. From the different study areas and archives used contradictory views have emerged regarding the onset, duration and intensity of hyperaridity and the interspersed 'wetter' periods.

This thesis presents geochronological, sedimentological and geomorphological investigations of endorheic basins, terrace-like features and alluvial fans preserved within the Coastal Cordillera and Central Depression of the Atacama Desert. The overall aim is to connect different dating techniques, archives and their interpretations to contribute to the ongoing discussion about the onset of hyperaridity and interspersed climate variability. The information obtained about episodes of surface activity and sedimentation are used for paleoenvironmental and climatological reconstructions in the respective study areas and subsequently synthesised to address the paleoclimate of the Atacama Desert at a broader scale.

Situated in the southern Central Depression of the Atacama Desert, linear features, resembling shoreline terraces are found around Cerro Soledad and adjacent topographic highs. These were analysed and dated using terrestrial cosmogenic nuclide exposure dating (^{10}Be, ^{26}Al, ^{21}Ne). The information obtained about the evolution and timing of shoreline formation reveals the chronology of lake phases and the related denudational history of the complex Quillagua-Llamara basin.

Ancient, inactive, alluvial fan surfaces and other preserved fluvial features in the Coastal Cordillera south of the Río Loa were analysed and dated to reconstruct their age of abandonment. This part of the study contributes to the ongoing debate about the onset of hyperaridity, interspersed 'wetter' (still arid) episodes and the spatial heterogeneity, or gradients of aridity in the Atacama Desert.

Paleoclimate records from the hyperarid core of the Atacama Desert are currently lacking. Endorheic sedimentary basins in the hyperarid Coastal Cordillera are capable of recording even subtle autochthonous changes in precipitation and surface modification. A ~6 m long sediment core was analysed from an isolated basin, covering a sedimentary depositional record beginning 215 ka ago. This archive reveals that the persistent hyperarid climate witnessed episodes of somewhat 'wetter' climate, which led to minor amounts of surface modification and sedimentation in an endorheic basin within the Coastal Cordillera, coinciding with warmer sea-surface temperatures (SST) off Chile, imitating El Niño-like conditions.

New data and interpretations from three individual publications, covering the above mentioned topics and collated in this thesis, were used to produce a synthesis of paleoenvironmental and climatological reconstructions for the Atacama Desert. As various archives and methods are used, an evaluation of these archives and methods is conducted within the scope of this thesis.

Kurzfassung

Die Atacama-Wüste im Norden Chiles und Perus ist einer der trockensten Orte der Erde, mit einem modernen hyperariden Kern mit weniger als 2 mm/a Niederschlag. Das anhaltend trockene Klima in der Atacama-Wüste bewahrt Spuren von zwischenzeitlichen „feuchteren“ Perioden. Diese Spuren zeigen, dass auch bei längerer Trockenheit; Oberflächenaktivität und biologischer Aktivität vorhanden war und ist. Die Entwicklung zur Wüste wird durch mehrere ineinandergreifende Prozesse gesteuert, wie z.B. atmosphärische Zirkulation, ozeanische Strömungen und tektonische Aktivität. Die wichtigsten Einflussfaktoren wurden bereits identifiziert, ihre zeitlichen Einflüsse und ihre Abfolge sind jedoch umstritten. Bis dato fokussierten sich die meisten Paläoklimauntersuchungen am Rand zur hyperariden Wüste und vermieden Regionen der extremen Hyperaridität (<2mm/a). Studien wurden in Regionen durchgeführt, die noch immer spürbare Niederschläge und/oder Einträge aus den hohen Anden erhalten. Basierend auf verschiedenen Untersuchungsgebieten und Archiven, sowie abhängig von Einschränkungen und Annahmen gewisser Proxies, entwickelte sich eine fortwährende Diskussion über den Beginn und die Dauer der Hyperaridität, sowie über den Zeitpunkt und die Intensität zwischenzeitlicher "feuchterer" Episoden.

Diese Arbeit stellt geochronologische, sedimentologische und geomorphologische Untersuchungen von endorheischen Becken, terassenartigen Landschaftsstrukturen und alluviale Fächer vor, die in der Küstenkordillere und der Zentralen Depression der Atacama Wüste erhalten sind. Aufgrund der langen Geschichte der Aridität in der Atacama, beschäftigt sich diese Dissertation mit der Verbindung verschiedener Datierungstechniken, Archiven und deren Interpretationen, um mithilfe neu gewonnener Erkenntnisse zur fortwährenden Diskussion über den Beginn der Aridität und zwischenzeitlichen Klimaschwankungen beizutragen. Die gewonnenen Erkenntnisse über Episoden mit Oberflächenaktivität werden für Paläoumwelt und -klima Rekonstruktionen im jeweiligen Untersuchungsgebiet, sowie für großräumige Implikationen für die Atacama-Wüste verwendet.

Im südlichen Zentraltal der Atacama-Wüste wurden lineare geomorphologische Strukturen, vermutlich Strandterrassen, um den Berg „Soledad“ und angrenzenden

topographischen Erhöhungen analysiert und mithilfe von kosmogener Expositiondatierung datiert (^{10}Be, ^{26}Al, ^{21}Ne). Die gewonnenen Informationen über die Entwicklung und den Zeitpunkt der Bildung jener Strandterrassen offenbaren das Auftreten diverser Seephasen und geben einen Einblick in die Denudationsgeschichte des Quillagua-Llamara-Beckens.

In der Küstenkordillere südlich des Río Loa wurden alte, inaktive, alluviale Schwemmfächer und fluviale Strukturen analysiert und datiert (^{21}Ne, ^{10}Be). Mithilfe dieser Daten wird ihre Entstehung und der zeitliche Rahmen des Endes der Aufgabe dieser Sedimentationssysteme rekonstruiert. Diese Studie leistet einen Beitrag zur laufenden Debatte über den Beginn der Hyperaridität, zwischenzeitlichen "feuchteren" (weiterhin arid) Episoden, und der räumlichen Heterogenität der Trockenheit in der Atacama Wüste.

Paläoklimarekonstruktionen aus dem hyperariden Kern der Atacama-Wüste fehlen derzeit. Endorheische Sedimentbecken in der hyperariden Küstenkordillere sind in der Lage, selbst subtile autochthone Veränderungen in der Niederschlagsmenge und deren Oberflächeneinfluss zu erfassen. Ein ~6 m langer Sedimentkern wurde aus einem geschlossenen Becken analysiert, welcher die letzten 215 ka Klimageschichte abdeckt. Dieses Archiv verdeutlicht, dass das anhaltende hyperaride Klima, von "feuchteren" Klimaepisoden unterbrochen wurde, welches zu geringer Oberflächenaktivität und Sedimentation in jenes endorheisches Becken innerhalb der Küstenkordilleren führte. Feuchte Phasen treten synchron mit erhöhten Meeresoberflächentemperaturen auf und ähneln vermutlich El Niño Bedingungen.

Neue Daten und Ergebnisse aus drei Veröffentlichungen werden in dieser Arbeit vereint. Diese werden für eine Synthese zur geomorphologischen und paläoklimatologischen Landschafts- und Umweltrekonstruktion verwendet. Des Weiteren wird im Rahmen dieser Arbeit eine kritische Bewertung der genutzten Archive und Methoden vorgenommen.

Acknowledgment

First of all, I want to thank my supervisor Prof. Tibor J. Dunai for giving me the opportunity to work in the incomparable and overwhelming Atacama Desert. Moreover, I am glad and thankful to Tibor, that I could, at least, contributed a little bit to the foundation and prosperous existence of the CRC 1211 "Earth-Evolution at the dry limit" at the University of Cologne. My deepest thanks go to Tibor, who imitable introduced me into the entire and complex Atacama Desert, including a lot of dust and sun burns. Along with the preparation and start of the CRC, I learned due to Tibor, among many other things, the interdisciplinary challenges and perceptions working in such a scientifically broad CRC. Tibor always supported me during my PhD with fruitful but also critical discussions and guidance. Moreover, I have to appreciate the opportunity, given by Tibor, to participate and guide several field campaigns to various deserts.

Many thanks also go to Prof. Martin Melles, who is more or less responsible, in line with Dr. Volker Wennrich, for the onset of my scientific career in 2009 as HiWi for the "Lake El'Gygytgyn Drilling Project" and many other projects. Additionally, I want to thank Martin Melles for being my second supervisor. In particular, I want to thank Dr. Steven Binnie for his support at every stage of my Phd and answering many difficult and complex questions concerning cosmogenic nuclides. Many thanks go to the entire 'cosmo' group in Cologne: Elena Voronina and Tomasz Góral for help and guidance processing samples for ^{10}Be and ^{26}Al data analysis. Especially I have to thank our 'crazy' Argentinean, Damian Lopez, for help during several field trips and during the normal chaotic daily-life at the university. Incredible thanks go to Barbara Bock, for her help and guidance, trying to understand the bureaucratic administration of the university. I want to thank the entire Quaternary working group, right at the start Nicole Mantke and Dorothea Klinghardt for their help and support in the lab.

For nice, idyllic and scientifically fruitful stays in East Kilbride at SUERC for my endlessly noble gas measurements, I want to thank Finlay Stuart and Luigia Di Nicola. Moreover, I want to thank Terry Donnelly and his family for the nice accommodation at their home during my prolonged stays in Scotland.

I would like to thank all my Chilean colleagues for their help and logistic support during several field campaigns. Furthermore, I want to express my gratitude to my various co-authors, i.e. Axel Gerdes, Alicia Medialdea Utande, Dominik Brill, Georgina King, Sascha Schneiderwind, Karin Niemann, Emma Fernandez Galego, Julia Diederich and Christian Rolf.

For financial support of my thesis, I want to thank the University of Cologne and the CRC 1211. As well as the Graduate School of Geoscience (GSGS) for financial support for international conferences.

For always feeling home after months of being in exile in Cologne, my indescribable gratitude's go to my old and best friends from Glehn. No matter how long I stayed abroad, coming and feeling home directly like I've never been off, was and is a tremendous feeling. For many jokes and fun about my life as geologist, I especially want to thank Andreas Lupp, Julian Meurer and Kevin Schriddels and all my other friends of the Jgz. Dat Löpp.

For frequent distractions in Cologne and intense high scientifically discussions after a few hop teas, I want to thank my friends and colleagues Raphael Gromig, Niklas Leicher, Jule Diederich, Wolf Dummann, Joel Mohren, Jonas Tusch, Matthias Lenz, Ascelina Hasberg, Paul Tauber, Tom Schulte, Vera Schmidt, Sarah Esteban-Lopez, Simon Schallenberg, Felix Blumenthal and Dominik Hofer.

Last but not least, I want to thank my parents and the rest of my family, which have been a constant source for encouragement and support, even though they sometimes made jokes about me collecting pebbles in the desert.

In remembrance and eternal gratitude, this work should be dedicated to my recently deceased grandparents, Aloys and Agnes Wienholt, who were always immensely proud of us children and gave us indescribable support.

"Denn man tau!"

Table of Contents

Preface

Aridity is defined by the limitation of water in the environment. Implementation and impact of aridity vary from place to place and through time, therefore its definition, appearance and environmental influences are complex and require careful investigations. One of the few places on Earth which experience pronounced effects of aridity is the Atacama Desert. This region is of major scientific interest, not only for space science and the search for Earth-Mars analogies, as shown by recent scientific collaborations such as the 'Collaborative Research Center 1211', which faces the significant 'mutual evolutionary relationships between Earth surface processes and biota' (CRC 1211). Under arid climate conditions surface processes operate relatively slow, especially in the absence of water. However, even short episodes of increased water availability are able to produce long-lasting traces of surface and biological activity. Defining the spatial extent and the temporal variations of aridity in a certain area is a complex issue. 'Spotiness' of rainfall events, heterogeneous catchments (size, elevation, moisture source and transport), drainage processes (surface abandonment, channel incision, drainage bypass) as well as tectonic activity (tectonic blocking or tilting) can result in considerable spatial and temporal inequalities of aridity in its hydrological, geomorphological and biological effects. Beside scientific questions about recent effects of aridity and processes, the way towards aridity of landscapes and evolution of life is of major social interest. Understanding and reconstructing forcing factors and processes leading to aridity as well as the temporary return of humid conditions are important to grasps our system 'Earth' and predict future climate conditions. To contribute to the investigation of those major research questions, this thesis is dedicated to the Atacama Desert in northern Chile.

1. Introduction

The Atacama Desert of northern Chile and Peru is one of the driest places on Earth. Its extension is bound and restricted by the high Andes to the east, the cold Humboldt current (Pacific Ocean) to the west (Fig. 1) and reaches from southern Peru in the north to the area near Santiago de Chile in the south. Arid conditions exist especially along the coast, above the Coastal cliff, and on the lower-elevated levels of the western Andean foreslope/foothills. Precipitation decreases and aridity increases towards the hyperarid core of the Atacama Desert (Fig. 2), which is recently restricted to an area of less than 2 mm/yr precipitation in the Coastal Cordillera and Central Depression between 19-23°S (Houston, 2006b). Precipitation increases by 1-2 orders of magnitude towards the east where the Andes increases in height. A pronounced influence/effect of Atlantic air masses is responsible for precipitation on the Altiplano-Puna Plateau. More frequent storms and an increase in precipitation occurs south of Antofagasta.

Regarding the climatic evolution of the Atacama Desert, three major forcing factors are responsible for the desertification. (1) The position of the Atacama Desert at the subtropical high-pressure belt, in a zone of descending stable air, which could have been established since the late Jurassic (Hartley et al., 2005). (2) The subduction of the Nazca Plate under the South American Plate, that led to the uplift and evolution of the Central Andes, implementing a significant rain-shadow effect for Atlantic air masses. (3) The establishment of the cold Humboldt Current to the west of the Atacama Desert, which inhibits moisture uptake of onshore winds. Forcing factors might be identified, however, the onset and permanency of the hyperarid conditions and its spatial extend is matter of an ongoing scientific debate.

Due to the nearly fixed latitudinal position of the South American continent since at least 150 Ma (Hartley et al., 2005) and the evolution of the Humboldt current since the establishment of the Antarctic Circumpolar Current after ~50 Ma (opening of the Drake passage, Scher and Martin, 2006; Lagabrielle et al., 2009; Cristini et al., 2012), arid conditions could have prevailed in the Atacama region since at least the early Oligocene (Hartley, 2003; Dunai et al., 2005). However, there is a wide range of other geological ages proposed for the onset of aridity (Sillitoe and McKee, 1996; Sáez et al.,

1999; Hartley and Chong, 2002; Rech et al., 2003; Dunai et al., 2005; Nishiizumi et al., 2005; Latorre et al., 2006; Rech et al., 2006; Kober et al., 2007; Nester et al., 2007; Evenstar et al., 2009; Placzek et al., 2010; Gayo et al., 2012b; Sáez et al., 2012; Jordan et al., 2014; Evenstar et al., 2017).

The diversity of proposed ages for the onset is partially due to the different proxies used and their interpretation, e.g. sensitivity to climate variation. For example, the termination of supergene copper enrichments in the Atacama Desert can be either related to the uplift of the Andes and subsequent incision and groundwater lowering (Clarke, 2006) or only to climate change as the result of increasing aridity (Alpers and Brimhall, 1988; Sillitoe and McKee, 1996; Bouzari and Clark, 2002). In addition, regarding modern climate gradients, the location of consulted archives/records may explain the difference in ages for the onset of hyperarid conditions (Coastal Cordillera vs. Andean foothills). To date, studies investigating archives in the driest part containing Miocene relict surfaces (Dunai et al., 2005; Carrizo et al., 2008; Evenstar et al., 2009; Jordan et al., 2014) are scarce, but may exhibit the greatest potential of identifying the onset of aridity.

The Atacama Desert experienced several interspersed episodes of 'wetter' (still arid) conditions, which facilitate surface activity, sediment transport and deposition (e.g. Jordan et al., 2014; Evenstar et al., 2017). These archives only exhibit short discontinuous glimpses into the past and are mainly recorded from the Central Depression, which also receives precipitation from the high Andes to the east.

On shorter time-scales (late Pleistocene and Holocene) there is a more or less consensus that the Atacama Desert and especially the hyperarid areas experienced phases of somewhat 'wetter' climate with enhanced surface activity. Marine archives indicate a migration of Pacific frontal systems 150-200 km to the north during glacials (Lamy et al., 1998; Lamy et al., 2000; Stuut and Lamy, 2004; Rojas et al., 2009), creating wetter conditions in the southern areas (>23°S) that are presently characterized by hyperarid conditions (Maldonado et al., 2005; Quade et al., 2008; Díaz et al., 2012). Climate archives from the Andean foothills indicate increased summer precipitation at the beginning of deglaciation, which led to an increased runoff from the Precordillera (Betancourt et al., 2000; Bobst et al., 2001; Gayo et al., 2012a; Gayo et al., 2012b; Latorre et al., 2013).

All of these archives/records skirt the zone of extreme hyperaridity (<2mm/yr precipitation) and are likely to be influenced by an allochthonous precipitation signal, as their headwaters of their catchment are partly lying deep in the high Andes and/or they are influenced by more than one moisture source. The chronology of climate records from the hyperarid Atacama Desert (Coastal Cordillera) has large gaps, which result from a limited number of adequate archives and suitable analysis methods. Longer-term continuous archives are currently lacking from the hyperarid Atacama Desert.

2. Background of Northern Chile

The following sections provide a first brief overview about the study area (Andes, Atacama), including geology and geomorphology, as well as about factors for aridity and recent climate conditions of the Atacama Desert. As this thesis is based on three individual publications, the reader is also referred to the respective chapters for more detailed information about each project and study site.

2.1 Tectonic framework of the Central Andes in Northern Chile

The central Atacama Desert is located in the fore-arc region of the Central Andes in northern Chile. The Peru-Chile trench is located just 70-150 km offshore (Allmendinger et al., 2005, and citations therein, Fig. 1). The Andean orogeny started during the Cretaceous (Haschke et al., 2002) with the beginning of the subduction of oceanic lithosphere beneath the western margin of South America, where the active magmatic arc was situated in the present-day Coastal Cordillera (Haschke et al., 2002). The emplacement of granitic and granodioritic plutons in the Coastal Cordillera witnesses its magmatic origin (Scheuber and Gonzalez, 1999). Repeated stepwise migration of the magmatic arc to the east resulted in the establishment of the recent arc in the Western Cordillera since the Miocene (Haschke et al., 2002). The former back-arc basin to the east resembles now the Altiplano Plateau, which experienced significant uplift and represents an endorheic high altitude basin. The Atacama Desert situated between the Western and Eastern Cordillera. During the Paleogene, continental sedimentation started to fill up basins in the forearc and backarc of the new magmatic arc (Hartley et al., 2005). From the Oligocene to the

Early Miocene on, the present-day morphological structure of Northern Chile evolved with the occurrence of large erosional surfaces and large depo-centres (e.g. Central Depression Evenstar et al., 2017, Fig. 1,2).

2.2 Geological and geomorphological overview of the Atacama Desert

Three main N-S trending physiographic units constitute the Atacama Desert (Hartley and Evenstar, 2010): the Costal Cordillera, the Central Depression or Longitudinal Valley and the Precordillera (Fig. 1). To the west, the 'forearc' zone is bounded by the Western Cordillera, which forms an active volcanic arc (Hartley and Evenstar, 2010). The term "Atacama Desert" is widely used for the entire coastal area (and higher elevated areas to the east) between southern Peru in the north up to La Serena in the south. As this area covers several magnitude differences in climate variability, there are certain inequalities by using the term Atacama Desert, implying to be in the hyperarid part of the desert. The focus of this thesis lies on the Atacama Desert between 23-18°S. For spatial differentiation, the classification of the Atacama Desert related to aridity are used following recent precipitation patterns (Houston, 2006b). In the following, the hyperarid Atacama Desert is considered to the region with less than >2mm/yr precipitation (Fig. 2, Houston, 2006b).

Precordillera

The Precordillera forms the transition from the low Central Depression towards the Altiplano and the Western Cordillera (Fig. 1) with heights between 1900-2300 m to the west and 3200-3670 m to the east (Hartley and Evenstar, 2010). The Precordillera consists of Late Cretaceous to Oligocene magmatic and volcanic rocks (Charrier et al., 2013). Miocene ignimbrites cover large parts of the Precordillera and were locally deformed (e.g. Garcia and Herail, 2005). The Precordillera south of 22°S is characterized by a series of Cenozoic foreland basins called the Pre-Andean basins (Fig. 1), including the Calama basin and the Salar de Atacama. The perennial Río Loa flows from the high Western Cordillera through the Calama basin into the Central Depression, more precisely into the Quillagua-Llamara basin. The Río Loa proceeds to the Pacific, creating an up to 800 m deep canyon (Fig. 2). The Precordillera proceeds westwards into the depositional system of the Central Depression.

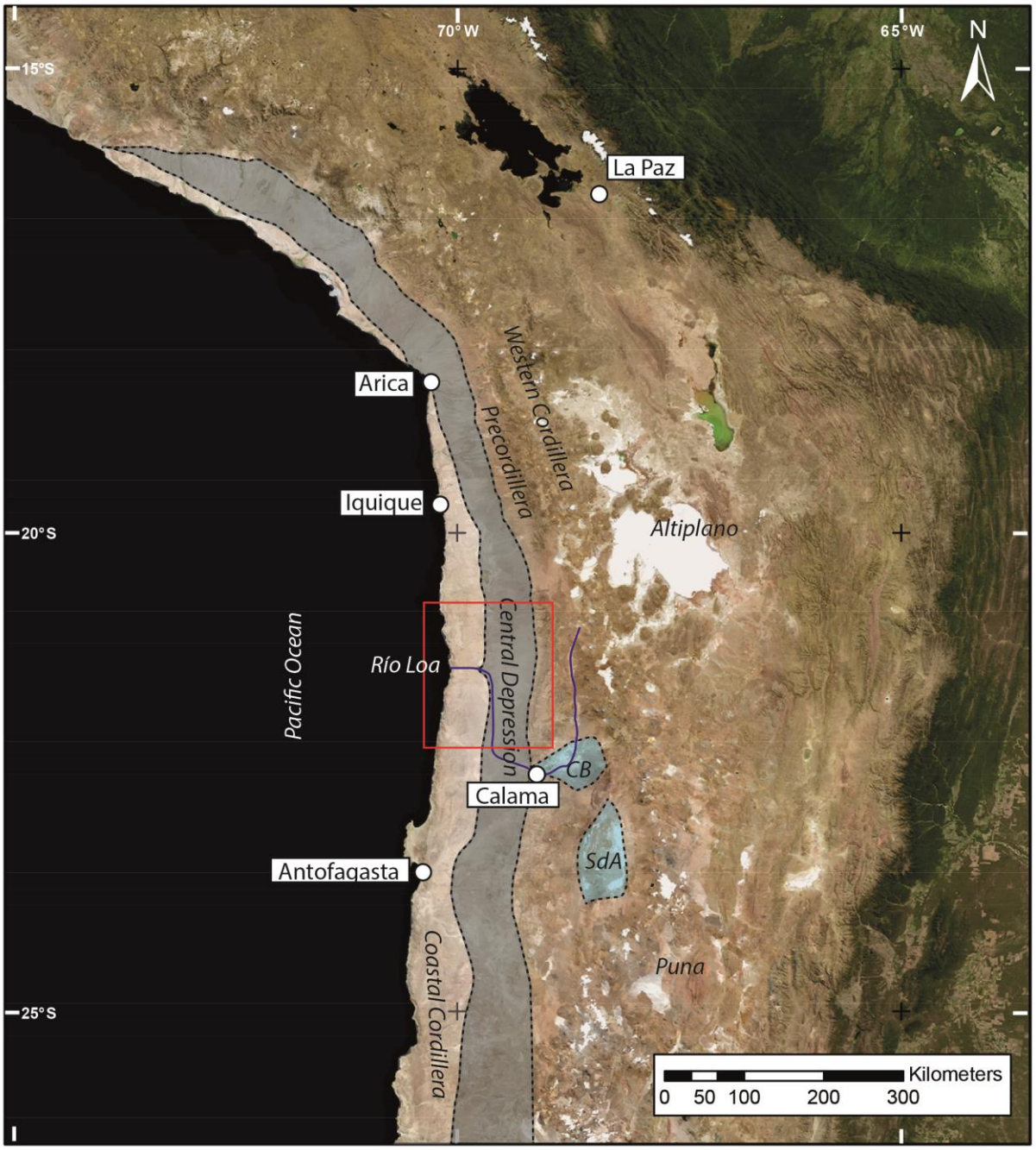

Figure 1: Natural-colour satellite image of west-central South America (NASA composite satellite image for March from Visible Earth - NASA's Earth Observatory) showing the most important morphotectonic units of the Atacama and Andes. Red square marks the research area of this thesis. CB = Calama Basin, SdA = Salar de Atacama.

Central Depression:

A long N-S stretched topographic basin between the Costal Cordillera and the Precordillera is referred to as the Central Depression/Basin or Longitudinal Valley (Fig. 1). In northern Chile, it contains the Pampa de Tamarugal in the north and the Quillagua-Llamara basin in the south. At Arica, where the Coastal Cordillera is absent, the Central Depression is directly connected to the Pacific. The mean altitude is about 1000 m; whereas in the east the elevation rises up to 2000 m. The Central Depression is separated to the west by the north-south trending Atacama Fault System (AFS) (Hartley and Evenstar, 2010). The AFS formed during the Jurassic and Early Cretaceous as intra-arc shear zone (Scheuber and Andriessen, 1990) and exhibits a long history of transitional and extensional dynamics (Okada, 1971). The Central Depression is filled up with a 1500 m thick sequence of sedimentary deposits and acts as the main depo-center for sediments shed from the high Andes to the east (e.g. Mortimer and Saric, 1975; Hartley et al., 2000). The northern part of the Central Depression is deeply incised by some 'Quebradas', draining catchments of the Pre- and Western Cordillera. Between 20°30'S and 19°30' the Central Depression is an endorheic basin (Evenstar et al., 2017) largely fed by groundwater of the Pampa de Tamarugal aquifer (Scheihing et al., 2017).

The southern Central Depression, locally termed Quillagua-Llamara Basin (QLB) extends to 23°S. This exoreic basin is drained by the perennial flowing Río Loa, which receives its water from higher elevated regions to the east (Fig. 2). The Río Loa is the only drainage which reaches the Pacific and drains the high Andes between Pisagua (in the north) and Taltal (in the south), ~600 km distance. However, large parts of the basin act as base level for most of the streams descending from the Andes. Sediments of the QLB reveal not only clastic sedimentation of alluvial fans proceeding into the basin from the east (e.g. Arcas fan). Endorheic deposition took place before opening of the QLB towards the Pacific, with several lacustrine and evaporitic episodes during the late Miocene and Plio/Pleistocene (e.g. Chong et al., 1999; Sáez et al., 1999; Quezada et al., 2012; Sáez et al., 2012; Quezada et al., 2013). The formation of lacustrine and evaporitic conditions in the QLB were controlled by climate and partly enhanced by tectonic activity of the adjacent Calama Basin (May et al., 1999; Sáez et al., 1999; Sáez et al., 2012). The incision of the Río Loa (precise onset unknown,

though Plio/Pleistocene is hypothesized) resulted in a base-level drop of up to 1000 m. Subsequent large-scale denudation took place and eroded most of the former lacustrine and evaporitic sediments.

Costal Cordillera in northern Chile

The Costal Cordillera is up to 3 km high with an average of 1 km and has a maximum width of 50 km. The Costal Cordillera extends along northern Chile (Fig. 1) and is bounded to the west by the coastal escarpment (600-1900 m), which represents a cliff of presumably Miocene age (Mortimer, 1973; Radtke, 1989; Hartley and Jolley, 1995; Ortlieb et al., 1996; Regard et al., 2010). The Coastal Cordillera vanishes near Arica at the axis of the Bolivian Orocline (Armijo et al., 2015) and reappears further north. The Central Depression, in this area, is also referred to as Pampa de Tamarugal, acts like a sedimentation trap for Neogene sediments mostly derived from the Precordillera to the east (Mortimer and Saric, 1975; Evenstar et al., 2009).

The Coastal Cordillera is dissected by several large 'Quebradas' (e.g. *Azapa*, *Camarones*, *Lluta*, Fig. 2) in the northern part (19.3°-18.0°S) and south of 24°S. In between, the only drainage system for over 600 km which reaches the Pacific through the Coastal Cordillera is the Río Loa. The bedrock consists of remnants of a Jurassic arc, containing granodiorites and andesites (Hartley and Evenstar, 2010). The magmatic arc replaced a crust consisting of Paleozoic sedimentary and Precambrian metamorphic rocks (Allmendinger et al., 2005). The Coastal Cordillera consists of a block-faulted Paleogene landscape (Mortimer and Saric, 1975; Tosdal et al., 1984; Dunai et al., 2005; Carrizo et al., 2008; Allmendinger and González, 2010). Three tectonic structures are responsible for the geomorphology of the Coastal Cordillera: a system of N-S orientated faults representing the Atacama Fault System (AFS), an E-W orientated reverse fault system (Allmendinger et al., 2005) and a system of faults with a NNW-SSO orientation. Within the Coastal Cordillera, several half-grabens created sedimentary basins, which were filled with Oligocene and Miocene alluvial deposits and also younger sediments (Hartley and Evenstar, 2010). Large scale sedimentation ceased at the end of the Oligocene and formed the regionally widespread 'Coastal Tarapaca pediplain' (Mortimer and Saric, 1972).

The old tectonically dissected landscape in the Coastal Cordillera has a notable lack of recent fluvial landscape features and is best preserved between Arica and Antofagasta (Mortimer and Saric, 1975; Dunai et al., 2005; Carrizo et al., 2008). Numerous surfaces with Miocene exposure ages have been recognized in the core of this area (Dunai et al., 2005; Carrizo et al., 2008). Most surfaces in the hyperarid core of the Coastal Cordillera (21°30'-19°30'S) are covered by powdery gypsum-rich material. Fossil traces of former fluvial activity are widespread and locally tectonically dissected (Carrizo et al., 2008; Allmendinger and González, 2010). A narrow band along the entire coast receives precipitation from fog ('*camanchaca*' , Cereceda et al., 2008) and rare rainstorms, causing localized denudation in the Coastal Cordillera and the corresponding deposition (Vargas et al., 2006; Carrizo et al., 2008; González et al., 2008; Baker et al., 2013). The fog usually does not exceed heights greater than 1000 m a.s.l.. However, fog can penetrate deep into the hinterland moving along topographic corridors, like '*Quebradas*', transporting moisture to the interior.

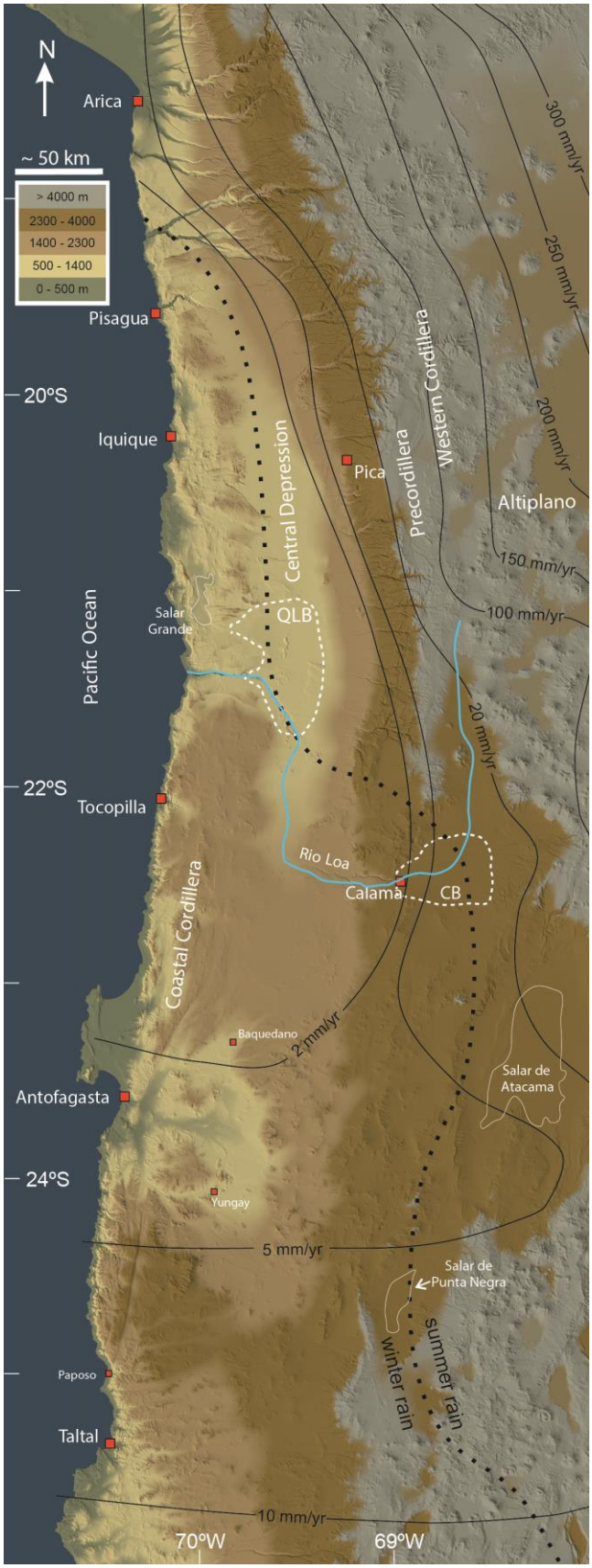

Figure 2: Colour shaded digital elevation model (derived from SRTM-data, created using ArcGIS 10.5.1) with isohyets (Houston, 2006b). Dashed black line indicates the border between winter- and summer-rain dominated areas (Houston, 2006b). Note the zone of extreme hyperaridity (<2mm/yr precipitation) in the Coastal Cordillera and parts of the Central Depression (19-23°S). Precipitation increase towards the Andean flanks with up to 1-2 orders of magnitude higher compared to the hyperarid zone. QLB = Quillagua-Llamara Basin, CB = Calama Basin. Modified after Ritter et al. (2018b).

2.3 Reasons for aridity

The Atacama Desert, likewise the Namib Desert, is a coastal desert. The primary causing factor for aridity is the position at the eastern boundary of the subtropical Pacific. A combination of several factors is responsible for the desertification:

(1) Subtropical atmospheric subsidence: a primary cause for aridity in the Atacama Desert is its position at the subtropical high-pressure belts, in a zone of descending stable air. Large-scale atmospheric subsidence creates dry conditions and lead to the evolution of a surface anticyclone over the southeast Pacific that prevents atmospheric influences from mid- and high latitudes (Maldonado et al., 2005; Houston, 2006b; Takahashi and Battisti, 2007; Garreaud et al., 2009). Rare and unreliable precipitation is mostly associated with seasonal movements of atmospheric systems of the intertropical convergence zone or northward shifting southern Westerlies (Houston, 2006b; Garreaud et al., 2009).

(2) Coastal upwelling of the Humboldt Current: The Humboldt or Peru-Chile current flows northward along the west coast. Upwelling of cold water masses from high-latitudes are induced by southerly winds (Martin et al., 2007), impeding the moisture uptake of coastal onshore winds by low-surface evaporation. This results in a strong temperature inversion layer at ~1000 m, leading to the evolution of a persistent cover of stratus clouds along the coastal cliff (Houston, 2006b).

(3) Rain shadow effect of the Andean Cordillera: The rise of the Andean mountain range to the east leads to orographic rainfall on the eastern side of the Andean mountains and prohibits moisture transport to most areas of the Atacama Desert (Houston, 2006b; Garreaud et al., 2009; Garreaud et al., 2010). However, precipitation sourced from the Atlantic, reaching the Andes and especially the Altiplano-Puna Plateau can significantly contribute to the groundwater supply of lower-elevated western parts of the Atacama, with headwaters deep in the high Andes (e.g. Río Loa, Fig. 2).

(4) High evaporation rates in most areas of the Atacama Desert additionally support hyperarid conditions (Houston and Hartley, 2003; Houston, 2006a; Surma et al., 2018).

2.4 Recent climate conditions

Increased precipitation tends to occur throughout the Precordillera and Altiplano when strong upper level easterly winds enhance moisture transport from Amazonia during austral summer (Fig. 3, December to February; Garreaud et al., 2003; Garreaud et al., 2009). As a consequence of the easterly moisture source, a rain shadow develops over the Precordillera and Atacama Desert. The Mean Annual Precipitation (MAP) declines rapidly from over 300 mm/yr at 5000 m to less than 20 mm/yr at 2300 m (Houston and Hartley, 2003, Fig. 2). Below 2300 m, associated with the Central Depression and the Coastal Cordillera, is a zone of extreme hyper-aridity for which MAP is <2 mm per year (Fig. 2, Houston, 2006b). Winter rainfall is largely sourced from northerly and easterly moving frontal systems originating from the Pacific (Fig. 3, Vuille and Ammann, 1997).

Due to the temperature inversion over the cold Peru-Chile Current (PCC), westerly precipitation originating from the Pacific Ocean is recently sparse. Although westerly precipitation events, like the recent flood of March 2015 in northern Chile, unfrequently occur in the Atacama (Bozkurt et al., 2016). These events can be either connected with cut-off north-migrating low-pressure cells from the Southern Westerlies (Vuille and Ammann, 1997) or *'El Niño'* conditions in the SE Pacific, which destabilize and reduce the temperature inversion (McKay et al., 2003). Regional warming of the subtropical southeast Pacific, as appearing during *'El Niño'* conditions, effectively increase precipitation and moisture along the west coast and especially on the arid western slopes of the Andes of South America due to reduction of thermal subsidence and anticyclonic flow, as confirmed by climate models (Garreaud et al., 2010).

Possible easterly precipitation arises from moist Atlantic air masses passing the Amazon basin, leading to relief rainfall at the eastern flanks of the Andes and in parts of the Altiplano (Fig. 3). The so called *'La Niña'* conditions occur predominantly during austral summer (Dec-March), which are characterized by cooler atmospheric temperatures, easterly wind anomalies and above-average precipitation in the sub- to tropical western South America (Aceituno, 1988; Vuille, 1999; Vuille et al., 2000). These rare conditions are directly connected to the strength and position of the Bolivian High (Vuille et al., 2000). A southward displacement and intensification of

the Bolivian High hamper upper tropospheric westerly wind flow and supports a strengthening of the easterlies and a corresponding moisture flux from the Amazon basin (Fig. 3). These air masses can spill over the Central Andes and reach the upper Western Andean flank (Vuille and Keimig, 2004). Precipitation originating from the Atlantic mostly affects the eastern high Andes and the Altiplano, indications of Atlantic-sourced moisture in the Central Depression and Coastal Cordillera are not evident.

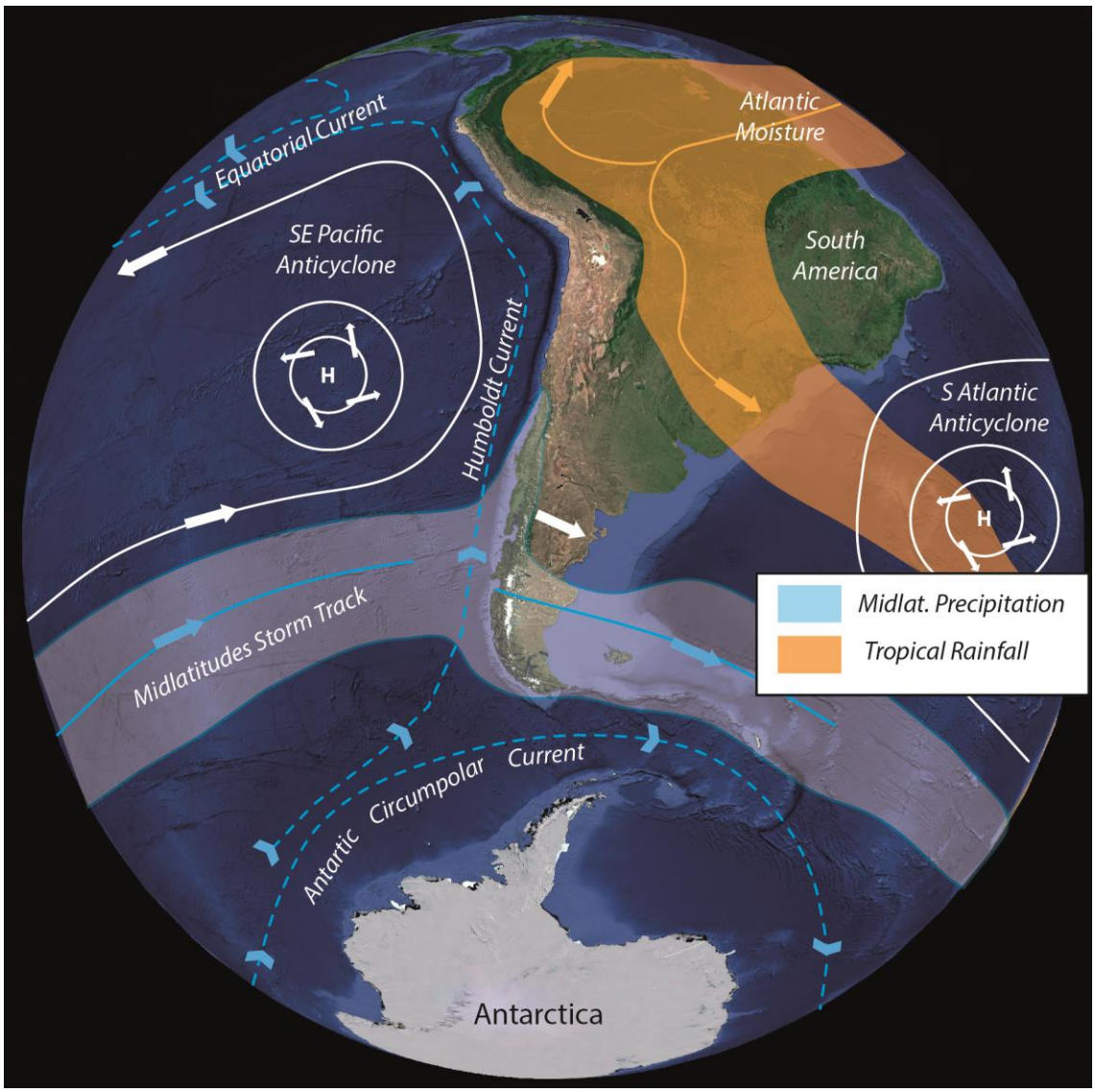

Figure 3: Schematic sketch of the low-level atmospheric flow (roughly from surface to about 1500 m.a.s.l., modified from Garreaud et al. (2009). Additionally, major ocean currents and climate features are shown.

The hypothesis that climate conditions/variability is out of phase or anti-phasing between the low-level Atacama Desert and the Altiplano-Puna is under debate and difficult to test due to the lack of continuous long paleoclimate records from the core of the Atacama Desert. However, preliminary research suggests such conditions may have occurred during the Holocene (Fontugne et al., 1999). During negative *El Niño* Southern Oscillation (ENSO), i.e. *El Niño* conditions, dry conditions persists on the Altiplano, which can be supported and reconstructed from lake sediments of Lake Titicaca (Fritz et al., 2004; Fritz et al., 2007; Baker and Fritz, 2015). On the other hand, during positive ENSO, i.e. *La Niña* conditions, a tendency towards wetter conditions, with enhanced flow of easterly Atlantic air masses from the Amazon Basin are observed (Garreaud et al., 2003; Houston, 2006b).

The third moisture source is fog, locally named '*camanchaca*' (Cereceda et al., 2002; Cereceda et al., 2008). The South Pacific Anticyclone and the position at the subtropical high pressure belt cause strong subsidence and the formation of a thermal inversion producing only stratus and stratocumulus clouds (Cereceda et al., 2008; del Río et al., 2017). These clouds reach the Coastal cliff between 400 and 1000 m altitude and create fog oases (Cereceda et al., 2002). Where the topography allows a deeper penetration through corridors, such as the Río Loa canyon, fog can penetrate deep into the hinterland. This type of moisture transport is the most important source of water in the otherwise arid desert and contributes significantly to the bio-geological formation of soils and soil crusts in the Atacama Desert (Cáceres et al., 2007; Wang et al., 2015; Cosentino and Jordan, 2017).

3. Objectives

Within this contextual framework, the research projects reported in this dissertation have the attempt to provide a better understanding of the landscape processes in the hyperarid Atacama Desert, as well as to give new insights into the evolution towards hyperarid conditions within the Atacama Desert. The overarching goal of these projects is to reconstruct long-term patterns of climate parameters, e.g. paleo-precipitation, in the central Atacama Desert, and their effects on geomorphology and geomorphological processes. Due to the application of complementary methods, which cover different timescales, a prolonged reconstruction is possible, combining different chronostratigraphic dating techniques. These studies link new results and reconstructions from the Central Depression and the Coastal Cordillera and contribute to a better understanding of the paleo-landscape and climate evolution in arid to hyperarid environments.

The obtained data were used to achieve the following objectives:

(1) Reconstruct paleoclimate conditions and landscape processes within the hyperarid core of the Atacama Desert and the evolution towards hyperaridity.

(2) Contribute to the ongoing debate of the onset of hyperaridity.

(3) Discuss the importance of spatial and temporal variations of hyperaridity and paleo-precipitation episodes, defining spatial borders of hyperaridity and their fluctuations.

(4) Identify short-term (Quaternary) and long-term (Paleogene/Neogene) climate variations in the Atacama Desert.

Chapter 4 presents research conducted in the southern Central Depression on linear features, resembling shoreline terraces, around Cerro Soledad and the adjacent topographic hills (Fig. 4). In order to improve the recent knowledge about paleo lacustrine systems in the Quillagua-Llamara Basin (QLB), a terrestrial cosmogenic nuclide (TCN) study was performed in order to contribute to the recent contradictory temporal reconstruction of the Soledad lake phase. Along with this study, further insights about the basin evolution were gathered. The main focus is set on the cessation of the paleo

endohereic Quillagua-Llamara Basin (Fig. 4) within the latest lacustrine stages and the possible cause for this substantial change.

Chapter 5 presents a TCN exposure dating study of ancient alluvial fan systems south of the lower course of the Río Loa within the Coastal Cordillera (Fig. 4). The Coastal Cordillera can be defined as a more or less independent system in the Atacama Desert, concerning precipitation pathways and drainage catchments. The data obtained in this study gives major insights in the evolution of hyperaridity in the Coastal Cordillera, at the southern edge of the hyperarid core of the Atacama Desert (preservation of Miocene surfaces). It contributes to the debate about the onset and spatial variation of aridity in the Atacama Desert and represents an explanation for the spatial and temporal discrepancies related to hyperaridity in the Atacama Desert. Moreover, the achieved age constraints give further insights in the tectonic history of fault systems in the Coastal Cordillera and permits the combination with previous published data about lacustrine phases within the southern Central Depression. This study contributes to the knowledge of the temporal onset and cessation of endorheic drainage systems in the Central Depression.

Chapter 6 focuses on a sedimentary paleoclimate record from a small endorheic basin within the Coastal Cordillera, one of the most isolated patches in the Atacama Desert (Fig. 4). To date, paleoclimatic and environmental records are restricted to the Central Depression and the Andean foothills. Records and paleoclimate archives from the Coastal Cordillera are currently lacking. The results of this project reveal information on the fluctuations of prevailing hyperarid climate conditions and the frequency of intervening “wet” phases in comparison to regional and global climate records. This study gives further insights into the complexity and difficulty of dating such sediments with common dating techniques.

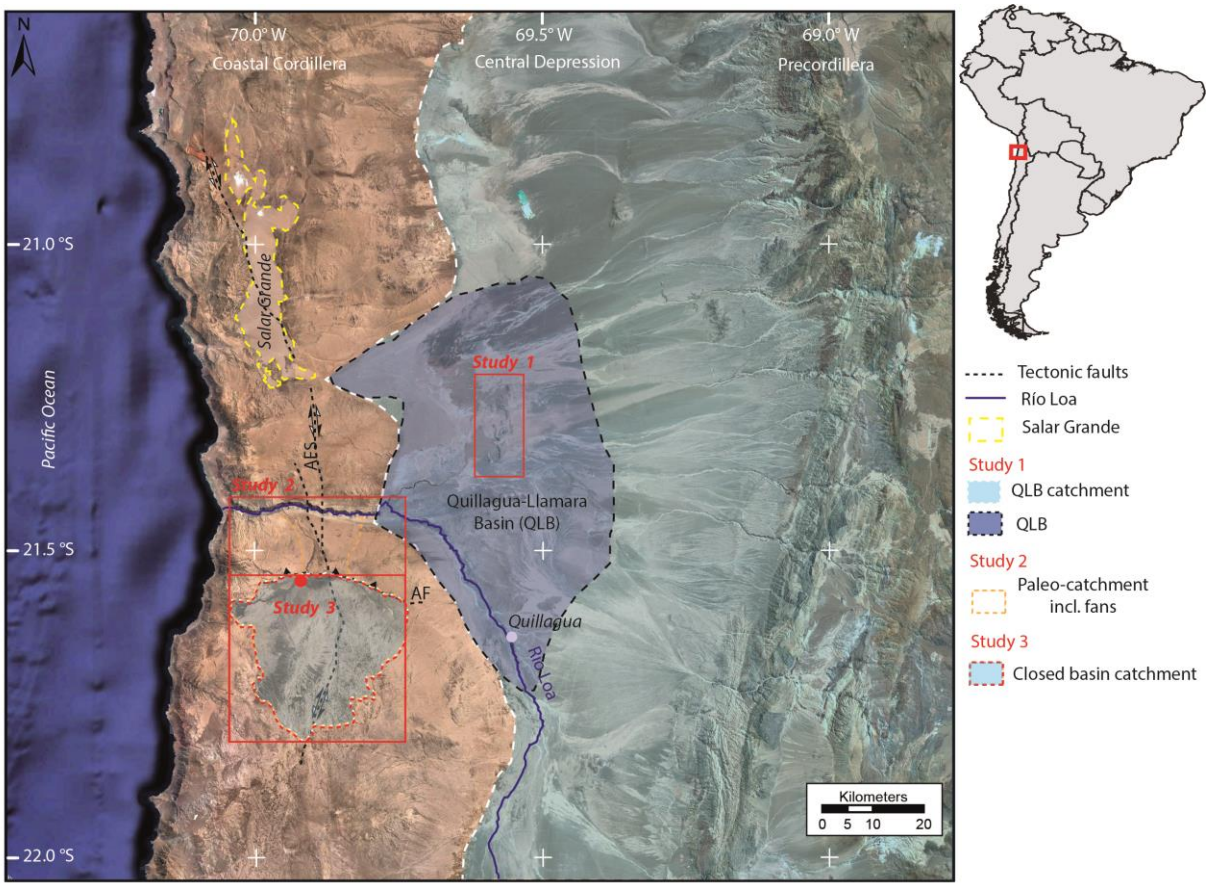

Figure 4: Google Earth Satellite Image (03.07.2018 Data Image Landsat / Copernicus) indicating all study sites dedicated to this thesis. Major landscape features are marked, e.g. Salar Grande, Río Loa, boundary between Coastal Cordillera and Central Depression (stippled white line). Drainage catchments for each study area are marked in light blue. Note that sedimentation systems in the Central Depression (Study 1) have headwaters deep in the Precordillera and Altiplano and are dominated by more distant precipitation sources than isolated drainage and depositional systems in the Coastal Cordillera (Studies 2 and 3).

Chapter 7.1 gives a synthesis of the major findings based on the presented publications in Chapters 4-6 and existing studies. It focusses on the limitations of landscape reconstruction and points to major uncertainties and gaps in our knowledge about the area. It points to the importance of the geographical position of climate archives to reconstructed climate variations. Although, the general expression of the Atacama Desert is to be the driest and the oldest desert on Earth, there are variable internal spatial and temporal delimitations, illustrating the heterogeneity of the climate history of the Atacama Desert. The question “Where does the moisture come from?” plays a major role in identifying the major influencing factors modifying the hyperarid Atacama Desert over longer time-scales.

Chapter 7.2 provides a brief discussion about potentials and limitations of the applied methods and investigated archives. It focusses on cosmogenic nuclide exposure dating and sediment archives.

Chapter 8 finally provides a brief discussion about outstanding questions, which evolved from the studies presented in this thesis. First ideas are shortly mentioned, which could answer these questions for future scientific research in the Atacama Desert.

4. Evidence for multiple Plio-Pleistocene lake episodes in the hyperarid Atacama Desert

Journal Article: (2018)

Received 4 July 2017, Revised 22 November 2017, Accepted 22 November 2017, Available online 24 November 2017.

Ritter, B., Binnie, S. A., Stuart, F. M., Wennrich, V., and Dunai, T. J., 2018, Evidence for multiple Plio-Pleistocene lake episodes in the hyperarid Atacama Desert: Quaternary Geochronology, v. 44, p. 1-12. doi.org/10.1016/j.quageo.2017.11.002

Quaternary Geochronology 44 (2018) 1–12

Contents lists available at ScienceDirect

Quaternary Geochronology

journal homepage: www.elsevier.com/locate/quageo

Evidence for multiple Plio-Pleistocene lake episodes in the hyperarid Atacama Desert

Benedikt Ritter[a,*], Steven A. Binnie[a], Finlay M. Stuart[b], Volker Wennrich[a], Tibor J. Dunai[a]

[a] Institute of Geology & Mineralogy, Zuelpicher Strasse 49b, 50674 Cologne, Germany University of Cologne, Germany
[b] Isotope Geosciences Unit, Scottish Universities Environmental Research Centre, East Kilbride G75 0QF, UK

ARTICLE INFO

Keywords:
Cosmogenic nuclide exposure dating
Atacama desert
Lake shorelines

ABSTRACT

Cosmogenic nuclide exposure dating of ancient shoreline terraces of the Quillagua-Llamara Soledad Lake in the central Atacama Desert of northern Chile provides new insights in the paleohydrology of the driest desert on Earth. The lake developed in a paleo-endorheic drainage system in the Central Depression prior to draining into the Pacific due to incision of the Río Loa canyon. The durations of lake stages were sufficiently long to form wave-erosion induced shoreline terraces on the wind-exposed slopes of former islands. Successively younger shoreline levels are preserved over an elevation range of 250 m due to progressive uplift of the islands coeval with the lake stages. Cosmogenic ^{10}Be- and ^{21}Ne-derived exposure ages of the shorelines reveals that the hyperarid conditions in the Río Loa catchment were interspersed by several pluvial stages during the Pliocene and Pleistocene, which generated a large and persistent lake in the Quillagua-Llamara basin. The exposure ages of the final lake stage provide the maximum age for the incision of the Río Loa canyon (274 ± 74 ka) and the subsequent breaching of the Coastal Cordillera.

1. Introduction

The Atacama Desert of northern Chile is one of the driest places on Earth; the extreme hyperarid core (Coastal Cordillera, Central Depression; Fig. 1) receives less than 10 mm/yr of precipitation (Houston and Hartley, 2003). While the main factors controlling hyperaridity in the Atacama Desert are established, the onset and permanence of hyper-aridity remain a matter of debate (e.g., Sillitoe and McKee, 1996; Sáez et al., 1999; Hartley and Chong, 2002; Rech et al., 2003; Dunai et al., 2005; Nishiizumi et al., 2005; Latorre et al., 2006; Rech et al., 2006; Kober et al., 2007; Nester et al., 2007; Evenstar et al., 2009; Placzek et al., 2010; Gayo et al., 2012; Sáez et al., 2012; Jordan et al., 2014; Evenstar et al., 2017). The nearly stable position of the South American continent over the last 150 million years (Hartley et al., 2005) and the establishment of the Peru-Chile Current system at around 50 Ma (Cristini et al., 2012) support the notion that predominantly arid conditions persisted since the early Miocene (Dunai et al., 2005), and potentially even earlier (Hartley et al., 2005). Secular variations of the global climate system during the Cenozoic (Zachos et al., 2001) led to punctuations of the prevailing hyperarid climate in the Atacama Desert by wetter (though still arid) periods (e.g., Betancourt et al., 2000; Dunai et al., 2005; Nester et al., 2007; Rech et al., 2010; Sáez et al., 2012; Jordan et al., 2014; Evenstar et al., 2017). These pluvial phases are evident from Miocene-Pliocene lacustrine and fluvial sediments in the Central Depression (e.g. Gaupp et al., 1999; Sáez et al., 2012; Kirk-Lawlor et al., 2013).

Here we present new insights into the timing of relatively wet periods in the Central Depression based on exposure dating of former shoreline terraces of the Quillagua-Llamara-Soledad lake. These terraces are preserved by uplift of topographic highs in the Quillagua-Llamara basin (QLB). New cosmogenic ^{10}Be and ^{21}Ne data constrain the timing of the most recent lacustrine phases, and the eventual draining of the Quillagua-Llamara-Soledad Lake by the incision of the Río Loa canyon.

2. Background

2.1. Regional geology

The central Atacama Desert is located in the fore-arc region of the Central Andes in northern Chile (Fig. 1). The area includes three morphotectonic units; the Coastal Cordillera, Central Depression, and Precordillera. The latter is bordered by the Western Cordillera, forming an active volcanic arc (Fig. 1). The study area is located in the southern Central Depression, bound to the west by the Coastal Cordillera and to the east by the Precordillera. The Central Depression is a N-S elongated

* Corresponding author. Zuelpicher Strasse 49a, 50674 Cologne, Germany.
E-mail address: benedikt.ritter@uni-koeln.de (B. Ritter).

https://doi.org/10.1016/j.quageo.2017.11.002
Received 4 July 2017; Received in revised form 22 November 2017; Accepted 22 November 2017
Available online 24 November 2017
1871-1014/

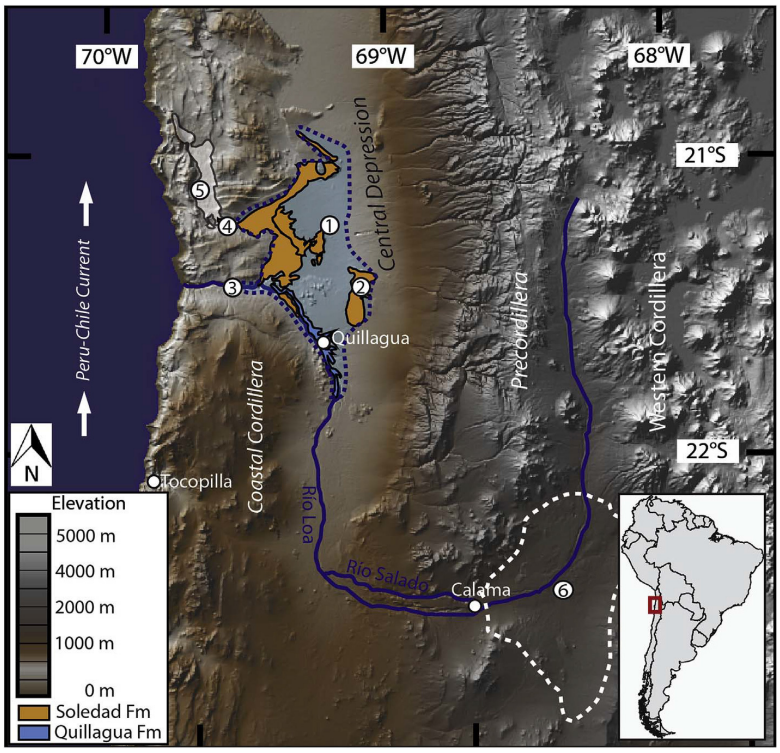

Fig. 1. Geographic setting of Quillagua-Llamara basin in the Central Depression (DEM based on ASTER GDEM data). Orange indicates outcrops of the Soledad Formation (Brüggen, 1950; Sáez et al., 2012; Quezada et al., 2013). Blue indicates outcrops of the Quillagua Formation (Sáez et al., 2012). (1) Cerro Soledad, (2) Lomas de Sal, (3) Westernmost extension of former lake, overflow of Río Loa, (4) Montón de Gloria Pass (831 m), (5) white area indicates Salar Grande, (6) dashed white line denotes the Calama basin. Translucent blue area indicates potential lake extension. (For interpretation of the references to colour in this figure legend, the reader is referred to the web version of this article.)

topographic basin that contains the Pampa de Tamarugal (PDT) and includes the QLB in the south (Fig. 1 translucent blue area). The Coastal Cordillera acts as a topographic barrier, prohibiting any appreciable sediment transport from the Precordillera to the Pacific Ocean. This has enabled the exceptional preservation of many tectonic deformation features that are caused by the coupling between the subducting oceanic Nazca plate and the South American plate in the Coastal Cordillera. E-W tectonic deformation commenced at least 6 million years ago, with fault slip rates that are typically less than 0.5 mm/year (Allmendinger and Gonzalez, 2010).

The incision of the Río Loa canyon transformed the QLB from an endorheic into an exorheic basin, while parts of the northern PDT, north of Quebrada Guatacondo, remained endorheic. Based on the age of the Soledad Formation this could have occurred during the late Pleistocene (Sáez et al., 2012) or early Pliocene (Quezada et al., 2013). Relict deposits of the former lacustrine and evaporitic facies and/or corresponding diagenetic equivalents of the Quillagua-Llamara-Soledad Lake (QLSL) are regionally widespread in the southern PDT (Fig. 1). These may reflect pluvial periods in the last 10 million years (Sáez et al., 2012). Although the sediment sequences have been dated several times, some ages are contradictory and allow alternative environmental reconstructions (Sáez et al., 1999; Sáez et al., 2012; Quezada et al., 2013; Jordan et al., 2014).

The Central Depression is a forearc basin (Jordan et al., 2014; Evenstar et al., 2017), bound to the west by normal faults in the Coastal Cordillera. The basement of the Central Depression consists of Palaeozoic and Mesozoic rocks, which are locally uplifted above the present-day valley floor. In the study area, the depression is filled by up to 1000 m of Eocene to Pliocene alluvial and lacustrine sediments, interbedded with volcanoclastic deposits (Jensen et al., 1995; Sáez et al., 1999; Hartley and Evenstar, 2010; Jordan et al., 2010; Jordan et al., 2014). Alluvial fan deposits are derived almost exclusively from the Precordillera to the east (Carrizo et al., 2008; Nester, 2008; Jordan et al., 2014). The Tertiary PDT basin was formed by the combination of N-S and NW-SE orientated fault system activity, predominantly of currently supratenuous faults (Sáez et al., 1999). Neogene reverse faulting on the Precordillera fault zone has been confirmed for the northern PDT (Victor et al., 2004; Nester, 2008), as well for the southern part (Nester, 2008; Nester and Jordan, 2012). Studies indicate that fault systems in the Coastal Cordillera were reactivated during the past 6 Ma and their effects extend into the Central Depression (Allmendinger et al., 2005).

North to South trending elongated hills on Mesozoic basement in the PDT (Cerro Soledad Figs. 1 and 3, Cerro Challacollo, and Cerro Longacho, see Nester (2008)) protrude up to 300 m above the plain. Carrizo et al. (2008) identified low angle reverse faults near the Salar de Bellavista to be responsible for the uplift of topographic highs after 18-19 Ma (see Fig. 16a in Carrizo et al., 2008). Evidence for young deformation within the basin can be found at Lomas de Sal (Fig. 1) where, a ~100 m thick Plio-Pleistocene sequence has been uplifted by reverse faulting (Nester, 2008). Geomorphological evidence for tectonic deformation in the vicinity includes folded diatomites at the base of Cerro Mogote (Sáez et al., 1999; for location see Fig. 3).

The detailed kinematics of the inferred uplift and deformation around Cerro Soledad, Cerro Mogote and Cerros de Hilaricos is poorly known. Recent mapping by SERNAGEOMIN (Quezada et al., 2012) provide a large scale framework for the structural geology, but the resolution of this mapping is not fine enough to resolve the tectonic kinematics around those exceptional highs within the Central Depression. Statements about the precise occurrence of faults and their appearance in conjunction with folds remain approximations and require more detailed studies.

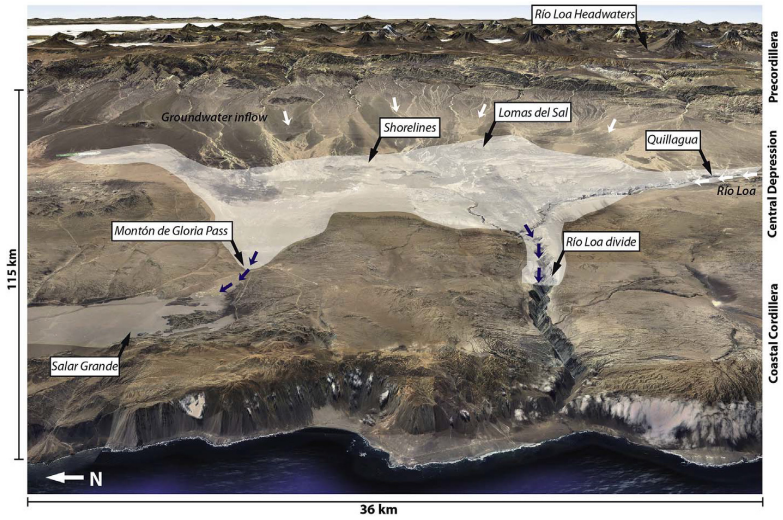

Fig. 2. Google Earth Satellite 3D Model (based on Image Landsat/Copernicus – Data SIO, NOAA, U.S. Navy, NGA, GEBCO) with a twofold altitude exaggeration. The pale shaded area displays potential lake extension based on outcrops. White arrows indicate major water inflow pathways, blue arrows mark overflow paths toward the (1) Salar Grande (present altitude 831 m ± 10 m) and (2) Río Loa (present altitude 830 ± 10 m). The latter was the outflow during the breach of the endorheic drainage system of the Quillagua basin. (For interpretation of the references to colour in this figure legend, the reader is referred to the web version of this article.)

2.2. Local hydrology – precipitation pathways

The catchment of the QLB/Río Loa (32,820 km^2 from Houston, 2006c; Jordan et al., 2015a) derives the majority of its water from the Western Cordillera to the East. It drains into the QLB via groundwater flow and surface flow in the perennial Río Loa (Figs. 1 and 2). Runoff and groundwater flow was higher during pluvial periods in the Plio-Pleistocene (Houston, 2006b).

Due to the temperature inversion above the cold Peru-Chile Current, westerly precipitation in the Atacama Desert originating from the Pacific Ocean is sparse. However, during infrequent rain events, surface drainage can occur due to precipitation coming from the Pacific as north migrating low pressure systems are diverted (e.g. Bozkurt et al., 2016). Such sporadic westerly precipitation events include the flood of March 2015 in northern Chile, which brought significant precipitation, though this decreased with increasing altitude and was limited to south of Quillagua (Bozkurt et al., 2016; Wilcox et al., 2016). Such events are connected to the establishment of El Niño conditions favouring either cut-off north-migrating low-pressure cells from the Southern Westerlies (Vuille and Ammann, 1997), or destabilization and reduction of the temperature inversion at the Chilean coast (McKay et al., 2003). Climate models predict regional warming of the subtropical southeast Pacific during 'El Niño' conditions that effectively increase precipitation and moisture along the west coast of South America, and on the arid western slopes of the Andes due to the reduction of thermal subsidence and anticyclonic flow (Garreaud et al., 2010). Torrential rain during the 'El Niño' of 1997-98, for example, created the second largest lake in Peru in the Sechura Desert (Woodman, 1998). Earlier, long-lasting lake stages in the QLB are evidenced by lacustrine deposits of the Quillagua Formation, which suggest permanent 'El Niño-like' conditions persisted during the Pliocene (Sáez et al., 2012). Similar 'El Niño-like' conditions in the Atacama were also postulated for several wet periods during the Pleistocene (Ortlieb et al., 1996; Contreras et al., 2010; Wang et al., 2015). The main and more regular source of moisture is Atlantic air masses, despite depletion by orogenic rainfall at the eastern flanks of the Andes and in parts of the Altiplano. These easterly rains, which are enhanced during typical 'La Niña' conditions, are usually characterized by cooler atmospheric temperatures, easterly wind anomalies, and above average precipitation in the sub-to tropical western South America (Aceituno, 1988; Vuille, 1999; Vuille et al., 2000). The amplitude of 'La Niña' conditions in South America is governed by the strength and position of the Bolivian High (Vuille et al., 2000). A southward displacement and intensification of the Bolivian High hampers upper tropospheric westerly wind flow as well as strengthening easterlies and the corresponding moisture flux from the Amazon basin. These air masses spill over the Central Andes and reach the upper Western Andean flank (Vuille and Keimig, 2004) causing precipitation that decreases rapidly with elevation (Houston and Hartley, 2003). For instance, the source region of the Río Loa at around 4000 m receives about 100 mm rain per year, whereas the Río Loa valley in the Central Depression, at about 1000 m elevation (e.g. at Quillagua Figs. 1 and 2), has annual rainfall of less than 1 mm (Houston and Hartley, 2003). As aridity is controlled by large-scale atmospheric circulation patterns, the current orographic precipitation gradient pattern has most-likely persisted over the longer-term, despite the overall amounts of precipitation having varied (Jordan et al., 2014).

Presently the flow rates of the perennial Río Loa are 0.6 m^3;/s (post 1976). In 1918 prior to the significant water extraction the discharge was 3.6 m^3;/s (both measured at the outflow into the Pacific; Salazar, 2003). Due to the high annual evaporation rates (i.e. > 3500 mm/a at 1000 m elevation; Houston, 2006a) even the higher discharge rate could not sustain an expansive lake in the central valley. For example, the outcrops of the Soledad Formation indicated a minimum lake extension of ~2,570 km^3 requiring more than the recent perennial inflow of the Rìo Loa (1.14*10^8 m^3/a) to sustain a lake by high evaporation rate of 9.01*10^{13} m^3/a.

2.3. Lacustrine sediments of QLB

The sedimentary sequence of the QLB consists of alluvial strata, interbedded with lacustrine sequences and volcanoclastic deposits (Sáez et al., 1999, 2012). Fluvial sedimentation predominantly occurred to the south of Quillagua and was presumably controlled by the sediment input of the Proto-Río Loa, whereas lacustrine sedimentation was concentrated in the central basin around Cerro Mogote, Cerro Soledad, and Quillagua (Sáez et al., 2012) (Figs. 1, 2 and 3a). The first Miocene sediment units are gypsum-anhydrite cemented siliciclastic deposits of the Hilaricos Fm. These are overlain by diatomites, marls, silty limestones, gravelly sandstones, and occasional volcanoclastic deposits of the Quillagua Fm (Sáez et al., 1999). The final lacustrine episode of the QLSL is represented by the Soledad Fm, consisting of halite-gypsum evaporitic sediments with minor siliciclastics (Chong et al., 1999; Pueyo et al., 2001; Sáez et al., 2012, Fig. 1). Massive (> 10 m thickness) open water evaporites with large, dm-scale, bottom

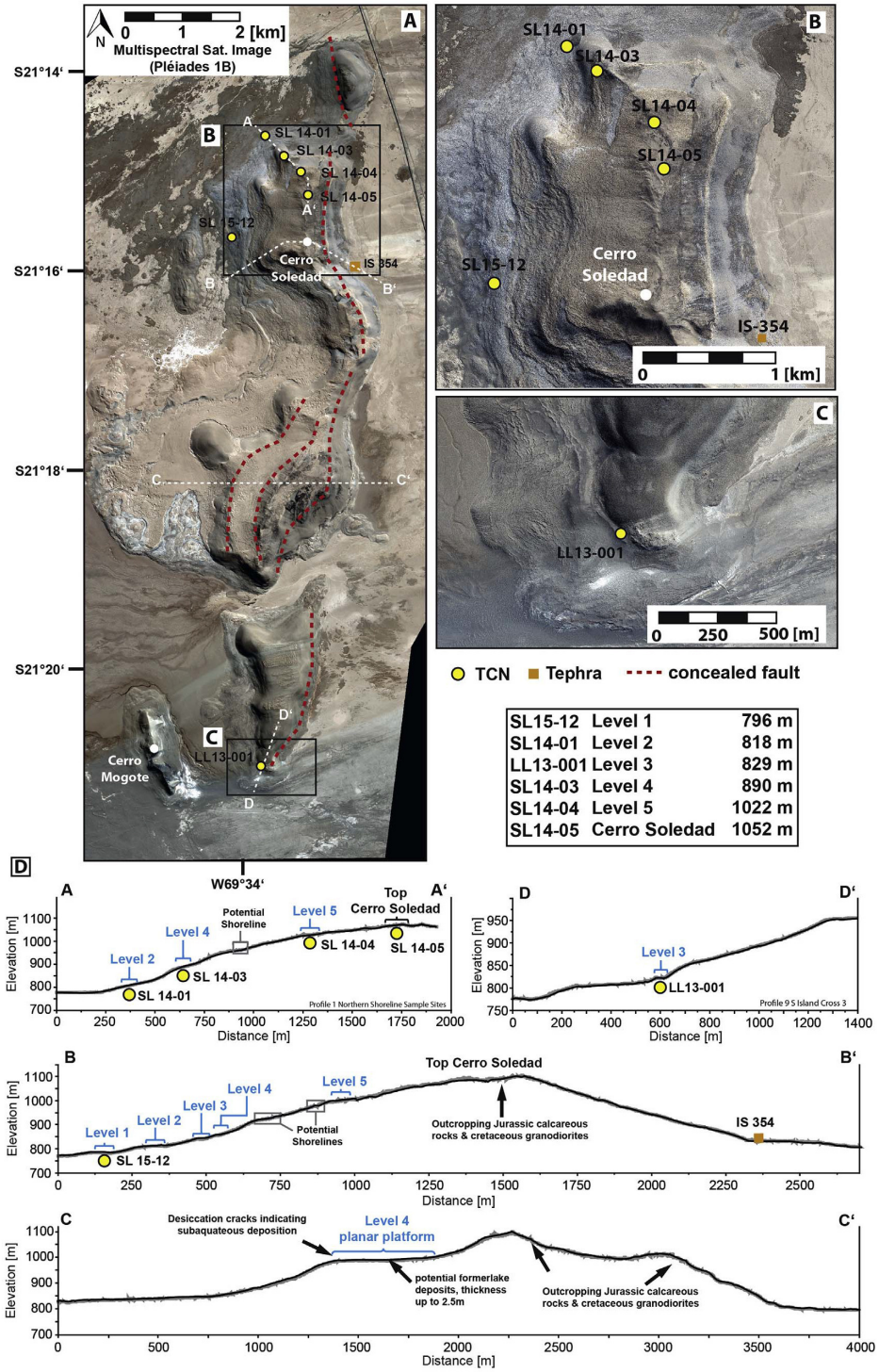

Fig. 3. (A-C) High resolution Pansharpened Multi-Spectral Image (Pléiades-1B) of the study area. Yellow dots indicate sampled shoreline terraces, orange square indicates dated tephra deposit (Quezada et al., 2013). White dashed lines highlight topographic profiles (D). Dashed red lines indicate potential concealed faults. (B) Northern island. (C) Southern island. (D) Topographic profiles based on a high resolution DEM (Pléiades-1B resolution ~60 cm) of shorelines features. Corresponding and sampled shoreline terraces are marked, including potential shorelines terraces derived by DEM analysis. (For interpretation of the references to colour in this figure legend, the reader is referred to the web version of this article.)

nucleated chevron gypsum crystals, occur as erosive remnants along the eastern section of the southern margin of the Rio Loa canyon (this study, supplementary data). The near-continuity of surficial deposits and the geochemical signature of the Soledad Fm evaporites (Br-content and S-isotopes, Pueyo et al., 2001), support the notion of a temporary connection between the QLB and the Salar Grande basin (Figs. 1 and 2, Chong et al., 1999; Sáez et al., 1999). This connection via the Montón de Gloria Pass (current elevation 830 m, Chong et al., 1999) is thought to have been disrupted by fault reactivation in the Coastal Cordillera (Allmendinger et al., 2005). Outcrops of the Soledad Fm remnants (Quezada et al., 2012; Quezada et al., 2013) indicate a minimum lake surface area of ~2570 km^2 (Figs. 1 and 6, this study). Spilling points at the Montón de Gloria pass towards the Salar Grande (current elevation 831 ± 10 m, Chong et al., 1999; Pueyo et al., 2001) and at the Río Loa (mean current elevation 830 ± 10 m, top of outcropping sediments, orange surface in Fig. 1, westernmost reconstructed lake extension, Sáez et al., 1999), indicate the lake level could not exceed 830 ± 10 m (Figs. 1, 2 and 6). A higher lake level would have drained the basin, presumably initiating the incision of the Río Loa. The elevation of present day outcrops of Soledad Formation rocks may exceed the present day elevation of the spilling points (up to 220 m, Fig. 3) due to differential tectonic uplift since deposition.

Although different approaches have been used to date the Soledad Fm, its chronology is still under debate (Sáez et al., 2012; Quezada et al., 2013). Ar/Ar ages of tephra layers in the halite sequence of the Lomas del Sal were used to constrain the deposition age of the lower Soledad formation to between 0.21 ± 0.06 Ma and 0.098 ± 0.042 Ma (Sáez et al., 2012). However, four ash layers, intercalated with anhydrite-sand successions of the Soledad Fm, exposed at Cerro Soledad, Salar Sur Viejo and at Cerro Cachango, yield Ar/Ar ages between 3.16 ± 0.07 Ma and 3.73 ± 0.02Ma Quezada et al. (2013). These contradictory ages mean that there is a considerable uncertainty in both the spatial assignment of sediments to the Soledad formation and its deposition age.

2.4. Shoreline terraces

The conspicuous linear features at Cerro Soledad were first suggested by Brüggen (1950) to represent abandoned shorelines (Fig. 3) of a lake, which was around 80 m deep. Subsequent studies suggested that the lake was deeper (200 m, Hollingworth, 1964). Stoertz and Ericksen (1974) and Naranjo and Paskoff (1982) noted that the former shorelines are not level, reflecting differential tectonic uplift across the region. In an alternative hypothesis, Rieu (1975) interpreted these linear features as a result of uplift and tectonic displacement in a horst-graben structure, without invoking the presence of a lake. Naranjo and Paskoff (1982) identified four distinct shoreline levels at Cerro Soledad, spanning more than 200 m vertical distance, and reported abundant well-rounded pebbles on all levels. They assigned the rounding of these pebbles to wave action of the paleo-lake 'gran lago salado de Soledad (*sensu* Brüggen, 1950)'. These shorelines are mostly cut into halite (Naranjo and Paskoff, 1982) but also into underlying bedrock (this work; see also Fig. 3). The occurrence of pebbles is laterally limited to bedrock outcrops and pebbles are of the same lithology as the underlying bedrock (this study). Presently all but the lowest shorelines are above the current elevation of topographic spilling points of the paleo-lake (Fig. 2), indicating significant differential tectonic movement since the creation of the shorelines.

The hypothesis that an ephemeral lake was responsible for the creation of the linear features on the Cerro Soledad and neighbouring topographic highs, as proposed by Brüggen (1950), Hollingworth (1964) and Naranjo and Paskoff (1982), is supported by the following observations: (1) the linear features nearly completely encircle Cerro Soledad, on near horizontal levels (supplementary data, Fig. 3); (2) they are preserved in soft sedimentary rocks as well as in bedrock notches, which occur at exactly the same elevation (supplementary data, Fig. 3); (3) rounded pebbles occur localized at the bedrock notches and bedrock outcrops, and are absent elsewhere; (4) the pebbles are of the same lithology as the local bedrock, pebbles of allochthonous lithology are absent; (5) western, wind-exposed, flanks of the hills have wider platforms, as would be expected if wind fetch is important for their creation; (6) the Soledad formation is dominated by salar/lake deposits (Sáez et al., 1999, 2012; Quezada et al., 2013) and (7) bottom nucleated evaporites (supplement, Fig. 2) record ephemeral open water conditions until the final stages of the deposition of the Soledad formation. Alternative explanations for the platforms in sedimentary rocks, such as differential erosion due to variable degree and type of cementation and an absence of a lake, do not explain the repeated coincidence between the elevation of platforms in sedimentary rocks and bedrock notches and the near-horizontal nature of these linear features. However, it is possible that the creation or preservation of platform levels in sedimentary rocks is linked to enhanced cementation rather than wave action, since near-shore groundwater levels during lake stages would be identical to the corresponding lake levels. Explaining the occurrence of rounded pebbles by fluvial transport from elsewhere would be in conflict with the observation that allochthonous lithologies are absent and that pebble occurrences are limited to rare local bedrock outcrops.

The terraces along the (north-)western flanks of the Cerro Soledad are most easily recognized, both from satellite imagery (Fig. 3) and in the field. They are traceable throughout the hills protruding from the floor of the PDT (Fig. 3). Shorelines at the eastern, wind-averted flanks are less developed or absent. Shoreline formation due to wave-erosion was likely enhanced by the long wind fetch and a sufficiently deep water body upwind, as was available during lake-high stands of the QLSL (prevailing westerly winds had > 15 km fetch; see also Fig. 6). Wave action in lakes can erode shorelines that are tens of metres wide into bedrock within a few hundred years (Oviatt et al., 1992; Garcin et al., 2012; Lifton et al., 2015). While we do not know the strength of the paleo-winds and the kinetics of the shore erosion, we note that the setting of the ancient islands in the QLSL is conducive for shoreline formation. The pronounced aridity of the Atacama Desert, and the uplift of the shorelines above possible future lake-levels after their formation, aided their long-term preservation.

2.5. Sampling locations

The bedrock of the paleo-islands, i.e. Jurassic marine sediments and volcanic rocks, at the northern island (Fig. 3A and B) joined by Cretaceous granodioritic rocks, is almost completely covered by evaporites of the Soledad Formation. Bedrock outcrops are limited to the tops of the paleo-islands (above ~1000 m elevation) and to spurs. Planar platforms are preserved in evaporitic cemented siliciclastic sediments and the bedrock spurs (Fig. 3A, D). Wave-cut platforms cut into the evaporites, however, are largely devoid of pebbles (and other rock clasts), whereas the wave-cut shorelines on bedrock have locally abundant pebbles. The variable abundance of pebbles suggests that they are locally derived, which is supported by the matching lithologies of pebbles and exposed bedrock. We sampled small platforms on, or near spurs (LL13-001; SL-14-01; SL14-3; SL14-4; Fig. 3A-C), below bedrock cliffs (LL13-001; SL-14-01; SL14-3), and on a planiform area near the summit of the northern island (SL14-05; Fig. 3A-C). SL15-12 samples were retrieved from a wide platform at the western flank of the northern island. While it was cut into evaporitic-cemented siliciclastics, it harboured bedrock clasts and some pebbles. The bedrock fragments give this platform a different appearance in the field and on aerial photography (grey shades in Fig. 3; as compared to beige colours of the other evaporite platforms). The height of the cliffs behind the bedrock platforms allows for a maximum of few meters of vertical erosion into the spurs (3-10 m), the amount of vertical erosion of rocks supplying the pebbles on surfaces without a backing cliff is not constrained. Incomplete shielding/pre-exposure can therefore be expected (Dunai,

2010). Since the shoreline deposits are thin (< 50 cm thickness, mostly < 10 cm), depth profile sampling would not constrain pre-exposure of the sediments (Dunai, 2010). Site SL14-04 on the spur had no bedrock cliff. It was a shallow depression (ca. 10 cm lower than surrounding bedrock; ca. 10 m^2 area) that had abundant, perfectly rounded pebbles, and only a few fragmented clasts. This pebble deposit exhibits a weak patterning due to pelo- or haloturbation (cryoturbation can be ruled out due to the prevailing climatic conditions). Generally, post-depositional shielding of samples from cosmic rays due to intermittent burial, or more likely in this case by exhumation of the samples originally deposited beneath a sedimentary cover, cannot be excluded. The nature of the shoreline deposits renders it difficult ascertain if they have eroded significantly since their deposition. The lack of extensive talus aprons downslope of the shorelines, however, indicates that the shoreline deposits are predominantly well preserved. At all sites our target materials were pebbles and bedrock clasts. The lithologies most amenable for exposure dating (e.g. vein quartz and quartz-rich lithologies), tend to be less rounded than quartz-poor/quartz-free lithologies; therefore, several clasts (n ≥ 6) were sampled (only if rounded pebbles were present at the same level). On finding localized concentrations of quartz fragments, which may indicate *kernsprung* (splitting of pebbles), only one fragment per cluster was sampled in order to avoid sampling multiple fragments of the same clast. In total we sampled six sites, five on the northern island and one on the southern one (Fig. 3). The preserved rounding of pebbles, and preserved angularity of clasts, allow for a few mm of erosion of the pebble surfaces at most.

3. Analytical methods

To determine single clast exposure ages we analysed quartz for ^{10}Be, ^{26}Al, and ^{21}Ne. The quartz was prepared as AMS (Accelerator Mass Spectrometry) targets following either the standard approach or the single-step column approach outlined in Binnie et al. (2015). The targets were measured for ^{10}Be at CologneAMS (Dewald et al., 2013), normalized to the standards of Nishiizumi et al. (2007). Neon isotope analyses were performed at SUERC following the procedures outlined in Codilean et al. (2008) using the CREU quartz (Vermeesch et al., 2015) as internal standard. Specific sample preparation and analysis details are in the supplementary data.

Exposure ages are derived from the CRONUS-Earth calculator version 2.0 (Marrero et al., 2016), using the scaling factors of Lifton et al. (2015). Topographic shielding factors for each sample site were measured in the field. We assumed a density of 2.65 g/cm^3, a zero erosion rate for the pebbles and employed the 07KNSTD flag in the CRONUS-Earth calculator. Mean ages of populations of clasts from one site were calculated after the removal of outliers, using Chauvenet's Criterion (Taylor, 1997). Note, all age uncertainties reported are one standard deviation. Specific details on the age calculation are in the supplementary data, including a geomagnetic database sensitivity test using CREp (Martin et al., 2017). Analytical results and ages are provided in Table 1.

4. Results

The mean ^{10}Be exposure ages obtained for the shoreline deposits (Table 1; Fig. 4) span a wide range: from ~275 ka at the lowest shoreline level (Level 1) to ~3 Ma for the deposits on the top of the Cerro Soledad (Top). Several individual clasts have significantly older exposure ages than the majority at a given site. Most probability density plots of exposure ages of the individual locations (Fig. 4) have a positive skewness, with a tail towards higher ages. All outliers identified by Chauvenet's Criterion (Taylor, 1997) are older ages. All ^{26}Al ages of individual clasts (n = 5; supplementary data) are concordant with the corresponding ^{10}Be ages. The combined ^{26}Al and ^{10}Be data are consistent with a simple, single stage exposure history (see Supplementary Data). In one instance, site SL14-04, the scatter of the limited data did not permit the determination of a meaningful average age (the limited number of measurements is due to the scarcity of quartz-bearing clasts at that site). Individual ^{21}Ne exposure ages of clasts are either significantly higher than the corresponding ^{10}Be ages of a specific site (shorelines SL14-01; SL14-03, SL14-04) or are concordant (e.g. SL14-05; top of Cerro Soledad).

In general, the cosmogenic nuclide data confound the expectation of significant pre-exposure for some clasts in each population, which is based on the limited mass removed for the creation of the shorelines. The first line of evidence for pre-exposure is the positive skewedness of ^{10}Be age-populations (Applegate et al., 2010); the second is the significantly higher ^{21}Ne-ages obtained in many samples (SL14-01, SL14-03, SL14-04), except for the highest shoreline (SL14-05). ^{21}Ne is stable, thus long-term production in partially shielded positions in the bedrock can add a higher pre-exposure signal than is possible for ^{10}Be, particularly if the duration of pre-exposure is protracted. In principle, the youngest age obtained would provide the most likely age, if periods of burial or exhumation have not occurred (Applegate et al., 2010). It appears that the process leading to the planation of the Top of Cerro Soledad removed sufficient material to obliterate a pre-exposure signal. Since we cannot exclude some exhumation (see previous section), the best estimations for the timing of shoreline formation are the arithmetic mean ^{10}Be ages, rather than the youngest ages obtained.

On top of Cerro Soledad (SL14-05, 1051 m) the mean ^{10}Be age is 2.92 ± 0.24 Ma (n = 3). The corresponding ^{21}Ne age is indistinguishable from this (3.05 ± 0.12 Ma). All ^{10}Be and ^{21}Ne ages of individual clasts are concordant; indicating a continuous exposure for the clasts at the sampling location and negligible post-depositional exhumation. One clast at this sampling location has a significantly older age (4.5 ± 0.6 Ma ^{10}Be and 4.8 ± 0.2 Ma ^{21}Ne) and was not included in the mean (see Methods section). On shoreline level 5 (SL14-04, 1022 m) ^{10}Be ages vary between 260 ka and 4.5 Ma, while ^{21}Ne ages range from 1.9 Ma to 21.6 Ma. The ^{10}Be and ^{21}Ne ages of individual clasts are not concordant, with the ^{21}Ne ages being 3 to 4 times higher than the corresponding ^{10}Be ages. The highest ^{21}Ne exposure age (21.6 ± 0.7 Ma) is amongst the oldest reported for the Atacama Desert (Dunai et al., 2005; Carrizo et al., 2008; Evenstar et al., 2009, 2017). Since a much longer exposure is unlikely, this indicates that the exhumation of the material that sourced the pebble was shallow. The high age dispersion is probably due to pre-exposure, combined with pelo-/haloturbation inferred for this site (see section on sample locations), and prevents the calculation of a meaningful age for this site. The mean ^{10}Be age from shoreline level 4 (SL14-03, 890 m) is 1.27 ± 0.47 Ma (n = 5, all clasts). The mean ^{21}Ne age is significantly older at 1.85 ± 0.12 Ma (n = 2). In one instance from this level, the ^{10}Be and ^{21}Ne ages of an individual clast agree. Shoreline level 3 (LL13-001, 829 m) gives a mean ^{10}Be age of 540 ± 160 ka (n = 5; one outlier). Due to the generally small size of pebbles on this level no material for ^{21}Ne measurements could be spared. On shoreline level 2 (SL14-01, 818 m) the mean ^{10}Be age is measured as 392 ± 37 ka (n = 5; one outlier). All ^{21}Ne ages of individual clasts are approximately twice the corresponding ^{10}Be ages. The lowest elevation site, shoreline level 1 (SL15-12, 796 m), produces a mean ^{10}Be age of 274 ± 74 ka (n = 5; one outlier). As with shoreline level 3, the paucity of quartz is such that no material for ^{21}Ne measurements was available.

The mean ^{10}Be ages of shoreline levels shows a strong positive relationship with present day elevation (Fig. 5), suggesting constant uplift. If shoreline levels were created at similar recurring relative lake levels (relative to the paleo-island), the average tectonic uplift rate of the emergent paleo-island is 94 ± 10 m/Ma (2σ). The present day elevations of the paleo-spillways are ~830 m elevation and the Coastal Cordillera is uplifting relative to the Central Depression. Assuming abandonment of the lowest preserved shoreline (level 5, 796 m) because the spilling level at the Río Loa canyon was breached (Fig. 2), the uplift rate of the Coastal Cordillera relative to this shoreline is 160 ± 80 m/Ma. Utilizing the elevation-shoreline relationship (Fig. 5),

Table 1
Cosmogenic isotope data for quartz clasts. Further information concerning site specific data, triple isotope plots and scaled production rates are given in the supplementary information section.

Shoreline Level 1	Elevation	cosm. ^{21}Ne	cosm. ^{10}Be	^{10}Be Age	^{10}Be int.	^{10}Be Total	^{21}Ne Age	^{21}Ne int.	^{21}Ne Total
	[m.a.s.l.]	[10^7atoms/g]	[10^6 atoms/g]	[kyr]	Uncert.[kyr]	Uncert. [kyr]	[kyr]	Uncert.[kyr]	Uncert. [kyr]
SL 15-012 a	796	–	3.42 ± 0.14	827	41	86			
SL 15-012 b	796	–	1.12 ± 0.06	231	15	28			
SL 15-012 c	796	–	0.82 ± 0.04	170	11	19			
SL 15-012 d	796	–	1.66 ± 0.07	358	20	45			
SL 15-012 e	796	–	1.21 ± 0.05	254	11	27			
SL 15-012 f	796	–	1.71 ± 0.06	375	17	44			
Mean SL15-12			1.65 ± 0.07	360	253	260			
Mean Subpop. SL15-12 (b-f)			1.30 ± 0.34	274	74	77			
Shoreline Level 2									
SL 14-01 a	818	1.98 ± 0.18	1.94 ± 0.07	430	21	52	946	76	128
SL 14-01 b	818	2.03 ± 0.20	1.82 ± 0.07	403	17	39	974	85	144
SL 14-01 c	818	1.55 ± 0.18	1.63 ± 0.06	355	19	43	782	56	82
SL 14-01 d	818	2.18 ± 0.13	2.00 ± 0.08	453	21	49	1038	65	146
SL 14-01 e	818	1.87 ± 0.16	1.64 ± 0.06	359	17	44	913	59	106
SL14-01 f	818	–	2.41 ± 0.84	564	23	56	928	64	105
Mean SL14-01			1.91 ± 0.07	417	74	84	953	72	128
Mean Subpop. SL14-01 (a-e)			1.80 ± 0.07	392	37	52			
Shoreline Level 3									
LL13-001 a	829	–	3.89 ± 0.13	934	33	83			
LL13-001 b	829	–	2.33 ± 0.08	525	17	48			
LL13-001 c	829	–	1.68 ± 0.06	358	18	44			
LL13-001 d	829	–	2.41 ± 0.08	542	19	49			
LL13-001 e	829	–	2.54 ± 0.11	575	29	65			
LL13-001 f	829	–	2.86 ± 0.09	676	24	77			
Mean Subpop. LL13-001 (b, c, d,e,f)			2.53 ± 0.09	540	160	160			
Shoreline Level 4									
SL14-03 a	890	4.02 ± 0.30	4.77 ± 0.17	1230	50	110	1840	150	270
SL14-03 b	890	4.07 ± 0.18	6.02 ± 0.21	1700	110	260	1870	80	270
SL14-03 c	890	–	6.53 ± 0.23	1960	100	250			
SL14-03 d	890	–	4.02 ± 0.15	1000	50	100			
SL14-03 f	890	–	2.76 ± 0.15	658	50	100			
SL14-03 g	890	–	5.32 ± 0.20	1380	100	170			
Mean SL14-03			4.90 ± 1.26	1270	470	490	1850	120	280
Shoreline Level 5									
SL14-04 a	1022	5.50 ± 0.27	–				2280	120	320
SL14-04 b	1022	43.13 ± 1.40	10.40 ± 0.35	4500	620	1500	21,600		700
SL14-04 c	1022	4.61 ± 0.21	1.36 ± 0.06	263	10	27	1920	90	230
SL14-04 g	1022	–	5.93 ± 0.23	1400	80	180			
SL14-04 h	1022	–	8.29 ± 0.28	2520	180	460			
Top Cerro Soledad									
SL14-05 a	1051	6.99 ± 0.32	8.99 ± 0.30	2880	230	590	2880	140	390
SL14-05 b	1051	11.57 ± 0.43	10.50 ± 0.35	4500	610	1500	4830	180	640
SL14-05 c	1051	7.03 ± 0.28	8.71 ± 0.29	2680	200	520	2900	120	390
SL14-05 e	1051	8.10 ± 0.28	9.47 ± 0.31	3340	300	780	3380	120	450
Mean SL14-05			9.42 ± 0.31	3220	610	910	3490	140	470
Mean Subpop. SL14-05 (a,c,e)			9.06 ± 0.31	2930	240	610	3050	130	410

we tentatively assign an age of 2.5–2.8 Ma for the highest shoreline-level (SL04-4, 1022 m).

5. Discussion

The results indicate that at least five ephemeral lake phases occurred in the southern Central Depression between the late Pliocene (3.2–2.7 Ma, Top of Cerro Soledad) until the mid-Pleistocene (350-200 ka). These phases lasted sufficiently long to cut shorelines into bedrock and pre-existing/coeval evaporites of the Soledad Formation. We take the lack of intermediate shorelines between the highest (1022 m; tentative age 2.5–2.8 Ma) and the next youngest (890 m; 1.27 ± 0.47 Ma) as indication that no lake existed for a significant period of time between 2.65 ± 0.15 Ma and 1.27 ± 0.47 Ma. While elevation differences clearly separate the four youngest shorelines (1.27 ± 0.47 Ma at 890 m; 540 ± 160 ka at 829 m; 392 ± 37 ka at 818 m; 274 ± 74 ka at 796 m), the age resolution is insufficient to separate these lake phases. It is clear from the existence of paleo shorelines, however, that between 1.27 ± 0.47 Ma and 274 ± 74 ka at least four distinct lake phases occurred. The age of the youngest and lowest shoreline (274 ± 74 ka) records the onset of the incision of the present day Río Loa Canyon (Fig. 6); the incision transformed the Río Loa catchment into an exoreic catchment and marks the cessation of lacustrine sedimentation in the QLB. This interpretation for the onset of incision is based on the assumption that shoreline terraces are only created during stable lake levels, which have to be of a sufficiently long duration to allow enough wind-induced wave erosion. Moreover, based on the susceptibility of basin sediments to erosion, we assume that the initial onset of incision happened fast as the sediments were removed and decelerated once resistant bedrock was encountered. Prior to the incision, the existence or absence of paleo-lakes mirrored the hydrological balance in the Río Loa catchment.

In the endoreic phase, i.e. prior to 274 ± 74 ka, the water balance in the lower Río Loa catchment was likely to have been governed by precipitation sources in the Precordillera (above ~2500 m; Houston and Hartley, 2003; Jordan et al., 2014) while evaporation (Houston, 2006a) and groundwater discharge towards the coast (e.g. towards the Salar Grande; Chong et al., 1999; Jordan et al., 2015a) provided the

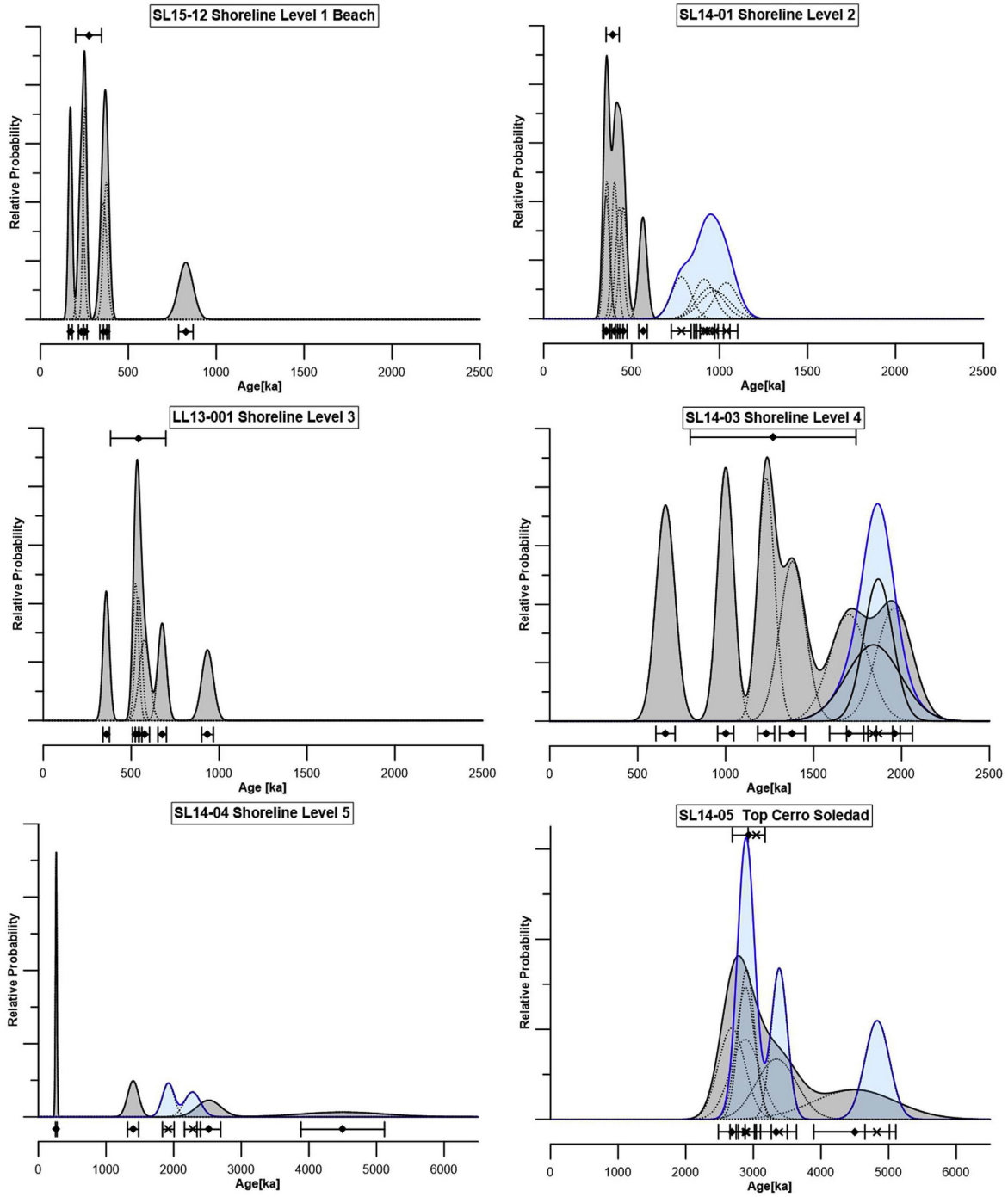

Fig. 4. Cumulative probability density plots of single clasts ^{10}Be (grey shading) and ^{21}Ne (blue shading). Exposure ages for ^{10}Be are plotted as diamonds and ^{21}Ne as crosses underneath the probability density plots. Error bars in this case are the 1 s.d. 'internal' age uncertainties (i.e. analytical uncertainty only). Above the shaded probability envelopes are the relevant arithmetic mean ages of shoreline terraces and hilltop deposits with one standard deviation error bars (see supplementary data). (For interpretation of the references to colour in this figure legend, the reader is referred to the web version of this article.)

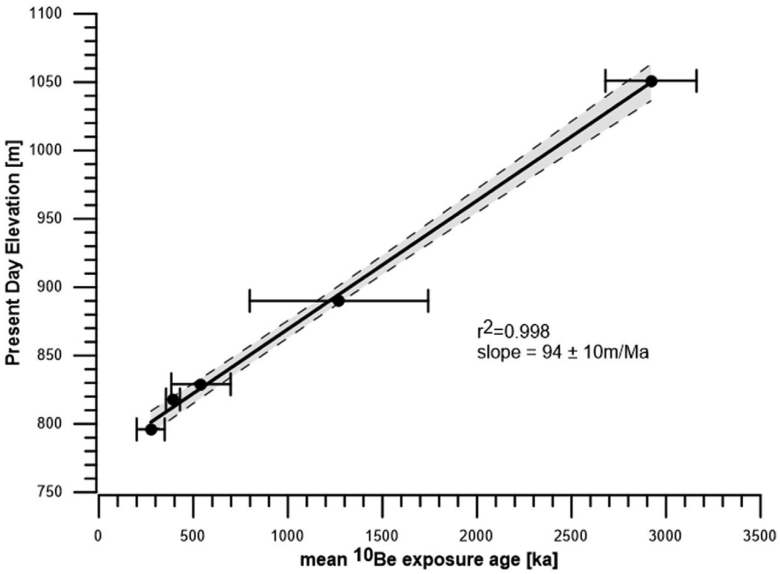

Fig. 5. Elevation versus mean ^{10}Be exposure ages for the five sample locations. Stippled lines represent the 95% confidence interval of the linear regression. Note the uncertainty on the slope (estimated uplift rate) is here ± 2σ.

sinks. To balance present levels of evaporation (Houston, 2006a), the supply of water from Río Loa channel flow and groundwater must have been about thirty times the modern discharge of the Río Loa at the coast (3.6 m^3/s; Salazar, 2003), in order to form a lake of the dimension inferred for the QLSL (Fig. 6).

Assuming that evaporation in the Central Depression and groundwater discharge potential are less variable than changes in precipitation, the paleo lake levels mostly represent changes in precipitation in the catchment, i.e. they indicate wetter climatic conditions in the source areas of the Precordillera. We therefore conclude that between 2.65 ± 0.15 Ma and 1.27 ± 0.47 Ma the source area in the Precordillera was predominantly (hyper-)arid. After 1.27 ± 0.47 Ma the climate in the source region had brief wetter interludes that were none-the-less long enough to erode shorelines. Due to the current orders of magnitude difference in precipitation between the Central Depression and the Precordillera (Houston and Hartley, 2003; Jordan et al., 2014) changes in the paleo-lake reflect the paleoclimate of the distant source (Precordillera) more strongly than the local (Central Depression) paleoclimate (Jordan et al., 2014). It is likely that the Central Depression (< 1500 m) remained (hyper-)arid throughout the wetter phases indicated for the Precordillera (Gayo et al., 2012; Jordan et al., 2014).

Two recent studies (Jordan et al., 2014; Wang et al., 2015) provide constraints on Plio-Pleistocene changes in climate within the Río Loa catchment. A soil profile in the Central Depression in the southernmost portion of the Río Loa catchment allowed Wang et al. (2015) to conclude that climatic conditions were wetter than present between 3.2 and 2.5 Ma, and between 1.3 and 0.6 Ma. Investigating soils and sediments of alluvial fan systems on the precordilleran foreslope, due east of our study area, Jordan et al. (2014) infer wetter conditions for the periods between 4 and 3.6, as well as between 2.6 and 2.2 Ma, but hyperarid conditions between 2.2 and 1 Ma. For the time since ~1 Ma the authors infer hyperarid conditions with century to millennial scale fluctuations to an arid climate in the alluvial fans source areas (Jordan et al., 2014). Our findings agree with previous evidence for the cessation of a 'pluvial' phase at ~3 Ma and a later phase of pluvial conditions around 1Ma in the Central Depression (Hartley, 2003; Placzek et al., 2010; Evenstar et al., 2017). These brief, centennial to millennial interludes of wetter climate in the last 1 Ma (Jordan et al., 2014) are sufficiently long to cut shorelines (Oviatt et al., 1992; Garcin et al., 2012; Lifton et al., 2015). South of the Río Loa catchment, Jungers et al. (2013) suggested that enhanced erosion and deposition between 250 and 400 ka are indicative of wetter conditions. We note that, despite the considerable uncertainties of the ages and the different nature of the proxies, the inferred pluvial periods (Jungers et al., 2013; Jordan et al., 2014; Wang et al., 2015) agree favourably with our shoreline ages. The age-constraints from these studies (this study, Jungers et al., 2013; Jordan et al., 2014; Wang et al., 2015), however, are not sufficiently precise to be able to associate them to particular stadials/interstadials.

The Plio-Pleistocene sediments of the QLSL provide important paleoclimatological information (Chong et al., 1999; Sáez et al., 1999; Pueyo et al., 2001; Sáez et al., 2012; Quezada et al., 2013). The currently available chronological constraints (Sáez et al., 2012; Quezada et al., 2013; Jordan et al., 2014; this study) are, however, contradictory. On Cerro Soledad (Figs. 1 and 3), the Soledad evaporites directly overlay the intrusive substrate, lacking older Cenozoic sediments (Pueyo et al., 2001). They cover the entire Cerro Soledad, bar the highest ridges (Pueyo et al., 2001; this study). Interbedded volcanic ash layers in these evaporites yield Ar/Ar ages of 3.16 ± 0.07 Ma and 3.73 ± 0.02Ma (Quezada et al., 2013), indicating the temporal hiatus between the deposition of the Soledad formation and the preceding Quillagua formation (termination ~4.5 Ma, Sáez et al., 2012) was less than 750 ka, if indeed there was a hiatus. Near the eastern fringe of the QLSL, the Lomas del Sal (Figs. 1 and 6) is a tectonically uplifted block of the Soledad formation, with massive displacive halite ~90 m thick topped with ~10 m of gypsum cover (Pueyo et al., 2001). The halite is devoid of fluvioclastic sediments (Pueyo et al., 2001), whereas the gypsum cover contains interfingering alluvium (Jordan et al., 2014). Volcanic ashes found in a canyon near the bottom of the massive halite yield Ar/Ar ages between 0.21 ± 0.07 Ma and 0.098 ± 0.042Ma (Sáez et al., 2012); consequently, Sáez et al. (2012) place the Soledad Formation in its entirety into the mid to late Pleistocene. Based on the sedimentary horizons underlying the geomorphic surfaces, Jordan et al. (2014) assigned a Pliocene age (i.e. > 2.6 Ma) for the evaporites at the top of the Lomas del Sal (Fig. 4 in Jordan et al., 2014). The latter clearly contradicts the findings of Sáez et al. (2012), however, it is in agreement with the ages of Quezada et al. (2013). While we cannot resolve the reasons for these contradictory results here, we note that our findings are rather in line with those of Jordan et al. (2014) and Quezada et al. (2013), since we present evidence for lake phases that

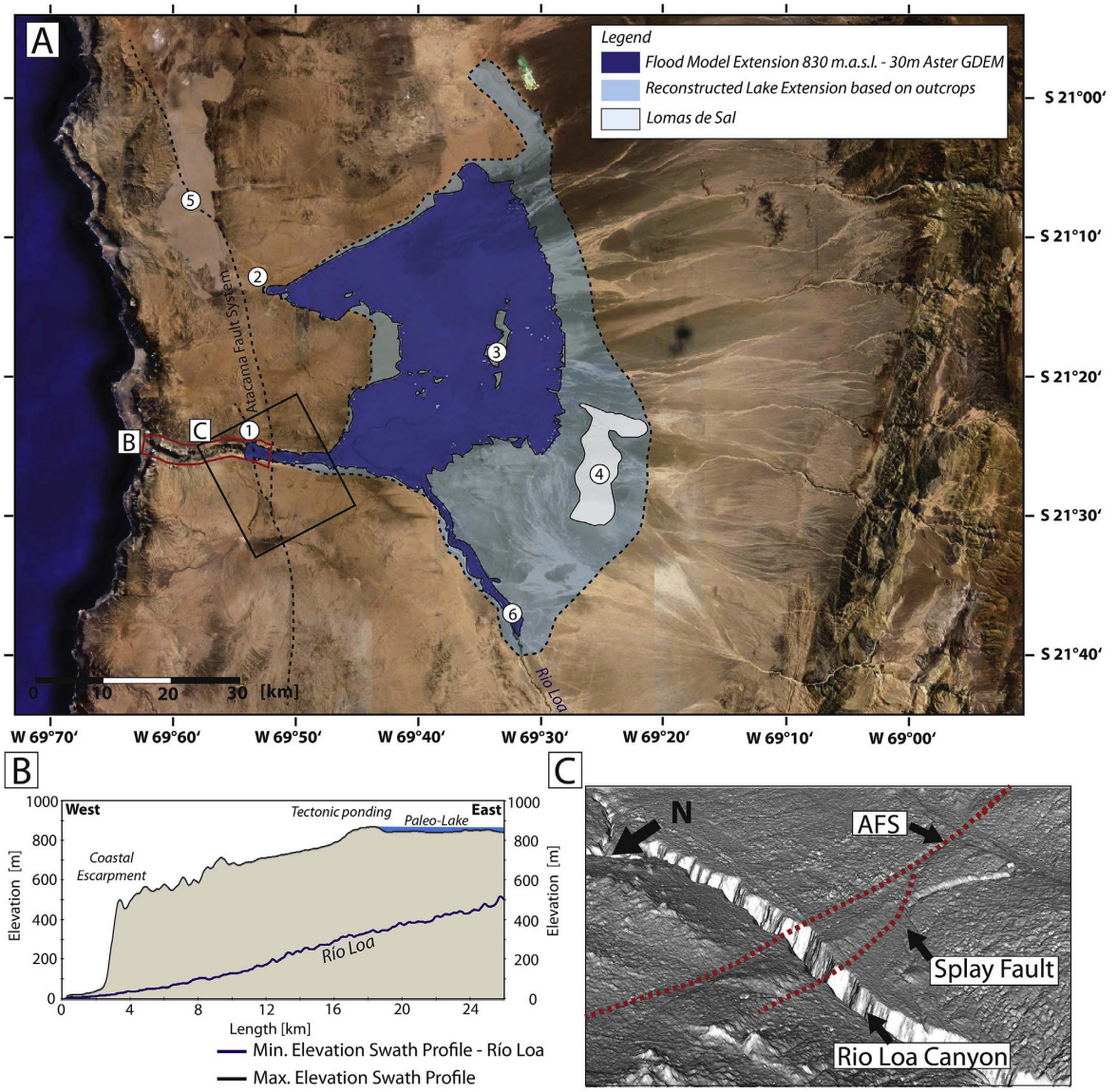

Fig. 6. Google Earth image with modelled lake extension (ASTER GDEM 30 m resolution) of a flooding level (dark blue) of 830 m.a.s.l. (Rivertools 3.0). Reconstruction only for the Quillagua-Llamara basin. Light blue indicates reconstructed estimated maximum paleo-lake extension based on outcrops and modelled lake extensions (Rivertools 3.0). (1) Río Loa potential overflow divide towards the Pacific, (2) Montón de Gloria pass, overflow divide towards Salar Grande, (3) Cerro Soledad with isolated topographic heights, (4) Lomas de Sal, (5) Salar Grande, and (6) Quillagua. (B). Maximum elevation indicates local tectonic uplift of a splay fault from the AFS responsible for potential tectonic ponding. Minimum elevation indicates recent Río Loa course. (C) 3D Image (ASTER GDEM data) displays the tectonic splay fault from the Atacama Fault System. (For interpretation of the references to colour in this figure legend, the reader is referred to the web version of this article.)

eroded Soledad evaporites since the late Pliocene.

The endohereic drainage system of the QLB (Sáez et al., 1999), had three main lake phases (Hilaricos Fm, Quillagua Fm, Soledad Fm, Sáez et al. (1999)). The evolution of an endohereic drainage system in the QLB was initiated by differential uplift of the Coastal Cordillera in relation to the Central Depression. At the same time, localized subsidence of the Central Depression created further accommodation space (Jordan et al., 2015b; Cosentino and Jordan, 2017). The inferred spilling point of the last lake phase is located at a transpressional topographic high associated with the strike slip fault of the AFS. Lake deposits (diatomites and open water evaporites; supplementary data) are found exclusively to the east of this high point (Fig. 1). The topographic high is made up from older, presumably early Miocene, coarse-grained fluvioclastic sediments (age-equivalents of the Azapa and/or El Diablo formation; Evenstar et al., 2017). These sediments are unconsolidated, thus prone to fast fluvial erosion once spilling occurred. The first phase of canyon down cutting and drainage of the lake was, therefore, probably very fast. Once the drainage hit bedrock, currently 150-200 m above the present valley floor, incision might have been slower. We cannot exclude that spilling of the lake occurred via headward erosion

of drainage from groundwater sapping (Hoke et al., 2004; May et al., 2005), since ground water conductivity is high in unconsolidated coarse grained sediments. From the preservation of open water evaporites at the same elevation (± 10 m relative) as the inferred spilling point (supplementary data) we infer that the lake spilled, though sapping by shallow groundwater might have accelerated the process. The change from an endohereic to an exohereic drainage system terminated the existence of lakes in the QLB, triggering subsequent incision and widespread denudation of its lacustrine deposits.

6. Conclusion

The exposure age dating undertaken here better constrains the timing of pluvial periods in the Atacama Desert and the age for deposition of the Soledad Formation throughout the late Pliocene and Pleistocene. Shoreline formation and rounded pebbles on isolated topographic highs indicate tectonic activity throughout the Pleistocene and their uplift at rates of 94 m/Ma. Our results place the timing of the deposition of the Soledad Fm in the late Pliocene and Pleistocene under a wetter climate than today. Exposure ages of the youngest shoreline (274 ± 74 ka) constrain the timing for the incision of the modern Río Loa through the Coastal Cordillera and the transformation of the Río Loa catchment from an endohereic to exohereic system. Despite the Central Depression of the Atacama Desert remaining hyperarid through the Quaternary, climate changes external to the region can still have significant environmental impacts.

Acknowledgments

Thanks go to Luigia Di Nicola from SUERC for assisting during noble gas analysis. Furthermore, for help processing ^{10}Be and ^{26}Al data at the University of Cologne we thank Elena Voronina, Damián López, and Tomasz Góral. We are grateful to Shasta Marrero for calculating ^{21}Ne ages with the new CRONUS Calculator MatLab version 2.0. We would like to thank Eduardo Campos and colleagues at the Universidad Catolica del Norte at Antofagasta for logistical support. Reviews by one anonymous reviewer, Teresa Jordan and Pierre-Henri Blard significantly improved the manuscript. This study was funded by the University of Cologne.

Appendix A. Supplementary data

Supplementary data related to this article can be found at http://dx.doi.org/10.1016/j.quageo.2017.11.002.

References

Aceituno, P., 1988. On the functioning of the Southern oscillation in the south american sector. Part I Surf. Clim. Mon. Weather Rev. 116 (3), 505–524.
Allmendinger, R.W., Gonzalez, G., 2010. Invited review paper: neogene to Quaternary tectonics of the coastal Cordillera, northern Chile. Tectonophysics 495 (1–2), 93–110.
Allmendinger, R.W., Gonzalez, G., Yu, J., Hoke, G., Isacks, B., 2005. Trench-parallel shortening in the northern chilean forearc: tectonic and climatic implications. Geol. Soc. Am. Bull. 117 (1–2), 89–104.
Applegate, P.J., Urban, N.M., Laabs, B.J.C., Keller, K., Alley, R.B., 2010. Modeling the statistical distributions of cosmogenic exposure dates from moraines. Geosci. Model Dev. 3 (1), 293–307.
Betancourt, J.L., Latorre, C., Rech, J.A., Quade, J., Rylander, K.A., 2000. A 22,000-year record of monsoonal precipitation from northern Chile's Atacama desert. Science 289, 1542–1546.
Binnie, S.A., Dunai, T.J., Voronina, E., Goral, T., Heinze, S., Dewald, A., 2015. Separation of Be and Al for AMS Using Single-step Column Chromatography: Nuclear Instruments and Methods in Physics Research Section B: Beam Interactions with Materials and Atoms.
Bozkurt, D., Rondanelli, R., Garreaud, R., Arriagada, A., 2016. Impact of warmer eastern tropical pacific SST on the March 2015 Atacama floods. Mon. Weather Rev. 144 (11), 4441–4460.
Brüggen, J., 1950. Fundamentos de la Gelogia de Chile. Inst. Geog. Milit. (Chile) 374.
Carrizo, D., Gonzalez, G., Dunai, T., 2008. Neogene constriction in the northern Chilean Coastal Cordillera: neotectonics and surface dating using cosmogenic 21Ne. Rev. Geol. De. Chile 35 (1), 1–38.
Chong, G., Mendoza, M., García-Veigas, J., Pueyo, J.J., Turner, P., 1999. Evolution and geochemical signatures in a neogene forearc evaporitic basin: the salar Grande (central Andes of Chile). Palaeogeogr. Palaeoclimatol. Palaeoecol. 151 (1), 39–54.
Codilean, A.T., Bishop, P., Stuart, F.M., Hoey, T.B., Fabel, D., Freeman, S.P., 2008. Single-grain cosmogenic 21Ne concentrations in fluvial sediments reveal spatially variable erosion rates. Geology 36 (2), 159–162.
Contreras, S., Lange, C.B., Pantoja, S., Lavik, G., Rincón-Martínez, D., Kuypers, M.M., 2010. A rainy northern Atacama Desert during the last interglacial. Geophys. Res. Lett. 37 (23).
Cosentino, N.J., Jordan, T.E., 2017. 87Sr/86Sr of calcium sulfate in ancient soils of hyperarid settings as a paleoaltitude proxy: Pliocene to Quaternary constraints for northern Chile (19.5–21.7° S). Tectonics 36 (1), 137–162.
Cristini, L., Grosfeld, K., Butzin, M., Lohmann, G., 2012. Influence of the opening of the drake passage on the cenozoic antarctic ice sheet: a modeling approach. Palaeogeogr. Palaeoclimatol. Palaeoecol. 339, 66–73.
Dewald, A., Heinze, S., Jolie, J., Zilges, A., Dunai, T., Rethemeyer, J., Melles, M., Staubwasser, M., Kuczewski, B., Richter, J., Radtke, U., von Blanckenburg, F., Klein, M., 2013. CologneAMS, a dedicated center for accelerator mass spectrometry in Germany. Nucl. Instrum. Methods Phys. Res. Sect. B-Beam Interact. Mater. Atoms 294, 18–23.
Dunai, T.J., 2010. Cosmogenic Nuclides: Principles, Concepts and Applications in the Earth Surface Sciences. Cambridge University Press.
Dunai, T.J., González López, G.A., Juez-Larré, J., 2005. Oligocene–Miocene age of aridity in the Atacama Desert revealed by exposure dating of erosion-sensitive landforms. Geology 33 (4), 321.
Evenstar, L., Mather, A., Hartley, A., Stuart, F., Sparks, R., Cooper, F., 2017. Geomorphology on geologic timescales: evolution of the late cenozoic pacific paleosurface in northern Chile and southern Peru. Earth-Science Rev. 171, 1–27.
Evenstar, L.A., Hartley, A.J., Stuart, F.M., Mather, A.E., Rice, C.M., Chong, G., 2009. Multiphase development of the Atacama Planation Surface recorded by cosmogenic 3He exposure ages: implications for uplift and Cenozoic climate change in western South America. Geology 37 (1), 27–30.
Garcin, Y., Melnick, D., Strecker, M.R., Olago, D., Tiercelin, J.-J., 2012. East African mid-Holocene wet–dry transition recorded in palaeo-shorelines of Lake Turkana, northern Kenya Rift. Earth Planet. Sci. Lett. 331, 322–334.
Garreaud, R.D., Molina, A., Farias, M., 2010. Andean uplift, ocean cooling and Atacama hyperaridity: a climate modeling perspective. Earth Planet. Sci. Lett. 292 (1–2), 39–50.
Gaupp, R., Kott, A., Worner, G., 1999. Palaeoclimatic implications of Mio-Pliocene sedimentation in the high-altitude intra-arc Lauca Basin of northern Chile. Palaeogeogr. Palaeoclimatol. Palaeoecol. 151 (1–3), 79–100.
Gayo, E.M., Latorre, C., Jordan, T.E., Nester, P.L., Estay, S.A., Ojeda, K.F., Santoro, C.M., 2012. Late Quaternary hydrological and ecological changes in the hyperarid core of the northern Atacama Desert (~21°S). Earth-Science Rev. 113 (3–4), 120–140.
Hartley, A.J., 2003. Andean uplift and climate change. J. Geol. Soc. Lond 160, 7–10.
Hartley, A.J., Chong, G., 2002. Late Pliocene age for the Atacama desert: implications for the desertification of western South America. Geology 30, 43–46.
Hartley, A.J., Chong, G., Houston, J., Mather, A.E., 2005. 150 million years of climatic stability: evidence from the Atacama Desert, northern Chile. J. Geol. Soc. 162, 421–424.
Hartley, A.J., Evenstar, L., 2010. Cenozoic stratigraphic development in the north Chilean forearc: implications for basin development and uplift history of the Central Andean margin. Tectonophysics 495 (1–2), 67–77.
Hoke, G.D., Isacks, B.L., Jordan, T.E., Jennifer, S.Y., 2004. Groundwater-sapping origin for the giant quebradas of northern Chile. Geology 32 (7), 605–608.
Hollingworth, S., 1964. Dating the uplift of the Andes of northern Chile. Nature 201, 17–20.
Houston, J., 2006a. Evaporation in the Atacama Desert: an empirical study of spatio-temporal variations and their causes. J. Hydrology 330 (3–4), 402–412.
Houston, J., 2006b. The great Atacama flood of 2001 and its implications for Andean hydrology. Hydrol. Process. 20 (3), 591–610.
Houston, J., 2006c. Variability of precipitation in the Atacama Desert: its causes and hydrological impact. Int. J. Climatol. 26 (15), 2181–2198.
Houston, J., Hartley, A.J., 2003. The Central Andean west-slope rainshadow and its potential contribution to the origin of hyper-aridity in the Atacama desert. Int. J. Climatol. 23, 1453–1464.
Jensen, A., Dörr, M., Gotze, H., Kiefer, E., Ibbeken, E., Wilke, H., 1995. Subsidence and sedimentation of a forearc-hosted, continental pull-apart basin: the Quillagua trough between 21 30 and 21 45 S, northern Chile. In: Proceedings Recent and Ancient Lacustrine Systems in Convergent Margins. GLOPALS-IAS Meeting, Antofagasta, Chile, pp. 5–6.
Jordan, T., Lameli, C.H., Kirk-Lawlor, N., Godfrey, L., 2015a. Architecture of the aquifers of the Calama Basin, Loa catchment basin, northern Chile. Geosphere 11 (5), 1438–1474 p. GES01176. 01171.
Jordan, T.E., Cosentino, N.J., Jensen, A., 2015b. Pliocene-quaternary Tectonic Subsidence of Part of the Central Depression Forearc, 20–22°S: XIV Congreso Geológico Chileno (La Serena).
Jordan, T.E., Kirk-Lawlor, N.E., Blanco, P.N., Rech, J.A., Cosentino, N.J., 2014. Landscape modification in response to repeated onset of hyperarid paleoclimate states since 14 Ma, Atacama Desert, Chile. Geol. Soc. Am. Bull. 126 (7–8), 1016–1046.
Jordan, T.E., Nester, P.L., Blanco, N., Hoke, G.D., Dávila, F., Tomlinson, A.J., 2010. Uplift of the Altiplano-Puna plateau: a view from the west. Tectonics 29 (5) p. n/a-n/a.
Jungers, M.C., Heimsath, A.M., Amundson, R., Balco, G., Shuster, D., Chong, G., 2013. Active erosion–deposition cycles in the hyperarid Atacama Desert of Northern Chile. Earth Planet. Sci. Lett. 125–133 371-372.
Kirk-Lawlor, N., Jordan, T.I., Rech, J.A., Lehman, S.B., 2013. Late Miocene to early

Pliocene paleohydrology and landscape evolution of northern Chile, 19° to 20° S. Palaegeogr. Palaeoclimatol. Palaeoecol. 387, 76–90.
Kober, F., Ivy-Ochs, S., Schlunegger, F., Baur, H., Kubik, P.W., Wieler, R., 2007. Denudation rates and a topography-driven rainfall threshold in northern Chile: multiple cosmogenic nuclide data and sediment yield budgets. Geomorphology 83, 97–120.
Latorre, C., Betancourt, J.L., Arroyo, M.T.K., 2006. Late Quaternary vegetation and climate history of a perennial river canyon in the Río Salado basin (22°S) of Northern Chile. Quat. Res. 65 (3), 450–466.
Lifton, N., Caffee, M., Finkel, R., Marrero, S., Nishiizumi, K., Phillips, F.M., Goehring, B., Gosse, J., Stone, J., Schaefer, J., Theriault, B., Jull, A.J.T., Fifield, K., 2015. In situ cosmogenic nuclide production rate calibration for the CRONUS-Earth project from Lake Bonneville, Utah, shoreline features. Quat. Geochronol. 26, 56–69.
Marrero, S.M., Phillips, F.M., Borchers, B., Lifton, N., Aumer, R., Balco, G., 2016. Cosmogenic nuclide systematics and the CRONUScalc program. Quat. Geochronol. 31, 160–187.
Martin, L., Blard, P.-H., Balco, G., Lavé, J., Delunel, R., Lifton, N., Laurent, V., 2017. The CREp program and the ICE-D production rate calibration database: a fully parameterizable and updated online tool to compute cosmic-ray exposure ages. Quat. Geochronol. 38, 25–49.
May, G., Hartley, A.J., Chong, G., Stuart, F., Turner, P., Kape, S.J., 2005. Litoestratigrafía, cronoestratigrafía durante el Eoceno al Pleistoceno y evolución tectono-sedimentaria de la Cuenca de Calama, norte de Chile. Rev. Geol. Chile 32 (1), 33–58.
McKay, C.P., Friedmann, E.I., Gómez-Silva, B., Cáceres-Villanueva, L., Andersen, D.T., Landheim, R., 2003. Temperature and moisture conditions for life in the extreme arid region of the Atacama Desert: four years of observations including the El Niño of 1997-1998. Astrobiology 3 (2), 393–406.
Naranjo, J.A., Paskoff, R.P., 1982. Estratigrafı´a de las unidades sedimentarias cenozoicas de la Cuenca del Rı´o Loa en la Pampa del Tamarugal, Regio'n de Antofagasta. Chile Rev. Geol. Chile 15 49-57.
Nester, P., 2008. Basin and paleoclimate evolution of the Pampa del Tamarugal forearc valley, Atacama Desert, northern Chile. Cornell Theses Diss. http://hdl.handle.net/1813/10484.
Nester, P., Jordan, T., 2012. The Pampa del Tamarugal Forearc Basin in Northern Chile: The Interaction of Tectonics and Climate, Tectonics of Sedimentary Basins. John Wiley & Sons, Ltd, pp. 369–381.
Nester, P.L., Gayo, E., Latorre, C., Jordan, T.E., Blanco, N., 2007. Perennial stream discharge in the hyperarid Atacama Desert of northern Chile during the latest Pleistocene. Proc. Natl. Acad. Sci. U. S. A. 104 (50), 19724–19729.
Nishiizumi, K., Caffee, M.W., Finkel, R.C., Brimhall, G., Mote, G., 2005. Remnants of a fossil alluvial fan landscape of Miocene age in the Atacama desert of northern Chile using cosmogenic nuclide exposure age dating. Earth Planet. Sci. Lett. 237, 499–507.
Nishiizumi, K., Imamura, M., Caffee, M.W., Southon, J.R., Finkel, R.C., McAninch, J., 2007. Absolute calibration of Be-10 AMS standards. Nucl. Instr. Meth. Phys. Res. B 258, 403–413.
Ortlieb, L., Diaz, A., Guzman, N., 1996. A warm interglacial episode during Oxygen Isotope Stage 11 in northern Chile. Quat. Sci. Rev. 15 (8), 857–871.
Oviatt, C.G., Currey, D.R., Sack, D., 1992. Radiocarbon chronology of lake bonneville, eastern great basin, USA. Palaeogeogr. Palaeoclimatol. Palaeoecol. 99 (3–4), 225–241.
Placzek, C.J., Matmon, A., Granger, D.E., Quade, J., Niedermann, S., 2010. Evidence for active landscape evolution in the hyperarid Atacama from multiple terrestrial cosmogenic nuclides. Earth Planet. Sci. Lett. 295 (1–2), 12–20.
Pueyo, J.J., Chong, G., Jensen, A., 2001. Neogene evaporites in desert volcanic environments: Atacama Desert, northern Chile. Sedimentology 48 (6), 1411–1431.
Quezada, A., Vásquez, P., Sepúlvedad, F., 2013. Soledad formation: detailed mapping and radiometric ages. In: Proceedings, International Geological Congress on the Southern Hemisphere (GEOSUR 2013): Viña del Mar, Chile, Bollettino di Geofisica Teorica ed Applicata Vol. 54 No. Supplement B.
Quezada, A., Vasquez, P., Sepúlveda, F., Blanco, N., Tomlinson, A.J., 2012. Mapa Compilación Geológica Área Quillagua - salar Grande 1:100.000: servicio Nacional de Geologica y Mineria Gobierno Regional de Tarapacá.
Rech, J.A., Currie, B.S., Michalski, G., Cowan, A.M., 2006. Neogene climate change and uplift in the Atacama Desert, Chile. Geology 34 (9), 761–764.
Rech, J.A., Currie, B.S., Shullenberger, E.D., Dunagan, S.P., Jordan, T.E., Blanco, N., Tomlinson, A.J., Rowe, H.D., Houston, J., 2010. Evidence for the development of the Andean rain shadow from a Neogene isotopic record in the Atacama Desert, Chile. Earth Planet. Sci. Lett. 292 (3–4), 371–382.
Rech, J.A., Quade, J., Hart, W.S., 2003. Isotopic evidence for the source of Ca and S in soil gypsum, anhydrite and calcite in the Atacama Desert, Chile. Geochim. Cosmochim. Acta 67, 575–586.
Rieu, M., 1975. Les formations sedimentaires de la Pampa del Tamarugal et le rı´o Loa (Norte Grande du Chili). Fr. Off. Rech. Sci. Tech. O.-m. Cah. Ser. Geol. 7 (2), 145–164.
Sáez, A., Cabrera, L., Garcés, M., Bogaard, P. v. d., Jensen, A., Gimeno, D., 2012. The stratigraphic record of changing hyperaridity in the Atacama desert over the last 10Ma. Earth Planet. Sci. Lett. 32–38 355-356.
Sáez, A., Cabrera, L., Jensen, A., Chong, G., 1999. Late Neogene lacustrine record and palaeogeography in the Quillagua–Llamara basin, Central Andean fore-arc (northern Chile). Palaeogeogr. Palaeoclimatol. Palaeoecol. 151 (1), 5–37.
Salazar, C., 2003. Situación de los recursos hídricos en Chile, Situación de los recursos hídricos en Chile, Centro del Tercer Mundo para el Manejo del Agua, A. C.
Sillitoe, R.H., McKee, E.H., 1996. Age of supergene oxidation and enrichment in the Chilean porphyry copper province. Econ. Geol. 91 (1), 164–179.
Stoertz, G.E., Ericksen, G.E., 1974. Geology of salars in northern Chile. U.S. Geol. Surv. Prof. Pap. 811, 65.
Taylor, J., 1997. Introduction to Error Analysis, the Study of Uncertainties in Physical Measurements.
Vermeesch, P., Balco, G., Blard, P.H., Dunai, T.J., Kober, F., Niedermann, S., Shuster, D.L., Strasky, S., Stuart, F.M., Wieler, R., Zimmermann, L., 2015. Interlaboratory comparison of cosmogenic Ne-21 in quartz. Quat. Geochronol. 26, 20–28.
Victor, P., Oncken, O., Glodny, J., 2004. Uplift of the western altiplano plateau: evidence from the Precordillera between 20° and 21°S (northern Chile). Tectonics 23 (4) (p. n/a-n/a).
Vuille, M., 1999. Atmospheric circulation over the Bolivian Altiplano during dry and wet periods and extreme phases of the Southern Oscillation. Int. J. Climatol. 19 (14), 1579–1600.
Vuille, M., Ammann, C., 1997. Regional Snowfall Patterns in the High, Arid Andes, Climatic Change at High Elevation Sites, Springer. pp. 181–191.
Vuille, M., Bradley, R.S., Keimig, F., 2000. Interannual climate variability in the Central Andes and its relation to tropical Pacific and Atlantic forcing. J. Geophys. Research-Atmostpheres 105 (D10), 12447–12460.
Vuille, M., Keimig, F., 2004. Interannual variability of summertime convective cloudiness and precipitation in the central Andes derived from ISCCP-B3 data. J. Clim. 17 (17), 3334–3348.
Wang, F., Michalski, G., Seo, J.-H., Granger, D.E., Lifton, N., Caffee, M., 2015. Beryllium-10 concentrations in the hyper-arid soils in the Atacama Desert, Chile: implications for arid soil formation rates and El Niño driven changes in Pliocene precipitation. Geochimica Cosmochimica Acta 160, 227–242.
Wilcox, A.C., Escauriaza, C., Agredano, R., Mignot, E., Zuazo, V., Otárola, S., Castro, L., Gironás, J., Cienfuegos, R., Mao, L., 2016. An integrated analysis of the March 2015 Atacama floods. Geophys. Res. Lett. 43 (15), 8035–8043.
Woodman, R.F., 1998. Los lagos de Sechura. Inf. Interno del Inst. Geofísico del Perú.
Zachos, J., Pagani, M., Sloan, L., Thomas, E., Billups, K., 2001. Trends, rhythms, and aberrations in global climate 65 Ma to present. Science 292 (5517), 686–693.

Supplementary Material

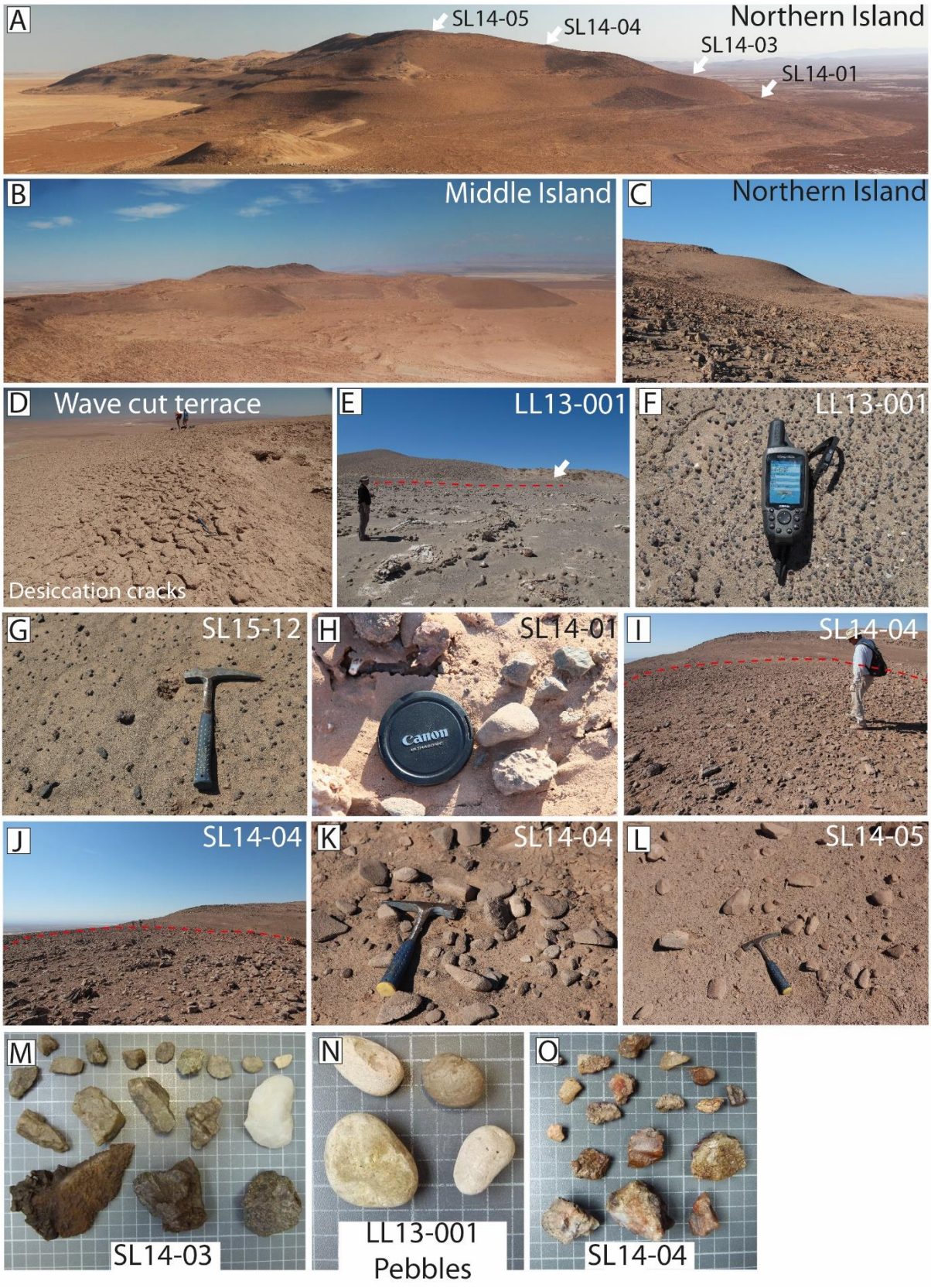

Figure Caption 1:

A) View to the south from smallest northern island towards the northern main island. Marked are sampled shoreline features.

B) View to the South from the top of Cerro Soledad (Northern Island). Apparent is the broad shoreline terrace/platform; corresponding to shoreline level 2 and remnants of the Soledad Fm.

C) Northern Island shoreline features. Visible are the horizontal erosional scarps of wave erosion during shoreline formation.

D) Sediments on the platform of the central island. Doline structures due to local dissolution are visible to the right. Desiccation cracks on the surface reflect the deposition during water coverage.

E) Sample Site LL13-001 southern island.

F) Sample Site LL13-001 surface sediments, including beach gravel.

G) Sample Site SL 15-12 surface sediments, including beach gravel.

H) Sample Site SL 14-01 rounded pebbles on shoreline terrace.

I) Sample Site SL 14-04 planar surface evolved due to shoreline erosion.

J) Sample Site SL 14-04, left in the background top surface of Cerro Soledad.

K) Sample Site SL 14-04 rounded clasts.

L) Sample Site SL 14-05 top of Cerro Soledad.

M) Sample variety of sample site SL 14-03.

N) Sample variety of sample site LL13-001.

O) Sample variety of sample site SL 14-04.

DEM Generation

The Digital Elevation Model (DEM) was generated using a stereo satellite image set provided by high resolution satellite Pléiades 1B system. Image recording was on 05.05.2015 with a ground resolution of 0.5 m in the panchromatic band. ExelisVIS ENVI 5.1 was used to derivate a surface model with the implemented DEM Extraction module. Tie Point determination between the two stereo images was manually obtained to subsequently generate epipolar images and a final Digital Surface Model. Study site adjusted settings for DEM extraction were applied. Post-processing, including filter methods reducing spikes (ENVI DEM Editing tools), were applied. The final model has a resolution of 1 m.

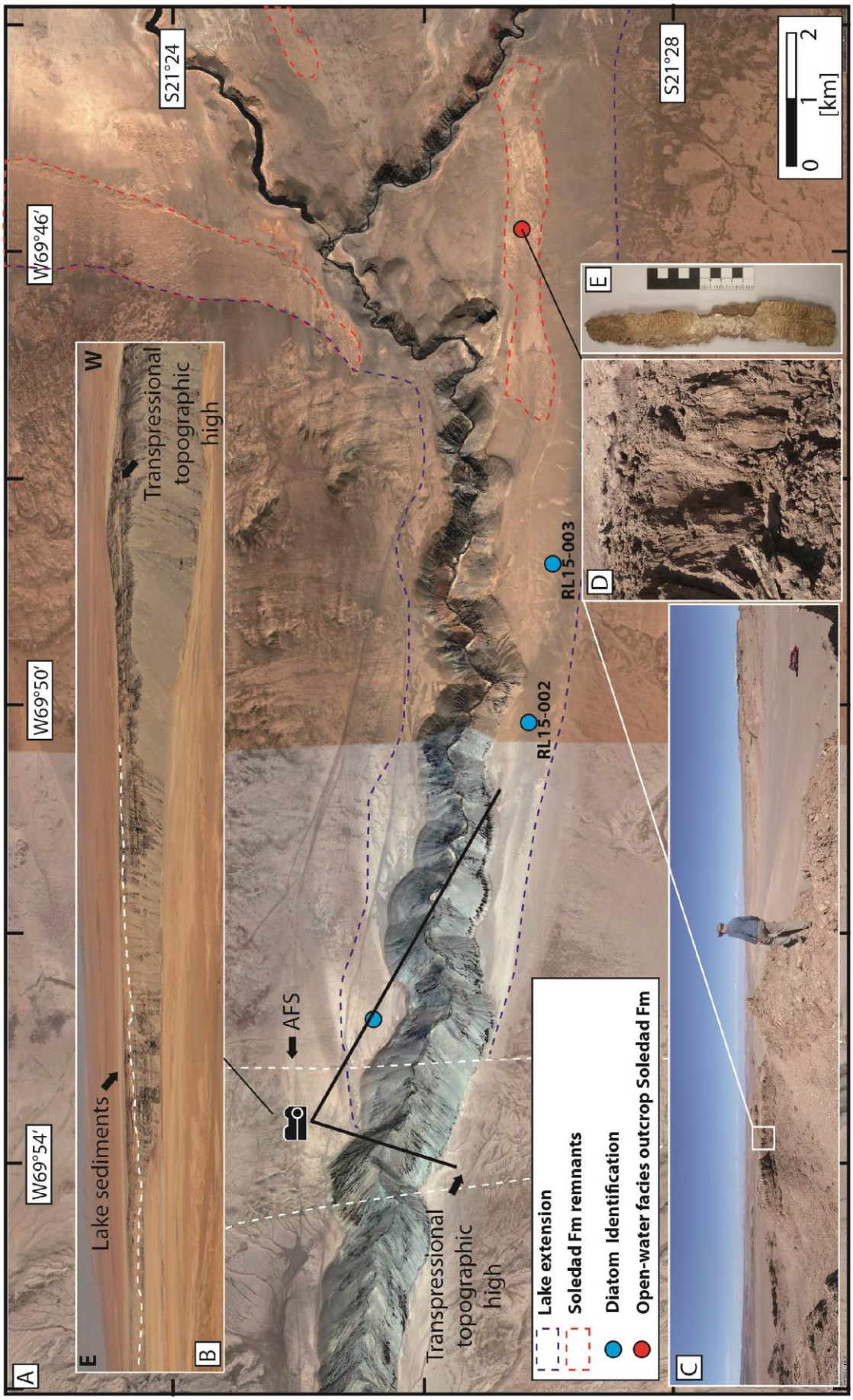
A
W69°54'
W69°50'
W69°46'
S21°24
S21°28
0 1 2 [km]
Lake sediments
E
W
B
Transpressional topographic high
AFS
RL15-002
RL15-003
Transpressional topographic high
Lake extension
Soledad Fm remnants
Diatom Identification
Open-water facies outcrop Soledad Fm
C
D
E

Figure Caption 2:

A.) Google Satellite Image of the westernmost Quillagua-Llamara basin and the Rio Loa canyon. Blue dots indicate sampling and identification locations of the Quillagua Fm. Red dot and red dashed areas indicate Soledad Fm remnants. B.) Panorama picture in the upper left shows the transpressional topographic high to the west and lake sediments to the east, which are only abundant on the eastern side of this topographic high. The red dot sampling site reveal large open-water evaporitic facies with large, dm-scale, bottom nucleated chevron gypsum crystals (sampling Site Fig. 2C, close-up of gypsum crystals Fig. 2D, 2E). Blue dashed line indicates potential lake extension. Spilling point height was chosen on the relative elevation of the westernmost outcropping lake sediments, the elevation of outcropping Soledad remnants (red dot) in conjunction with the overflow divide at the Montón de Gloria pass.

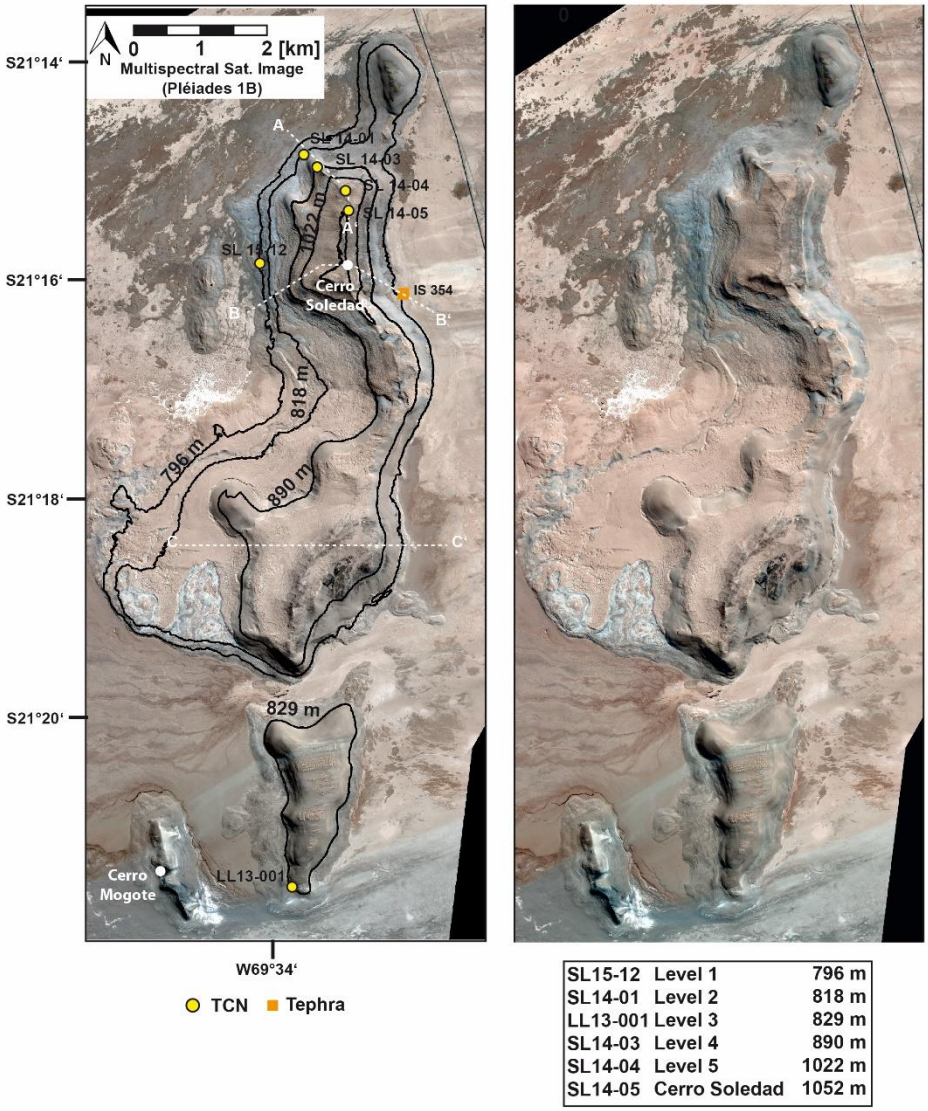

Figure Caption 3: Pléiades 1-B multispectral image of the study area, including contour lines of each sampled shoreline level (based on Pléiades 1-B generated 1m resolution DEM).

Sample and Methods

Samples were collected during field campaigns in 2013, 2014 and 2015. Quartz clast and pebbles were collected from selected shoreline terraces and from the Top of Cerro Soledad. Clasts were relative small with min. 1 to max. 6 cm in size. Desert patina is abundant. We avoided sampling near slopes to exclude downward transport of higher deposited sediments.

Samples were grounded and sieved to 250-1000 μm. Quartz grains were isolated, cleaned of any meteoric ^{10}Be and enriched through a series of acid treatments (Kohl and Nishiizumi, 1992). All purified quartz separates were verified under a microscope, those with a high abundance of fluid inclusions and/or chalcedony fragments were further cleaned or excluded, especially for ^{21}Ne purposes. ICP-OES was used to verify the purity of the quartz before dissolution.

^{10}Be and ^{26}Al AMS (Accelerator Mass Spectrometry) targets were prepared using the approaches outlined in (Binnie et al., 2015). A reagent blank was prepared in tandem with each batch of typically 6-9 quartz samples. AMS measurements were made on CologneAMS (Dewald et al., 2013) normalized to the ICN and NBS standard dilutions prepared by Nishiizumi for ^{10}Be and ^{26}Al, respectively (Nishiizumi, 2004; Nishiizumi et al., 2007). Stable Al was determined by standard addition (n=4) using ICP-OES. Concentrations of ^{10}Be and ^{26}Al are reported following blank subtractions, which were typically less than 1% of the total number of nuclides measured. In a few cases, where the quartz masses dissolved were extremely low, blank subtractions were <3.5%. The 1 standard deviation analytical precision of the nuclide concentrations was estimated by summing in quadrature the relative uncertainties on the AMS measurements, both the samples and the blank, along with a 1% (1 s.d.) estimate for the precision of the mass of ^{9}Be added during spiking.

For age calculation, we used a ^{10}Be half-life of 1.36±0.07 Ma (Nishiizumi et al., 2007) and a 'nuclide dependent scaling' after Lifton et al. (2014), calculated with the CRONUS Web calculator (Wrapper Script 0.2 Version, Main Calculator 2.0 Version) (Marrero et al., 2016). This employed a high-latitude, sea-level spallogenic ^{10}Be production rate of 3.92 ± 0.31 atoms g^{-1} a^{-1}, and for ^{26}Al 28.5 ± 3.1 atoms g^{-1} a^{-1} (Flux-based LSD scaling, Borchers et al., 2016).

For cosmogenic ^{21}Ne, cleaned and purified samples were sieved to <125µm and packed into aluminium foil cups. The samples were measured with a noble-gas mass spectrometer at SUERC (Scottish Universities Environmental Research Centre) applying the standard procedure (Vermeesch et al., 2012). We used a high-altitude, sea-level production rate of 18.7±2.3 atoms $g^{-1}a^{-1}$ (Kober et al., 2011). Age calculation was obtained using the CRONUS EARTH Calculator Version 2.0 (Marrero et al., 2016).

An uplift correction for the production rate of cosmogenic nuclides was obtained. We assumed the potential uplift based on the assumption that wave cut shoreline formation took place at the altitude of the lowest terrace and altitude of the overflow points towards Salar Grande and Río Loa section. Tectonic displacement, especially at the Montón de Gloria pass towards the Salar Grande, is proven (Allmendinger et al., 2005). Good preservation of shoreline features and abundance of rounded pebbles indicate low erosion rates. A precise erosion rate reconstruction was not possible due to the lack of data. Calculated exposure ages therefore reveal only minimum ages.

It is known that secular changes of the Earth magnetic field have a significant influence on calculated production rates, particularly at low latitude (Dunai, 2001). We performed a sensitivity test (see Table 6) utilizing different magnetic reconstructions implemented in CREp (Martin et al., 2017) and found a maximum deviation of 11% (LSD Geomagnetic framework vs. Atmospheric ^{10}Be-based VDM 0-60 ka: Muscheler et al. (2005) - 60-2000 ka: SINT2000 Valet et al. (2005). We note that this difference is smaller than the stated uncertainties of our ages.

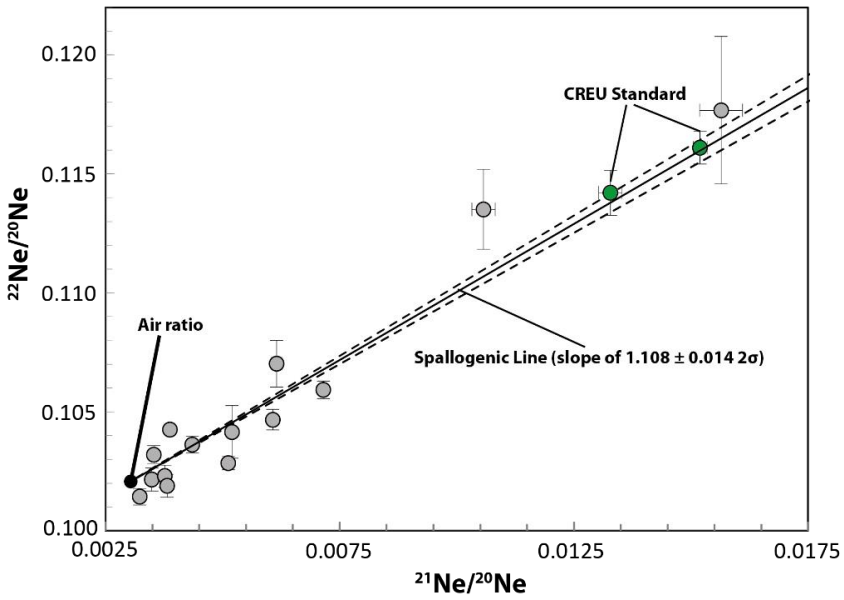

Figure Caption 4:

Neon Isotope Triple diagram. The spallogenic line indicates the mixture of air and the spallogenic end-member, which are present in every surface sample. Grey circles indicate measured samples at the noble-gas mass spectrometer in Glasgow/Scotland (SUERC). Data is shown with ±1σ error. Green circles represent measured CREU standards (Vermeesch et al., 2012).

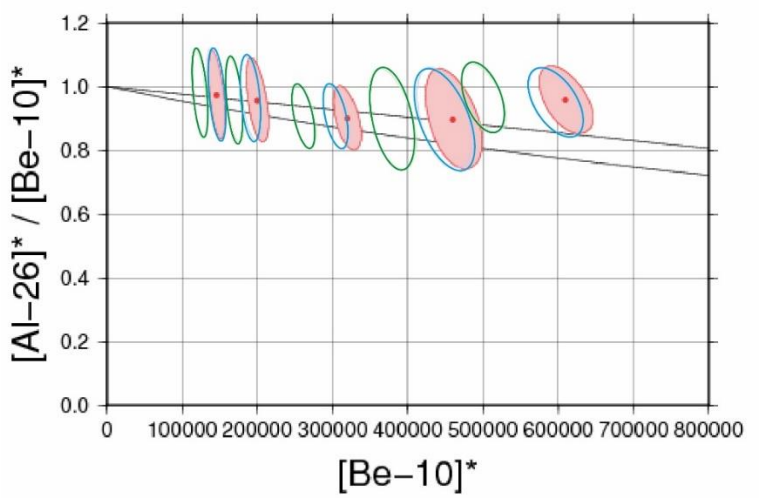

Figure Caption 5:

Two-nuclide diagrams calculated using CRONUS-Earth online calculator (Developmental Version 3) by Greg Balco (http://hess.ess.washington.edu/). The uncertainty ellipses reveal the 68% confidence interval. Different colours display three different scaling methods; Stone (2000) is red; Lifton et al. (2008) is green; LSDn Lifton et al. (2014) is blue. All measured samples indicate, within their error no signs of a complex exposure history, e.g. erosion and/or burial.

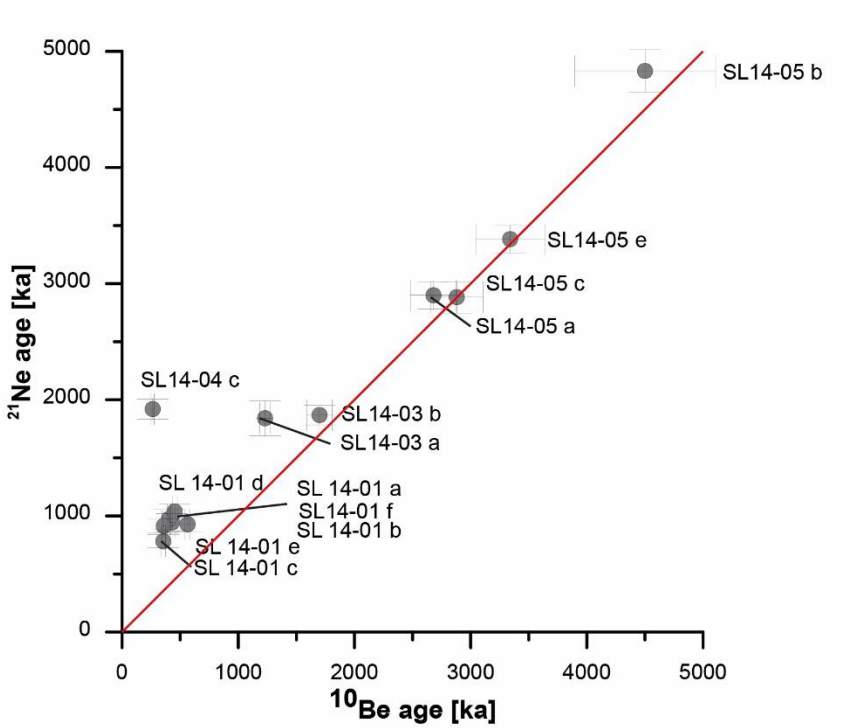

Figure Caption 6: ^{10}Be ages plotted against ^{21}Ne ages. Red line indicates 1:1 relationship of ^{10}Be/^{21}Ne ages. Samples to the left of this line reveal inheritance of the ^{21}Ne component.

Table 1: Sample location and site-specific data.

Sample name	Latitude	Longitude	Elevation (m)	Uplift corr. Elevation (m)	Thickness (cm)	Density ($g\ cm^{-2}$)	Shielding correction	Clast Mineral	Clast Shape
Shoreline Level 1									
SL 15-012 a	S 21°15'43.8''	W 69°34'05.1''	796	796	1	2.65	0.98747	Qtz	no patina, rounded, small
SL 15-012 b	S 21°15'43.8''	W 69°34'05.1''	796	796	1.5	2.65	0.98747	Qtz	clear white, rounded
SL 15-012 c	S 21°15'43.8''	W 69°34'05.1''	796	796	1.5	2.65	0.98747	Qtz	no patina, clear white
SL 15-012 d	S 21°15'43.8''	W 69°34'05.1''	796	796	2	2.65	0.98747	Qtz	white, slightly red, slightly rounded
SL 15-012 e	S 21°15'43.8''	W 69°34'05.1''	796	796	2	2.65	0.98747	Qtz	flat chip, no patina, clear white
SL 15-012 f	S 21°15'43.8''	W 69°34'05.1''	796	796	2.5	2.65	0.98747	Qtz	flat chip, no patina, clear white
Mean SL15-12			796	796	2	2.65	0.98747	Qtz	
Mean Subpop. SL15-12 (b-f)			796	796	2	2.65	0.98747	Qtz	
Shoreline Level 2									
SL 14-01 a	S 21°14'45.3''	W 69°33'42.3''	818	809	3	2.65	0.98747	Qtz	dull, grey, rounded
SL 14-01 b	S 21°14'45.3''	W 69°33'42.3''	818	809	4	2.65	0.98747	Qtz	dull, grey, rounded
SL 14-01 c	S 21°14'45.3''	W 69°33'42.3''	818	809	5	2.65	0.98747	Qtz	dull, grey, rounded
SL 14-01 d	S 21°14'45.3''	W 69°33'42.3''	818	809	4	2.65	0.98747	Qtz	dull, grey, rounded
SL 14-01 e	S 21°14'45.3''	W 69°33'42.3''	818	809	5	2.65	0.98747	Qtz	dull, grey, rounded
SL14-01 f	S 21°14'45.3''	W 69°33'42.3''	818	809	6	2.65	0.98747	Qtz	dull, brownish, slightly rounded
Mean SL14-01			818	809	4	2.65	0.98747	Qtz	
Mean Subpop. SL14-01 (a-e)			818	809	4	2.65	0.98747	Qtz	
Shoreline Level 3									
LL13-001 a	S 21°21'05.0''	W 69°33'49.0''	829	815	1	2.65	0.98747	Qtz	small, slightly rounded, light desert patina
LL13-001 b	S 21°21'05.0''	W 69°33'49.0''	829	815	2	2.65	0.98747	Qtz	white, slightly rounded, no patina
LL13-001 c	S 21°21'05.0''	W 69°33'49.0''	829	815	2.5	2.65	0.98747	Qtz	white, slightly rounded, elongate, no patina
LL13-001 d	S 21°21'05.0''	W 69°33'49.0''	829	815	2	2.65	0.98747	Qtz	white, rounded, no patina
LL13-001 e	S 21°21'05.0''	W 69°33'49.0''	829	815	2	2.65	0.98747	Qtz	white, one side with patina
LL13-001 f	S 21°21'05.0''	W 69°33'49.0''	829	815	3	2.65	0.98747	Qtz	rectangular, flat, white
Mean Subpop. LL13-001 (b, c, d,e, f)			829	815	2	2.65	0.98747	Qtz	
Shoreline Level 4									
SL14-03 a	S 21°14'51.7''	W 69°33'36.2''	890	845	4	2.65	0.95778	Qtz	dull, darker, edges rounded
SL14-03 b	S 21°14'51.7''	W 69°33'36.2''	890	845	4	2.65	0.95778	Qtz	dull, darker, edges rounded
SL14-03 c	S 21°14'51.7''	W 69°33'36.2''	890	845	5	2.65	0.95778	Qtz	dull, slightly greenish,rounded
SL14-03 d	S 21°14'51.7''	W 69°33'36.2''	890	845	4	2.65	0.95778	Qtz	dull, white, slightly rounded
SL14-03 f	S 21°14'51.7''	W 69°33'36.2''	890	845	4	2.65	0.95778	Qtz	angular, dull white-grey
SL14-03 g	S 21°14'51.7''	W 69°33'36.2''	890	845	1.5	2.65	0.95778	Qtz	grey, sharp edges, flat
Mean SL14-03			890	845	4	2.65	0.95778	Qtz	
Shoreline Level 5									
SL14-04 a	S 21°15'4.24''	W 69°33'19.92''	1022	911	3	2.65	1	Qtz	clear, small, slightly rounded, angular
SL14-04 b	S 21°15'4.24''	W 69°33'19.92''	1022	911	3	2.65	1	Qtz	slightly reddish, top with desert patina
SL14-04 c	S 21°15'4.24''	W 69°33'19.92''	1022	911	4	2.65	1	Qtz	top with patina, bottom white, angular, partly rounded
SL14-04 g	S 21°15'4.24''	W 69°33'19.92''	1022	911	1	2.65	1	Qtz	small, light patina,slightly rounded
SL14-04 h	S 21°15'4.24''	W 69°33'19.92''	1022	911	4	2.65	1	Qtz	desert patina on top, angular
Top Cerro Soledad									
SL14-05 a	S 21°15'16.3''	W 69°33'18.5''	1052	926	3	2.65	1	Qtz	more angular edges, with desert patina
SL14-05 b	S 21°15'16.3''	W 69°33'18.5''	1052	926	3	2.65	1	Qtz	dark patina, slightly rounded, angular
SL14-05 c	S 21°15'16.3''	W 69°33'18.5''	1052	926	3	2.65	1	Qtz	dark patina, angular
SL14-05 e	S 21°15'16.3''	W 69°33'18.5''	1052	926	4	2.65	1	Qtz	dark patina on one side, other white, slightly rounded
Mean SL14-05			1052	926	3	2.65	1	Qtz	
Mean Subpop. SL14-05 (a,c,e)			1052	926	3	2.65	1	Qtz	

Table 2: Measured cosmogenic nuclide concentration. All uncertainties in the table are 1 standard deviation.

Sample name	^{10}Be conc. atoms g^{-1}	^{10}Be conc. Uncertainty	^{26}Al conc. atoms g^{-1}	^{26}Al conc. Uncertainty	^{21}Ne conc atoms g^{-1}	^{21}Ne conc. Uncertainty	Attenuation Length g/cm^2
Shoreline Level 1							
SL 15-012 a	3.42E+06	1.4E+05	2.08E+07	1.4E+06			161.3
SL 15-012 b	1.12E+06	6E+04	6.79E+06	5.6E+05			161.3
SL 15-012 c	8.15E+05	4.4E+04	5.04E+06	4.4E+05			161.3
SL 15-012 d	1.66E+06	7E+04					161.3
SL 15-012 e	1.21E+06	5E+04					161.3
SL 15-012 f	1.71E+06	6E+04					161.3
Mean SL15-12	1.65E+06	8.5E+05					161.3
Mean Subpop. SL15-12 (b-f)	1.30E+06	3.4E+05					161.3
Shoreline Level 2							
SL 14-01 a	1.94E+06	7E+04			1.98E+07	1.8E+06	161.3
SL 14-01 b	1.82E+06	7E+04	1.04E+07	7E+05	2.03E+07	2.0E+06	161.3
SL 14-01 c	1.63E+06	6E+04			1.55E+07	1.7E+06	161.3
SL 14-01 d	2.00E+06	8E+04			2.18E+07	1.3E+06	161.3
SL 14-01 e	1.64E+06	6E+04			1.87E+07	1.6E+06	161.3
SL14-01 f	2.41E+06	8E+04					161.3
Mean SL14-01	1.91E+06	2.6E+05					161.3
Mean Subpop. SL14-01 (a-e)	1.80E+06	1.5E+05					161.3
Shoreline Level 3							
LL13-001 a	3.89E+06	1.3E+05					161.3
LL13-001 b	2.33E+06	8E+04					161.3
LL13-001 c	1.68E+06	6E+04					161.3
LL13-001 d	2.41E+06	8E+04					161.3
LL13-001 e	2.54E+06	1.1E+05					161.3
LL13-001 f	2.86E+06	9E+04					161.3
Mean Subpop. LL13-001 (b, c, d,e,f)	2.36E+06	3.9E+05					161.3
Shoreline Level 4							
SL14-03 a	4.77E+06	1.7E+05			4.02E+07	3.0E+06	161.4
SL14-03 b	6.02E+06	2.1E+05			4.07E+07	1.8E+06	161.4
SL14-03 c	6.53E+06	2.3E+05					161.4
SL14-03 d	4.02E+06	1.5E+05					161.4
SL14-03 f	2.76E+06	1.5E+05	1.57E+07	1.6E+06			161.4
SL14-03 g	5.32E+06	2.0E+05					161.4
Mean SL14-03	4.90E+06	1.26E+06					161.4
Shoreline Level 5							
SL14-04 a					5.50E+07	2.7E+06	161.6
SL14-04 b	1.04E+07	3E+05			4.31E+08	1.4E+07	161.6
SL14-04 c	1.36E+06	6E+04			4.61E+07	2.1E+06	161.6
SL14-04 g	5.93E+06	2.3E+05					161.6
SL14-04 h	8.29E+06	2.8E+05					161.6
Top Cerro Soledad							
SL14-05 a	8.99E+06	3.0E+05			6.99E+07	3.2E+06	161.6
SL14-05 b	1.05E+07	4E+05			1.16E+08	4E+06	161.6
SL14-05 c	8.71E+06	2.9E+05			7.03E+07	2.8E+06	161.6
SL14-05 e	9.47E+06	3.1E+05			8.10E+07	2.8E+06	161.6
Mean SL14-05	9.42E+06	6.8E+05					161.6
Mean Subpop. SL14-05 (a,c,e)	9.06E+06	3.1E+05					161.6

Table 3: ^{10}Be cosmogenic nuclide exposure ages and production/calculation data

SF (LSD) scaling ^{10}Be	Age	Internal Uncertainty	Total Uncertainty	Elevation/latitude scaling factor (unitless)		Contemporary depth average production rate (atoms/g/yr)				
Sample name	(kyr)	(σ kyr)	(σ kyr)	For neutrons	For muons, fast	For muons, slow	Be, spallation	Mu, spallation	Qs (unitless)	Qmu (unitless)
Shoreline Level 1										
SL 15-012 a	827	41	86	1.104	1.015	1.015	4.4224	0.068998	0.9919	1.0005
SL 15-012 b	231	15	28	1.104	1.015	1.015	4.4043	0.069014	0.98788	1.0007
SL 15-012 c	170	11	19	1.104	1.015	1.015	4.4043	0.069014	0.98788	1.0007
SL 15-012 d	358	20	45	1.104	1.015	1.015	4.3863	0.06903	0.98388	1.0009
SL 15-012 e	254	11	27	1.104	1.015	1.015	4.3863	0.06903	0.98388	1.0009
SL 15-012 f	375	17	44	1.104	1.015	1.015	4.3684	0.069034	0.97991	1.001
Mean SL15-12	360	253	260	1.104	1.015	1.015	4.3863	0.06903	0.98388	1.0009
Mean Subpop. SL15-12 (b-f)	274	74	77	1.104	1.015	1.015	4.3863	0.06903	0.98388	1.0009
Shoreline Level 2										
SL 14-01 a	430	21	52	1.1149	1.0205	1.0205	4.3933	0.069346	0.97595	1.0007
SL 14-01 b	403	17	39	1.1149	1.0205	1.0205	4.3576	0.069323	0.96811	1.0004
SL 14-01 c	355	19	43	1.1149	1.0205	1.0205	4.3223	0.06929	0.96035	0.99993
SL 14-01 d	453	21	49	1.1149	1.0205	1.0205	4.3576	0.069323	0.96811	1.0004
SL 14-01 e	359	17	44	1.1149	1.0205	1.0205	4.3223	0.06929	0.96035	0.99993
SL14-01 f	564	23	56	1.1149	1.0205	1.0205	4.2875	0.069253	0.95268	0.9994
Mean SL14-01	417	74	84	1.1149	1.0205	1.0205	4.4293	0.069348	0.98388	1.0008
Mean Subpop. SL14-01 (a-e)	392	37	52	1.1149	1.0205	1.0205	4.4293	0.069348	0.98388	1.0008
Shoreline Level 3										
LL13-001 a	934	33	83	1.1209	1.025	1.025	4.4899	0.069577	0.9919	1.0003
LL13-001 b	525	17	48	1.1209	1.025	1.025	4.4533	0.069598	0.98388	1.0006
LL13-001 c	358	18	44	1.1209	1.025	1.025	4.4351	0.069598	0.97991	1.0006
LL13-001 d	542	19	49	1.1209	1.025	1.025	4.4533	0.069598	0.98388	1.0006
LL13-001 e	575	29	65	1.1209	1.025	1.025	4.4533	0.069598	0.98388	1.0006
LL13-001 f	676	24	77	1.1209	1.025	1.025	4.417	0.069591	0.97595	1.0005
Mean Subpop. LL13-001 (b, c, d, e, f)	540	160	160	1.1209	1.025	1.025	4.3812	0.069564	0.96811	1.0001
Shoreline Level 3										
SL14-03 a	1230	50	110	1.146	1.0369	1.0369	4.3446	0.068138	0.96811	0.99978
SL14-03 b	1700	110	260	1.146	1.0369	1.0369	4.3446	0.068138	0.96811	0.99978
SL14-03 c	1960	100	250	1.146	1.0369	1.0369	4.3094	0.068103	0.96035	0.99926
SL14-03 d	1000	50	100	1.146	1.0369	1.0369	4.3446	0.068138	0.96811	0.99978
SL14-03 f	658	50	100	1.146	1.0369	1.0369	4.3446	0.068138	0.96811	0.99978
SL14-03 g	1380	100	170	1.146	1.0369	1.0369	4.4342	0.068172	0.98788	1.0003
Mean SL14-03	1270	470	490	1.146	1.0369	1.0369	4.3446	0.068138	0.96811	0.99978
Shoreline Level 5										
SL14-04 a										
SL14-04 b	4500	620	1500	1.205	1.0676	1.0676	4.8094	0.072931	0.9761	0.99921
SL14-04 c	263	10	27	1.205	1.0676	1.0676	4.7706	0.072893	0.9683	0.99869
SL14-04 g	1400	80	180	1.2049	1.0676	1.0676	4.7704	0.072895	0.9683	0.99868
SL14-04 h	2520	180	460	1.2049	1.0676	1.0676	4.8881	0.072977	0.99195	0.9998
Top Cerro Soledad										
SL14-05 a	2880	230	590	1.2187	1.0748	1.0748	4.8642	0.073343	0.9761	0.99896
SL14-05 b	4500	610	1500	1.2187	1.0748	1.0748	4.8642	0.073343	0.9761	0.99896
SL14-05 c	2680	200	520	1.2187	1.0748	1.0748	4.8642	0.073343	0.9761	0.99896
SL14-05 e	3340	300	780	1.2187	1.0748	1.0748	4.825	0.073303	0.9683	0.99842
Mean SL14-05	3220	610	910	1.2187	1.0748	1.0748	4.8642	0.073343	0.9761	0.99896
Mean Subpop. SL14-05 (a,c,e)	2930	240	610	1.2187	1.0748	1.0748	4.8642	0.073343	0.9761	0.99896

Table 4: ^{26}Al cosmogenic nuclide exposure ages and production/calculation data

SF (LSD) scaling ^{26}Al	Age	Internal Uncertainty	Total Uncertainty	Elevation/latitude scaling factor (unitless)		Contemporary depth average production rate (atoms/g/yr)				
Sample name	(kyr)	(σ kyr)	(σ kyr)	For neutrons	For muons, fast	For muons, slow	Mu, spallation	Qs (unitless)	Qmu (unitless)	
Shoreline Level 1										
SL15-012 a	870	71	140	1.104	1.015	1.015	0.65271	0.9919	1.0005	
SL15-012 b	208	19	32	1.104	1.015	1.015	0.65288	0.98788	1.0008	
SL15-012 c	153	15	25	1.104	1.015	1.015	0.65288	0.98788	1.0008	
SL15-012 d										
SL15-012 e										
SL15-012 f										
Mean SL15-12										
Mean Subpop. SL15-12 (b-f)										
Shoreline Level 2										
SL14-01 a										
SL14-01 b	350	31	60	1.1149	1.0205	1.0205	0.65593	0.96811	1.0005	
SL14-01 c										
SL14-01 d										
SL14-01 e										
SL14-01 f										
Mean SL14-01										
Mean Subpop. SL14-01 (a-e)										
Shoreline Level 3										
LL13-001 a										
LL13-001 b										
LL13-001 c										
LL13-001 d										
LL13-001 e										
LL13-001 f										
Mean Subpop. LL13-001 (b, c, d, e, f)										
Shoreline Level 4										
SL14-03 a										
SL14-03 b										
SL14-03 c										
SL14-03 d										
SL14-03 f	590	85	120	1.146	1.0369	1.0369	0.64502	0.96811	0.99985	
SL14-03 g										
Mean SL14-03										
Shoreline Level 5										
SL14-04 a										
SL14-04 b										
SL14-04 c										
SL14-04 g										
SL14-04 h										
Top Cerro Soledad										
SL14-05 a										
SL14-05 b										
SL14-05 c										
SL14-05 e										
Mean SL14-05										
Mean Subpop. SL14-05 (a,c,e)										

Table 5: ^{21}Ne cosmogenic nuclide exposure ages and production/calculation data

SF (LSD) scaling ^{21}Ne Sample name	Age (kyr)	Ext uncerts (σ kyr)	Scaling factor	Production rate (at/g/yr)	Int uncerts (σ kyr)
Shoreline Level 1					
SL 15-012 a					
SL 15-012 b					
SL 15-012 c					
SL 15-012 d					
SL 15-012 e					
SL 15-012 f					
Mean SL15-12					
Mean Subpop. SL15-12 (b-f)					
Shoreline Level 2					
SL 14-01 a	946	128	1.11	18.22	76
SL 14-01 b	974	144	1.11	18.07	85
SL 14-01 c	782	82	1.11	17.92	56
SL 14-01 d	1038	146	1.11	18.07	65
SL 14-01 e	913	106	1.11	17.92	59
SL14-01 f	928	105	1.11	17.92	64
Mean SL14-01					
Mean Subpop. SL14-01 (a-e)					
Shoreline Level 3					
LL13-001 a					
LL13-001 b					
LL13-001 c					
LL13-001 d					
LL13-001 e					
LL13-001 f					
Mean Subpop. LL13-001 (b, c, d,e,f)					
Shoreline Level 4					
SL14-03 a	1840	270	1.15	18.02	150
SL14-03 b	1870	270	1.15	18.02	80
SL14-03 c					
SL14-03 d					
SL14-03 f					
SL14-03 g					
Mean SL14-03					
Shoreline Level 5					
SL14-04 a	2280	320	1.20	19.94	120
SL14-04 b	21600	700	1.20	19.94	*
SL14-04 c	1920	230	1.20	19.78	90
SL14-04 g					
SL14-04 h					
Top Cerro Soledad					
SL14-05 a	2880	390	1.22	20.17	140
SL14-05 b	4830	640	1.22	20.17	180
SL14-05 c	2900	390	1.22	20.17	120
SL14-05 e	3380	450	1.22	20.01	120
Mean SL14-05					
Mean Subpop. SL14-05 (a,c,e)					

* beyond CRONUS EARTH Calculator max. age, recalculated

Table 6: Sensitivity test utilizing different magnetic reconstructions using CREp.

	Applied Scaling: LSD Atmosphere: ERA40 Geomagn.Database: Lifton et al. 2014 Prod. Rate: 3.99 +/- 0.22 at/g/yr Global Average				Applied Scaling: LSD Atmosphere: ERA40 Geomagnetic Database: Atm. 10Be-based VDM Production Rate: 4.11 +/-0.26 at/g/yr Global Average			Deviation from LSD Geomagnetic Framework	Applied Scaling: LSD Atmosphere: ERA40 Geomagn.Database: Lifton VDM 2016 Prod. Rate: 4.08 +/- 0.23 at/g/yr Global Average			Deviation from LSD Geomagnetic Framework
Sample	Scaling	Age [ka]	Uncertainty 1s	Uncert. without P error	Scaling	Age [ka]	Uncertainty 1s	Uncert. without P error		Scaling	Age [ka]	Uncertainty 1s	Uncert. without P error	
LL13-001 A	1.3	967.06	53.64	27.7	1.17	1059.14	64.96	31.23	10%	1.26	972.85	54.47	27.34	1%
LL13-001 B	1.28	534.77	31.89	16.08	1.16	581.3	38.48	18.75	9%	1.25	535.16	31.59	15.89	0%
LL13-001 C	1.3	365.7	28.02	16.23	1.16	402.75	32.77	16.89	10%	1.27	366.91	27.66	15.92	0%
LL13-001 D	1.28	553.76	33.68	17.77	1.16	603.07	46.16	20.96	9%	1.26	554.24	33.42	17.64	0%
LL13-001 E	1.28	589.68	41.64	25.11	1.14	650.97	53.99	32.4	10%	1.26	590.26	41.39	24.89	0%
LL13-001 F	1.27	695.71	49.22	22.68	1.13	770.99	49.29	22.46	11%	1.24	696.8	48.84	22.53	0%
SL 15-012a	1.24	864.93	52.7	31.06	1.13	939.9	59.72	34.12	9%	1.22	867.69	52.48	31.13	0%
SL 15-012b	1.28	237.18	19.59	13.55	1.14	259.95	21.24	13.77	10%	1.25	239.55	19.35	13.31	1%
SL 15-012c	1.26	173.52	13.33	9.45	1.14	186.64	13.57	8.38	8%	1.21	176.65	12.52	8.87	2%
SL 15/12d	1.26	370.73	29.08	17.75	1.12	408.98	33.83	19.74	10%	1.23	372.83	28.7	17.4	1%
SL 15/12e	1.28	259.67	17.72	10.22	1.15	283.19	19.94	10.41	9%	1.24	262.55	17.51	9.82	1%
SL 15/12f	1.26	386.11	27.84	14.99	1.11	429.11	34.37	18.57	11%	1.23	388.2	27.33	14.55	1%
SL 14-01-a	1.27	442.53	33.1	18.67	1.12	490.3	36.11	18.53	11%	1.24	443.29	32.8	18.41	0%
KL 512 Sl 14-(	1.28	412.16	29.83	16.71	1.13	458.56	35.5	18.26	11%	1.25	413	29.52	16.55	0%
SL 14-01-c	1.29	364.75	28.52	17.24	1.15	401.76	33.34	17.8	10%	1.26	366.02	28.15	16.98	0%
KL 514 SL 14-	1.26	465.79	33.63	19.24	1.13	513.25	34.48	18.3	10%	1.24	466.53	33.23	19	0%
SL 14-01-e	1.29	369.08	27.77	15.41	1.14	406.38	32.5	16.82	10%	1.26	370.37	27.42	15.14	0%
SL 14-01-f	1.27	582.05	37.98	20.39	1.14	639.4	51.24	27.99	10%	1.24	582.71	37.76	20.25	0%

References

Allmendinger, R. W., González, G., Yu, J., Hoke, G., and Isacks, B., 2005, Trench-parallel shortening in the Northern Chilean Forearc: Tectonic and climatic implications: Geological Society of America Bulletin, v. 117, no. 1, p. 89.

Binnie, S. A., Dunai, T. J., Voronina, E., Goral, T., Heinze, S., and Dewald, A., 2015, Separation of Be and Al for AMS using single-step column chromatography: Nuclear Instruments and Methods in Physics Research Section B: Beam Interactions with Materials and Atoms.

Borchers, B., Marrero, S., Balco, G., Caffee, M., Goehring, B., Lifton, N., Nishiizumi, K., Phillips, F., Schaefer, J., and Stone, J., 2016, Geological calibration of spallation production rates in the CRONUS-Earth project: Quaternary Geochronology, v. 31, p. 188-198.

Dewald, A., Heinze, S., Jolie, J., Zilges, A., Dunai, T., Rethemeyer, J., Melles, M., Staubwasser, M., Kuczewski, B., Richter, J., Radtke, U., von Blanckenburg, F., and Klein, M., 2013, CologneAMS, a dedicated center for accelerator mass spectrometry in Germany: Nuclear Instruments & Methods in Physics Research Section B-Beam Interactions with Materials and Atoms, v. 294, p. 18-23.

Dunai, T. J., 2001, Influence of secular variation of the geomagnetic field on production rates of in situ produced cosmogenic nuclides: Earth and Planetary Science Letters, v. 193, no. 1-2, p. 197-212.

Kober, F., Alfimov, V., Ivy-Ochs, S., Kubik, P. W., and Wieler, R., 2011, The cosmogenic (NE)-N-21 production rate in quartz evaluated on a large set of existing Ne-21-Be-10 data: Earth and Planetary Science Letters, v. 302, no. 1-2, p. 163-171.

Kohl, C., and Nishiizumi, K., 1992, Chemical isolation of quartz for measurement of< i> in-situ</i>-produced cosmogenic nuclides: Geochimica et Cosmochimica Acta, v. 56, no. 9, p. 3583-3587.

Lifton, N., Sato, T., and Dunai, T. J., 2014, Scaling in situ cosmogenic nuclide production rates using analytical approximations to atmospheric cosmic-ray fluxes: Earth and Planetary Science Letters, v. 386, p. 149-160.

Lifton, N. A., Smart, D. F., and Shea, M. A., 2008, Scaling time-integrated in situ cosmogenic nuclide production rates using a continuous geomagnetic model: Earth Planet. Sci. Lett., v. 268, no. 1-2, p. 190-201.

Marrero, S. M., Phillips, F. M., Borchers, B., Lifton, N., Aumer, R., and Balco, G., 2016, Cosmogenic nuclide systematics and the CRONUScalc program: Quaternary Geochronology, v. 31, p. 160-187.

Martin, L., Blard, P.-H., Balco, G., Lavé, J., Delunel, R., Lifton, N., and Laurent, V., 2017, The CREp program and the ICE-D production rate calibration database: A fully parameterizable and updated online tool to compute cosmic-ray exposure ages: Quaternary geochronology, v. 38, p. 25-49.

Muscheler, R., Joos, F., Müller, S. A., and Snowball, I., 2005, How unusual is today's solar activity?: Nature, v. 436, p. doi:10.1038/nature04045.

Nishiizumi, K., 2004, Preparation of 26 Al AMS standards: Nuclear Instruments and Methods in Physics Research Section B: Beam Interactions with Materials and Atoms, v. 223, p. 388-392.

Nishiizumi, K., Imamura, M., Caffee, M. W., Southon, J. R., Finkel, R. C., and McAninch, J., 2007, Absolute calibration of Be-10 AMS standards: Nucl. Instr. Meth. Phys. Res. B, v. 258, p. 403-413.

Stone, J. O., 2000, Air pressure and cosmogenic isotope production: J. Geophys. Res., v. 105, no. B10, p. 23753-23759.

Valet, J. P., Meynadier, L., and Guyodo, Y., 2005, Geomagnetic dipole strength and reversal rate over the past two million years: Nature, v. 435, p. 802-805.

Vermeesch, P., Balco, G., Blard, P.-H., Dunai, T. J., Kober, F., Niedermann, S., Shuster, D. L., Strasky, S., Stuart, F. M., and Wieler, R., 2012, Interlaboratory comparison of cosmogenic 21 Ne in quartz: Quaternary Geochronology.

5. Neogene fluvial landscape evolution in the hyperarid core of the Atacama Desert

Journal Article: (2018)

Received 7 March 2018, Accepted 28 August 2018, Published online 17 September 2018.

Ritter, B., Binnie, S.A., Stuart, F.M., Gerdes, A., Wennrich, V., Dunai, T.J. 2018 – Neogene fluvial landscape evolution in the hyperarid core of the Atacama Desert – Scientific Reports 8:13952 | DOI:10.1038/s41598-018-32339-9

www.nature.com/scientificreports

OPEN

Neogene fluvial landscape evolution in the hyperarid core of the Atacama Desert

Received: 7 March 2018
Accepted: 28 August 2018
Published online: 17 September 2018

Benedikt Ritter[1], Finlay M. Stuart[2], Steven A. Binnie[1], Axel Gerdes[3], Volker Wennrich[1] & Tibor J. Dunai[1]

Dating of extensive alluvial fan surfaces and fluvial features in the hyperarid core of the Atacama Desert, Chile, using cosmogenic nuclides provides unrivalled insights about the onset and variability of aridity. The predominantly hyperarid conditions help to preserve the traces of episodic climatic and/or slow tectonic change. Utilizing single clast exposure dating with cosmogenic ^{10}Be and ^{21}Ne, we determine the termination of episodes of enhanced fluvial erosion and deposition occurring at ~19, ~14, ~9.5 Ma; large scale fluvial modification of the landscape had ceased by ~2–3 Ma. The presence of clasts that record pre-Miocene exposure ages (~28 Ma and ~34 Ma) require stagnant landscape development during the Oligocene. Our data implies an early onset of (hyper-) aridity in the core region of the Atacama Desert, interrupted by wetter but probably still arid periods. The apparent conflict with interpretation that favour a later onset of (hyper-) aridity can be reconciled when the climatic gradients within the Atacama Desert are considered.

The Atacama Desert of northern Chile is one of the driest places on Earth, with an extreme hyperarid core (Coastal Cordillera & Central Depression between 19° and 22°S), receiving less than 2 mm/yr modern precipitation[1,2]. Subtropical atmospheric subsidence[3], and the temperature inversion due to coastal upwelling of cold waters of the Peru-Chile Current[1] have led to hyperarid conditions. The Andes Mountains to the east (Fig. 1) cast a rainshadow over the Atacama Desert as moisture originating from the Atlantic becomes orographically elevated, causing precipitation on the eastern Andean flank and a relative absence westwards[4]. These effects, coupled with high evaporation rates in most areas of the Atacama Desert strengthen hyperarid conditions[4,5]. While the main factors controlling hyperaridity in the Atacama Desert are established, the onset and permanence of hyperaridity remain a matter of debate[6–17].

The nearly stable position of the South American continent over the least 150 Ma[18] and the establishment of the Peru-Chile Current system at around 50 Ma[19] support the notion that predominantly arid conditions persisted since the early Miocene[9] or potentially earlier[18]. Secular changes of the global climate system during the Cenozoic[20], led to punctuations of the prevailing arid climate in the Atacama Desert by pluvial phases e.g.[9,10,12,21,22].

The absence of fluvial erosion means that long-term tectonic activity is a prominent control on landscape evolution in the hyperarid core of the Atacama Desert. Between 19°S and 21.4°S E-W reverse faults[23] play a major role in generating relief. The resulting scarps, commonly at the angle of repose (35–40°) and devoid of signs of fluvial incision, are up to 300 m high and have formed since at least the Mid-Miocene >15 Ma[24]. The slow vertical movement of these reverse faults (<20 m/Myr) has truncated fluvial channels and blocked drainage[24]. The Atacama Fault System (AFS), a system of primarily trench-parallel strike-slip faults in the area around the Río Loa (Salar Grande Segment)[23] is a subtler agent of surface modification, largely in the form of horizontal displacement (at unknown rates) and moderate (<50 m) vertical uplift along flower structures. The AFS was active throughout the Cenozoic[23,25]; the topographically subtle surface expressions of its trace are preserved throughout the hyperarid core of the Atacama Desert.

In the present study, we exploit the interplay between slow fault displacement and intermittent fluvial activity to delineate the timing of less-arid periods interrupting the long-term background hyperaridity. We use multiple

[1]Institute of Geology & Mineralogy, University of Cologne, Cologne, Germany. [2]Isotope Geosciences Unit, Scottish Universities Environmental Research Centre, East Kilbride, UK. [3]Institute of Geosciences, Goethe-University Frankfurt, Frankfurt, Germany. Correspondence and requests for materials should be addressed to B.R. (email: benedikt.ritter@uni-koeln.de)

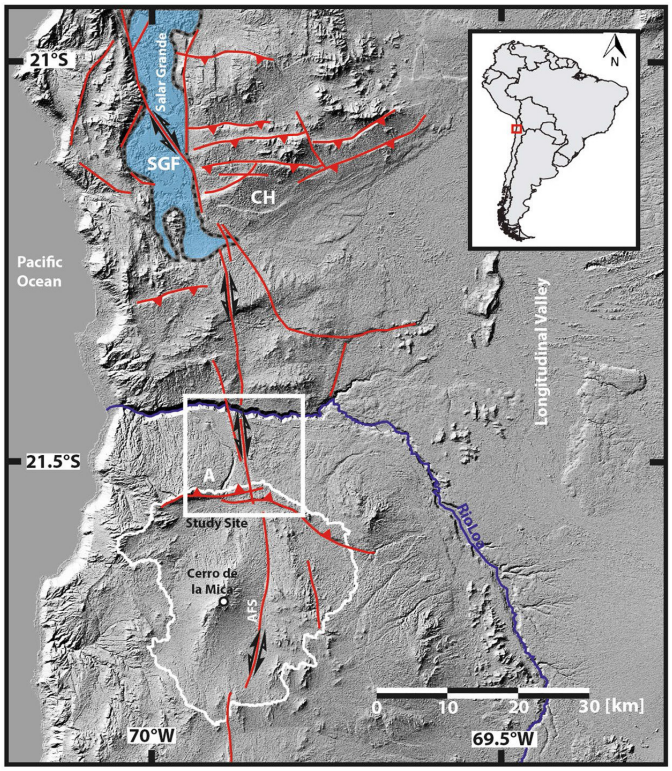

Figure 1. Hillshade image based on Aster GDEM data (30 m resolution, produced using ArcGIS 10.5.1). The study area (white square) is bound toward the north by the perennial Río Loa and to the south by the display source area (white stippled line). Red lines indicate major tectonic fault systems. The enorheic basin that once supplied the sediments investigated in this study is marked with the stippled white line. SGF = Salar Grande Fault, CH = Chuculay Fault, A = Adamito Fault[24,31,92], this study.

single-clast exposure ages to determine the timing of tectonically fossilized depositional surfaces, and to detect possible pre-exposure of clasts and/or post-depositional erosion. Our results indicate an Oligocene onset of aridity in the core of the Atacama Desert, with interspersed episodes of enhanced fluvial activity in the Miocene and Pliocene. Preservation of Early Miocene alluvial fan surfaces indicate a predominantly (hyper-) arid climate conditions since the Early Miocene.

Geological Setting

The central Atacama Desert is located in the fore-arc region of the Central Andes of northern Chile. The Andes mountain orogeny is a consequence of the subduction of the oceanic Nazca plate under the continental South American plate since the Cretaceous[23]. The Peru-Chile trench is located just 70–50 km offshore[23]. The study site is situated in the Coastal Cordillera (Fig. 1), an eroded Jurassic magmatic arc, which consists of a series of Early Cretaceous extensional basins, filled up with Late Oligocene to Early Miocene volcanoclastic sediments[26]. The Coastal Cordillera reaches elevations of between 1000–1800 m, with its westwards extent limited by a coastal cliff that reaches 1000 m above current sea-level and its eastward extend demarcated by the sedimentary infill of the Central Depression. The development of the Oligocene-Miocene (~20 Ma) coastal Tarapaca pediplain coincided with the end of sedimentation in the Coastal Cordillera and the onset of hyperaridity in the Atacama region e.g.[27,28]. Since the formation of this erosional surface, the Coastal Cordillera has experienced tectonic activity; that has produced as much as 300 m of local relief[24]. The stress field of the slightly oblique plate subduction[29] gave rise to reverse faults, orthogonal to the plate boundary and approximately parallel to the convergence direction[23]. The resulting exposed fault scarps occur between 19° and 21.6°S in the Costal Cordillera[23]. ^{21}Ne exposure ages of planation surfaces east of the Salar Grande (Chuculay Fault system), bisected by these reverse faults, range between 15 and 24 Ma[24], while a truncated paleo-channel gives an age of 4 Ma[24]. The ages of the planation surfaces place an upper limit for the onset of reverse faulting at the corresponding locations; the age of the truncated paleo-channel indicates the faulting was active after 4 Ma[24].

Study Area

The study area is bound to the north by the Río Loa canyon and in the south by the extensions of the paleo catchment (Fig. 1). The main geomorphological features of the study area are, (i) the Atacama and the Adamito fault system (ii) an alluvial fan system east of the Atacama fault (Fig. 2A), with three distinct alluvial fans and feeder channels; and (iii) a system of paleo-channels lying to the west of the Atacama fault system (Fig. 2A). The Adamito fault system[30] (Fig. 1) bisects the study area. This fault is also named Aguirre Fault[31], however in accordance with the initial description we will use the name Adamito fault. Prior its truncation by the Adamito fault system, the source area of the alluvial fans (i.e. drainage area above apex[32]) encompassed the Cerro de la Mica (1817 m elevation) and surrounding areas up to 25 km further south (~560 km^2 - stippled white line Fig. 1), which is now part of an endorheic basin containing a clay pan (Figs 2A and 3D). Based on modern elevation topography, we assume a flow direction from south to north. After the onset of uplift along the Adamito fault the fans' apex was at or north of the fault. Prior to fault movement the apex of the eastern-most fan might have been south of the fault; however, we found no indication for the latter.

The Adamito (Aguirre) fault system is the southernmost reverse fault system in the Coastal Cordillera[23]. It forms a steep scarp, partially modified by gravitational slumping (Fig. 3D). The cumulative vertical offset created by the set of two faults (Adamito and Atacama) is up to 130 m; truncating the paleo-drainages. The three paleo-drainages are identified by the continuity of incised-channel forms, yet the paleo-thalwegs have an intermediate high-elevation position, referred to as the vertex, which now divide the incised channels into a south-draining and a north draining region.

The elevation of the dissected channels, measured at the highest present day water-divide, decreases from 1090 m for the easternmost channel (Fig. 2B,C) to 1000 m for the westernmost paleo-channel with a value of 1050 m for the middle channel (Fig. 2B,C). Assuming that the kinematics of fault movement did not change during the incision of the paleo-drainage, it follows that the ages of the paleo-drainage decrease moving from east to west.

The elongated N-S extending trench-parallel Atacama fault zone runs through the study site (Figs. 1, 2). The AFS extends north to the Salar Grande, where it causes vertical displacement of up to 50 m[23,25,33]. In conjunction with an inferred splay fault (sub-parallel secondary fault of the AFS) close to the Río Loa (Figs 2A and 3A), the AFS creates a local topographic high, about 20–30 m higher than the alluvial fan surface to the east and up to 90 m higher than the west. No visible vertical offset could be observed at the Río Loa canyon walls, as hillslopes are largely covered by debris. The vertical offset is evident from incised fluvial channels in the uplifted block north of the Río Loa, (Supplementary Fig. 5). Surface deposits obscure signs of recent horizontal displacement.

Results

Alluvial Fans. The alluvial fan system consists of three distinct alluvial fan surfaces (Fig. 2A). Their outline can be identified on satellite imagery (Google earth, Pleiades used here, Fig. 2, and supplementary data set) and on the eastern-most fan indicative surface structures (sediment lobes in the direction of paleo-flow) are visible. Due to extensive gypsum soil cover the fan surfaces are less conspicuous on the ground, on first sight resembling any near-horizontal surface in the dry core of the Atacama. Feeder channels and lateral fan boundaries, however, are discernible on the ground. Identification and selection of sampling sites was always guided by satellite imagery.

The fan surfaces are dipping to the north, (0.9°–1.6°), with decreasing slopes from east to west (eastern fan 1.46°, central fan 1.3°, western fan 0.9°). The source area of the depositional surfaces can be related to the endorheic catchment to the south (Fig. 1). This assumption is based on the modern flow direction of the closed catchment and the direction of paleo-channels and feeder channel of alluvial fans north of the Adamito fault. Distal fan surfaces near the Río Loa canyon are buried by lacustrine sediments related to lake episodes in the Central Depression (diatom-rich sediments and evaporitic remnants of the Quillagua (Pliocene) and Soledad Fm (Plio-Pleistocene)[13,34]). Cross-cutting relationships of the fans are partially obscured by the lake deposits; however, the eastern-most margin of the central fan can be inferred as cutting into the eastern fan (Fig. 2A black stippled lines and Fig. 6D supplementary data set). The maximum sediment thickness of alluvial and lacustrine strata is approximately 85 m, as exposed in outcrops along the Río Loa canyon. The lacustrine deposits occur exclusively east of the topographic high formed by the AFS (Fig. 2A). The distal portions of the alluvial fans resemble an inverted landscape, whereby lateral fan boundaries commonly end abruptly and narrow, channel-like sediment lobes are several meters (up to 8 m) above their surroundings. The steep lateral fan boundaries are probably enhanced by differential erosion of (coarse) fan-sediment covered areas and areas that lack this cover. Areas adjacent to the flanks are commonly endorheic deflation hollows. Strong westerly anabatic winds, associated with the diurnal heating of the Altiplano to the East[35,36], are the likely cause of deflation of neighbouring – presumably (since they are now missing) finer grained sedimentary rocks.

The surfaces of the eastern and central fan are essentially flat, with long-wavelength (10–100 m scale) topography variations on the cm-scale. The surfaces are covered by gypsum-rich soils that typically comprise a 10–30 cm powdery, locally friable, layer chuca, senu Ericksen[37], underlain by a moderately to firmly cemented sediment layer costra, senu Ericksen[37]. Due to the cementation of this layer its depth could not be determined in this study; usually it is 0.5 to 2 m thick[37]. The gypsum accumulations in the soils are due to atmospheric deposition of calcium sulphate[16,38,39] onto the alluvial fan surfaces. Following the 'born at the surface' model of Wells *et al.*[40] stones of a desert pavement remain at the surface on an accretionary mantle of soil-modified dust and are successively lifted from the bedrock/original sediment surface; this process has been confirmed as being operational in hyper-arid soils of the Atacama[38] and allows the continuous exposure of clasts on the surface of the alluvial fans. Any modifications of the soil-surface by deflation or gentle fluvial erosion would keep clasts at the surface.

The surfaces of the eastern and central fan were devoid of any indication of recent runoff able to erode the gypsum soil. The observed polygonal pedogenic surface patterns do not relate to gradient and are not used for runoff. The

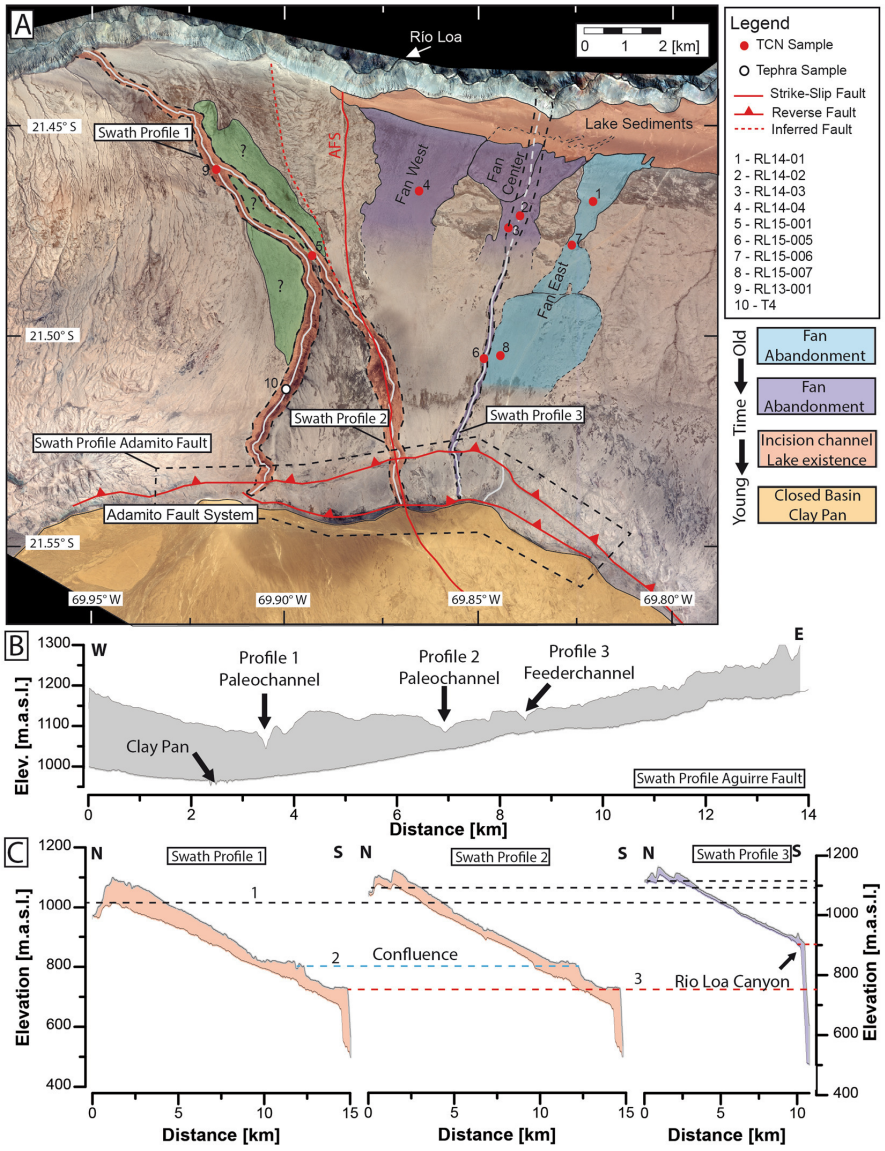

Figure 2. (**A**) Pléiades 1B Multi-Spectral Image of the study area. Red dots indicate locations of samples taken for *in situ* cosmogenic nuclide determinations, and the white dot is the location of the tephra sample. Red lines indicate mapped fault systems (this study), the dashed red line indicates an inferred splay fault. Colour shading provides the relative surface age from geomorphological evidence. No reasonable relative age estimation could be achieved for the green area, based on field and satellite observation. White lines mark major fluvial channels and channel remnants. The areas bound by black dashed lines are used for swath profiles (ArcGIS 10.5.1) of the Adamito fault (**B**) and for Channel swath profiles (**C**) of the three major S-N flowing channels. Black dashed lines (1) in the channel profiles (**C**) mark the elevation of the vertex of the corresponding channels. Blue dashed line (2) marks the confluence area of the two paleo-channel to the east. The red dashed line (3) indicates the elevation of the Río Loa canyon top. Note that these elevations decrease from east to west, here taken as evidence for tectonic tilting of the area and relocation of drainage from east to west.

surface of the westernmost fan has medium-wavelength (horizontal ~10 m scale) variations in the micro-topography on the dm-scale. Traces of recent (Quaternary) runoff are ubiquitous, resembling shallow braided channel systems. Powdery gypsum-rich soils are largely absent, possible remnants (each $<1\,m^2$) remain in the centre of some braids.

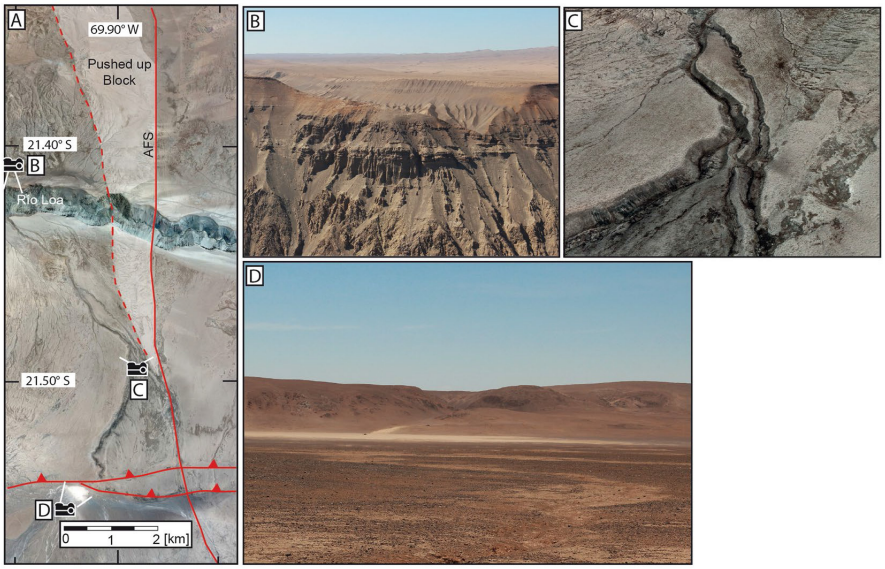

Figure 3. (**A**) Google Earth image (Image data: ©2018 CNES/Airbus & Digital Globe, image recoding 11/7/2014) highlighting the course of the splay fault and uplifted tectonic block. (**B**) Photograph from the northern rim of the Río Loa towards the hanging outflow of the main, westernmost paleo channel (made by B. Ritter). (**C**) Pléiades 1B Pansharped Multi-Spectral 3D image (ArcScene 10.5.1) showing an oblique view of the paleo-channel upstream of the confluence. Except for one tributary channel, the lack of incision of the surrounding flat areas in response to incision of the main channel and generally the smooth valley flanks, points to a predominantly hyper-arid climate since at least the incision of the main channel. (**D**) Photograph (made by B. Ritter) looking north to the endorheic clay pan that was created by the activity of the Adamito thrust fault, blocking its drainage. The ~110 m high ridge in the background is the scarp of the Adamito fault. The depression in the ridge is the wind gap of the main, westernmost paleo channel. The vertex in the wind gap is presently ~50 m above the surface of the clay pan.

Rock fragments are rare on the fan surfaces (on average less than 1 clast per 25 m^2) and consist predominantly of vein-quartz (>95%). Some clasts retain fluvial rounding, most have angular shapes, which derive from 'kernsprung' (insolation weathering). On the central and eastern fan, angular fragments commonly occur in clusters on the surface, due to 'kernsprung' of former larger clasts (vein quartz – polymineral quartz would already have disintegrated and eroded) and the limited amount of observed dispersion of these fragments (mostly <2 m) indicates surface stability and limited diffusive transport. Advective fluvial transport would have dispersed the clasts further and destroy clusters. Sharp edges of quartz clasts that were destroyed by 'kernsprung' limit aeolian modification/erosion to less than 1 mm. We found no evidence of windkanter-like modification of quartz clasts (ventifacts), which is probably due to the dominance of gypsum surface materials in the study area and the rarity of quartz in the size fractions transported by wind (i.e. sand and smaller).

Vein-quartz is a trace constituent of the rocks in the feeder (paleo-) catchment (Jurassic granitoids and Devonian/Carboniferous metasediments[30]). As such the vein-quartz constitute a lag deposit, with fine-grained and/or polymineralic rocks removed by physical erosion (salt-weathering, abrasion) and chemical weathering[41]. The study area experiences regular sea fog[42] which has probably enhanced chemical weathering. Modern analogues for the channels that would have shed sediments onto the paleo-fans exist as 10–15 m wide active channels, presently draining towards the clay pan adjacent to the Adamito fault (Fig. 2A). In these channels, granitoid and metasediment clasts dominate; vein quartz clasts, equivalent to those found on the fan surface, constitute less than <1% of clasts found in the large channels. The feeder channel of the central fan is well preserved and deeply (~12 m) incised into older fan-deposits. Several faint feeder channels are visible near the fault scarp (Fig. 2A white lines).

Paleo channel System. A paleo channel system with one main channel (~16 km length) lies to the west of the alluvial fans and one lateral tributary (~11 km length) to the east. (Figs 2A and 3C). The formation of the eastern tributary channel coincides with the topography along the Atacama fault zone and its irregular morphology is affected by fault activity and slumping. Both paleo-channels were deflected north of the Adamito fault from a north to northwest direction by a topographic high, presumably developed by the interaction of the AFS and an adjacent splay fault. To the west of the Atacama fault zone, both channels have smooth V- shaped cross-sections, which are occasionally modified by gravitational mass-movement on their steep slopes. In the central section, (ca. 5 km north of the Adamito fault and south of the confluence of the central and tributary channel) fluvial modification of channel hillslopes is limited to isolated patches with rill-erosion. The dominant hill-slope process is

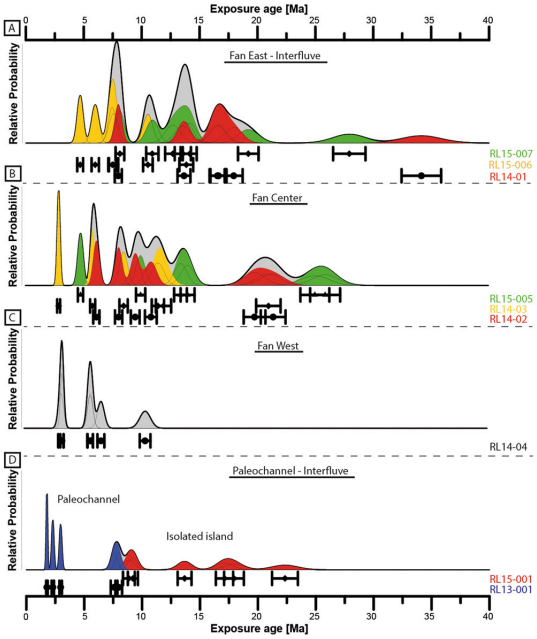

Figure 4. Cumulative probability density plots of ^{21}Ne ($\pm 1\sigma$) single-clast exposure ages from the study area. Sub-plots display the data for each fan/channel system. Grey areas reflect the cumulative distribution of all samples of one system, coloured areas reveal cumulative probability of individual sampling sites within a system. The data is also presented as points and error bars ($\pm\sigma$) arranged in lines for individual sampling location (corresponding sample names are shown at the left; the text colours reflect the colour of the density plot) below the density plots. The locations of the systems and sampling sites area shown in Fig. 2.

gravitational movement. Hillslopes have prominent cracks at a steep angle to the gradient. Minor cracks are gravitationally modified soil polygons. The morphology of the cracks is not fluvially enhanced. The channel downstream of the confluence shows signs of fluvial incision, resembling badland erosion near to the confluence with the Río Loa canyon. At the confluence with the Río Loa the paleo-channel terminates as a hanging-valley, ~450 m above the channel bed of the perennial Río Loa (Fig. 3B).

The two paleo-channels incise 40–60 m into the surrounding gypsum-soil covered flats, with the incised depth increasing downstream. There is no indication of any sedimentation by the paleo-channels onto the adjacent flats, prior to their incision. The paleo-channels run straight for most of their course, though some portions have noticeable sinuosity. For the first 1.5 km just north of the Adamito fault zone the main paleo-channel has a sinuosity of ~1.3; a short segment (600 m) in the lower reaches of the tributary channel has a sinuosity of ~1.15 (Fig. 2A). Portions of the main channel, particularly on the western side of the channel, are covered by up to 1 m thick pure pristine tephra (i.e. without xenolithic/extraneous lithic fragments) with a thin surficial coating (<5 mm) of friable gypsum crust.

Zircon U/Pb dating. Single zircon tephra ages (n = 62) derived by U/Pb dating range from 438 to 0.86 Ma (see Supplementary Table 3). U/Pb zircon ages reflect different degrees of contamination by zircons derived from pre-eruption country-rock and reworking. The youngest cluster of zircons within 2σ represents the eruption age. The age spectrum is dominated by zircon ages around 1 Ma. The oldest group, less numerous, represents xenocrystic grains which could result from assimilation of local bedrock material during magma ascent or eruption (zircon U/Pb ages older than 20 Ma). Taking the cluster of youngest zircon ages as indication for the eruption ages, is based on the assumption that young zircons are unlikely to have experienced significant Pb loss, which would result in anomalously young ages[43]. Based on published eruption data from volcanic complexes within the Atacama Desert, the zircon ages of the tephra can be linked to the latest eruption of the Purico Complex, with an eruption age of 0.98 ± 0.03 Ma (2σ) (Ar/Ar-dating on biotite[44]) or the Tatio ignimbrite 0.703 ± 0.010 Ma (2σ) (Ar/Ar-dating on sanidine[45]). Both belong to the Altiplano Puna Volcanic Complex[46]. Due to a potential pre-eruptive crystallization history, and the early crystallization duration of zircons[46], a direct assignment to one of those eruptions is not possible. The pre-eruptive evolution of the Purica centre lasted 290 ka[46]. The purity of the sampled ash, i.e. the absence of extraneous lithic fragments, precludes fluvial reworking since its deposition in the paleo-channel. This implies that the paleo-channel has not carried surface run off since at latest 0.7–1 Ma.

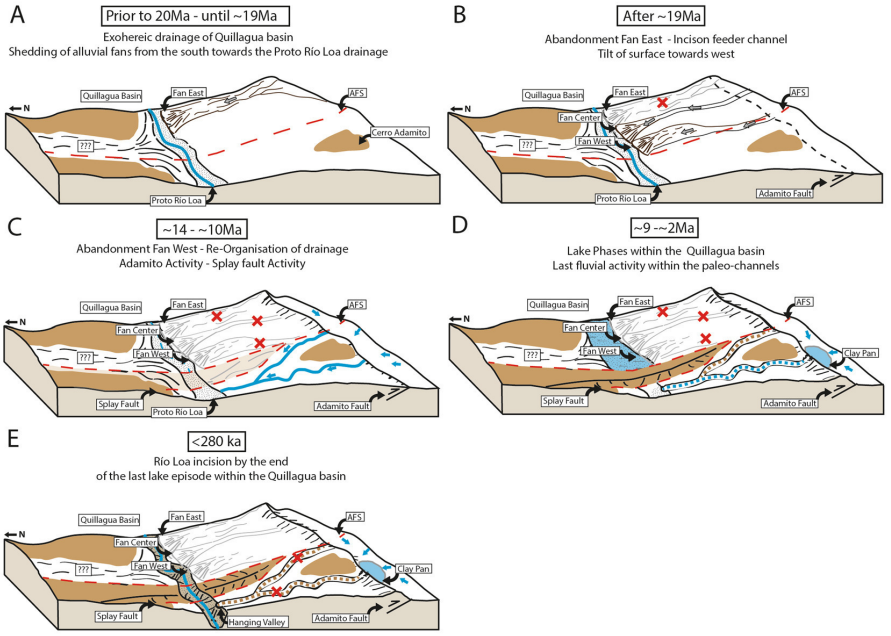

Figure 5. Sketches of the geologic and geomorphologic evolution of the study area through time, based cosmogenic nuclide exposure data (this study).

Cosmogenic exposure ages. *^{21}Ne exposure ages.* Cosmogenic ^{21}Ne concentrations have been measured in 53 samples from 9 sample sites (Fig. 2A, Supplementary data Table 1). Exposure ages (^{21}Ne) range from ~2 Ma to up to ~34 Ma (Fig. 4). The majority of ages (>80%) are younger than 15 Ma and the fan surfaces yield no age younger than 3 Ma. In the following three or more ages with overlapping uncertainty envelopes are used to delineate a group of ages.

On aggregate, the ages of the three samples from the eastern fan system (RL15–006 & 7; RL14-01) have one negatively skewed group of ages between ~16.5–19.5 Ma and one symmetrical group of ages between ~13–14.5 Ma (9 of 18 ages; Fig. 4A, Supplementary data Table 1), a third group around ~7.5–8 Ma (3 of 18 ages), and individual ages at ~4.7, ~6, ~11, ~28, and ~34 Ma. Individual, old, clasts (>20 Ma) occur in two of the three samples (RL14-01, RL15-007). The highest exposure age (~34 Ma) is amongst the oldest reported for the Atacama Desert[9,10,24].

In total the ages of the three samples from the central fan system (RL15-005; RL14-02 and 3) have a main negatively skewed group of ages between ~14 and 8 Ma (9 of 18 ages; Fig. 4B, Supplementary data Table 1). Additional groups occur between 19–25 Ma (5 ages), two ages at ~6 Ma, and individual ages at ~5 Ma and ~3 Ma.

The six ages of the westernmost fan surface (RL14-04) range between ~10.5 and ~3 Ma, with a group of three ages around ~5.5–6.5 Ma (Fig. 4C).

The samples from the surface that was isolated by the incision of the two branches of the paleo-channel system in the west (RL15-001), range between Early to Late Miocene (Fig. 4D), with individual ages at ~22, ~17.5 (n = 2), ~14, and ~9 Ma (n = 2). The samples taken from the incised paleo-channel (RL13-001) show similar ages at ~8 Ma (n = 2), and the youngest being ~2 Ma (n = 2).

Cosmogenic ^{10}Be exposure ages. Concentrations of *in situ* produced cosmogenic ^{10}Be were determined for six quartz clasts (Supplementary data Table 2), four from the easternmost (RL14-001) and two from the central fan system (RL14-02). The ^{21}Ne ages of the RL14-001 clasts range between ~14–18 Ma, those of the RL14-02 clasts between ~8–10 Ma. Within typical measuring precision of several percent, cosmogenic ^{10}Be concentrations reach saturation (secular equilibrium) after around two to three half-lives (^{10}Be 1.36 ± 0.07 Ma[47]), when the rate of ^{10}Be lost via radioactive decay and the rate of cosmogenic ^{10}Be production become similar. In such cases, the ^{10}Be concentration becomes time invariant and no further information can be obtained from the sample, other than it has been exposed for the minimum time required to reach saturation[48]. All but one sample are at, or near, saturation with respect to ^{10}Be, indicating a continuous exposure at the surface over at least the last 4 Ma, approximately. One sample (RL14-02 clast e) yields a ^{10}Be exposure age of 1.8 ± 0.2 Ma. The saturated (or near-saturation) samples correspond to high ^{21}Ne ages; the single age of 1.8 ± 0.2 Ma (RL14-02 clast e) indicates the recent exhumation of this particular clast from a temporarily (partially) shielded position.

Interpretation. *Cosmogenic exposure ages of depositional surfaces.* *In situ* cosmogenic nuclide concentrations are now widely used to determine the timing of sediment deposition in the Atacama Desert[6,8–10,21,24,28,49,50].

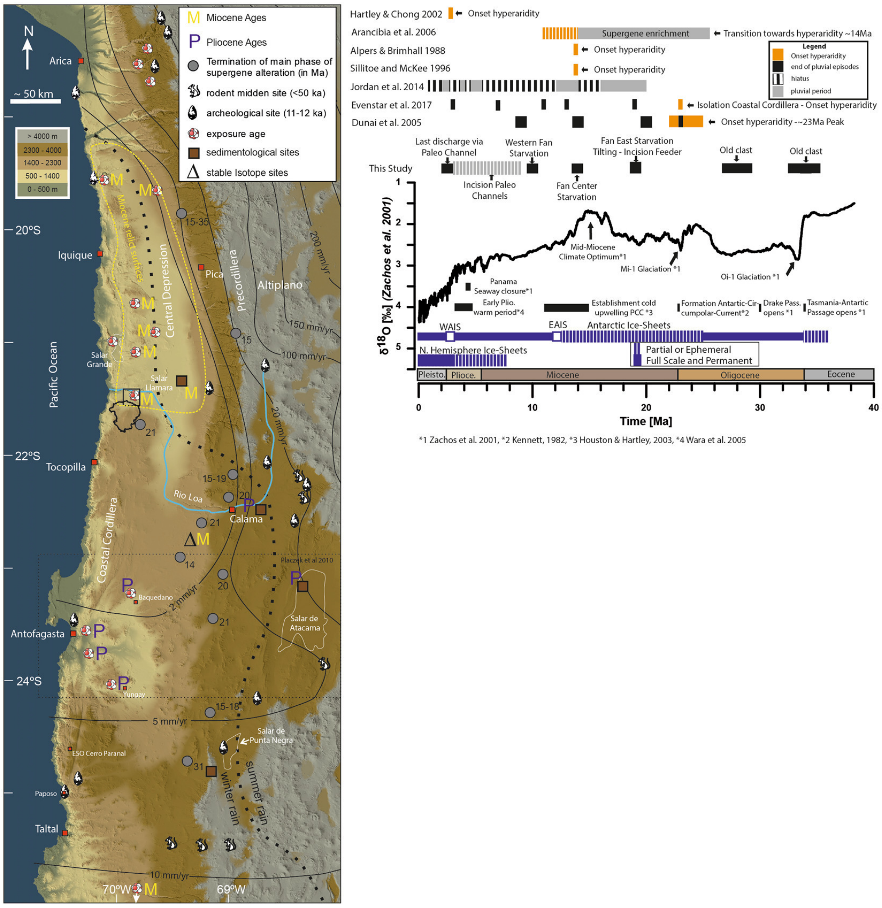

Figure 6. (**A**) Colour shaded digital elevation model (derived from SRTM-data, created using ArcGIS 10.5.1) with isohyets[1]. Dashed black line indicates the border between winter- and summer-rain dominated areas[1]. Sites from the literature are: terminations of phases of supergene enrichment of porphyry ore-deposits[14,93–95], rodent midden sites[22,62], earliest archaeological sites[60], stable isotope studies[96], sedimentological studies[12,21,97], exposure ages and erosion rates determined with cosmogenic nuclides[7–10,24,28,49,50,61,97,98]. The stippled yellow outline for Miocene relict surfaces is derived from studies yielding Miocene exposure ages (M) for sediment surfaces[9,10,24,28] and sedimentological studies[21]. Studies yielding Pliocene ages for the onset of aridity are marked with P. Study site is marked with a black rectangle and drainage catchment in black. (**B**) Global deep-sea oxygen isotope stack based on data from Zachos, *et al.*[20]. Vertical blue bars indicate a qualitative representation of ice volume in each hemisphere relative to the LGM, dashed parts indicate episodes of minimal ice cover (<50%), full bars represent close to maximum ice coverage (>50% of present) from Zachos, *et al.*[20]. Major global tectonic and climatic periods/events are marked. Terminations of periods of landscape modification, in the case of fan and drainage abandonment (this study), and onset of channel incision (this study, dashed grey line) are marked with black bars. The duration of these wetter periods are derived by combing our data with the regional chronostratigraphy[28] and paleo-environmental reconstructions[21,28]. Black bars indicate reference records from Atacama Desert, which reveal the end of wetter conditions at certain times and places. Reconstructed pluvial phases and hiatuses are marked in grey and black-white dashed lines, respectively[21]. Arancibia, *et al.*[94] reconstructed a rapid decrease in the frequency of supergene oxidation ages from 14 Ma onwards, with a final cessation at about 9 Ma (dashed orange bars). Alpers and Brimhall[93] and Sillitoe and McKee[14] dated the end of supergene enrichment at ~14 Ma. End of supergene oxidation is interpreted to reflect the transition from semi-arid towards hyperarid conditions[99]. Wet phases reconstructed for the Andean fore-slope, due east of our study area, are from Jordan, *et al.*[21]. Regional episodes of deposition and surface stabilization in the Atacama Desert are from Evenstar, *et al.*[28]. The proposed onset of hyperaridity based on sedimentary deposits within the Calama basin by Hartley and Chong[12] is marked in orange. TCN exposure ages from the northern Coastal Cordillera, indicating the end of wetter episodes (black) and onset of hyperaridity (orange) are from Dunai, *et al.*[9].

Accurate deposition ages require that the accumulation of cosmogenic nuclides during erosion and transport prior to deposition are negligible, or can be determined, and the effect of post-depositional erosion/exhumation can be identified. Significant pre-exposure leads to erroneously old deposition ages, whereas post-depositional erosion/exhumation lowers the age of deposition[48]. Multiple single clast ages from a depositional surface can be used to test these effects[51]. Tight groups of ages are expected if the clasts were previously unexposed material with short transport times relative to deposition time. Erosion of low-angle surfaces will result in the dispersal to younger ages, as the resulting lag-deposits contain material exhumed from various depths of shielding. In the absence of pre-exposure, the highest ages obtained on such a surface are the best estimate for the minimum deposition age.

Pre-exposure, however, can be significant, particularly in (hyper-) arid environments that are mosaics of ancient surfaces. In the core of the Atacama Desert, Early- to Mid-Miocene surfaces are widespread and even traces of older, Oligocene surface material have been reported[9,10,21,24,28].

In this setting there are three main scenarios during which pre-exposure occurs: (i) accumulation of cosmogenic nuclides during exhumation of material in the source region, (ii) during protracted sediment transport; and (iii), a supply of sediment from a formerly stable, older sedimentary surface. Scenario (iii) would require clasts to be deposited on the fan surfaces with a significant and similar pre-exposure signal, which is unlikely given the stochastic nature of erosion and transport processes that tend to add variable amounts of inheritance to the age-signal[52,53]. Clustered, non-random, pre-exposure signals would be possible only where clast source areas were old, stable surfaces. Proximity of such a hypothetical old source (similar to the recent (hyper)-arid core of the Atacama Desert) surface to the sedimentary deposit to be dated is required to prevent dilution (beyond recognition) of the clustered pre-exposure signal, by 'normal' randomly pre-exposed material.

We observe differing modes of pre-exposure in our data set: the common random pre-exposure and likely traces of clustered pre-exposure. Several ages of the eastern fan deposits (samples RL15-007, RL14-01) show signs of significant pre-exposure, with two individual ages ~7 and ~15 Myr older than the next oldest age in the main age group (~19 Ma, Fig. 4A). These pre-exposure signals signify that at the time of deposition of the eastern alluvial fan, remnants of an Early Miocene/Oligocene landscape existed in the source area south of the Adamito fault system. The minimum deposition age of the eastern fan system is the oldest age in the main group, ~19 Ma. The ages <19 Ma reflect post depositional modification of the fan surface. The youngest ^{21}Ne age of ~5 Ma and the saturated ^{10}Be samples (Supplementary data Table 2) indicate that significant surface modification on this fan ended prior to ~5 Ma.

Several samples from the central fan system also contain pre-exposure age signals. The central fan-system is stratigraphically younger than the eastern system - it cuts the eastern fan near the Río Loa (Fig. 2A) - but yields five ages older than the main group of the eastern fan (Fig. 4A,B). The upper (older) age limit of the main age group of the central fan is ~14 Ma. The five older ages show signs of clustering, three are overlapping ages around ~19–21.5 Ma, and two at ~25 and ~26 Ma. Since the feeder channel of the central fan system incised into the substrate of the older eastern fan, it is evident that this substrate must have been eroded and transported to the surface of central fan .The initial incision of the feeder channel, possibly laterally less well defined at its onset, is a possible source of the clasts carrying the Early- to Mid-Miocene ages. We cannot rule out that the pre-exposed clast came from the catchment south of the Adamito fault system; however, this is unlikely given the requirement for a proximal source to preserve clustered pre-exposure. Younger ages reflect post depositional modification of the fan surface. The youngest ^{21}Ne age,~3 Ma and the ^{10}Be age of ~1.8 Ma indicate that surface modification on this fan continued into the Quaternary.

The ages of the western fan do not cluster and potential pre-exposure cannot be resolved. However, since the maximum age is ~10.5 Ma, a sediment contribution from Early- to Mid-Miocene surfaces can be excluded in this case (Fig. 4C).

Chronology of erosion, deposition, tectonic displacement and incision. From the geochronological constraints and the observed field relationships we reconstruct a history of erosion, deposition, tectonic displacement, and incision. From the exposure ages obtained for alluvial fan surfaces, it is striking that one in six clasts analysed (7 of 43) have an Early Miocene or older age exposure age, with a conspicuous group (n = 5) of ages bracketing the Oligocene/Miocene boundary (Fig. 4). It is likely that the source area of the sediments contained areas that had been stable since the Oligocene/Miocene transition. The interfluve preserved between the branches of the paleo-valley (sampling site RL15-001, Fig. 3C) may be an analogue of these past source regions, since it preserves ages up to the earliest Miocene.

The oldest ages, ~28 and ~34 Ma, indicate that the denudation of the source regions prior to the deposition of the fans (i.e. prior to Early Miocene) was insufficient to remove all surface material of a pre-existing landscape. These old clasts had been at or close to the surface for 9 to 15 Myr, or longer if intermittent burial is assumed. Possible source areas could not have been much higher (the summit of the Cerro de Mica is 800 m higher, Fig. 1), thus surface exposure cannot be reduced by much by postulating periods of early exposure at higher altitudes. We conclude that the time-integrated denudation in the source region was low throughout the Oligocene.

Deposition of the easternmost fan north of the Adamito fault terminated in the Early Miocene (~19 Ma), based on the oldest ages of the main group from the eastern fan (Figs 4A and 5A). The absence of any visible feeder channel on the main alluvial fan surface may indicate that this fan system became inactive due to a slow backfilling, rather than by tectonic truncation. Remnants of a former feeder channel are just visible at the Adamito fault scarp, as a small incised channel (Fig. 2A, white line trending only across the Adamito fault). Subsequent deposition switched to the central fan, which terminated during the late Mid Miocene (~14 Ma), based on the oldest ^{21}Ne ages for the central fan (Figs 4B and 5B). The central fan has a well-developed feeder channel, indicating that the truncation of the drainage rather occurred due to tectonic uplift along the Adamito fault, which had

commenced by this time *and* had outpaced fluvial incision. Lastly, sediments of the western fan were deposited during the Late Miocene (~10.5–9.0 Ma), from the age range defined by the oldest clast on the fan and the onset of incision of the paleo-channels to the west (Figs 4C and 5C). A likely candidate for the feeder channel of the western fan is the eastern channel of the deeply incised paleo-channel system straddling the Atacama fault zone (Fig. 2A). This possibility, however, could not be substantiated in the field, due to extensive surface cover by dust Chuca[37]. Fan deposition to the north of the Adamito fault terminated with the incision of the large paleo-channels straddling west of the AFS, during the Late Miocene (≤~9.0 Ma), indicated by the youngest age on interfluve and oldest age of clasts the in channel (Figs 4D and 5C).

Lake sediments deposited on alluvial fan surfaces constrain a minimum age for the deposition of the alluvial fans to be earlier than 5.54/5.36 Ma[13]). Based on our field observations, sediments of the Quillagua and Soledad Formation lie on top of the distal portions of the alluvial fans. The first appearance of a closed basin within the Quillagua basin occurred around 8.8 Ma (Hilaricos Unit[13]). Thus, the course of a proto-Río Loa through the Coastal Cordillera was blocked at or prior to 8.8 Ma. Fluvial sediments of a 'Proto-Río Loa' system are visible on both sides of the AFS (Fig. 4 supplementary data set). Likely causes for the shift from an exohereic drainage system to a closed, endorheic, system in the Quillagua basis are the relative uplift of the Coastal Cordillera with respect to the Central Depression and/or a blocking due to the activity and interaction of the AFS and NW-SE occurring splay faults (Fig. 5C,D).

The youngest ages from clasts in the paleo-channel (~2–3 Ma) and the age of the volcanic ash in the channel (0.7–1 Ma) constrain the minimum age for the last fluvial transport in the channel (Fig. 5D). The fact that the main paleo-channel terminates as a hanging valley at the Río Loa canyon, incised into unconsolidated clastic sediments (Fig. 3C), indicates that the incision of the paleo-channel terminated prior to the incision of the Río Loa (Fig. 5E) in the Middle/Upper-Pleistocene (post MIS 10)[54,55].

Sedimentation in the basin, south of the Adamito Fault, commenced at the *latest* after the termination of fluvial incision and transport in the paleo-channels (see previous paragraph). Since incision of the paleo-channel could have also been driven by spilling of an (ephemeral) paleolake at the position of the present-day clay pan, lacustrine sedimentation south of the Adamito fault may have commenced at any time after ~9 Ma (Fig. 5D). Recent drilling of the clay pan in the course of the CRC 1211 (http://sfb1211.uni-koeln.de/) revealed that at least 50 m of sediment was deposited in the pan since tectonic truncation of the paleo-channel. Cumulative tectonic displacement since ≤9 Ma on the adjacent section of the Adamito fault is at least 150 m, translating into a long-term average rate of vertical tectonic displacement of at least 15 m/Myr.

Similar to soil studies by Wang, *et al.*[38], major surface modification on the alluvial fans ceased around ~5 Ma, coincident with a major drying of the Atacama Desert. The youngest ages obtained from the fan surfaces (^{21}Ne ~3 Ma, n = 3; ^{10}Be ~2 Ma n = 1) Fig. 4), indicate that significant fluvial surface modification in the study area terminated around 2–3 Ma. Thereafter, fluvial processes were unable to excavate pebbles from previously shielded positions.

The displacement of the drainage from east to west and the relative chronology is supported by the cross-cutting relationship of the central and eastern fans (Fig. 2A), and the decreasing altitude of the wind gaps (i.e. the highest elevation of the fossil drainage channels) from east to west (Fig. 2B,C). Differential uplift along the Adamito fault, tilted the surface to the west and drove the direction of channel diversion (Fig. 2C). The uplift along the Adamito fault, in conjunction with insufficient discharge to allow fluvial incision to keep pace with fault uplift caused progressive abandonment of the fans and subsequent abandonment of the paleo-channel. To address whether temporary, discontinuous uplift or temporal fluctuations in the water availability provided the timing for the diversions and abandonment, and to make statements on the paleoclimate of the study area, we compare our chronology to other records from the region.

A recent compilation of the regional chronostratigraphy of sediments in the Longitudinal Valley in northern Chile, due east of our study area (Fig. 1) identifies regional, abrupt terminations of sedimentary deposition at ~23 Ma, ~19 Ma, ~13 Ma, ~11 Ma, ~7 Ma, and ~3 Ma[28]. These correspond to the timing of aggradational and degradational surfaces in the Coastal Cordillera and the Andean foreslope[21,28]. Hiatuses in the sedimentary record of the Longitudinal Valley are predominantly climate-induced due to intensification of (hyper-) aridity[28]. We note a good agreement with our ages for inferred surface stabilization in the source area at ~23 Ma (the O/M boundary) and terminations of fan deposition at ~19 Ma and ~14 Ma, as well as the termination of fluvial surface modification at ~2–3 Ma. The Late Miocene incision of the paleo-channel (≤9 Ma), is equivalent to the deposition of sedimentary unit 5 of Evenstar, *et al.*[28]. We note that discontinuous tectonic movement is not required to explain the *timing* of hydrological re-arrangement in our study area. However, it remains a possibility. In the following we treat the chronological constraints derived for our study area as synchronous to the regional chronostratigraphy[28], and thus synchronous with changes in the regional climate.

Paleoclimate of the Coastal Cordillera near the dry core of the Atacama. The study area is unique in its position, located in the Coastal Cordillera near the core region of the Atacama (in terms of dryness), with a present-day annual rain precipitation well below 2 mm[1]. The climate-sensitive changes of erosion, deposition, and drainage re-arrangement provide a glimpse into the past climatic conditions. Most climatic reconstructions of the Atacama Desert rely on records that owe their existence to rainfall on the Andean foothills, the Precordillera, or even the Altiplano e.g.,[12,13,17,21,22,28,56–60] or are located in areas south of 23°S that sometimes receive appreciable, Winter-rainfall e.g.,[61–66]. Currently, the Andean foothills of the Atacama receives 10–100 times more precipitation than the region of this study in the Coastal Cordillera[1]. Thus, while the *timing* of changes in the regional climate are probably synchronous throughout most of the Atacama Desert (see above), the local expression of climatic conditions and surface processes were most likely different, subject to sometimes steep climatic gradients.

The oldest clasts found in our study (~28 and ~34 Ma) are age-equivalent to the Azapa formation of the Longitudinal Valley[28]. Similarly, high ages have been reported for fluvial clasts in the Coastal Cordillera at ~19.5°S (~27 and ~37 Ma[9]). Earlier we have argued that their long surface exposure during transit points to low erosion rates in their source region in the Coastal Cordillera during the Oligocene. During the same period, up to 500 meters of Azapa sediments were deposited in the Longitudinal Valley[67] in response to Andean uplift and aided by orographic rainfall[28]. Thus, while the Oligocene climate in the proto-Andes was sufficiently wet to allow a significant denudational response to steepening and hillslope gradients, denudation and sediment transport in the Coastal Cordillera appears to have been much more subdued, despite significant local relief of ≤800 m. It is difficult to accurately constrain the climatic conditions that leave pebbles in a fluvial system in transit at or near to the surface for at least 9–15 Myr, though it is likely arid rather than semi-arid, since the latter is prone to accelerated erosion[68]. Aridification at the Oligocene/Miocene boundary, presumably to hyper-arid conditions, brought erosion and deposition in both areas to a temporary standstill[9,28]. This hiatus in sedimentation led to the long-term preservation of the regionally occurring Tarapaca Paleosurface[28,69], which was formed by erosion of the Coastal Cordillera, the emerging Andes and sedimentation in the Coastal Cordillera to form an Oligocene low-relief surface[28]. Our results and a previous study[9] indicate that, at least in some areas of the Costal Cordillera significant deposition and erosion terminated as early as the Oligocene/Eocene boundary.

The volume of sediment preserved in the alluvial fans investigated is small (~0.3 km^3; estimated 60 km^2 surface area, ~5 m thickness) considering the size of their catchment (~560 km^2). A time-integrated (from 23 Ma to ~9.5 Myr) catchment-wide average of as little as ~55–60 cm erosion could explain the amount of sediment deposited. Although we cannot quantify the amount of material eroded from the catchment upstream that has not become part of the fan deposit, it appears that average erosion rates throughout the Early and Mid-Miocene could have been well below 1 m/Myr. Again it is difficult to define the climatic conditions; however, a persistent semi-arid climate as has been suggested previously[23] is probably out of the question. A possible scenario is that arid phases (fan deposition) interrupted a predominantly hyper-arid climate in this portion of the Coastal Cordillera in the Early- to Mid-Miocene.

Onset of (hyper-) aridity. Whether the onset of (hyper-) aridity in the Atacama Desert is relatively recent Pliocene e.g.,[12,13,18,61,70] or ancient Miocene or earlier e.g.,[9,10,14,21,28,57] is subject of ongoing debate (Fig. 6). The differences in interpretations are largely related to the regional distribution of the evidence and on the sensitivity of the proxies used[71] (Fig. 6). Figure 6 displays a compilation of studies that have estimated the onset of hyper-aridity in the Atacama Desert. The map (Fig. 6) reveals locations of studies in the Atacama Desert and illustrate how they relate to recent precipitation patterns[1]. The additional graph displays age constrains for the onset of hyper-aridity of selected studies, compared to global climate reconstruction based on deep-sea oxygen isotope stack on data from Zachos, *et al.*[20].

Recent studies, e.g.[21,28,72] (Fig. 6) demonstrate that the relative regional climatic gradients in the Miocene were not unlike those of today[1,73]. As is found presently, the aridity in the Miocene became more extreme towards the dry core of the Atacama (Coastal Cordillera & Central Depression between 19° and 22°S) from the North[28,72], and from the East[21] (Fig. 6). The Andes control the distribution of available moisture on their western flank through a combination of orographic precipitation and deflection of atmospheric circulation in the Summer-rainfall-dominated areas of the Andean foothills[1,4,21,72]. Moisture sources of the Summer-rainfall-dominated areas are located east of the Andes[1,4,21,72,73].

Winter-rainfall sourced in the Pacific Ocean dominates south of the dry core (Fig. 6)[1,73]. This area has experienced a dynamic geomorphological response to Quaternary climate change e.g.,[8,74]. The position of the Winter-rain-dominated region may have shifted up to 2 degrees northwards during stadials in the Quaternary[75]. In the Summer-rain-dominated areas, ephermal and perennial rivers with headwaters in the Pre-Cordillera or Altiplano, and areas above 2000 m, also respond readily to Quaternary climate change e.g.,[15,22,56,60].

The evidence for a recent (Pliocene) onset of aridity e.g.,[12,13,18,50,61,70] is sourced from the same regions that are demonstrably sensitive to Quaternary climate changes (Fig. 6). The Summer-rain dominated areas, below 2000 m, reveal the evidence for an early (Miocene or older) onset. North of 22°S, below 2000 m, surfaces of Miocene age (Fig. 6) are regionally widespread[9,21,24,28], while they constitute rare relicts south of 22°S[6,76].

The aridity in the Winter-rain-dominated areas of the Atacama is sensitive to long-term secular changes in the sea-surface temperature of the Pacific[71]; and also to the ENSO phenomenon increased rainfall during El Niño-like conditions[73], as evidenced by the El Niño-induced extreme rain event in 2015[77]. The strengthening of the Humboldt Current since the Late Miocene and particularly during the Pliocene/Pleistocene transition[71] (Fig. 6) is a likely cause for the late (Plio-/Pleistocene) aridification observed in the Winter-rain region[50,61,76]. Indicators for past aridity, such as material from preserved stable surfaces, are absent in the Winter-rain-dominated areas because of higher rates of erosion[8,50,61,76], though under favourable conditions relicts remain[6].

The aridity in the Summer-rain-dominated areas is due to large-scale tropospheric subsidence[3] and the rain shadow-effect of the Andes[1], both of which have existed over the long-term. Due to the distant moisture source[78], changes in the Summer-rain-dominated areas are less sensitive to changes in the offshore SE Pacific, but governed by global changes in temperature; which are commonly, but not necessarily, synchronous[20,79]. Long-term El Niño-like conditions postulated for the Pliocene[79] that had profound effects in the Winter-rain region[8,50,61,76], caused only subtle changes in the core of the Atacama e.g.[24], this study.

A hyper-arid Atacama Desert core with preserved Miocene surfaces is outlined in Fig. 6 by yellow stippled line. This region is within the present day 2 mm/yr isohyet[1,4], but would have been smaller due to the northward migration of the winter-rainfall area during glacials[75,80]. Surfaces are generally covered by gypsum soils (Chuca and Costra, sensu Ericksen[37]) and lack signs of recent run-off erosion. Fluvial channels are often dissected by fault activity[24,31] and in some cases we observed in the field that their bottoms are filled with gypsum dust and/or (un-reworked) volcanic ash.

The region studied here is near the southern fringe of the dry core of the Atacama (Fig. 6). The preservation of Miocene surfaces north of the Adamito fault demonstrate that significant fluvial landscape modification was absent. The headwaters of the paleo-catchments (source area) that supplied the gravels of the fossil alluvial fans north of the Adamito faults are outside the core. Indeed, modern analogues of the channels carrying the gravels show signs of sub-recent fluvial activity in the catchment of the closed basin; the channels are free of the otherwise ubiquitous dust while sediment bars and channels are mostly sharp-edged. The >50 m thick fluvial and lacustrine sediments (cored in October & November 2017) in the clay pan abutting the Adamito fault, are a testament to the continued sedimentation that occurred after the channel and fan abandonment we observe. Without the drainage modifications brought about by faulting, the sedimentary surfaces investigated here could well have been buried. The Early- to Mid-Miocene ages obtained from the fan surfaces indicate that a background of (hyper-) arid conditions (Fig. 6), supported the preservation of sediment surfaces that were shed during intermittent wetter periods[21,28]. The presence of clasts with Oligocene exposure ages (Fig. 6) on the early Miocene fans, indicate that at the time of fan deposition remnants of older (older by ≥9–15 Myr) surfaces existed; indicating that a (hyper-) arid climate might have prevailed already during the Oligocene in this part of the Atacama Desert. Considering the position of our study area on the southern fringe of the dry core, it is likely that the core areas further to the North also had a background (hyper-) aridity since the early Oligocene; similarly, old clasts are found near ~19.5°S[9], Fig. 6.

Oligocene (hyper-) aridity in the core of the Atacama Desert coincides with the global cooling in the Oligocene[20] (Fig. 6). Global warming at the end of the Oligocene that reversed at the Miocene/Oligocene boundary[20] appears to coincide with the main phase of deposition and the termination of the regionally important Azapa sediments, respectively[28]. Wetter periods throughout the Miocene and Pliocene largely coincide with globally warmer periods (Fig. 6).

Conclusions

The core region of the Atacama, here defined as areas in the Coastal Cordillera and the Central Depression between 19°S and 22°S below 2000 m, was predominantly (hyper-) arid throughout the Miocene, possibly even through much of the Oligocene. The (hyper-) aridity was repeatedly interrupted by slightly wetter phases that were synchronous with the climate-induced changes recorded on the Andean foothills[21,28]. Truncation of drainage systems by moderately active faults in conjunction with the prevailing (hyper-) aridity, was instrumental in preserving the sedimentary surfaces. The ancient (Mio-/Oligocene) onset of (hyper-) arid conditions inferred for the study area (and for the core region to the north of it), contradict the evidence that indicates a Pliocene age for the onset. Considering present day climatic gradients and their causes, and how they have evolved in the past, it is consistent that areas in the Winter-rain-dominated regions south of 22°S or above ~2000 m respond strongly to short-term climatic change whereas the core areas of the Atacama are mostly stagnant. Statements on the aridity of the Atacama and its variability are specific to the areas/catchments investigated and generalizing statements on paleoclimate encompassing the entire geographic entity called 'Atacama Desert' that are based on point observations are best avoided.

Methods

We used geological field observations and a high resolution Digital Elevation Model (DEM) of the study area, based on Pléiades 1B data (s. supplementary), and Aster GDEM data to delineate the drainage catchment (closed basin) and calculate slope maps. Optical satellite imagery (Pléiades 1B Multispectral Image) was additionally used to identify geomorphological landscape features, such as alluvial fan extensions and channels. One volcanic ash layer was dated utilizing U/Pb dating of zircons at the University of Frankfurt. The chronology of the alluvial fan development and the incision of the paleo-drainage is reconstructed using cosmogenic nuclide exposure dating. The sampling strategy and calculation of exposure ages are outlined in the following. Zircon U/Pb isotope analysis was conducted with LA-ICP-MS, for methodological details see Frei and Gerdes[81]. Further details and details pertaining to the DEM-generation and U/Pb dating are provided in the supplementary data set.

Cosmogenic exposure ages were determined for quartz clasts sampled from inactive alluvial fan surfaces during field expeditions in 2013, 2014, and 2015. Quartz clasts were sampled from flat fan surfaces (RL14-01-04, RL15-006, and RL15-007) and from a feeder channel (RL15-005) (Fig. 2A). Furthermore, quartz clasts from a surface isolated by the incision of the paleo-channel were sampled (RL15-001), as well as pebbles in the western paleo channel (RL13-001). The sampling sites on the central and eastern alluvial fans (RL14-01-04, RL15-007) and the isolated surface (RL15-001) are essentially flat, at each location quartz clasts were collected from an area of about 0.5 ha. On the western fan, which had minor relief due to shallow channel incision (see above), the samples were taken exclusively on dispersed interfluves (RL15-006). Pebbles from the feeder channel (RL15-005) and the paleo-channel (RL13-001) were sampled on local highs (former sand bars) in the centre of the channel, remote from material shed from the channel's hill-slopes.

The majority of the sampled quartz clasts have a reddish-brown desert varnish. They often retain rounded shapes from fluvial transport, occasionally modified by fragments spallation. In instances of 'kernsprung', indicated by a localized cluster (usually <2 m diameter) of quartz fragments, only one fragment per cluster was sampled and no other samples collected within a 5 m radius. Dimensions of sampled clasts range between 2–5 cm. The abundance of quartz, of the required clast size (>2 cm), on the surfaces is very low, commonly less than one clast per 25 m^2. Accordingly attempts at retrieving quartz from the subsurface were not successful. Furthermore, cemented *costra*[37] in the shallow subsurface, rendered depth profile sampling[48,82] impossible. Instead, to identify and correct for possible pre-exposure and exhumation, we utilize the multiple-clast approach[83,84], using 5–7 samples per sampling site.

The individual quartz clasts were crushed, sieved to retain the 250–710 µm grain size; then etched several times in a dilute HF-HNO_3 mixture[85]. Splits of the etched material were used for ^{10}Be and ^{21}Ne analysis. ^{10}Be sample

preparation and measurement followed single stacked column approach detailed in[86]. $^{10}Be/^{9}Be$ ratios were measured on CologneAMS[87], normalized to the ICN standard dilution series values reported by Nishiizumi, *et al.*[47]. ^{21}Ne analyses were performed at SUERC following the procedures outlined in[88].

Exposure ages were calculated using the LSD scaling scheme of Lifton, *et al.*[89] as implemented in version 3 of 'the online calculators formerly known as the CRONUS-Earth online calculators' https://hess.ess.washington.edu/math/v3/v3_age_in.html described in[90]; see also supplement. At the latitude and altitude of the study area, exposure ages calculated with the LSD scaling are 22% lower than those calculated with Stone (based on 'Lal magnetic') scaling[89]. We assume a time integrated linear uplift 40 m/Ma[9,91]; since 20 Ma, and report uplift-corrected ages accordingly (see supplement).

Data Availability Statement

All data generated or analysed during this study are included in this published article (and its Supplementary Information files).

References

1. Houston, J. Variability of precipitation in the Atacama Desert: its causes and hydrological impact. *International Journal of Climatology* **26**, 2181–2198, https://doi.org/10.1002/joc.1359 (2006).
2. Muñoz, J. Levantamiento Hidrogeológico para el desarrollo de nuevas fuentes de agua en áreas prioritarias de la zona norte de Chile, regiones XV, I, II Y III. Etapa II. (2009).
3. Takahashi, K. & Battisti, D. S. Processes controlling the mean tropical Pacific precipitation pattern. Part II: The SPCZ and the southeast Pacific dry zone. *Journal of Climate* **20**, 5696–5706 (2007).
4. Houston, J. & Hartley, A. J. The Central Andean west-slope rainshadow and its potential contribution to the origin of hyper-aridity in the Atacama desert. *International Journal of Climatology* **23**, 1453–1464 (2003).
5. Houston, J. Evaporation in the Atacama Desert: An empirical study of spatio-temporal variations and their causes. *Journal of Hydrology* **330**, 402–412, https://doi.org/10.1016/j.jhydrol.2006.03.036 (2006).
6. Nishiizumi, K., Caffee, M. W., Finkel, R. C., Brimhall, G. & Mote, T. Remnants of a fossil alluvial fan landscape of Miocene age in the Atacama Desert of northern Chile using cosmogenic nuclide exposure age dating. *Earth and Planetary Science Letters* **237**, 499–507, https://doi.org/10.1016/j.epsl.2005.05.032 (2005).
7. Kober, F. *et al.* Denudation rates and a topography-driven rainfall threshold in northern Chile: Multiple cosmogenic nuclide data and sediment yield budgets. *Geomorphology* **83**, 97–120 (2007).
8. Placzek, C. J., Matmon, A., Granger, D. E., Quade, J. & Niedermann, S. Evidence for active landscape evolution in the hyperarid Atacama from multiple terrestrial cosmogenic nuclides. *Earth and Planetary Science Letters* **295**, 12–20, https://doi.org/10.1016/j.epsl.2010.03.006 (2010).
9. Dunai, T. J., González López, G. A. & Juez-Larré, J. Oligocene–Miocene age of aridity in the Atacama Desert revealed by exposure dating of erosion-sensitive landforms. *Geology* **33**, 321, https://doi.org/10.1130/g21184.1 (2005).
10. Evenstar, L. A. *et al.* Multiphase development of the Atacama Planation Surface recorded by cosmogenic 3He exposure ages: Implications for uplift and Cenozoic climate change in western South America. *Geology* **37**, 27–30, https://doi.org/10.1130/g25437a.1 (2009).
11. Rech, J. A., Currie, B. S., Michalski, G. & Cowan, A. M. Neogeneclimate change and uplift in the Atacama Desert, Chile. *Geology* **34**, 761–764, https://doi.org/10.1130/g22444.1 (2006).
12. Hartley, A. J. & Chong, G. Late Pliocene age for the Atacama Desert: Implications for the desertification of western South America. *Geology* **30**, 43–46 (2002).
13. Sáez, A. *et al.* The stratigraphic record of changing hyperaridity in the Atacama desert over the last 10 Ma. *Earth and Planetary Science Letters* **355-356**, 32–38, https://doi.org/10.1016/j.epsl.2012.08.029 (2012).
14. Sillitoe, R. H. & McKee, E. H. Age of supergene oxidation and enrichment in the Chilean porphyry copper province. *Economic Geology* **91**, 164–179 (1996).
15. Latorre, C., Betancourt, J. L. & Arroyo, M. T. K. Late Quaternary vegetation and climate history of a perennial river canyon in the Río Salado basin (22°S) of Northern Chile. *Quaternary Research* **65**, 450–466, https://doi.org/10.1016/j.yqres.2006.02.002 (2006).
16. Rech, J. A., Quade, J. & Hart, W. S. Isotopic evidence for the source of Ca and S in soil gypsum, anhydrite and calcite in the Atacama Desert, Chile. *Geochim. Cosmochim. Acta* **67**, 575–586 (2003).
17. Nester, P. L., Gayo, E., Latorre, C., Jordan, T. E. & Blanco, N. Perennial stream discharge in the hyperarid Atacama Desert of northern Chile during the latest Pleistocene. *Proceedings of the National Academy of Sciences of the United States of America* **104**, 19724–19729, https://doi.org/10.1073/pnas.0705373104 (2007).
18. Hartley, A. J. & Rice, C. M. Controls on supergene enrichment of porphyry copper deposits in the Central Andes: A review and discussion. *Mineralium Deposita* **40**, 515–525, https://doi.org/10.1007/s00126-005-0017-7 (2005).
19. Cristini, L., Grosfeld, K., Butzin, M. & Lohmann, G. Influence of the opening of the Drake Passage on the Cenozoic Antarctic Ice Sheet: a modeling approach. *Palaeogeography, Palaeoclimatology, Palaeoecology* **339**, 66–73 (2012).
20. Zachos, J., Pagani, M., Sloan, L., Thomas, E. & Billups, K. Trends, rhythms and aberrations in Global Climate 65 Ma to present. *Science* **292**, 686–693 (2001).
21. Jordan, T. E. *et al* Landscape modification in response to repeated onset of hyperarid paleoclimate states since 14 Ma, Atacama Desert, Chile. *Geological Society of America Bulletin*, https://doi.org/10.1130/b30978.1 (2014).
22. Betancourt, J. L., Latorre, C., Rech, J. A., Quade, J. & Rylander, K. A. A 22,000-year record of Monsoonal precipitation from Northern Chile's Atacama Desert. *Science* **289**, 1542–1546 (2000).
23. Allmendinger, R. W., Gonzalez, G., Yu, J., Hoke, G. & Isacks, B. Trench-parallel shortening in the Northern Chilean Forearc: Tectonic and climatic implications. *Geological Society of America Bulletin* **117**, 89–104, https://doi.org/10.1130/B25505.1 (2005).
24. Carrizo, D., Gonzalez, G. & Dunai, T. Neogene constriction in the northern Chilean Coastal Cordillera: Neotectonics and surface dating using cosmogenic ^{21}Ne. *Revista Geologica De Chile* **35**, 1–38 (2008).
25. Reijs, J. & McClay, K. Salar Grande pull-apart basin, Atacama fault system, northern Chile. *Geological Society, London, Special Publications* **135**, 127–141 (1998).
26. Coira, B., Davidson, J., Mpodozis, C. & Ramos, V. Tectonic and magmatic evolution of the Andes of northern Argentina and Chile. *Earth-Science Reviews* **18**, 303–332 (1982).
27. Mortimer, C. The Cenozoic history of the southern Atacama Desert, Chile. *Journal Geol. Soc. Lond.* **129**, 505–526 (1973).
28. Evenstar, L. *et al.* Geomorphology on geologic timescales: Evolution of the late Cenozoic Pacific paleosurface in Northern Chile and Southern Peru. *Earth-Science Reviews* **171**, 1–27 (2017).
29. McCaffrey, R. Estimates of modern arc-parallel strain rates in fore arcs. *Geology* **24**, 27–30 (1996).
30. Skarmeta, J. & Marinovic, N. *Hoja Quillagua: región de Antofagasta: carta geológica de Chile escala 1: 250.000*. (Instituto de Investigaciones Geológicas, 1981).
31. Allmendinger, R. W. & González, G. Invited review paper: Neogene to Quaternary tectonics of the coastal Cordillera, northern Chile. *Tectonophysics* **495**, 93–110, https://doi.org/10.1016/j.tecto.2009.04.019 (2010).

32. Denny, C. S. *Alluvial fans in the Death Valley region, California and Nevada*. (US Government Printing Office, 1965).
33. Chong, G., Mendoza, M., García-Veigas, J., Pueyo, J. J. & Turner, P. Evolution and geochemical signatures in a Neogene forearc evaporitic basin: the Salar Grande (Central Andes of Chile). *Palaeogeography, Palaeoclimatology, Palaeoecology* **151**, 39–54 (1999).
34. Sáez, A., Cabrera, L., Jensen, A. & Chong, G. Late Neogene lacustrine record and palaeogeography in the Quillagua–Llamara basin, Central Andean fore-arc (northern Chile). *Palaeogeography, Palaeoclimatology, Palaeoecology* **151**, 5–37 (1999).
35. Rodwell, M. J. & Hoskins, B. J. Subtropical anticyclones and summer monsoons. *Journal of Climate* **14**, 3192–3211 (2001).
36. Egger, J. *et al*. Diurnal circulation of the Bolivian Altiplano. Part I: observations. *Monthly weather review* **133**, 911–924 (2005).
37. Ericksen, G. E. *Geology and origin of the Chilean nitrate deposits*. Report No. 1188, 37 (USGS, Washington, 1981).
38. Wang, F. *et al*. Beryllium-10 concentrations in the hyper-arid soils in the Atacama Desert, Chile: Implications for arid soil formation rates and El Niño driven changes in Pliocene precipitation. *Geochimica et Cosmochimica Acta* **160**, 227–242, https://doi.org/10.1016/j.gca.2015.03.008 (2015).
39. Michalski, G., Bohlke, J. K. & Thiemens, M. Long term atmospheric deposition as the source of nitrate and other salts in the Atacama Desert, Chile: New evidence from mass-independent oxygen isotopic compositions. *Geochimica et Cosmochimica Acta* **68**, 4023–4038, https://doi.org/10.1016/j.gca.2004.04.009 (2004).
40. Wells, S. G., McFadden, L. D., Poths, J. & Olinger, C. T. Cosmogenic 3He surface-exposure dating of stone pavements: Implications for landscape evolution in deserts. *Geology* **23**, 613–616 (1995).
41. Parsons, A. J. & Abrahams, A. D. In *Geomorphology of Desert Environments*. (Springer, 2009).
42. Cereceda, P., Larrain, H., Osses, P., Farías, M. & Egaña, I. The spatial and temporal variability of fog and its relation to fog oases in the Atacama Desert, Chile. *Atmospheric Research* **87**, 312–323, https://doi.org/10.1016/j.atmosres.2007.11.012 (2008).
43. Amidon, W. H. *et al*. U-Pb ages of detrital and volcanic zircons of the Toro Negro Formation, northwestern Argentina: Age, provenance and sedimentation rates. *Journal of South American Earth Sciences* **70**, 237–250 (2016).
44. Barquero-Molina, M. *40Ar/39Ar chronology and paleomagnetism of ignimbrites and lavas from the central volcanic zone, northern Chile, and 40Ar/39Ar chronology of silicic ignimbrites from Honduras and Nicaragua*. (University of Wisconsin–Madison, 2003).
45. Salisbury, M. J. *et al*. 40Ar/39Ar chronostratigraphy of Altiplano-Puna volcanic complex ignimbrites reveals the development of a major magmatic province. *Geological Society of America Bulletin* **B30280**, 30281 (2010).
46. Kern, J. M. *et al*. Geochronological imaging of an episodically constructed subvolcanic batholith: U-Pb in zircon chronochemistry of the Altiplano-Puna Volcanic Complex of the Central Andes. *Geosphere* **12**, 1054–1077 (2016).
47. Nishiizumi, K. *et al*. Absolute calibration of Be-10 AMS standards. *Nucl. Instr. Meth. Phys. Res. B* **258**, 403–413 (2007).
48. Dunai, T. J. *Cosmogenic Nuclides: Principles, concepts and applications in the Earth surface sciences*. (Cambridge University Press, 2010).
49. González, G., Dunai, T. J., Carrizo, D. & Allmendinger, R. Young displacements on the Atacama Fault System, northern Chile from field observations and cosmogenic Ne-21 concentrations. *Tectonics* **25**, https://doi.org/10.1029/2005TC001846 (2006).
50. Jungers, M. C. *et al*. Active erosion–deposition cycles in the hyperarid Atacama Desert of Northern Chile. *Earth and Planetary Science Letters* **371–372**, 125–133, https://doi.org/10.1016/j.epsl.2013.04.005 (2013).
51. Binnie, A., Binnie, S. A., Parteli, E. J. R. & Dunai, T. J. The implications of sampling approach and geomorphological processes for cosmogenic ^{10}Be exposure dating of marine terraces. *Nuclear Instruments and Methods- B: Beam Interactions with Materials and Atoms* (submitted).
52. Anderson, R. S., Repka, J. L. & Dick, G. S. Explicit treatment of inheritance in dating depositional surfaces using *in situ* ^{10}Be and 26Al. *Geology* **24**, 47–51 (1996).
53. Repka, J. L., Anderson, R. S. & Finkel, R. C. Cosmogenic dating of fluvial terraces, Fremont River, Utah. *Earth and Planetary Science Letters* **152**, 59–73, https://doi.org/10.1016/S0012-821X(97)00149-0 (1997).
54. Lisiecki, L. E. & Raymo, M. E. A Pliocene-Pleistocene stack of 57 globally distributed benthic δ18O records. *Paleoceanography* **20** (2005).
55. Ritter, B., Binnie, S. A., Stuart, F. M., Wennrich, V. & Dunai, T. J. Evidence for multiple Plio-Pleistocene lake episodes in the hyperarid Atacama Desert. *Quaternary Geochronology* **44**, 1–12, https://doi.org/10.1016/j.quageo.2017.11.002 (2018).
56. Gayo, E. M. *et al*. Late Quaternary hydrological and ecological changes in the hyperarid core of the northern Atacama Desert (~21°S). *Earth-Science Reviews* **113**, 120–140, https://doi.org/10.1016/j.earscirev.2012.04.003 (2012).
57. Rech, J. A. *et al*. Evidence for the development of the Andean rain shadow from a Neogene isotopic record in the Atacama Desert, Chile. *Earth and Planetary Science Letters* **292**, 371–382, https://doi.org/10.1016/j.epsl.2010.02.004 (2010).
58. Kirk-Lawlor, N., Jordan, T. L., Rech, J. A. & Lehman, S. B. Late Miocene to Early Pliocene paleohydrology and landscape evolution of Northern Chile, 19° to 20°S. *Palaeogeography Palaeoclimatology Palaeoecology* **387**, 76–90 (2013).
59. Evenstar, L. *et al*. Miocene-Pliocene climate change in the Peru-Chile desert. *6th International symposium on Andean Geodynamics* (ISAG 2005, Barcelona) (2005).
60. Latorre, C. *et al*. Late Pleistocene human occupation of the hyperarid core in the Atacama Desert, northern Chile. *Quaternary Science Reviews* **77**, 19–30, https://doi.org/10.1016/j.quascirev.2013.06.008 (2013).
61. Amundson, R. *et al*. Geomorphologic evidence for the late Pliocene onset of hyperaridity in the Atacama Desert. *Geological Society of America Bulletin* **124**, 1048–1070, https://doi.org/10.1130/b30445.1 (2012).
62. Maldonado, A., Betancourt, J. L., Latorre, C. & Villagran, C. Pollen analyses from a 50 000-yr rodent midden series in the southern Atacama Desert (25° 30′S). *Journal of Quaternary Science* **20**, 493–507, https://doi.org/10.1002/jqs.936 (2005).
63. Quade, J. *et al*. Paleowetlands and regionalclimate change in the central Atacama Desert, northern Chile. *Quaternary Research* **69**, 343–360, https://doi.org/10.1016/j.yqres.2008.01.003 (2008).
64. Díaz, F. P., Latorre, C., Maldonado, A., Quade, J. & Betancourt, J. L. Rodent middens reveal episodic, long-distance plant colonizations across the hyperarid Atacama Desert over the last 34,000 years. *Journal of Biogeography* **39**, 510–525, https://doi.org/10.1111/j.1365-2699.2011.02617.x (2012).
65. Bozkurt, D., Rondanelli, R., Garreaud, R. & Arriagada, A. Impact of Warmer Eastern Tropical Pacific SST on the March 2015 Atacama Floods. *Monthly Weather Review* **144**, 4441–4460 (2016).
66. Wilcox, A. C. *et al*. An integrated analysis of the March 2015 Atacama floods. *Geophysical Research Letters* **43**, 8035–8043 (2016).
67. Hartley, A. J. & Evenstar, L. Cenozoic stratigraphic development in the north Chilean forearc: Implications for basin development and uplift history of the Central Andean margin. *Tectonophysics* **495**, 67–77, https://doi.org/10.1016/j.tecto.2009.05.013 (2010).
68. Knighton, A. & Nanson, G. Distinctiveness, diversity and uniqueness in arid zone river systems. *Arid Zone Geomorphology: Process, Form and Change in Drylands*, Thomas, D. S. G. (ed.). 2nd Edition (John Wiley & Sons, 185–203, 1997).
69. Mortimer, C. & Saric, N. Landform evolution in the coastal region of Tarapacá Province, Chile. *Revue de géomorphologie dynamique* **21**, 162–170 (1972).
70. Oerter, E. *et al*. Early to middle Miocene climate in the Atacama Desert of northern Chile. *Palaeogeography, Palaeoclimatology, Palaeoecology* **441**, 890–900 (2016).
71. Garreaud, R. D., Molina, A. & Farias, M. Andean uplift, ocean cooling and Atacama hyperaridity: A climate modeling perspective. *Earth and Planetary Science Letters* **292**, 39–50, https://doi.org/10.1016/j.epsl.2010.01.017 (2010).
72. Schlunegger, F., Norton, K. P., Delunel, R., Ehlers, T. A. & Madella, A. Late Miocene increase in precipitation in the Western Cordillera of the Andes between 18–19°S latitudes inferred from shifts in sedimentation patterns. *Earth and Planetary Science Letters* (2017).

73. Garreaud, R. D., Vuille, M., Compagnucci, R. & Marengo, J. Present-day South American climate. *Palaeogeography Palaeoclimatology Palaeoecology* **281**, 180–195, https://doi.org/10.1016/j.palaeo.2007.10.032 (2009).
74. De Porras, M., Maldonado, A., Pol-Holz, D., Latorre, C. & Betancourt, J. Late Quaternary environmental dynamics in the Atacama Desert reconstructed from rodent midden pollen records. *Journal of Quaternary Science* **32**, 665–684 (2017).
75. Lamy, F., Klump, J., Hebbeln, D. & Wefer, G. Late Quaternary rapidclimate change in northern Chile. *Terra Nova* **12**, 8–13 (2000).
76. Placzek, C., Granger, D. E., Matmon, A., Quade, J. & Ryb, U. Geomorphic process rates in the central Atacama Desert, Chile: Insights from cosmogenic nuclides and implications for the onset of hyperaridity. *American Journal of Science* **314**, 1462–1512 (2014).
77. Scott, C., Lohman, R. & Jordan, T. InSAR constraints on soil moisture evolution after the March 2015 extreme precipitation event in Chile. *Scientific Reports* **7**, 4903 (2017).
78. Ehlers, T. A. & Poulsen, C. J. Influence of Andean uplift on climate and paleoaltimetry estimates. *Earth and Planetary Science Letters* **281**, 238–248 (2009).
79. Fedorov, A. *et al*. The Pliocene paradox (mechanisms for a permanent El Niño). *Science* **312**, 1485–1489 (2006).
80. Stuut, J. B. W. & Lamy, F. Climate variability at the southern boundaries of the Namib (Southwestern Africa) and Atacama (northern Chile) coastal deserts during the last 120,000 yr. *Quaternary Research* **62**, 301–309, https://doi.org/10.1016/j.yqres.2004.08.001 (2004).
81. Frei, D. & Gerdes, A. Precise and accurate *in situ* U–Pb dating of zircon with high sample throughput by automated LA-SF-ICP-MS. *Chemical Geology* **261**, 261–270 (2009).
82. Hein, A. S. *et al*. Middle Pleistocene glaciation in Patagonia dated by cosmogenic-nuclide measurements on outwash gravels. *Earth and Planetary Science Letters* **286**, 184–197 (2009).
83. Binnie, A. *et al*. Accelerated late quaternary uplift revealed by 10 Be exposure dating of marine terraces, Mejillones Peninsula, northern Chile. *Quaternary Geochronology* **36**, 12–27 (2016).
84. Farbod, Y. *et al*. Spatial variations in late Quaternary slip rates along the Doruneh Fault System (Central Iran). *Tectonics* **35**, 386–406 (2016).
85. Kohl, C. P. & Nishiizumi, K. Chemical isolation of quartz for measurement of *in-situ* produced cosmogenic nuclides. *Geochim. Cosmochim. Acta* **56**, 3583–3587 (1992).
86. Binnie, S. A. *et al*. Separation of Be and Al for AMS using single-step column chromatography. *Nuclear Instruments and Methods in Physics Research Section B: Beam Interactions with Materials and Atoms* (2015).
87. Dewald, A. *et al*. CologneAMS, a dedicated center for accelerator mass spectrometry in Germany. *Nuclear Instruments & Methods in Physics Research Section B-Beam Interactions with Materials and Atoms* **294**, 18–23, https://doi.org/10.1016/j.nimb.2012.04.030 (2013).
88. Codilean, A. T. *et al*. Single-grain cosmogenic ^{21}Ne concentrations in fluvial sediments reveal spatially variable erosion rates. *Geology* **36**, 159–162 (2008).
89. Lifton, N., Sato, T. & Dunai, T. J. Scaling *in situ* cosmogenic nuclide production rates using analytical approximations to atmospheric cosmic-ray fluxes. *Earth and Planetary Science Letters* **386**, 149–160, https://doi.org/10.1016/j.epsl.2013.10.052 (2014).
90. Balco, G., Stone, J. O., Lifton, N. A. & Dunai, T. J. A complete and easily accessible means of calculating surface exposure ages or erosion rates from (10)Be and (26)Al measurements. *Quaternary Geochronology* **3**, 174–195, https://doi.org/10.1016/j.quageo.2007.12.001 (2008).
91. Evenstar, L. A., Stuart, F. M., Hartley, A. J. & Tattitch, B. Slow Cenozoic uplift of the western Andean Cordillera indicated by cosmogenic ^{3}He in alluvial boulders from the Pacific Planation Surface. *Geophysical Research Letters* **42**, 8448–8455 (2015).
92. Quezada, A., Vasquez, P., Sepúlveda, F., Blanco, N. & Tomlinson, A. J. Mapa Compilación Geológica Área Quillagua - Salar Grande 1:100.000. *Servicio Nacional de Geologica y Mineria Gobierno Regional de Tarapacá* (2012).
93. Alpers, C. N. & Brimhall, G. H. Middle Miocene climatic change in the Atacama Desert, northern Chile: Evidence from supergene mineralization at La Escondia. *Geol. Soc. Am. Bull.* **100**, 1640–1656 (1988).
94. Arancibia, G. & Matthews, S. & de Arce, C. P. K–Ar and 40Ar/39Ar Geochronology of supergene processes in the Atacama Desert, northern Chile: Tectonic and climatic relations. *Journal of the Geological Society* **163**, 107–118 (2006).
95. Bouzari, F. & Clark, A. H. Anatomy, evolution, and metallogenic significance of the supergene orebody of teh Cerro Colorado porpyry copper deposit, I region, northern Chile. *Economic Geology* **97**, 1701–1740 (2002).
96. Sun, T., Bao, H., Reich, M. & Hemming, S. R. More than Ten Million Years of Hyper-aridity recorded in the Atacama Gravels. *Geochimica et Cosmochimica Acta* (2018).
97. Sáez, A., Godfrey, L. V., Herrera, C., Chong, G. & Pueyo, J. J. Timing of wet episodes in Atacama Desert over the last 15 ka. The Groundwater Discharge Deposits (GWD) from Domeyko Range at 25°S. *Quaternary Science Reviews* **145**, 82–93 (2016).
98. Owen, J. *et al*. In *AGU Fall Meeting*. Abstract T31C-0857 (AGU) (2003).
99. Clark, A. H., Tosdal, R. M., Ferrar, E. & Plazolles, A. Geomorphologic envrionment and age of supergene enrichment of the Cuajone, Quellaveco, and Toquepala porphyry copper deposits, southeastern Peru. *Economic Geology* **85**, 1604–1628 (1990).

Acknowledgements

Thanks go to Luigia Di Nicola at SUERC for assisting during noble gas analysis, and to Elena Voronina, Damián López, and Tomasz Góral for help processing samples for ^{10}Be analysis at the University of Cologne. For supporting DEM extraction, we want to thank Andreas Bolten. Finally, we would like to thank Eduardo Campos and colleagues at the Universidad Catolica del Norte at Antofagasta for their patient and essential support. This project is affiliated to the Collaborative Research Center (CRC) 1211, funded by German Science Foundation (DFG).

Author Contributions

B.R. fieldwork, sample preparation, sample measurement & data evaluation, manuscript writing; F.S. sample measurement & data evaluation ^{21}Ne; S.A.B. sample measurement & data evaluation ^{10}Be; A.G. sample measurement U/Pb; V.W. sample preparation tephra, sample measurement & data evaluation tephra; T.J.D. data evaluation, manuscript writing. All authors reviewed the manuscript.

Additional Information

Supplementary information accompanies this paper at https://doi.org/10.1038/s41598-018-32339-9.

Competing Interests: The authors declare no competing interests.

Publisher's note: Springer Nature remains neutral with regard to jurisdictional claims in published maps and institutional affiliations.

Supplementary data

"Neogene fluvial landscape evolution in the hyperarid core of the Atacama Desert"

Benedikt Ritter[a*], Finlay M. Stuart[b], Steven A. Binnie[a], Axel Gerdes[c], Volker Wennrich[a], Tibor J. Dunai[a]

[a] Institute of Geology & Mineralogy, University of Cologne, Germany

[b] Isotope Geosciences Unit, Scottish Universities Environmental Research Centre, East Kilbride, UK

[c] Institute of Geosciences, Goethe-University Frankfurt, Germany

Methods

Digital Elevation Model (DEM) Extraction

The Digital Elevation Model (DEM) was generated using a high resolution stereo satellite image set obtained from Pléiades 1B system. Image recording was on 05.05.2015 with a ground resolution of 0.5 m in the panchromatic band. ExelisVIS ENVI 5.1 was used to derive a surface model with the DEM Extraction module. Tie point determination between the two stereo images was conducted manually. Post-processing tools, including filter methods to reduce spikes (ENVI DEM Editing tools), were applied. The final model has a resolution of 1 m. A pansharped image was produced using ExelisVIS ENVI 5.1. Optical satellite imagery (Pléiades 1B Multispectral Image) was used to identify landscape features, such as alluvial fan extensions and channels. Further GIS analysis was obtained by using ArcGIS® 10.5.1 (ESRI http://www.esri.com), such as watershed delineation or hill shading (Spatial Analyst – Hydrology). Swath profiles were calculated using the high resolution Pléiades 1B DEM and focal statistics (Spatial Analyst ArcGIS® 10.5.1). Slope map (Fig. 6C in supplementary) was calculated using ArcGIS 10.5.1 using Spatial Analyst – Slope tool on an aggregated DEM (5x5 m).

Tephra U/Pb dating

Tephra sample T4 was processed using standard mineral separation techniques at the University of Cologne. Isotope mass spectrometry was conducted at the Institute for Geosciences at Frankfurt University. Hand-picked zircon grains were mounted in a 25 mm diameter circular epoxy mount and polished to expose their grain interiors. The internal structure of zircons was investigated using cathodoluminescence imaging. Zircon U/Pb isotope analysis was conducted with laser ablation inductively coupled plasma mass spectrometry (LA-ICP-MS), for methodological details see Frei and Gerdes [1]. The laser-

ICPMS U–Pb data of the detrital zircons (n= 62) are reported with 2σ uncertainties in Table 3.

Cosmogenic nuclide exposure dating

Samples were ground and sieved to 250-1000 µm and subsequently purified by sequential HF-leaching [2]. Purified quartz separates were investigated under a microscope. Those with a high abundance of visible fluid inclusions and/or fragments resembling chalcedony were further etched or excluded for ^{21}Ne. Inductively coupled plasma optical emission spectrometry (ICP-OES) was used to verify the purity of the quartz before dissolution.

^{10}Be target for accelerator mass spectrometry (AMS) were prepared using the stacked column approach outlined in Binnie et al. [3]. A reagent blank was prepared in tandem with the sample batch ^{10}Be/^{9}Be AMS measurements were made on CologneAMS [4] normalized to the ICN standard dilutions prepared by Nishiizumi [5]. Concentrations of ^{10}Be are reported following blank subtraction, which was less than 1% of the total number of nuclides measured in each case. The 1 standard deviation analytical precision of the nuclide concentrations was estimated by summing in quadrature the relative uncertainties on the AMS measurements of both the samples and the blank, along with a 1% (1 s.d.) estimate for the precision of the mass of ^{9}Be added during spiking.

For cosmogenic ^{21}Ne, cleaned and purified samples were sieved to <125 µm and packed into aluminium foil cups. The samples were measured with a noble-gas mass spectrometer at Scottish Universities Environmental Research Centre (SUERC) applying the standard procedure [6-8].

For age calculation, we used a ^{10}Be half-life of 1.36 ± 0.07 Ma [5] and a 'nuclide dependent scaling' after Lifton, et al. [9], calculated with "The online exposure age calculator formerly known as the CRONUS-Earth online exposure age calculator." Version 3, http://hess.ess.washington.edu/math/v3/v3_age_in.html; [10]. This employed a high-latitude, sea-level spallogenic ^{10}Be production rate of 3.92 ± 0.31 atoms g^{-1} a^{-1} [11] and for ^{21}Ne 18.7 ± 2.3 atoms $g^{-1}a^{-1}$ [12] and ERA40 atmospheric model.

We applied a time-integrated inverse modelling of cosmogenic nuclide production rates by subsequent modelled subsidence to paleo elevations. We used a linear uplift model of

40 m/Ma [13,14] with uplift commencing at 20 Ma (assuming that uplift of the alluvial fans started from a vertical position near sea-level). To apply uplift correction using LSDn scaling as implemented the CRONUS-Earth online calculator (V.3), we calculated the uplift-dependant change by using an erosion rate (the reduction of the mass air above the sample by uplift is mathematically equivalent to erosion).

The density of air decreases with altitude (rising from sea-level to 1100 m, our mean sample elevation) the density of air is reduced by~10% (U.S. Standard Atmosphere 1976, NASA-TM-X-74335). For the purpose of calculating the effect of atmospheric mass removal by uplift we utilize the mean density of air at 500 m.a.s.l. (1.167 kg/m^3, NASA-TM-X-74335). The $\rho_{air\ 500m}/\rho_{Qtz}$ multiplied by the uplift rate provides the 'erosion rate' (in our case 1,762 x*10^{-6} cm/yr) for input into the online calculator. Since we use the density of air at 500 m at all elevations, we assign a 5% internal uncertainty for our uplift correction (caused by the utilization of a mean density of air).

For samples with concentrations implying an age >20 Ma, we use the scaling calculated for a virtual 20 Ma sample at the sampling location, to calculate the exposure prior to 20 Ma (from the concentration that is in excess of that produced since 20 Ma); which is added to 20 Ma to obtain the exposure age.

The uplift correction is relatively insensitive to deviation of the assumption of linear uplift (within the bounds of the same long-term average). Ages change by ±10% if the uplift rate decreased/increased fourfold after half the exposure time (Dunai et al. 2005). We assign a ±10% external uncertainty to the uplift-corrected ages. Ages without uplift correction would be younger. Early Miocene ages would be younger by ~30%, differences decrease towards younger ages (~2% at 2 Ma).

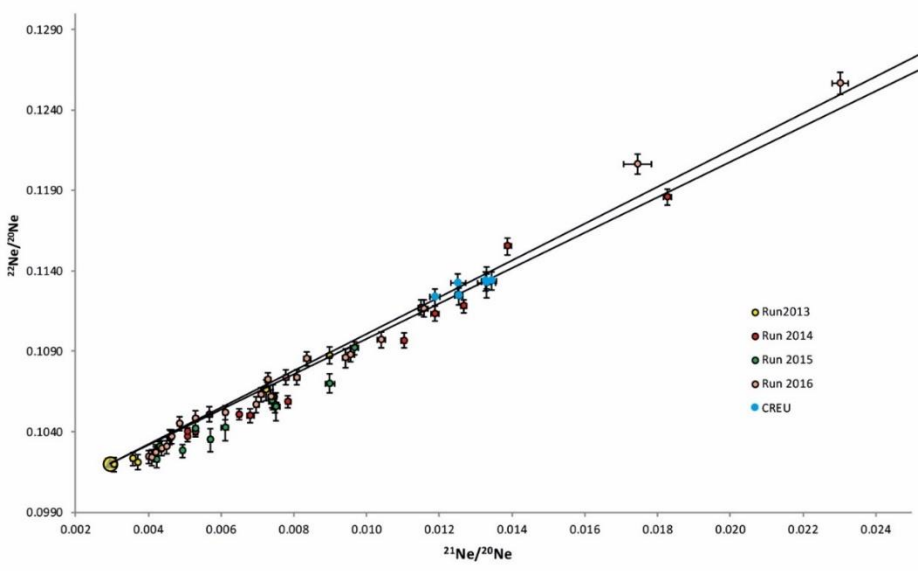

Fig. 2 Neon isotope data of all analysis reported in this paper. The lines represent a mixture of air and the spallation-derived Ne in quartz. Sample and standard (CREU, [6]) measurements are shown.

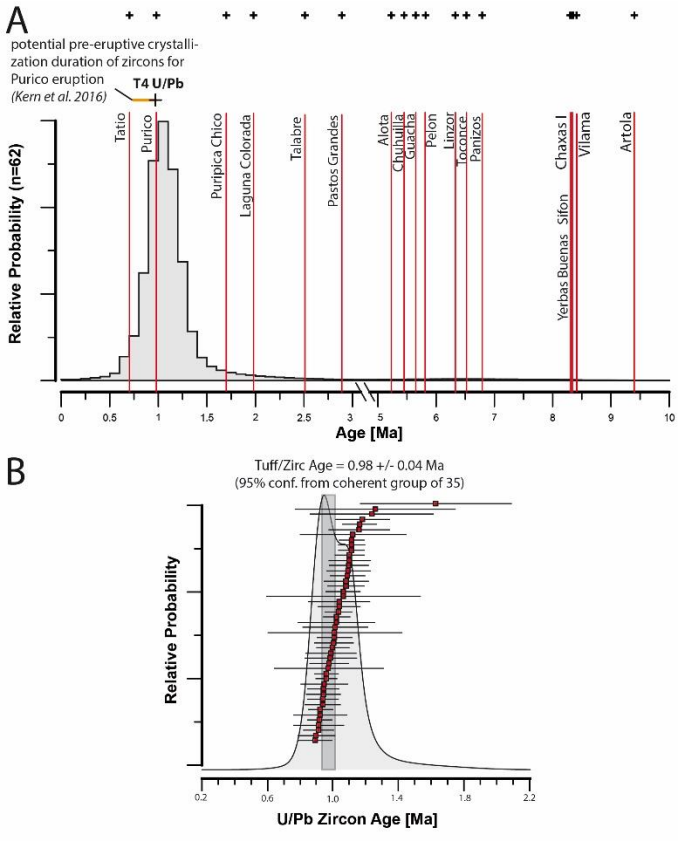

Fig. 3 (A) The zircon U/Pb age record is represented by histograms and associated probability density function curve for zircons ages between 0 and 10Ma, determined for the sampled tephra T4. Note that the scale of age axis is interrupted and changes between 3 and 5 Ma. Eruption ages (Ar/Ar) of adjacent volcanic complexes are marked as vertical bars [15]. Orange bar indicates potential pre-

eruptive crystallization duration of zircons within the Purico magma chamber [16]. U/Pb zircon ages could therefore be related to the Purico or the Tatio eruptions. (B) Rank order plots (ROP) and zircon U/Pb ages as probability density function (PDF) curves. The shaded PDF curve represents the distribution for the ROP displayed. The normal distribution is interpreted to represent a single population of crystals from an individual eruption. Horizontal lines display 2σ analytical uncertainty of data from which cumulative probability curves were calculated. The age of 0.98 ± 0.04 is the weighted mean and 2σ error for the dominant peak in the distribution of 35 zircons of T4.

Additional Site Data

The easternmost fan (Fan East) has a maximum width of 1.5 km and length of 4 km, moderately dipping (1.46°) to the north. The lower 1.5 km are buried under lacustrine sediments, related to lake stages in the Quillagua-Llamara basin [17]. Diatom-rich sediments indicate deposits of the Quillagua Formation 5.5-4.5 Ma, [17,18] outcrop at the surface. Deflation removed material to the bed-rock level adjacent to the fans resulting that the fan surface is elevated approximately 5-10 m above the adjacent surface, resembling an inverted landscape topography in the lower part of the fan.

The central fan (Fan Center) has a maximum length of 3 km, including the final 1 km covered by lacustrine sediments, and a maximum width of 2.4 km. Similar like the eastern fan, the center fan is surrounded by an inverted landscape-like topography. The fan surface dips moderately to the north (1.29°). A feeder channel (RL15 005) is well preserved and has incised into blocks of the Adamito Fault System, indicating synchronous evolution/activity.

The determination of the outline of the western-most fan (Fan West) is difficult; is due to significant surface modification by fluvial erosion in the distal portions, and dust cover approaching its apex. To the west, the fan is bound by the Atacama Fault. The east is limited by deflation sinks, and the western margin of the Central Fan in its lower section. The surface dips moderately to the north (0.93°), with a maximum width of 2 km and maximum length of 4.5 km. Fan sediments are buried under lacustrine sediments in the distal part.

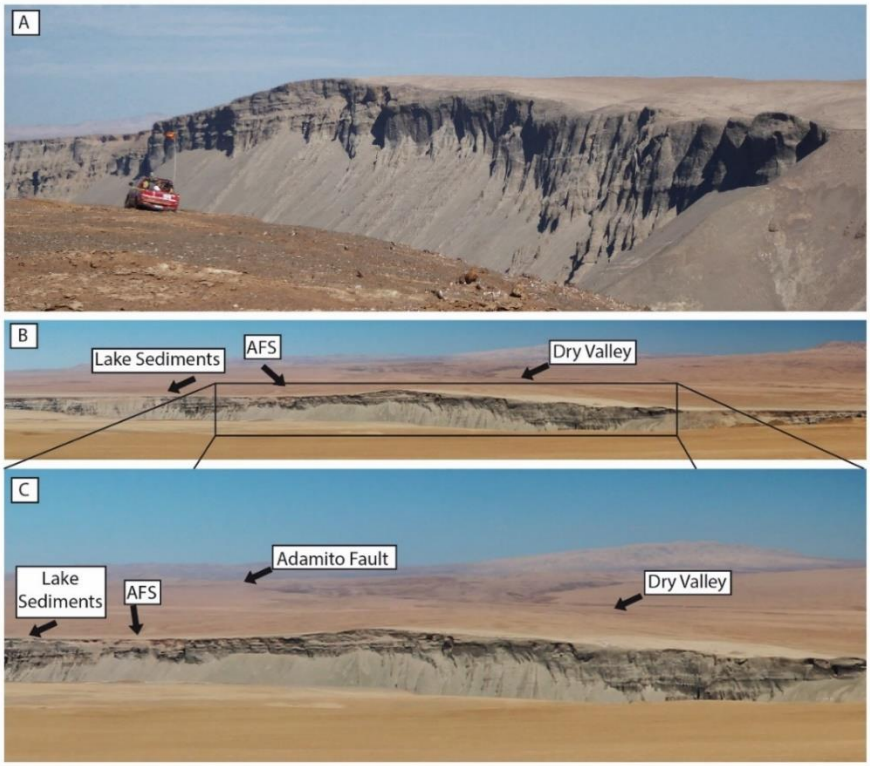

Fig. 4 Photographs (made by B. Ritter) taken from the northern rim of the Rìo Loa canyon towards the transpressional topographic high. Lacustrine sediments are exclusively found to the east of this high (left side in the images). Fluvial sediments of a 'Proto-Rio Loa' system are visible on both sides of the AFS.

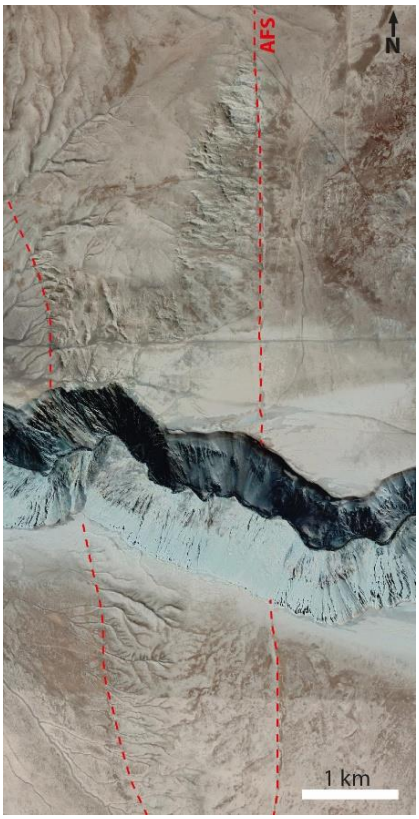

Fig. 5 Google Earth image (Image data: ©2018 CNES/Airbus & Digital Globe, image recoding 11/7/2014) highlighting the course of the splay fault and uplifted tectonic block. Note, the vertical displacement north of the Río Loa.

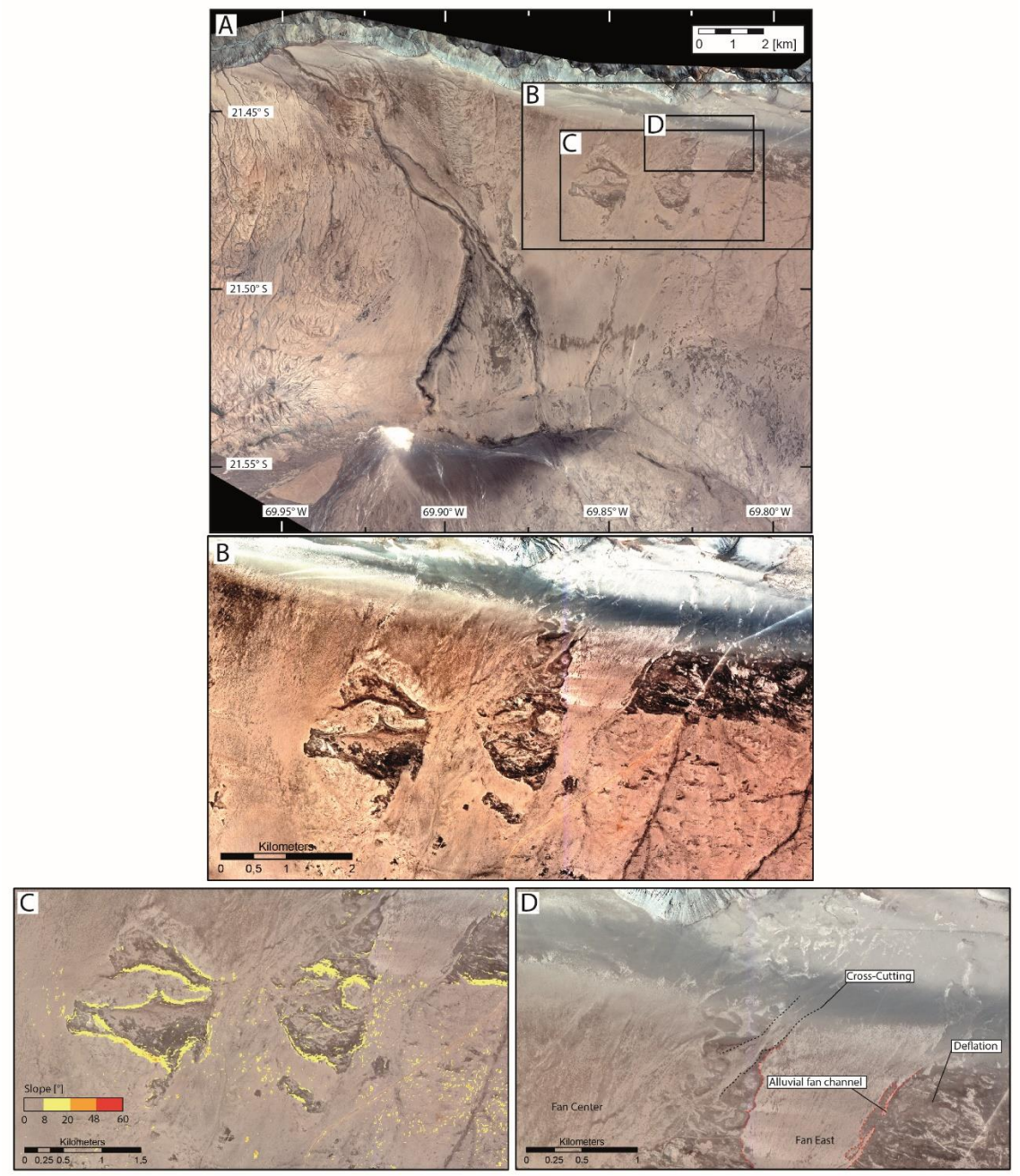

Fig. 6: A) Pléiades 1B Multi-Spectral Image of the study area (maps created using ArcGIS® 10.5.1, ESRI http://www.esri.com). This is identical to Figure 2A. Black rectangles indicate clipping of Fig. 6B-D. B) Enlarge image of depositional fan surfaces north of the Adamito fault. To increase the visibility of boundaries between alluvial fans and inverted landscape, the Pléiades 1B Multi-Spectral Image was modified using contrast enhancement. C) Pléiades 1B Multi-Spectral Image including calculated slope map using ArcGIS 10.5.1® Slope angles >8° are displayed in colour and indicate boundaries between alluvial fan sediments and deflation hollows. D) Enlarge image of the eastern alluvial fan surface north of the Adamito fault (Pléiades 1B Multi-Spectral Image). Visible are former topographic lows (channels with gravel infill), which are now topographic highs due landscape

inversion at the eastern limit of the eastern fan. Cross-cutting on the center fan towards the eastern fan is marked.

Table 1: Cosmogenic ^{21}Ne isotope data for quartz clasts. Internal uncertainty 5% of exposure age, external uncertainty 10% of exposure age for samples older than 20 Ma.

Sample	Lat.	Long.	Elevation [m]	Mean Thickness [cm]	^{21}Ne [atoms/g]	^{21}Ne Uncert.	Exposure Age [Ma]	Internal Uncert.[Ma]	External Uncert. [Ma]
RL 14/01a	S 21°28'02.5"	W 69°49'15.0"	898	1	5.32E+08	1.6E+07	34.15	1.71	3.42
RL 14/01b	S 21°28'02.5"	W 69°49'15.0"	898	1.5	3.10E+08	1.0E+07	17.94	0.76	2.01
RL 14/01c	S 21°28'02.5"	W 69°49'15.0"	898	2	2.90E+08	9E+06	16.55	0.66	1.81
RL 14/01d	S 21°28'02.5"	W 69°49'15.0"	898	2.5	2.87E+08	9E+06	16.64	0.67	1.82
RL 14/01e	S 21°28'02.5"	W 69°49'15.0"	898	3.5	2.43E+08	8E+06	13.66	0.53	1.43
RL 14/01f	S 21°28'02.5"	W 69°49'15.0"	898	3	1.62E+08	5E+06	7.98	0.30	0.77
RL 14/02	S 21°28'14.5"	W 69°50'21.6"	907	1.5	2.16E+08	8E+06	10.85	0.50	1.12
RL 14/02b	S 21°28'14.5"	W 69°50'21.6"	907	1.5	3.34E+08	1.1E+07	19.80	0.92	2.31
RL 14/02c	S 21°28'14.5"	W 69°50'21.6"	907	1	1.37E+08	5E+06	6.14	0.26	0.59
RL 14/02d	S 21°28'14.5"	W 69°50'21.6"	907	2	1.92E+08	7E+06	9.49	0.37	0.94
RL 14/02e	S 21°28'14.5"	W 69°50'21.6"	907	1.5	1.70E+08	6E+06	8.06	0.31	0.78
RL 14/02f	S 21°28'14.5"	W 69°50'21.6"	907	2.5	3.56E+08	1.2E+07	21.41	1.07	2.14
RL 14/03a	S 21°28'21.33"	W 69°50'33.8"	910	1.5	1.30E+08	4E+06	5.82	0.21	0.54
RL 14/03b	S 21°28'21.33"	W 69°50'33.8"	910	1.5	2.33E+08	1.0E+07	11.94	0.64	1.30
RL 14/03c	S 21°28'21.33"	W 69°50'33.8"	910	1.5	1.78E+08	7E+06	8.49	0.35	0.84
RL 14/03d	S 21°28'21.33"	W 69°50'33.8"	910	2	2.23E+08	9E+06	11.46	0.52	1.19
RL 14/03e	S 21°28'21.33"	W 69°50'33.8"	910	2.25	6.90E+07	2.8E+06	2.88	0.12	0.27
RL 14/03f	S 21°28'21.33"	W 69°50'33.8"	910	4	3.28E+08	1.1E+07	21.00	0.99	2.49
RL 14/04a	S 21°27'54.1"	W 69°51'54.4"	880	1.5	1.25E+08	5E+06	5.71	0.24	0.55
RL 14/04b	S 21°27'54.1"	W 69°51'54.4"	880	1.25	7.77E+07	3.2E+06	3.28	0.14	0.31
RL 14/04c	S 21°27'54.1"	W 69°51'54.4"	880	1.75	1.25E+08	4E+06	5.73	0.22	0.54
RL 14/04d	S 21°27'54.1"	W 69°51'54.4"	880	2.25	1.40E+08	5E+06	6.64	0.29	0.65
RL 14/04e	S 21°27'54.1"	W 69°51'54.4"	880	2.25	7.38E+07	4.9E+06	3.19	0.22	0.34
RL 14/04f	S 21°27'54.1"	W 69°51'54.4"	880	2.75	2.00E+08	7E+06	10.46	0.45	1.07
RL13001a	S 21°27'35.2"	W 69°55'07.8"	764	1	4.05E+07	1.3E+06	1.78	0.06	0.16
RL13001b	S 21°27'35.2"	W 69°55'07.8"	764	1	1.47E+08	5E+06	7.58	0.28	0.73
RL13001c	S 21°27'35.2"	W 69°55'07.8"	764	1	1.53E+08	5E+06	7.98	0.29	0.77
RL13001d	S 21°27'35.2"	W 69°55'07.8"	764	1	6.51E+07	2.3E+06	2.96	0.11	0.27
RL13001e	S 21°27'35.2"	W 69°55'07.8"	764	1	5.17E+07	2.1E+06	2.28	0.10	0.21
RL 15-001a	S 21°28'54.0"	W 69°53'34.1"	877	1.75	1.79E+08	9E+06	8.85	0.50	0.94
RL 15-001b	S 21°28'54.0"	W 69°53'34.1"	877	2.5	2.46E+08	8E+06	13.67	0.58	1.45
RL 15-001c	S 21°28'54.0"	W 69°53'34.1"	877	2.5	1.81E+08	7E+06	9.20	0.42	0.93
RL 15-001d	S 21°28'54.0"	W 69°53'34.1"	877	3.5	3.69E+08	1.2E+07	22.34	1.12	2.23

RL 15-001e	S 21°28'54.0"	W 69°53'34.1"	877	3	2.95E+08	1.0E+07	17.93	0.81	2.03
RL 15-001f	S 21°28'54.0"	W 69°53'34.1"	877	2.5	2.89E+08	9E+06	17.11	0.72	1.90
RL 15-005a	S 21°30'17.3"	W 69°50'55.8"	1003	0.75	2.77E+08	9E+06	13.41	0.55	1.41
RL 15-005b	S 21°30'17.3"	W 69°50'55.8"	1003	0.75	4.18E+08	1.4E+07	25.90	1.29	2.59
RL 15-005c	S 21°30'17.3"	W 69°50'55.8"	1003	1	2.20E+08	8E+06	9.96	0.40	0.99
RL 15-005d	S 21°30'17.3"	W 69°50'55.8"	1003	0.75	2.87E+08	1E+07	14.02	0.60	1.49
RL 15-005e	S 21°30'17.3"	W 69°50'55.8"	1003	1.5	4.06E+08	1.4E+07	25.01	1.25	2.50
RL 15-005f	S 21°30'17.3"	W 69°50'55.8"	1003	1.5	1.18E+08	5E+06	4.77	0.23	0.46
RL 15-006a	S 21°28'39.9"	W 69°49'33.8"	930	2	1.61E+08	6E+06	7.46	0.33	0.74
RL 15-006b	S 21°28'39.9"	W 69°49'33.8"	930	2.5	2.58E+08	9E+06	13.85	0.58	1.47
RL 15-006c	S 21°28'39.9"	W 69°49'33.8"	930	2.5	2.10E+08	7E+06	10.54	0.40	1.06
RL 15-006d	S 21°28'39.9"	W 69°49'33.8"	930	2.5	1.07E+08	5E+06	4.69	0.25	0.47
RL 15-006e	S 21°28'39.9"	W 69°49'33.8"	930	2.5	1.61E+08	8E+06	7.58	0.40	0.78
RL 15-006f	S 21°28'39.9"	W 69°49'33.8"	930	2.5	1.32E+08	6E+06	5.99	0.31	0.60
RL 15-007a	S 21°30'14.8"	W 69°50'39.7"	1008	1.5	3.53E+08	1.2E+07	19.21	0.87	2.21
RL 15-007b	S 21°30'14.8"	W 69°50'39.7"	1008	2.25	2.31E+08	9E+06	10.91	0.51	1.14
RL 15-007c	S 21°30'14.8"	W 69°50'39.7"	1008	2	2.82E+08	9E+06	14.15	0.59	1.50
RL 15-007d	S 21°30'14.8"	W 69°50'39.7"	1008	2.5	1.81E+08	7E+06	8.12	0.36	0.81
RL 15-007e	S 21°30'14.8"	W 69°50'39.7"	1008	2.5	2.70E+08	1.1E+07	13.55	0.68	1.48
RL 15-007f	S 21°30'14.8"	W 69°50'39.7"	1008	3.25	4.46E+08	1.5E+07	27.93	1.40	2.79
RL 15-007g	S 21°30'14.8"	W 69°50'39.7"	1008	3.5	2.51E+08	1.0E+07	12.69	0.64	1.37

Table 2: Cosmogenic ^{10}Be isotope data for quartz clasts.

Sample	**Lat.**	**Long.**	**Elevation [m]**	**^{10}Be [atoms/g]**	**^{10}Be Uncert.**	**Exposure Age [Ma]**	**Internal Uncert.[Ma]**	**External Uncert. [Ma]**
RL 14/01 b	S 21°28'02.5''	W 69°49'15.0''	898	9.50E+06	3.1E+05	2.89	0.22	0.46
RL 14/01 c	S 21°28'02.5''	W 69°49'15.0''	898	1.20E+07	4E+05	saturated	saturated	saturated
RL 14/01 d	S 21°28'02.5''	W 69°49'15.0''	898	1.00E+07	3E+05	4.62	0.70	1.44
RL 14/01 e	S 21°28'02.5''	W 69°49'15.0''	898	9.87E+06	3.3E+05	5.39	1.15	2.36
RL 14/02 d	S 21°28'14.5"	W 69°50'21.6"	907	8.87E+06	2.9E+05	3.09	0.28	0.57
RL 14/02 e	S 21°28'14.5"	W 69°50'21.6"	907	7.15E+06	2.4E+05	1.75	0.10	0.21

Table 3: U/Pb analysis data to measured zircons of T4.

LA-ICP-MS data of zircons from T4. Spot size = 30 µm depth of crater ≈15 µm. ^{206}Pb/^{238}U error is the quadratic additions of the within run precision (2 SE) and the external reproducibility (2 SD) of the reference zircon. ^{207}Pb/^{206}Pb error propagation (^{207}Pb signal dependent) following Gerdes and Zeh [19]. ^{207}Pb/^{235}U error is the quadratic addition of the ^{207}Pb/^{206}Pb and ^{206}Pb/^{238}U uncertainty.

Grain	^{207}Pba (cps)	Ub (ppm)	Pbb (ppm)	Thb U	^{206}Pbcc (%)	^{206}Pbd ^{238}U	±2s (%)	^{207}Pbd ^{235}U	±2s (%)	^{207}Pbd ^{206}Pb	±2s (%)	rhoe	^{206}Pb ^{238}U	±2s (Ma)	^{207}Pb ^{235}U	±2s (Ma)
A339	114	807	0	1.49	24.4	0.00009955	9.5	0.001588	73	0.1157	73	0.13	0.6	0.1	1.6	1.2
A340	74	355	0	1.45	14	0.0001461	11.2	0.0009503	14	0.0472	8	0.81	0.9	0.1	1	0.1
A341	280	559	0	1.31	31	0.0001387	11.6	0.0009034	15	0.0473	8.7	0.8	0.9	0.1	0.9	0.1
A342	77	624	0	1.39	7.7	0.0001433	8.4	0.0009054	11	0.0458	6.4	0.79	0.9	0.1	0.9	0.1
A343	628	979	0	1.22	35.4	0.0001418	17.2	0.0009271	19	0.0474	8.6	0.89	0.9	0.2	0.9	0.2
A344	1918	1226	0	1.84	60.2	0.0001356	13.6	0.0008498	16	0.0455	8.1	0.86	0.9	0.1	0.9	0.1
A345	1514	350	0	1.43	71.8	0.0001512	34.5	0.0009046	60	0.0434	49	0.57	1	0.3	0.9	0.6
A346	109	753	0	1.75	9.6	0.0001367	8.4	0.0008633	10	0.0458	6.3	0.8	0.9	0.1	0.9	0.1
A347	1760	1367	0	2.4	52.1	0.0001585	23.2	0.001074	25	0.0492	10	0.91	1	0.2	1.1	0.3
A348	6043	964	0	1.68	73.2	0.0001571	40.7	0.001731	97	0.08	88	0.42	1	0.4	1.8	1.7
A349	78	756	0	1.88	6.9	0.000147	15.6	0.0009159	17	0.0452	6.8	0.92	0.9	0.1	0.9	0.2
A351	606	873	0	1.35	49.7	0.0001576	19.8	0.0009938	22	0.0458	8.7	0.91	1	0.2	1	0.2
A352	2073	854	0	2.01	63.4	0.0001803	16.2	0.001137	18	0.0457	8.5	0.88	1.2	0.2	1.2	0.2
A353	1131	649	0	1.4	57.6	0.000161	12.5	0.001009	15	0.0455	8.1	0.84	1	0.1	1	0.2
A354	1314	1090	0	2.26	45.3	0.0001731	7.5	0.001084	12	0.0454	9.4	0.62	1.1	0.1	1.1	0.1
A355	3092	599	0	1.37	54	0.0001923	30.4	0.001788	310	0.0674	310	0.1	1.2	0.4	1.8	5.6
A356	102	713	0	1.34	12.2	0.0001313	12	0.0008292	14	0.0458	8	0.83	0.8	0.1	0.8	0.1
A357	2345	1441	0	2.89	43	0.0001568	10.9	0.001016	13	0.047	7.3	0.83	1	0.1	1	0.1
A358	6096	884	0	1.4	83.1	0.000253	28.4	0.002899	87	0.0831	82	0.33	1.6	0.5	2.9	2.6
A359	8847	497	0	1.26	68.3	0.0009604	18.1	0.006326	20	0.0478	8.2	0.91	6.2	1.1	6.4	1.3
A360	883	554	2	1.05	3.3	0.003094	2.4	0.02016	11	0.0473	11	0.21	19.9	0.5	20.3	2.3
A361	221	898	0	2.13	14.3	0.0001589	8.1	0.001018	10	0.0465	6.4	0.79	1	0.1	1	0.1
A362	4218	722	0	0.9	35.1	0.0001741	29	0.001787	65	0.0745	59	0.44	1.1	0.3	1.8	1.2
A363	2479	1073	0	2.87	45.8	0.0001529	16.3	0.0009696	18	0.046	7.1	0.92	1	0.2	1	0.2
A364	39702	1440	100	0.82	0.2	0.07023	1.6	0.5351	2	0.0553	1.4	0.77	438	7	435	7
A365	4734	559	0	0.84	66	0.0001956	38.9	0.001255	290	0.0465	290	0.13	1.3	0.5	1.3	3.7
A366	387	568	0	1.21	29.8	0.0001676	10.6	0.001073	14	0.0465	8.7	0.77	1.1	0.1	1.1	0.1
A367	3440	410	0	0.74	59.9	0.000165	44.3	0.0009012	60	0.0396	40	0.74	1.1	0.5	0.9	0.5
A368	3930	2171	0	2.58	60.5	0.0001651	10.1	0.001051	12	0.0462	6.7	0.83	1.1	0.1	1.1	0.1
A369	4052	236	0	1.44	67.3	0.001175	17.4	0.007916	20	0.0489	9.2	0.88	7.6	1.3	8	1.6
A370	59	688	0	1.27	3.3	0.000149	7	0.0009543	9	0.0465	6.3	0.75	1	0.1	1	0.1
A371	1238	1133	0	1.6	64.9	0.0001551	10.3	0.00128	49	0.0599	48	0.21	1	0.1	1.3	0.6
A372	1008	2017	0	5.06	54.5	0.0001491	7.8	0.001352	55	0.0658	55	0.14	1	0.1	1.4	0.8
A373	49840	1666	1	2.16	66.8	0.0008061	31.8	0.004954	33	0.0446	8.8	0.96	5.2	1.6	5	1.7
A374	30687	1050	72	0.81	0	0.0691	1.8	0.5438	2	0.0571	0.99	0.87	431	7	441	7
A375	1947	1191	0	1.06	18.7	0.0001713	8.4	0.001099	9	0.0466	4.2	0.89	1.1	0.1	1.1	0.1
A377	593	319	0	1.17	48.4	0.0001833	14	0.00118	17	0.0467	8.8	0.85	1.2	0.2	1.2	0.2
A378	60	313	0	1.39	10.7	0.0001699	12.4	0.00109	15	0.0465	8.4	0.83	1.1	0.1	1.1	0.2
A379	100	678	0	1.23	13.5	0.0001417	10.4	0.0008914	13	0.0457	7.8	0.8	0.9	0.1	0.9	0.1
A380	11611	550	13	0.77	9.2	0.02486	1.8	0.168	10	0.049	10	0.18	158	3	158	15
A381	573	555	0	1.16	42.1	0.0001694	9.9	0.001066	13	0.0457	8.5	0.76	1.1	0.1	1.1	0.1
A382	87	629	0	1.25	6.8	0.0001728	7.3	0.001093	10	0.0459	6.4	0.75	1.1	0.1	1.1	0.1
A388	239	491	0	1.07	26.4	0.0001604	8.3	0.0009806	11	0.0444	7.7	0.73	1	0.1	1	0.1
A389	2791	2363	0	1.69	51.3	0.0001462	10.3	0.0009547	12	0.0474	6.5	0.85	0.9	0.1	1	0.1
A390	3009	603	0	1.1	52.1	0.0001611	18.2	0.001017	45	0.0458	41	0.41	1	0.2	1	0.5
A391	17932	2341	1	4	67	0.0003433	25.4	0.002308	27	0.0488	7.5	0.96	2.2	0.6	2.3	0.6
A392	529	671	0	1.11	40.7	0.0001514	12.4	0.0009611	15	0.0461	8.9	0.81	1	0.1	1	0.1
A393	46	295	0	1.29	10.2	0.0001456	11.7	0.0009179	14	0.0457	8.5	0.81	0.9	0.1	0.9	0.1
A394	1802	1084	0	0.97	26.7	0.0001564	12	0.0009985	14	0.0463	7.8	0.84	1	0.1	1	0.1
A395	12283	665	27	0.97	2.1	0.04135	1.7	0.3214	4	0.0564	3.8	0.4	261	4	283	10
A396	135	667	0	1.13	15.6	0.0001396	12.6	0.0008633	15	0.0449	7.5	0.86	0.9	0.1	0.9	0.1
A397	87	749	0	1.33	10.2	0.0001385	9.8	0.0008819	12	0.0462	7	0.81	0.9	0.1	0.9	0.1
A398	4311	376	0	1.05	66.3	0.0008027	14.5	0.005101	17	0.0461	8.1	0.87	5.2	0.7	5.2	0.9
A399	579	1146	0	0.77	0	0.0001677	12.7	0.001063	15	0.046	8.4	0.83	1.1	0.1	1.1	0.2
A400	1585	1057	0	0.64	12.1	0.0001705	11.1	0.001127	14	0.0479	7.8	0.82	1.1	0.1	1.1	0.2
A401	3148	1010	0	0.51	45	0.0001535	15.8	0.001046	31	0.0494	26	0.51	1	0.2	1.1	0.3
A402	1172	1260	0	1.89	44.4	0.0001458	10.3	0.0009177	13	0.0457	7.9	0.79	0.9	0.1	0.9	0.1
A403	148	607	0	1.28	13.8	0.0001732	7	0.001076	10	0.0451	7.5	0.68	1.1	0.1	1.1	0.1
A404	5462	678	9	0.99	6.7	0.01396	2	0.1345	9	0.0699	9.2	0.21	89	2	128	11
A405	2192	1114	0	0.61	41.2	0.0001805	9.3	0.001411	35	0.0567	34	0.27	1.2	0.1	1.4	0.5
A406	63	631	0	1.13	8.5	0.0001428	8.5	0.0009055	12	0.046	7.8	0.74	0.9	0.1	0.9	0.1
A407	4280	1646	0	0.77	43.6	0.0001712	11.7	0.001107	14	0.0469	7	0.86	1.1	0.1	1.1	0.2

References:

1 Frei, D. & Gerdes, A. Precise and accurate in situ U–Pb dating of zircon with high sample throughput by automated LA-SF-ICP-MS. Chemical Geology 261, 261-270 (2009).

2 Kohl, C. & Nishiizumi, K. Chemical isolation of quartz for measurement of in-situ-produced cosmogenic nuclides. Geochimica et Cosmochimica Acta 56, 3583-3587 (1992).

3 Binnie, S. A. et al. Separation of Be and Al for AMS using single-step column chromatography. Nuclear Instruments and Methods in Physics Research Section B: Beam Interactions with Materials and Atoms (2015).

4 Dewald, A. et al. CologneAMS, a dedicated center for accelerator mass spectrometry in Germany. Nuclear Instruments & Methods in Physics Research Section B-Beam Interactions with Materials and Atoms 294, 18-23, doi:10.1016/j.nimb.2012.04.030 (2013).

5 Nishiizumi, K. et al. Absolute calibration of Be-10 AMS standards. Nucl. Instr. Meth. Phys. Res. B 258, 403-413 (2007).

6 Vermeesch, P. et al. Interlaboratory comparison of cosmogenic Ne-21 in quartz. Quaternary Geochronology 26, 20-28, doi:10.1016/j.quageo.2012.11.009 (2015).

7 Ma, Y. & Stuart, F. M. The use of in-situ cosmogenic 21 Ne in studies on long-term landscape development. Acta Geochimica, 1-13 (2017).

8 Codilean, A. T. et al. Single-grain cosmogenic 21Ne concentrations in fluvial sediments reveal spatially variable erosion rates. Geology 36, 159-162 (2008).

9 Lifton, N., Sato, T. & Dunai, T. J. Scaling in situ cosmogenic nuclide production rates using analytical approximations to atmospheric cosmic-ray fluxes. Earth and Planetary Science Letters 386, 149-160, doi:10.1016/j.epsl.2013.10.052 (2014).

10 Balco, G., Stone, J. O., Lifton, N. A. & Dunai, T. J. A complete and easily accessible means of calculating surface exposure ages or erosion rates from (10)Be and (26)Al measurements. Quaternary Geochronology 3, 174-195, doi:10.1016/j.quageo.2007.12.001 (2008).

11 Borchers, B. et al. Geological calibration of spallation production rates in the CRONUS-Earth project. Quaternary Geochronology 31, 188-198 (2016).

12 Kober, F., Alfimov, V., Ivy-Ochs, S., Kubik, P. W. & Wieler, R. The cosmogenic (NE)-N-21 production rate in quartz evaluated on a large set of existing Ne-21-Be-10 data. Earth and Planetary Science Letters 302, 163-171, doi:10.1016/j.epsl.2010.12.008 (2011).

13 Dunai, T. J., González López, G. A. & Juez-Larré, J. Oligocene–Miocene age of aridity in the Atacama Desert revealed by exposure dating of erosion-sensitive landforms. Geology 33, 321, doi:10.1130/g21184.1 (2005).

14 Evenstar, L. A., Stuart, F. M., Hartley, A. J. & Tattitch, B. Slow Cenozoic uplift of the western Andean Cordillera indicated by cosmogenic 3He in alluvial boulders from the Pacific Planation Surface. Geophysical Research Letters 42, 8448-8455 (2015).

15 Salisbury, M. J. et al. 40Ar/39Ar chronostratigraphy of Altiplano-Puna volcanic complex ignimbrites reveals the development of a major magmatic province. Geological Society of America Bulletin, B30280. 30281 (2010).

16 Kern, J. M. et al. Geochronological imaging of an episodically constructed subvolcanic batholith: U-Pb in zircon chronochemistry of the Altiplano-Puna Volcanic Complex of the Central Andes. Geosphere 12, 1054-1077 (2016).

17 Sáez, A., Cabrera, L., Jensen, A. & Chong, G. Late Neogene lacustrine record and palaeogeography in the Quillagua–Llamara basin, Central Andean fore-arc (northern Chile). Palaeogeography, Palaeoclimatology, Palaeoecology 151, 5-37 (1999).

18 Sáez, A. et al. The stratigraphic record of changing hyperaridity in the Atacama desert over the last 10Ma. Earth and Planetary Science Letters 355-356, 32-38, doi:10.1016/j.epsl.2012.08.029 (2012).

19 Gerdes, A. & Zeh, A. Zircon formation versus zircon alteration—new insights from combined U–Pb and Lu–Hf in-situ LA-ICP-MS analyses, and consequences for the interpretation of Archean zircon from the Central Zone of the Limpopo Belt. Chemical Geology 261, 230-243 (2009).

6. Climatic fluctuations in the hyperarid core of the Atacama Desert during the past 215 ka

Journal article

Received: 2 October 2018 Accepted: 8 March 2019 Published: 27 March 2019

Ritter, B., Wennrich, V., Medialdea, A., Brill, D., King, G., Schneiderwind, S., Niemann, K., Fernandez-Galego, E., Diederich, J., Rolf, C., Bao, R., Melles, M., Dunai, T.J., (2019) – Climatic fluctuations in the hyperarid core of the Atacama Desert during the past 215 ka. Scientific reports, 9(1), 5270.

Original figure numbers of the manuscript are used.

www.nature.com/scientificreports

SCIENTIFIC REPORTS

OPEN

"Climatic fluctuations in the hyperarid core of the Atacama Desert during the past 215 ka"

Received: 2 October 2018
Accepted: 8 March 2019
Published online: 27 March 2019

Benedikt Ritter[1], Volker Wennrich[1], Alicia Medialdea[2], Dominik Brill[2], Georgina King[3], Sascha Schneiderwind[4], Karin Niemann[4], Emma Fernández-Galego[1], Julia Diederich[1], Christian Rolf[5], Roberto Bao[6], Martin Melles[1] & Tibor J. Dunai[1]

Paleoclimate records from the Atacama Desert are rare and mostly discontinuous, mainly recording runoff from the Precordillera to the east, rather than local precipitation. Until now, paleoclimate records have not been reported from the hyperarid core of the Atacama Desert (<2 mm/yr). Here we report the results from multi-disciplinary investigation of a 6.2 m drill core retrieved from an endorheic basin within the Coastal Cordillera. The record spans the last 215 ka and indicates that the long-term hyperarid climate in the Central Atacama witnessed small but significant changes in precipitation since the penultimate interglacial. Somewhat 'wetter' climate with enhanced erosion and transport of material into the investigated basin, commenced during interglacial times (MIS 7, MIS 5), whereas during glacial times (MIS 6, MIS 4–1) sediment transport into the catchment was reduced or even absent. Pelagic diatom assemblages even suggest the existence of ephemeral lakes in the basin. The reconstructed wetter phases are asynchronous with wet phases in the Altiplano but synchronous with increased sea-surface temperatures off the coasts of Chile and Peru, i.e. resembling modern El Niño-like conditions.

The Atacama Desert of northern Chile is one of the driest places on Earth; its extreme hyperarid core receives less than 2 mm/yr of precipitation[1]. These hyperarid conditions are the consequence of subtropical atmospheric subsidence[2] and temperature inversion due to coastal upwelling of the cold Peru-Chile Current (PCC) (or Humboldt Current[1]). Furthermore, a continental effect (distance to the Atlantic) and rainshadow effect at the eastern flank of the Andes (Fig. 1A) effectively harvests sparse moisture arriving from the Atlantic[3–6]. High evaporation rates in most areas of the Atacama Desert additionally intensify the hyperarid conditions[3,7]. Although the main factors causing aridity are known, the onset of predominantly hyperarid conditions and variability in the degree of aridity in this area remain disputed[8–18]. Presently the core of the hyperarid Atacama Desert covers parts of the Coastal Cordillera and Central Depression between 22–19°S (Fig. 1A). Water availability increases, albeit moderately, away from this core. The Mean Annual Precipitation (MAP) increases rapidly from less than 20 mm/yr at 2300 m to over 300 mm/yr at 5000 m elevation[3]. At the southern edge of the hyperarid core, moisture sources are connected to south-westerly airflows that allow extratropical cyclone systems to migrate northwards bringing moisture to areas south of 24°S during austral winter[1]. These northward migrating cut-off low systems can penetrate further north, as occurred during recent flood events such as in March 2015[19,20]. Similar rain events in the (sub-) recent past may be reflected by widespread traces of fluvial erosion and transport in the southernmost region of the dry core (i.e. south of 21°30′S), whereas comparable features are largely absent further to the north.

Regional climate records from the Coastal Cordillera and the Central Depression are scarce and where available mostly cover only the Holocene and the Last Glacial Maximum (LGM)[6,16,18,21–25]. Climate records spanning the mid to late Pleistocene, exist from lake sediment sequences in the Bolivian Altiplano[26] and from near-shore marine sediment-cores[27,28], all of which are >400 km away from the desert interior, and cross steep climatic gradients[1,3] (Fig. 1B). In this paper, we present a first mid to late Pleistocene record of precipitation changes close to

[1]Institute of Geology & Mineralogy, University of Cologne, Cologne, Germany. [2]Institute of Geography, University of Cologne, Cologne, Germany. [3]Institute of Earth Surface Dynamics, University of Lausanne, Lausanne, Switzerland. [4]Institute of Neotectonics and Natural Hazards, RWTH Aachen University, Aachen, Germany. [5]Leibniz Institute for Applied Geophysics (LIAG), Hannover, Germany. [6]Centro de Investigacións Científicas Avanzadas (CICA), Facultade de Ciencias, Universidade da Coruña, Coruña, Spain. Correspondence and requests for materials should be addressed to B.R. (email: benedikt.ritter@uni-koeln.de)

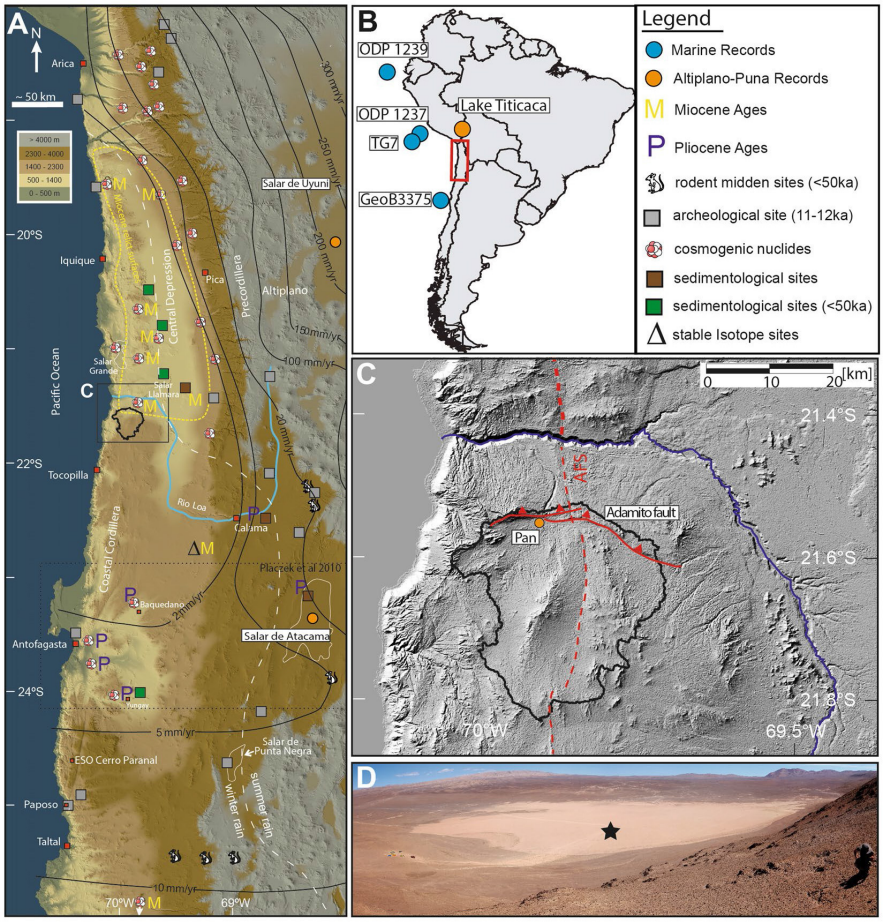

Figure 1. (**A**) Colour shaded digital elevation model (derived from SRTM-data, created using ArcGIS 10.5.1) with isohyets[1] after Ritter, *et al.*[31]. Dashed white line indicates the border between winter-rain dominated areas in the SW and summer-rain dominated areas in the[1]. Sites from the literature are: rodent midden sites[23,64], earliest archaeological sites[65], stable isotope studies[66], sedimentological studies[14,25,67,68], cosmogenic nuclide exposure ages and erosion rates determined with cosmogenic nuclides[9–12,68–74]. The stippled yellow outline for Miocene relict surfaces is derived from studies yielding Miocene exposure ages (M) for sediment surfaces[11,12,70,71] and sedimentological studies[67]. Studies yielding Pliocene ages for the onset of aridity are marked with P. The study area is marked with a black rectangle and drainage catchment of the sediment record is encircled with a black line. (**B**) Overview map of South America with positions of reference studies marked with coloured circles and the location of the Atacama Desert marked with a red rectangle. (**C**) Hillshade image based on Aster GDEM data (30 m resolution, produced using ArcGIS 10.5.1). Red lines indicate major tectonic fault systems (AFS = Atacama Fault System). The coring site (orange circle) is located in the mud pan in the northern part of an endorheic basin, whose drainage catchment is indicated with the black line. (**D**) View from the North onto the mud pan with the drilling location indicated by a star (Photo made by V. Wennrich).

the driest part of the Atacama as preserved in lacustrine clay pan sediments of a tectonically blocked endorheic basin within the Coastal Cordillera.

Site Information

The study site is situated in the Coastal Cordillera, which forms a 1000–1800 m high and 50–70 km wide structural high that is restricted to the west by a 1000 m coastal cliff and bounded to the east by the Central Depression (Fig. 1A,C). The studied clay pan (21° 32.5′′S, 69° 54.8′′W) is located at the northern end of an endorheic basin (Fig. 1C), which was formed by tectonic drainage displacement by reverse faulting (Adamito or Auguire fault)[29–31]. The clay pan at its terminus has a maximum surface area of 640 by 1000 m, and a catchment area of 560 km^2 (Fig. 1A,C). Since the catchment is entirely contained within the Coastal Cordillera, and completely disconnected

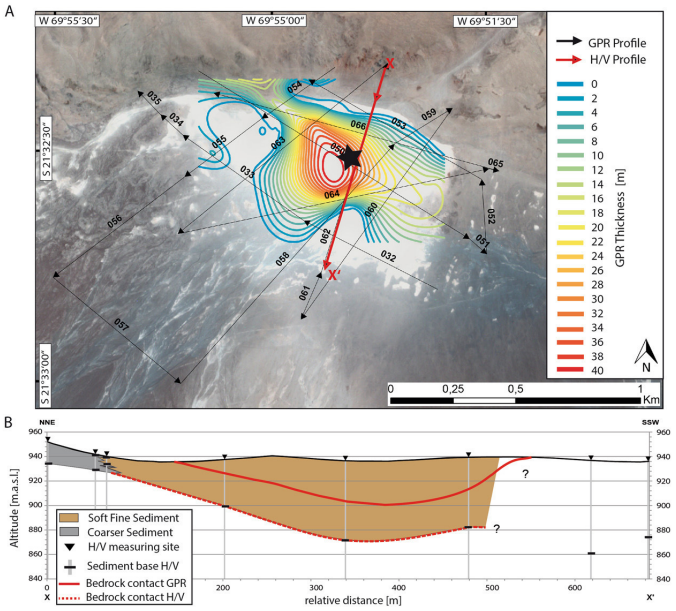

Figure 2. (**A**) Google Earth image (Image data: ©2018 CNES/Airbus & Digital Globe, image recoding 11/7/2014) including GPR and H/V profiles and GPR modelled contour lines of bedrock contact. Location of the drill site is indicated by a star. (**B**) Basin profile (solid red line in (**A**) derived from GPR (GPR data and extrapolation of bedrock contact based on inclination, solid red line) and H/V seismic (dashed red line). Bedrock contact derived from GPR (solid red line) is lower than that derived from H/V seismic derived (dashed red line).

from groundwater influences from the Central Depression to the east, sediments in the terminal lake potentially record past fluvial processes from local to regional rainfall sources rather than from areas outside the Coastal Cordillera.

Three-dimensional Basin Infill

The superficial extent of the clay pan is obvious from satellite imagery (Figs 1C and 2A). The three-dimensional basin morphology was reconstructed from dipping reflectors revealed from a net of Ground Penetrating Radar (GPR; for further information, see supplementary) profiles. As visible in Fig. 2B, the dipping appears to only be flat-angle throughout the basin, and can be extrapolated to a maximum depth of 41 ± 10 m at the centre of the clay pan (Fig. 2A,B). According to the GPR data, the basin morphology is not concentric and symmetric, but exhibits a shallower dipping at the southern part towards the centre and much steeper slopes at the thrusting scarp in the north (Fig. 2A,B). H/V seismic data (Fig. 2A profile red line, for further information see supplementary) were able to resolve soft sediment/bedrock contact, with a maximum depth of approximately 64 +/− 10 m (Fig. 2B). Due to the low soft-sediment density variations, a higher resolution model of the internal structure of the sediment infill could not be obtained from H/V seismic analysis.

Lithological Characterisation

In 2014 and 2015 the uppermost 6.2 m of the sediment record (composite of PAG5 and 6) in the central part of the clay pan were recovered using hand-held percussion drilling system (Eijkelkamp). No macroscopically visible organic remains were found. Relative XRF intensities of sulphur (S) and calcium (Ca) are mostly stable throughout the sediment core, only between ~500–525 cm depth, S and Ca counts increase fourfold as compared to remainder of the core. The almost perfect correlation of S and Ca counts (R^2 of 0.98) indicate the presence of calcium sulphate as sulphur bearing phase, in the interval between ~500–525 cm gypsum is macroscopically visible. We observe a strong positive correlation between the sediment grain-size and the Zr/Rb ratio (Fig. 3). Low Zr/Rb ratios are found in the silt to clay fraction, Zr is enriched in the sand fraction. Magnetic susceptibility covaries with increasing grain size and indicates a grain-size dependency. The core can be subdivided into three major sediment types (Lithofacies), differing distinctly in grain size, evaporite content, and inorganic geochemistry.

A coarser sediment type (Lithofacies 1), consisting predominantly of fine to medium sand and gravel, dominates the sediment record from 360 to 625 cm depth (Fig. 3). The abundance of gravel, especially medium gravel (>6.3 mm) increases towards the base of the core, with up to 50 wt.% for in few samples. The grain-size distributions (GSD) < 2 mm are unimodal. Above 360 cm Lithofacies 1 occurs as intercalation within Lithofacies 3, with bi- to trimodal GSDs (Fig. 3, see supplementary). Magnetic susceptibility exhibits high values, coincident

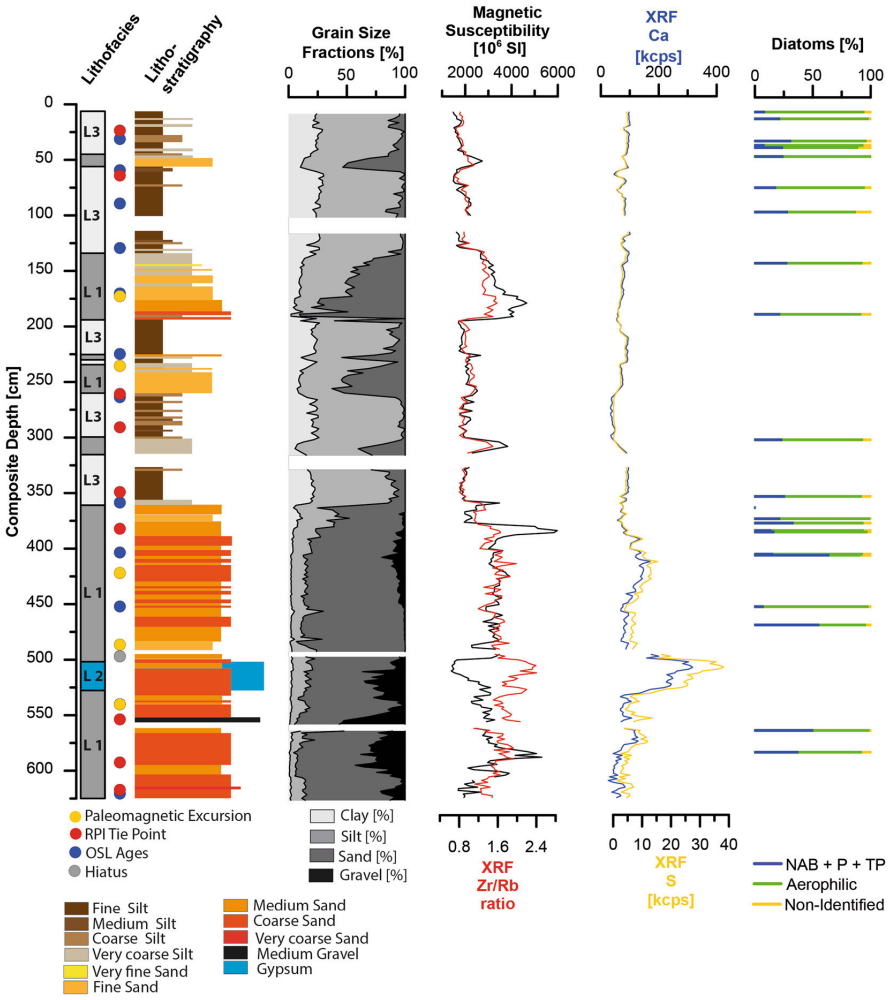

Figure 3. Lithofacies, lithology, grain-size distributions, magnetic susceptibility (MS), Zr/Rb ratio, S and Ca intensities, diatom assemblages and lithofacies of the record. Data gaps are due to recovery loss during drilling. Coloured dots mark age tie points, see age-depth model (Fig. 5C).

with coarse grain-sizes. Lithofacies 2 is found in a brief interval between ~5.00–5.25 m and is a matrix supported gypsum-cemented sandy gravel (Fig. S3, see Supplementary Fig. S3), resembling a gypsum duricrust. This unit has the lowest magnetic susceptibility in the core, which can be attributed to a dilution effect due to the high gypsum content. Lithofacies 3, fine- to medium silt-size sediments with polymodal GSDs, constitutes the uppermost part of the section (0–360 cm). Intercalations of Lithofacies 1 occasionally interrupt Lithofacies 3 (Fig. 3). In line with the fine grain-size magnetic susceptibility is low.

Biostratigraphical Characterisation

Phytoliths were found in every sample, however, they were not further analysed for this study. Diatom frustules were found in 22 of the 28 samples examined (Figs 3 and 4, see Supplementary Dataset Fig. S5). They were absent in the 5 samples from the interval 616 to 505 cm and at 363 cm depth. The diatom-free horizons could be the result of either taphonomic processes preventing the preservation of diatoms, or of prevailing dry conditions incompatible with the presence of diatoms. Where present, diatoms in general are scarce and highly fragmented. Most samples are characterized by highest percentages of aerophilic species, primarily *Pinnularia borealis* Ehrenberg, *Hantzschia amphioxys* (Ehrenberg) Grunow and *Denticula* cf. *elegans* Kützing. An allochthonous transport of non-aerophilic diatom taxa into the clay pan cannot be excluded, but is rather unlikely due to the lack of lacustrine deposits within the drainage catchment. Nevertheless, non-aerophilic benthic and, in some

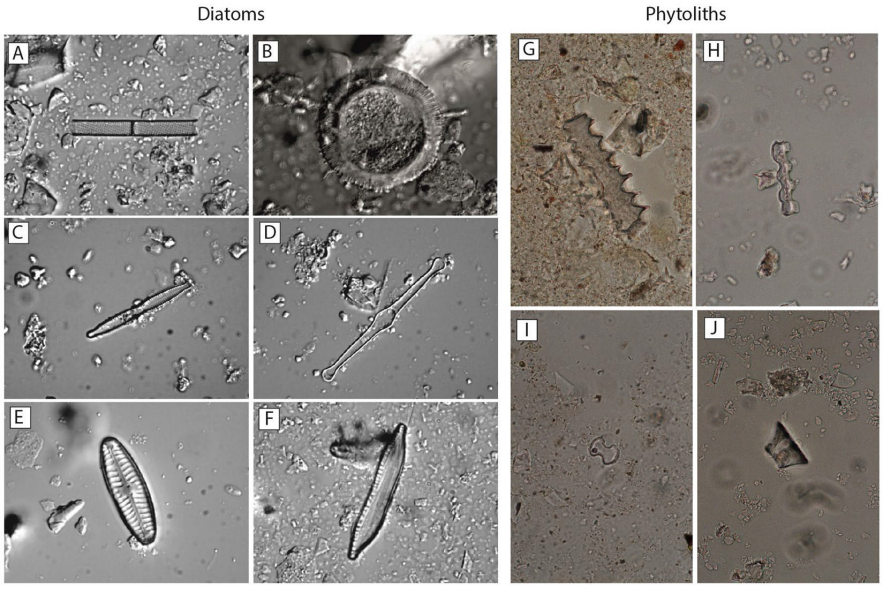

Figure 4. (**A**–**F**) Photographs of some representative diatom taxa (1000x magnification). (**A**) *Aulacoseira* cf. *ambigua* (Grunow) Simsonsen (**B**) *Cyclotella* sp. (**C**) *Fragilaria mesolepta* Rabenhorst (**D**) *Tabellaria flocculosa* (Roth) Kützing (**E**) *Pinnularia* cf. *borealis* (**F**) *Hantzschia amphioxys* (Ehrenberg) Grunow. (**G**–**J**) Photographs of some phytoliths found in the samples (1000x magnification).

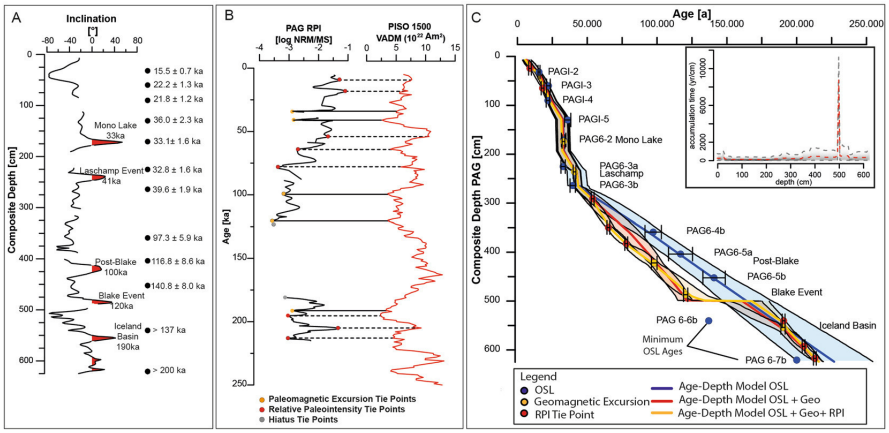

Figure 5. (**A**) Paleomagnetic inclination record of core PAG 6 from the PAG mud pan. Geomagnetic inclination excursion recorded in the sediment record are marked in red with proposed geomagnetic events. Black dots display measured OSL ages. (**B**) Relative paleointensity (RPI) record vs. used RPI stacks PISO1500[40]. Orange dots and solid lines indicate geomagnetic excursion tie points, red dots and dashed lines mark RPI tie points. Grey dots mark tie points for resembling phases of sedimentation stagnancy (hiatus). (**C**) Bayesian age-depth model using 'Bacon' from Blaauw and Christen[48]. Orange dots indicate geomagnetic excursion tie points, red dots RPI tie points and blue OSL ages. Accumulation time is given in yr/cm (calculated using 'Bacon'[48] without event-layers). Note that abrupt changes in the sedimentation rate is tightly linked to used tie points and most likely does not reflect natural smooth transitions. The lowest OSL ages (PAG 6-6b, PAG 6-7b) represent minimum ages (see text).

cases, tychoplanktonic and euplanktonic diatoms were also found in low abundances, indicating the presence of shallow, ephemeral water bodies in the clay pan during the time of deposition (Fig. 4). This pattern is interrupted at 406 cm (Fig. 4), where the percentage of aerophilic diatoms drops below 30%, and non-aerophilic benthic (e.g.,

Sample	Depth (m)	Environmental dose rate (Gy/ka)	Burial dose (Gy)	Age (ka)
PAG I-2	0.32	5.26 ± 0.23	81.6 ± 0.9	15.5 ± 0.7
PAG I-3	0.6	5.17 ± 0.23	115.0 ± 4.4	22.2 ± 1.3
PAG I-4	0.9	5.27 ± 0.23	115.0 ± 4.1	21.8 ± 1.2
PAG I-5	1.3	5.22 ± 0.24	188.0 ± 8.1	36.0 ± 2.3
PAG 6-2	1.7	4.38 ± 0.20	145.0 ± 3.0	33.1 ± 1.6
PAG 6-3a	2.25	4.85 ± 0.21	159.0 ± 2.8	32.8 ± 1.6
PAG 6-3b	2.64	4.85 ± 0.21	192.0 ± 3.5	39.6 ± 1.9
PAG 6-4b	3.59	4.47 ± 0.24	435.0 ± 13.0	97.3 ± 5.9
PAG 6-5a	4.03	3.89 ± 0.20	454.0 ± 24.0	116.8 ± 8.6
PAG 6-5b	4.52	3.50 ± 0.17	493.0 ± 14.0	140.8 ± 8.0
PAG 6-6b	5.40	3.90 ± 0.17	>534	>137
PAG 6-7b	6.20	3.55 ± 0.15	>712	>200

Table 1. Calculated dose rates and derived ages.

Cocconeis placentula Ehrenberg, *Tabularia fasciculata* (C. Agardh) D.M. Williams & Round), tychoplanktonic (e.g. *Fragilaria* spp.) and even euplanktonic species (mainly *Aulacoseira* spp.) reach their maximum abundances in the sequence. This sharp change in the diatom assemblage is compatible with deeper and more permanent lacustrine conditions in the clay pan. In the samples above 406 cm the diatom assemblage is again dominated by aerophilic taxa, illustrating the recurrence of the occasional presence of only shallow ephemeral water bodies. Aerophilic diatoms can inhabit a range of different subaerial or terrestrial habitats[32]. Among them, *Pinnularia borealis*, the main component of diatom assemblages in the upper part of the sediment sequence, seem to prefer the driest habitats[33]. It is one of the main freshwater algae taxa found in soil crusts of hot deserts around the world, i.e.[34], and its high relative abundances seems compatible with the existence of arid to hyper-arid conditions. We cannot differentiate between the allochthonous input from the catchment and the autochthonous presence of aerophilic diatoms. Detailed information about specific taxa distributions can be found in the Supplementary Dataset.

Core Chronology

Optically Stimulated Luminescence (OSL). The age-depth modelling followed a multi-faceted approach using OSL ages together with paleomagnetic tie points. OSL ages are based on the measurement of polymineralic fine-grained (4–11 µm) extracts of each sample, and were measured using post-infrared infrared stimulated luminescence at 225 °C (pIR-IR225[35]). The suitability of this protocol was determined through a series of dose recovery experiments. A fraction of each sample was bleached in a solar simulator and then either measured, to quantify the residual dose, or given a beta dose and then measured to calculate the recovered to given dose ratio. Samples show residual doses of between 1.9 and 6.7 Gy, which account for less than 3% of the respective burial doses across both signals. The recovered to given dose ratios are consistent with unity within 1σ for all samples. Both tests confirm the suitability of the protocol used.

All samples were screened for anomalous fading[36]. Fading measurements show an average fading rate (i.e. g-value) of <1.0%/decade for samples down to 500 cm depth, suggesting that fading correction is not required for these samples[35]. In contrast, the average g-value for the $pIRIR_{225}$ signal of the two samples below 500 cm, PAG6-6b and PAG6-7b, is 4.8%/decade and these samples have been fading corrected using the model of Huntley[37] and the approach of Kars, *et al.*[38]. The results show that the natural signal is above saturation of the corrected dose response curve (DRC), and thus only minimum ages based on $2D_0$ of the DRC can be estimated for these samples from deepest within the sediment core, Table 1. Final dose rates calculated and derived ages are summarized in Table 1. Measured radionuclide concentrations can be found in the Supplementary Dataset Table S1. The OSL ages are in stratigraphic order and are in agreement with the trends of the paleomagnetic chronology (Table 1, Fig. 5A), within 2σ uncertainties. The two stratigraphically lowest ages (PAG6-6b and PAG6-7b) are younger than the paleomagnetic tie points (Fig. 5C), which is due to the fact that these samples are in field-saturation.

Paleomagnetic data. Geomagnetic field excursions are short-term, usually a few thousands of years, periods of anomalous geomagnetic directional behavior that emerge from the mean 'background' normal secular variability of the Earth's magnetic field[39]. For the last normal magnetic Brunhes chron, up to 17 excursions are recorded[39]. Geomagnetic turn-overs are attended by relative paleointensity (RPI) minima[40]. This fact makes geomagnetic excursions a valuable tool to date sediment archives beyond the temporal range of ^{14}C and OSL dating. Characteristic directions (inclination) and amplitude changes of RPI proxy were used to identify age tie points to further constrain a reliable age-depth model (Fig. 5A,B). Global records indicate the occurrence of at least six geomagnetic excursions in the time interval between 15 and 250 ka, the relative age range of our record according to the OSL data (see Supplementary Dataset Table S2).

We used a multi-stage approach to identify geomagnetic excursion, taking into account the previously described OSL data, lithostratigraphy, and comparison of the measured RPI proxy to global RPI stacks[40,41]. Comparison of excursions and the RPI record from the clay pan to the global RPI stack PISO1500[40] and to the record of known excursions (e.g.[42]) were used to generate age-depth tie points (Fig. 5A,B). The comparison of

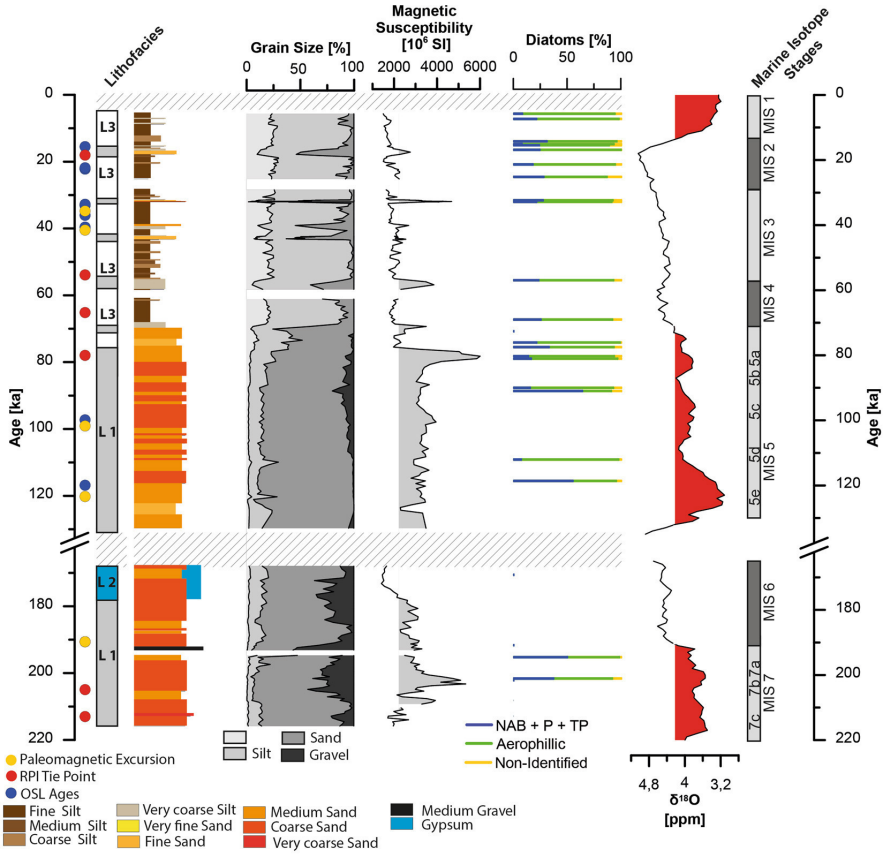

Figure 6. Lithofacies (L1, L2, L3), sediment types, grain size fractions (0–>6.3 mm), magnetic susceptibility (MS), and diatoms assemblages (non-aerophilic benthic (NAB), euplanktonic (P), tychoplanktonic (TP) in core PAG5/6 from the mud pan in the Atacama Desert, displayed against depth (for age-depth model see supplementary online material, coloured points mark age tie points) and the global deep-sea oxygen isotope stack with marine isotope stages from Lisiecki and Raymo[75].

both RPI records (this record vs. PISO1500) indicates that the occurrence of geomagnetic excursions mostly coincides with RPI lows, as recorded in other archives[40] (Fig. 5B).

Due to the complexity of the depositional environment, we have to assume phases of non-deposition or even erosion. The short durations of geomagnetic excursions have important consequences for the precision of sedimentary paleomagnetic recording, if the signal is acquired during low sedimentation rates. It implies that the recovered sediments may not have recorded all geomagnetic excursions and that RPI data will have gaps. Some geomagnetic excursions are reliably recorded, while others may not be recorded at all due to low sedimentation rates or even hiata[43].

We find five distinct anomalous inclination excursions in our record (Fig. 5A). These features are interpreted as coeval to global time markers such as the Mono Lake excursion (Depth: 171 cm, 33 ± 1 ka)[39,44], the Laschamp Event (Depth: 243 cm, 41 ± 1.5 ka[45]), the Post-Blake (Depth: 422 cm, 98 ± 2 ka[40]) and Blake Events (Depth: 486 cm 120.5 ± 1.5 ka[39,40]) and the Iceland-Basin excursion (Depth: 555 cm, 190.2 ± 1.77 ka[46]). An alternative assignment of one of the geomagnetic excursion, i.e. Blake excursion at 422 cm and subsequent shift of geomagnetic excursions, would indicate the occurrence of the Pringle Falls excursion (211 ± 1.5 ka[42]) at the lowest inclination excursion at 555 cm (Fig. 5A). This alternative assignment, however, results in an age-model that is in disagreement with the sedimentological findings (hiatus at the pedogenic gypsum horizon), we therefore do not consider it further (it is discussed in the supplementary data set). Note that application of the alternative assignment/age-model would not affect the main conclusions of this study (asynchonicity of wet phases in the Altiplano and the Coastal Cordillera; see below).

The identification and depth of Mono Lake is supported by an OSL (post-IR225) age at 33.1 +/− 1.6 ka (PAG 6-2). The Laschamp Event could be identified with very high confidence due to the proximal occurrence following

the Mono Lake excursion and characteristic RPI minima at 41 ka (PISO1500 and this record). The assignment of the inclination excursion to the Laschamp Event implies that the existing OSL ages in this part of the record are slightly too young (PAG 6-3a, PAG 6-3b). Inclination excursions at 422 cm and 486 cm can be attributed to the Post-Blake (98 +/− 2 ka) and the Blake Event (120.5 +/− 1.7 ka). Both excursions are marked by a characteristic RPI pattern of two minima in PISO1500 stack and our RPI record (~420–490 cm). This assignment to those discrete geomagnetic excursions leads to an age offset in OSL ages of up to 30 ka (Fig. 5C), implying potential incomplete pre-bleaching of the sediment during transport into the clay pan and insufficient resetting of the OSL signal. As the two OSL ages adjacent to the geomagnetic excursion at ~555 cm represent only minimum ages, we assign this excursion to the next known geomagnetic event, the Iceland Basin (190 ± 5 ka).

Comparing our record to PISO1500[40] using the Iceland Basin excursion, our RPI record fits the characteristic pattern of RPI during this time range (Fig. 5A,B). The comparison with the PISO-1500 RPI stack[40] yields partial agreement for the last 215 ka (Fig. 5B). This provides additional and independent support for the core chronology. We identified five RPI minima associated to geomagnetic excursions and additionally eight tie points related to characteristic RPI trends (Fig. 5B). A preliminary age-depth model was calculated using AnalySeries 2.0[47] and linear interpolation between assigned chronological tie points and calculated ages. With the data, age-depth sedimentation histories of the sediment record were modelled using the 'rBacon' (V2.3.3) Bayesian statistics approach of Blaauw and Christen[48] (Fig. 5C). OSL data and geomagnetic excursion tie points indicate two potential event layer and/or episodes of high sedimentation at around ~33 ka (PAG6-2, PAG6-3a, Mono Lake) and ~40 ka (Laschamp, PAG6-3b) related to coarser layers between 131–191 cm and 236–264 cm (Fig. 5C). The OSL age at 130 cm (PAGI-5 36 ± 1.6 ka) is slightly too old and is possibly influenced by partial bleaching.

OSL data and geomagnetic excursion tie points indicate an episode of low or lacking sedimentation between ~135–168 ka (depth ~500 cm). This episode is characterized in the global PISO1500 RPI stack by a broad RPI maxima, which could not be found in our RPI record (Fig. 5A,B). This discrepancy in the correlation/assignment of our record with the PISO stack, together with sedimentological evidence ('*costra*' gypsum crust as indication of surface activity stagnancy, Fig. 3) indicates the existence of a hiatus in our sediment record (including gypsum crust ~500–525 cm, ~135–180 ka). Additionally, we identified a smaller hiatus of a few thousand years at the top of the sediment record. The occurrence of other smaller hiata is possible, but cannot be resolved.

Paleoclimate and Sedimentation in the hyperarid Coastal Cordillera

According to the chronology of core PAG 5,6 the investigated sediment succession covers the transition of MIS 7 to MIS 6 until the early Holocene (Fig. 6). However, the sediment sequence is not continuous. Besides presumed multi-year sedimentation breaks between rain events, two major hiata occur, from early MIS 6 to the onset of MIS 5, and from the mid Holocene to present. Hiata in the record may represent either erosion of fluvial sediments in the terminal pan and/or a paucity of sediment transported into the pan.

The sediments covering the end of MIS 7 until MIS 6, are dominated by coarse sand, e.g. high fluvial energy reflecting an allochthonous signal (Lithofacies 1; Fig. 6). The diatom assemblages found in these sediments are mostly composed of euplanktonic, tychoplanktonic and non-aerophilic benthic taxa, thus indicating water depths of a few metres at the time of deposition. Their occurrence in coarse-grained sediments points to high-energy discharge events of the main tributaries of the ephemeral lake, that created lacustrine environments favourable for non-aerophilic diatoms. A pedogenic gypsum crust in the uppermost ~25–30 cm of these coarse sediments (Lithofacies 2) marks a ~50 ka hiatus during the remainder of MIS 6.

Sedimentation resumed during the last interglacial (MIS 5e). Sand-sized sediments (Lithofacies 1) indicate high-energetic supply to the pan. However, the energy-level presumably was lower than during late MIS 7 and early MIS 6, as suggested by significantly lower concentrations of the coarse sand and gravel fractions (Fig. 6). The diatom assemblages in the MIS 5e deposits are variable. Euplanktonic, tychoplanktonic and non-aerophilic benthic diatoms characteristic of permanent/more evolved lacustrine water conditions, have total relative abundances > 50% during MIS 5e and MIS 5b. By contrast, aerophilic diatoms, typical of very shallow ephermal ponds, wet soils, or nearshore wetlands subjected to desiccation, dominate the assemblages during MIS 5d and MIS 5a-b.

Towards MIS 4 and throughout the Holocene, the sands are progressively replaced by finer, silt-sized deposits (Lithofacies 3), which along with the overall dominance of aerophilic diatoms indicate a period of reduced fluvial activity with temporary lacustrine conditions in shallow ponds (Fig. 6). Interspersed coarser sediments (Lithofacies 1) at ~33 and 40 ka, may indicate intense flooding events of the pan. The latter scenario could have its present analogue in the occurrence of lacustrine conditions after a major rain event in the Atacama Desert during the El Niño in 1997/98 creating a temporary lake in the Sechura Desert of southern Peru[49], or in the occurrence of small ponds and lagoons after anomalous rain events in 2017 in the Yungay area of the Atacama Desert[50].

In general, the dominance of benthic and aerophilic species with meso-polysaline to eurytopic salinity optima suggest episodes with shallow ephemeral ponds where elevated evaporation rates prompted higher salinity conditions. Those ponds could have originated from less frequent and small rain events. The co-occurrence of peaks in the relative abundances of euplanktonic and tychoplanktonic species with peaks in the sand fraction detected in the lithostratigraphy indicate that a higher water table resulted from abrupt flooding. Regular rain events would have enabled the recurrence of more permanent water bodies and development of pelagic habitats. The presence of phytolith remains in samples containing diatoms further suggests that the environment surrounding the clay pan was at least temporally/partially covered by grass, in contrast to the present day barren landscape (Fig. 4). Overall, the sediment record clearly indicates a higher fluvial activity and sediment deposition during interglacial and interstadial stages (MIS 7, MIS 5, Figs 6 and 7) as compared to glacial/interglacial stages. A large interjacent hiatus, which we assign to MIS 6, indicates conditions of enhanced aridity in the catchment of the pan, by the absence of fluvial activity and deposition (Fig. 6).

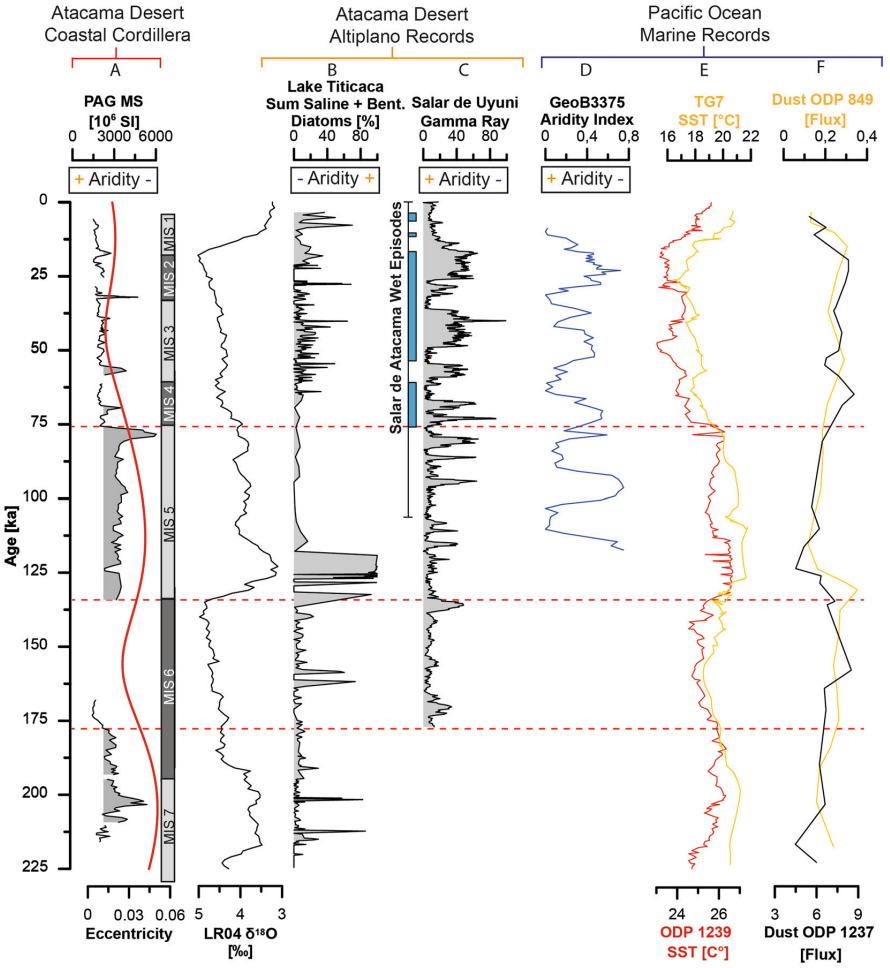

Figure 7. Paleoclimate record of fluvial episodes of the terminal pan record compared to selected regional and over regional terrestrial and marine paleo-records. (**A**) Magnetic susceptibility record and local eccentricity red line[76]. (**B**) Global deep-sea oxygen isotope stack[75]. (**C**) Lake Titicaca summation plot of saline and benthic diatoms species[26]. (**D**) Salar de Uyuni gamma-ray record[77] and wet episodes from Salar de Atacama[54]. (**E**) Aridity index (27°S) reconstructed by Stuut and Lamy[57]. (**F**) SST reconstructions from the East Pacific at 17°S TG7[61], and equatorial Pacific ODP 1239[59]. (**G**) Dust flux records from 16°S[60] and the equatorial Pacific[62].

Regional climate records

We observe in our record an inverse correlation of wetter phases (Fig. 7) compared to high-resolution mid to late Pleistocene climate records from the Altiplano, Lake Titicaca, and adjacent lacustrine lakes and salars (Fig. 1A,B; e.g.[51–54]). Climate fluctuations in the Altiplano have been related to eccentricity-paced glacial-interglacial cycles, with glacials generally characterized by higher water input in lacustrine systems, whereas interglacials are generally indicated by drier conditions (Fig. 7; e.g.[51–54]). These changes coincide with variations in the intensity of the South American summer monsoon[53]. Furthermore, a causing factor for changing lacustrine conditions can be related to 'El Nino Southern Oscillation' (ENSO) changes, where warm events (El Niño-like conditions) supress moisture transport over much of the Altiplano[26]. Whereas the PAG record implies wetter phases in the Coastal Cordillera during MIS 7 and 5e, the Altiplano synchronously experienced pronounced arid conditions (Fig. 7). In contrast, during MIS 4 to MIS 1, aridity in the Coastal Cordillera was more enhanced while wetter conditions prevailed in the Altiplano, including large lake phases[51–54] (Fig. 7).

A recent compilation of paleowetlands and paleolakes, covering the last <50 ka, from the Central Depression[25], just a few 10 s of km away to the east (Fig. 1A), reveals a similar pattern and dependency on wetter episodes in the Altiplano, especially of the Central Andean Pluvial Events (CAPE, 17.5–14.2 ka, 13.8–9.7 ka[25]). Those paleowetlands were groundwater-fed by precipitation collected in the high Andes to the east[25]. The Coastal

Cordillera is mostly hydrologically disconnected from the Central Depression and thus ground and surface water sourced from the Andes to the east does not reach Coastal Cordillera drainage systems. Despite the near proximity of our Coastal Cordilleran record and paleowetlands in the Central Depression[25] (Fig. 1A), we cannot observe any significant fluvial activity in the Coastal Cordillera during the CAPE, which further underlines the particular position of our record within the Costal Cordillera and its valuable potential to record the regional climate of the hyperarid core. Wetter stages in the Coastal Cordillera must be rather controlled by moisture advection, which could reach the Coastal Cordillera and would provide enough precipitation within closed and smaller catchments therein. This setting can explain most likely the opposite trend found of arid/wet episodes in the Coastal Cordillera compared to those of the Altiplano and Central Depression (Figs 1A and 7). We conclude that the paleoclimate signal in the Coastal Cordillera, indicates past autochthonous precipitation signals.

Comparing our record to near-shore and distal marine drill-cores[28,55,56], some dependencies become apparent (Figs 1B and 7). Stuut and Lamy[57] reconstructed, based on grain size end-member data, a paleo-aridity index for northern Chile (27°S). They relate changes in continental aridity to changes in the latitudinal position of moisture-bearing Southern Westerlies, which could be driven by sea-ice extent around Antarctica and stimulated by tropical forcing in the equatorial Pacific Ocean. Strong rainfall events (positive index) are related to the occurrence of El Niño-like conditions, due to a weakening and northward displacement of the SE Pacific anticyclone[58]. Alternating wetter episodes during MIS5 reconstructed by Stuut and Lamy[57] cannot be resolved in our record, where the entire MIS 5 is characterized by higher fluvial activity (Fig. 7). Due to the low temporal resolution of our record, short-term episodes of higher fluvial activity cannot be resolved with accuracy. We cannot observe any similarities between the aridity index and our record during the time period from MIS 4-MIS 1. Thus, we conclude that the aridity index from Stuut and Lamy[57] does not represent the paleoclimate conditions for the hyperarid section of the Coastal Cordillera.

Marine records from offshore Peru and Ecuador (ODP1239, ODP849, ODP1237, TG7 Fig. 1B[59–62]), cover the last 225 ka (Fig. 7). Rincón-Martínez, *et al.*[59] used paleo sea surface temperatures (SST) and sedimentological proxies, to identify a predominance of El Niño-like conditions off the coast of Ecuador during interglacial times with higher continental moisture advection and runoff; whereas glacial times are characterized by predominantly La Niña-like conditions. Similar SST reconstruction were published by Calvo, *et al.*[61] from the more southern Nazca ridge (17°S). Warmer SST can be connected to a warmer East Equatorial Pacific cold tongue and a southward shift of the equatorial front ITCZ system. A 'rainy' northern Atacama Desert was inferred using terrigenous biomarkers from marine sediments off Peru OPD 1229, 11°S[56]. Aeolian dust input into the near-shore Pacific Ocean off Peru ODP 1237[60], and in the equatorial Pacific ODP 849[62], indicates higher dust availability and deposition during glacial times (Fig. 7[60]). The fluctuations in the extent of arid and barren surface areas as sources of aeolian dust, accompanied with a meridional shift of the atmospheric circulation system in the Southeast Pacific, can be seen as the driving force for the variability in dust input in the East Pacific. Comparison of SSTs off Peru and Ecuador[59,61] with our record, reveals a close synchronicity of rising SSTs and enhanced water availability in our study area. (Fig. 7). Higher SSTs are reconstructed for MIS 7, the onset of MIS 5e and most of the remaining MIS 5, accompanied by a sharp drop during MIS 4 and an increase towards the transition from MIS 3 to MIS 2. Only the most recent increase in SSTs during the Holocene is not preserved in our record (Fig. 7). Decreasing aeolian dust deposition in the East Pacific during MIS 7, onset and remaining of MIS 5[60] can be connected to reconstructed wetter episodes in the Coastal Cordillera and higher SSTs in the East Pacific[59]. Recent climate models, simulating past precipitation events in the Atacama Desert, which controlled the floods in 2015, indicate that both, the northward moving cut-off low systems, and the existence of anomalous high SSTs off the coast of Chile are instrumental for high-intensity precipitation events[19].

The paleoclimate reconstruction for the Coastal Cordillera indicates an opposite trend of moisture availability compared to continental Atacama/Altiplano records, which are mostly influenced by moisture advection from Atlantic air masses and precipitation in the high Andes (Fig. 7). This shows the separation of moisture sources affecting the Coastal Cordillera drainage systems. Coincidence with paleoclimate records from the marine Pacific, points to a connection of 'wetter' episodes in the Coastal Cordillera with increased SSTs off Chile/Peru during interglacial times (Fig. 7). Our reconstruction indicates that moist periods, characterized by enhanced fluvial activity within the catchment that carries coarse sand into an ephemeral lake, predominantly occurred during interglacial times, whereas dry periods, with subdued sedimentation of fine sediments took place during glacial times. The glacial-interglacial alternation during MIS 7 and MIS 5 mimics an eccentricity paced control on moisture in the Coastal Cordillera (Fig. 7).

Conclusion

For the first time, we provide a paleoclimate record of the hyperarid core of the Atacama Desert from a clay pan in the Coastal Cordillera spanning the last 215 ka. Within the limits of the age model, the paleoclimate reconstruction points to wetter episodes with higher fluvial activity during MIS 7 and MIS 5 and reduced fluvial activity since MIS 4. Wetter periods in this section of the Coastal Cordillera are largely synchronous with enhanced East Pacific SST (conditions similar to modern 'El Niño'), but are asynchronous with wet periods in the Altiplano, which can be explained by the different moisture sources (Pacific vs. Atlantic). During drier, glacial times low but still present sedimentation of mostly fine-grained material occurs, demonstrating that also during hyperarid conditions there is some surface activity in the study area, probably related to single rain events. Exceptions are large parts of the MIS 6 glacial period, when the absence of fluvial activity in the catchment caused a hiatus of more than 50 kyr in the record.

Methods

To determine the sediment thickness in the terminal basin we conducted a GPR survey using a 100 MHz antenna with GSSI SIR-3000 system. For deeper penetration we utilized H/V ambient-noise seismometry. During two field campaigns in 2014 and 2015 two overlapping sediment cores (PAG 5, 6), with a maximum length of 6.2 m, were recovered using hand-held percussion drilling system (Eijkelkamp). Sediment cores were retrieved in opaque plastic liners. The unopened cores were analysed for their paleomagnetic properties, including inclination, declination and relative paleo-intensity, at LIAG (Grubenhagen). The elemental composition of the samples was determined using a ITRAX XRF core scanner (Cox Analytical Systems) at the University of Cologne and subsequently subsampled with a 2 cm resolution. Magnetic susceptibility was measured using a Kappa-Bridge KLY2 (Agico) sensor. GSD (<2 mm) were analysed, after a cation exchange pre-treatment to correct for gypsum, using a Beckman Coulter LS13320 laser particle sizer and evaluated using GRADISTAT[63]. Coarser grain sizes (>2 mm) were quantitatively affiliated. Diatom analysis was performed on 28 sediment samples. The age-depth model was obtained combining OSL (University of Cologne) and paleomagnetic data using AnalySeries V. 2.0[47]; and Bayesian statistics using 'Bacon'[48]. Further information and details on the applied methods are provided in the supplementary dataset.

References

1. Houston, J. Variability of precipitation in the Atacama Desert: its causes and hydrological impact. *International Journal of Climatology* **26**, 2181–2198, https://doi.org/10.1002/joc.1359 (2006).
2. Takahashi, K. & Battisti, D. S. Processes controlling the mean tropical Pacific precipitation pattern. Part II: The SPCZ and the southeast Pacific dry zone. *Journal of Climate* **20**, 5696–5706 (2007).
3. Houston, J. & Hartley, A. J. The Central Andean west-slope rainshadow and its potential contribution to the origin of hyper-aridity in the Atacama desert. *International Journal of Climatology* **23**, 1453–1464 (2003).
4. Garreaud, R. D., Vuille, M., Compagnucci, R. & Marengo, J. Present-day South American climate. *Palaeogeography Palaeoclimatology Palaeoecology* **281**, 180–195, https://doi.org/10.1016/j.palaeo.2007.10.032 (2009).
5. Garreaud, R. D., Molina, A. & Farias, M. Andean uplift, ocean cooling and Atacama hyperaridity: A climate modeling perspective. *Earth and Planetary Science Letters* **292**, 39–50, https://doi.org/10.1016/j.epsl.2010.01.017 (2010).
6. Rech, J. A. *et al.* Evidence for the development of the Andean rain shadow from a Neogene isotopic record in the Atacama Desert, Chile. *Earth and Planetary Science Letters* **292**, 371–382, https://doi.org/10.1016/j.epsl.2010.02.004 (2010).
7. Houston, J. Evaporation in the Atacama Desert: An empirical study of spatio-temporal variations and their causes. *Journal of Hydrology* **330**, 402–412, https://doi.org/10.1016/j.jhydrol.2006.03.036 (2006).
8. Nishiizumi, K., Caffee, M. W., Finkel, R. C., Brimhall, G. & Mote, T. Remnants of a fossil alluvial fan landscape of Miocene age in the Atacama Desert of northern Chile using cosmogenic nuclide exposure age dating. *Earth and Planetary Science Letters* **237**, 499–507, https://doi.org/10.1016/j.epsl.2005.05.032 (2005).
9. Kober, F. *et al.* Denudation rates and a topography-driven rainfall threshold in northern Chile: Multiple cosmogenic nuclide data and sediment yield budgets. *Geomorphology* **83**, 97–120 (2007).
10. Placzek, C. J., Matmon, A., Granger, D. E., Quade, J. & Niedermann, S. Evidence for active landscape evolution in the hyperarid Atacama from multiple terrestrial cosmogenic nuclides. *Earth and Planetary Science Letters* **295**, 12–20, https://doi.org/10.1016/j.epsl.2010.03.006 (2010).
11. Dunai, T. J., González López, G. A. & Juez-Larré, J. Oligocene–Miocene age of aridity in the Atacama Desert revealed by exposure dating of erosion-sensitive landforms. *Geology* **33**, 321, https://doi.org/10.1130/g21184.1 (2005).
12. Evenstar, L. *et al.* Geomorphology on geologic timescales: Evolution of the late Cenozoic Pacific paleosurface in Northern Chile and Southern Peru. *Earth-Science Reviews* (2017).
13. Rech, J. A., Currie, B. S., Michalski, G. & Cowan, A. M. Neogene climate change and uplift in the Atacama Desert, Chile. *Geology* **34**, 761–764, https://doi.org/10.1130/g22444.1 (2006).
14. Hartley, A. J. & Chong, G. Late Pliocene age for the Atacama Desert: Implications for the desertification of western South America. *Geology* **30**, 43–46 (2002).
15. Sillitoe, R. H. & McKee, E. H. Age of supergene oxidation and enrichment in the Chilean porphyry copper province. *Economic Geology* **91**, 164–179 (1996).
16. Latorre, C., Betancourt, J. L. & Arroyo, M. T. K. Late Quaternary vegetation and climate history of a perennial river canyon in the Río Salado basin (22°S) of Northern Chile. *Quaternary Research* **65**, 450–466, https://doi.org/10.1016/j.yqres.2006.02.002 (2006).
17. Rech, J. A., Quade, J. & Hart, W. S. Isotopic evidence for the source of Ca and S in soil gypsum, anhydrite and calcite in the Atacama Desert, Chile. *Geochim. Cosmochim. Acta* **67**, 575–586 (2003).
18. Nester, P. L., Gayo, E., Latorre, C., Jordan, T. E. & Blanco, N. Perennial stream discharge in the hyperarid Atacama Desert of northern Chile during the latest Pleistocene. *Proceedings of the National Academy of Sciences of the United States of America* **104**, 19724–19729, https://doi.org/10.1073/pnas.0705373104 (2007).
19. Bozkurt, D., Rondanelli, R., Garreaud, R. & Arriagada, A. Impact of Warmer Eastern Tropical Pacific SST on the March 2015 Atacama Floods. *Monthly Weather Review* **144**, 4441–4460 (2016).
20. Wilcox, A. C. *et al.* An integrated analysis of the March 2015 Atacama floods. *Geophysical Research Letters* **43**, 8035–8043 (2016).
21. Betancourt, J., Latorre, C., Rech, J., Quade, J. & Rylander, K. A 22,000-year record of monsoonal precipitation from northern Chile's Atacama Desert. *Science* **289**, 1542–1546 (2000).
22. Gayo, E. M. *et al.* Late Quaternary hydrological and ecological changes in the hyperarid core of the northern Atacama Desert (~21°S). *Earth-Science Reviews* **113**, 120–140, https://doi.org/10.1016/j.earscirev.2012.04.003 (2012).
23. Maldonado, A., Betancourt, J. L., Latorre, C. & Villagran, C. Pollen analyses from a 50 000-yr rodent midden series in the southern Atacama Desert (25° 30′ S). *Journal of Quaternary Science* **20**, 493–507, https://doi.org/10.1002/jqs.936 (2005).
24. Quade, J. *et al.* Paleowetlands and regional climate change in the central Atacama Desert, northern Chile. *Quaternary Research* **69**, 343–360, https://doi.org/10.1016/j.yqres.2008.01.003 (2008).
25. Pfeiffer, M. *et al.* Chronology, stratigraphy and hydrological modelling of extensive wetlands and paleolakes in the hyperarid core of the Atacama Desert during the late quaternary. *Quaternary Science Reviews* **197**, 224–245 (2018).
26. Fritz, S. C. *et al.* Quaternary glaciation and hydrologic variation in the South American tropics as reconstructed from the Lake Titicaca drilling project. *Quaternary Research* **68**, 410–420, https://doi.org/10.1016/j.yqres.2007.07.008 (2007).
27. Lamy, F., Hebbeln, D. & Wefer, G. Late Quaternary precessional cycles of terrigenous sediment input off the Norte Chico, Chile (27.5°S) and palaeoclimatic implications. *Palaeogeography, Palaeoclimatology, Palaeoecology* **141**, 233–251 (1998).
28. Lamy, F., Klump, J., Hebbeln, D. & Wefer, G. Late Quaternary rapid climate change in northern Chile. *Terra Nova* **12**, 8–13 (2000).
29. Skarmeta, J. & Marinovic, N. *Hoja Quillagua: región de Antofagasta: carta geológica de Chile escala 1: 250.000*. (Instituto de Investigaciones Geológicas, 1981).
30. Allmendinger, R. W., Gonzalez, G., Yu, J., Hoke, G. & Isacks, B. Trench-parallel shortening in the Northern Chilean Forearc: Tectonic and climatic implications. *Geological Society of America Bulletin* **117**, 89–104, https://doi.org/10.1130/B25505.1 (2005).

31. Ritter, B. *et al.* Neogene fluvial landscape evolution in the hyperarid core of the Atacama Desert. *Scientific Reports* **8**, 13952, https://doi.org/10.1038/s41598-018-32339-9 (2018).
32. Johansen, J. R. Diatomsofaerial habitats. *The diatoms: applications for the environmental and earth sciences*, **465** (2010).
33. Van de Vijver, B., Beyens, L., Vincke, S. & Gremmen, N. J. Moss-inhabiting diatom communities from Heard Island, sub-Antarctic. *Polar biology* **27**, 532–543 (2004).
34. Rosentreter, R. & Belnap, J. *Biological Soil Crusts: Structure, Function, and Management. USGS Canyonlands Research Station, Moab*, UT 84532 (2003).
35. Buylaert, J. P. *et al.* A robust feldspar luminescence dating method for Middle and Late Pleistocene sediments. *Boreas* **41**, 435–451 (2012).
36. Spooner, N. A. The anomalous fading of infrared-stimulated luminescence from feldspars. *Radiation Measurements* **23**, 625–632 (1994).
37. Huntley, D. An explanation of the power-law decay of luminescence. *Journal of Physics: Condensed Matter* **18**, 1359 (2006).
38. Kars, R., Wallinga, J. & Cohen, K. A new approach towards anomalous fading correction for feldspar IRSL dating—tests on samples in field saturation. *Radiation Measurements* **43**, 786–790 (2008).
39. Lund, S., Stoner, J. S., Channell, J. E. & Acton, G. A summary of Brunhes paleomagnetic field variability recorded in Ocean Drilling Program cores. *Physics of the Earth and Planetary Interiors* **156**, 194–204 (2006).
40. Channell, J., Xuan, C. & Hodell, D. Stacking paleointensity and oxygen isotope data for the last 1.5 Myr (PISO-1500). *Earth and Planetary Science Letters* **283**, 14–23 (2009).
41. Stoner, J., Laj, C., Channell, J. & Kissel, C. South Atlantic and North Atlantic geomagnetic paleointensity stacks (0–80 ka): implications for inter-hemispheric correlation. *Quaternary Science Reviews* **21**, 1141–1151 (2002).
42. Laj, C. & Channell, J. Geomagnetic excursions, *in Treatise on Geophysics. Geomagnetism* **5**, 373–416 (2007).
43. Roberts, A. P. & Winklhofer, M. Why are geomagnetic excursions not always recorded in sediments? Constraints from post-depositional remanent magnetization lock-in modelling. *Earth and Planetary Science Letters* **227**, 345–359 (2004).
44. Channell, J. Late brunhes polarity excursions (mono lake, laschamp, iceland basin and pringle falls) recorded at odp site 919 (Irminger basin). *Earth and Planetary Science Letters* **244**, 378–393 (2006).
45. Channell, J., Riveiros, N. V., Gottschalk, J., Waelbroeck, C. & Skinner, L. Age and duration of Laschamp and Iceland Basin geomagnetic excursions in the South Atlantic Ocean. *Quaternary science reviews* **167**, 1–13 (2017).
46. Channell, J. The Iceland Basin excursion: Age, duration, and excursion field geometry. *Geochemistry, Geophysics, Geosystems* **15**, 4920–4935 (2014).
47. Paillard, D., Labeyrie, L. & Yiou, P. AnalySeries 1.0: a Macintosh software for the analysis of geophysical time-series. *Eos* **77**, 379 (1996).
48. Blaauw, M. & Christen, J. A. Flexible paleoclimate age-depth models using an autoregressive gamma process. *Bayesian analysis* **6**, 457–474 (2011).
49. Woodman, R. F. Los lagos de Sechura. *Informe Interno del Instituto Geofisico del Perú* (1998).
50. Azua-Bustos, A. *et al.* Unprecedented rains decimate surface microbial communities in the hyperarid core of the Atacama Desert. *Scientific reports* **8**, 16706 (2018).
51. Baker, P. A. *et al.* Tropical climate changes at millennial and orbital timescales on the Bolivian Altiplano. *Nature* **409**, 698–701 (2001).
52. Fritz, S. C., Baker, P., Tapia, P., Spanbauer, T. & Westover, K. Evolution of the Lake Titicaca basin and its diatom flora over the last ~370,000 years. *Palaeogeography, Palaeoclimatology, Palaeoecology* **317**, 93–103 (2012).
53. Baker, P. A. & Fritz, S. C. Nature and causes of Quaternary climate variation of tropical South America. *Quaternary Science Reviews* **124**, 31–47 (2015).
54. Bobst, A. L. *et al.* A 106 ka paleoclimate record from drill core of the Salar de Atacama, northern Chile. *Palaeogeography, Palaeoclimatology, Palaeoecology* **173**, 21–42 (2001).
55. Ho, S. L. *et al.* Sea surface temperature variability in the Pacific sector of the Southern Ocean over the past 700 kyr. *Paleoceanography* **27**, https://doi.org/10.1029/2012pa002317 (2012).
56. Contreras, S. *et al.* A rainy northern Atacama Desert during the last interglacial. *Geophysical Research Letters* **37** (2010).
57. Stuut, J. B. W. & Lamy, F. Climate variability at the southern boundaries of the Namib (Southwestern Africa) and Atacama (northern Chile) coastal deserts during the last 120,000 yr. *Quaternary Research* **62**, 301–309, https://doi.org/10.1016/j.yqres.2004.08.001 (2004).
58. Rutllant, J. & Fuenzalida, H. Synoptic aspects of the central Chile rainfall variability associated with the Southern Oscillation. *International Journal of Climatology* **11**, 63–76 (1991).
59. Rincón-Martínez, D. *et al.* More humid interglacials in Ecuador during the past 500 kyr linked to latitudinal shifts of the equatorial front and the Intertropical Convergence Zone in the eastern tropical Pacific. *Paleoceanography* **25** (2010).
60. Saukel, C. *Tropical Southeast Pacific Continent-Ocean-Atmosphere Linkages Since the Pliocene Inferred from Eolian Dust* PhD thesis, University of Bremen, (2011).
61. Calvo, E., Pelejero, C., Herguera, J. C., Palanques, A. & Grimalt, J. O. Insolation dependence of the southeastern Subtropical Pacific sea surface temperature over the last 400 kyrs. *Geophysical Research Letters* **28**, 2481–2484 (2001).
62. Winckler, G., Anderson, R. F., Fleisher, M. Q., McGee, D. & Mahowald, N. Covariant glacial-interglacial dust fluxes in the equatorial Pacific and Antarctica. *science* **320**, 93–96 (2008).
63. Blott, S. J. & Pye, K. GRADISTAT: a grain size distribution and statistics package for the analysis of unconsolidated sediments. *Earth surface processes and Landforms* **26**, 1237–1248 (2001).
64. Betancourt, J. L., Latorre, C., Rech, J. A., Quade, J. & Rylander, K. A. A 22,000-year record of Monsoonal precipitation from Northern Chile's Atacama Desert. *Science* **289**, 1542–1546 (2000).
65. Latorre, C. *et al.* Late Pleistocene human occupation of the hyperarid core in the Atacama Desert, northern Chile. *Quaternary Science Reviews* **77**, 19–30, https://doi.org/10.1016/j.quascirev.2013.06.008 (2013).
66. Sun, T., Bao, H., Reich, M. & Hemming, S. R. More than Ten Million Years of Hyper-aridity recorded in the Atacama Gravels. *Geochimica et Cosmochimica Acta* (2018).
67. Jordan, T. E. *et al.* modification in response to repeated onset of hyperarid paleoclimate states since 14 Ma, Atacama Desert, Chile. *Geological Society of America Bulletin*, https://doi.org/10.1130/b30978.1 (2014).
68. Sáez, A., Godfrey, L. V., Herrera, C., Chong, G. & Pueyo, J. J. Timing of wet episodes in Atacama Desert over the last 15 ka. The Groundwater Discharge Deposits (GWD) from Domeyko Range at 25°S. *Quaternary Science Reviews* **145**, 82–93 (2016).
69. Amundson, R. *et al.* Geomorphologic evidence for the late Pliocene onset of hyperaridity in the Atacama Desert. *Geological Society of America Bulletin* **124**, 1048–1070, https://doi.org/10.1130/b30445.1 (2012).
70. Carrizo, D., Gonzalez, G. & Dunai, T. Neogene constriction in the northern Chilean Coastal Cordillera: Neotectonics and surface dating using cosmogenic 21Ne. *Revista Geologica De Chile* **35**, 1–38 (2008).
71. Evenstar, L. A. *et al.* Multiphase development of the Atacama Planation Surface recorded by cosmogenic 3He exposure ages: Implications for uplift and Cenozoic climate change in western South America. *Geology* **37**, 27–30, https://doi.org/10.1130/g25437a.1 (2009).
72. González, G., Dunai, T. J., Carrizo, D. & Allmendinger, R. Young displacements on the Atacama Fault System, northern Chile from field observations and cosmogenic Ne-21 concentrations. *Tectonics* **25**, https://doi.org/10.1029/2005TC001846 (2006).

73. Jungers, M. C. *et al.* Active erosion–deposition cycles in the hyperarid Atacama Desert of Northern Chile. *Earth and Planetary Science Letters* **371–372**, 125–133, https://doi.org/10.1016/j.epsl.2013.04.005 (2013).
74. Owen, J. *et al.* In *AGU Fall Meeting* Vol. 84(46) Fall meeting Suppl. Abstract T31C- 0857 (2003) (AGU, San Francisco, 2003).
75. Lisiecki, L. & Raymo, M. E. A Pliocene-Pleistocene stack of 57 globally distibuted benthic d18O-records. *Paleoceonography* 20, PA1003, 1010.1029/2004PA001071 (2005).
76. Berger, A. Long-term variations of daily insolation and Quaternary climatic changes. *Journal of the Atmospheric Sciences* **35**, 2362–2367 (1978).
77. Fritz, S. C. *et al.* Hydrologic variation during the last 170,000 years in the southern hemisphere tropics of South America. *Quaternary Research* **61**, 95–104 (2004).

Acknowledgements

Thanks go to the field campaign groups in 2014 and 2015 and to all colleagues and students who helped analysing all the material. Special thanks go to Dorothea Klinghardt and Nicole Mantke for their support in the quaternary lab. Moreover, we would like to thank Eduardo Campos and colleagues at the Universidad Catolica del Norte in Antofagasta for their support. Funded by the Deutsche Forschungsgemeinschaft (DFG, German Research Foundation) – Projektnummer 268236062 – SFB 1211.

Author Contributions

B.R.: fieldwork, sediment sample preparation, sample measurement & data evaluation, manuscript writing. V.W.: fieldwork, paleomagnetic data acquisition, data evaluation. D.B., A.M. and G.K. OSL dating and data evaluation. S.S. and K.N. GPR and H/V seismic measurements and evaluation. E.F.G. and R.B. diatom analysis. J.D. fieldwork, sample measurements. C.R. paleomagnetic analysis. M.M. supervision of this project. T.J.D. supervision of this project and manuscript writing.

Additional Information

Supplementary information accompanies this paper at https://doi.org/10.1038/s41598-019-41743-8.

Competing Interests: The authors declare no competing interests.

Publisher's note: Springer Nature remains neutral with regard to jurisdictional claims in published maps and institutional affiliations.

Supplementary Material

"Climatic fluctuations of the hyperarid core of the Atacama Desert during the past 215 ka"

Benedikt Ritter [1], Volker Wennrich [1], Alicia Medialdea Utande[2], Dominik Brill [2], Georgina King [3], Sascha Schneiderwind [4], Karin Niemann [4], Emma Fernández-Galego [1], Julia Diederich [1], C. Rolf [5], Roberto Bao [6], Martin Melles [1], Tibor J. Dunai [1]

[1] Institute of Geology & Mineralogy – University of Cologne, Cologne, Germany

[2] Institute of Geography – University of Cologne, Cologne, Germany

[3] Institute of Earth Surface Dynamics – University of Lausanne, Lausanne, Switzerland

[4] Institute of Neotectonics and Natural Hazards - RWTH Aachen University, Aachen, Germany

[5] Leibniz Institute for Applied Geophysics (LIAG), Hannover, Germany

[6] Centro de Investigacións Científicas Avanzadas (CICA), Facultade de Ciencias, Universidade da Coruña, Spain

*Correspondence to benedikt.ritter@uni-koeln.de

1. Methods

1.1. Geophysical Site Survey

At the terminal pan, 35 ground-penetrating radar (GPR) profiles extending to approx. 23 km were obtained using a GSSI 100 MHz antenna (+survey wheel) and a GSSI SIR-3000 system. For spatial referencing the profiles were GPS-tracked. Data pre-processing using the REFLEXW ® software Version 7.2, [1], includes tools to enhance visibility of subsurface structures. In general, the processing includes start time correction, background removal, manual gain adjustments, and 1D-filtering followed by topographic correction. Afterwards, transition layers were picked in each profile and stored as xyz-point data, where x and y represent global UTM coordinates and z is the layer depth delineated by the two-way-travel time of the electromagnetic waves and their velocity in the ground. The point data depict measurements of a surface that can be estimated by interpolation functions provided in the Matlab Curve Fitting ToolboxTM including outlier removal, splines, and biharmonic fitting. The resulting surface function was applied to an artificial point cloud dataset with point spacing of 5 m and for a better visualisation transformed into a raster format of 5 m resolution in ArcGIS.

For further estimation of total sediment thickness and bedrock contact of the basin, the horizontal-to-vertical (H/V) ambient-noise seismic method was applied, which was originally proposed by Nogoshi and Igarashi [2] and widely applied by Nakamura [3]. A seismic profile (NNW-SSW) with up to 16 noise measurements across the clay pan was conducted. Recording the resonance frequencies of basin deposits with a Lennartz LE3D5s seismometer and a LEAS City Shark II data logger was carried out with a 200 Hz sampling rate and 30 min sampling duration. In order to avoid disturbances by external influences (wind), the seismometer was installed in a small hole.

Processing steps and peak evaluation using GEOPSY processing software were carried out according to Acerra, et al. [4]. H/V ratios were calculated from time windows of min. 20 s to max. 40 s length extracted from raw data. Calculation of soft-layer thickness (h) for each measurement was made on the assumption that resonance occurs at frequencies (fr), where uneven multiples of $\lambda/4$ fit the layer's thickness (h). For constant S-wave velocity in sediment layers' resonance occurs at:

$$f_r = \frac{v_{S,clay}}{4 * h_r}$$

hr depth of transition between hard and soft rock [m]

vS,clay approx. shear wave velocity in clay (≈ 300 m/s) [m/s]

fr fundamental frequency (derived by H/V ratios) [Hz]

Calibrating with GPR measurements to approximate average shear wave velocity vS, clay failed due to hard cover of the first few cm of sediments and low impedance contrasts between sediment layers. An approximation of shear wave velocity with respect to a reference value [5,6] was used. Calculation of h was done according to (z = altitude):

$$h = z - h_r.$$

1.2. Drilling

In 2014 and 2015 the uppermost 6.2 m (Composite of PAG 5 and 6) of the sediment record in the central part of the clay pan have been recovered by hand-held percussion drilling system (Eijkelkamp). Opaque liners were used to avoid any UV radiation destroying the luminescence signal. Whole-core scanning was conducted at the University of Cologne (Multi-Sensor-Core Logger for magnetic susceptibility for further paleomagnetic analysis, Institute of Geology & Mineralogy) and at the Leibniz Institute for Applied Geophysics (Paleomagnetic). Subsampling was carried out with a sample resolution of 2 cm. Gaps in the sediment record are due to recovery loss during drilling.

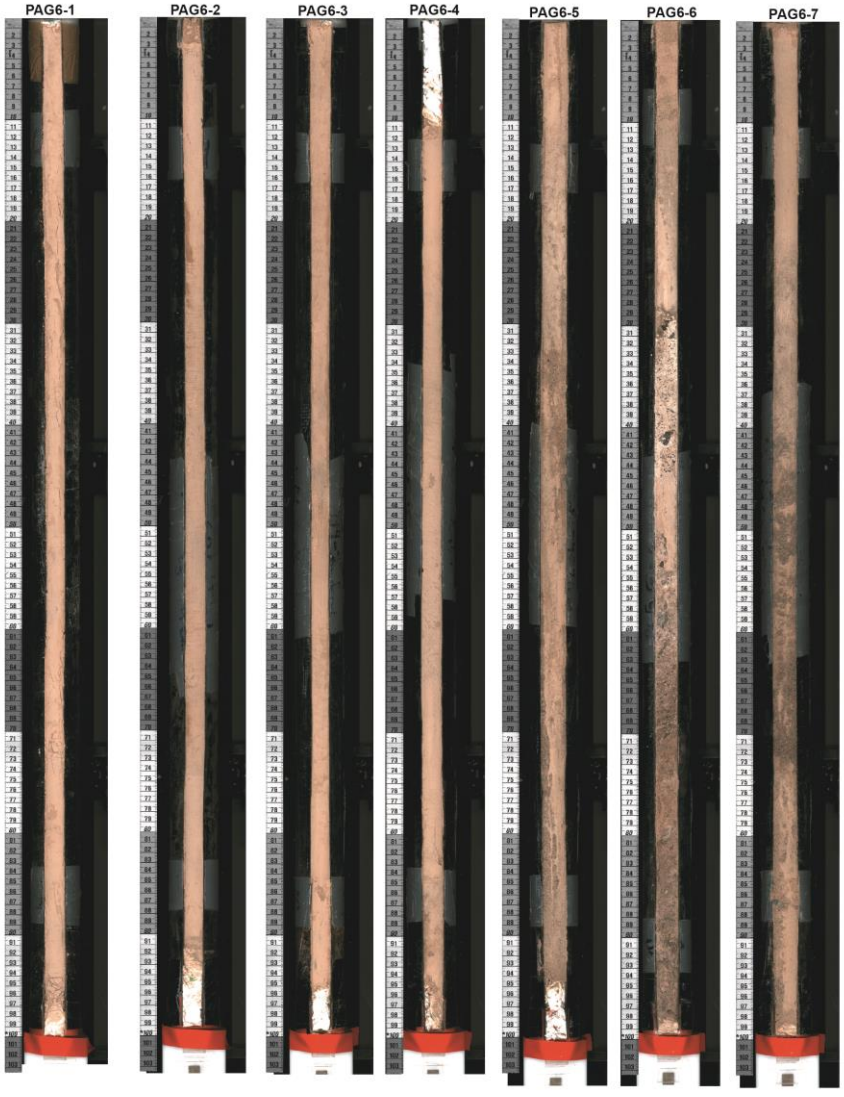

Fig. S1: Sediment core images of PAG6.

1.3. Inorganic Geochemistry and Physical Properties

ITRAX (Cox AnalyticalSystems, Sweden) XRF scanning was conducted to gain information about the inorganic geochemistry the sediment record. The X-ray generator used in this study provides 1.9 kW (Cr-tube). Each sample was measured with 30 kV and 55 mA. Data processing was performed with the software QSpec 6.5 (Cox Analytical Systems, Sweden). Relative element amounts are represented by counts per 20 second [7].

Magnetic Susceptibility (MS) was measured on 2 cm paleomagnetic sample cubes (PAG5, 6) using a Kappa-Bridge KLY2 (Agico). Grain-size analysis was performed at a 2 cm resolution, on aliquots of 1.0 g. Samples were first sieved (dry) by 2 mm and 6.3 mm meshes, with subsequent weighing of the resulting gravel (>2 mm) and finer (<2 mm) fraction. In general, terrigenous sediments of depositional systems in arid to hyperarid climates can be considered as a mixture of aeolian input, fluvial deposits, lacustrine products and evaporitic precipitates. In order to detect the grain-size distributions of past allochthonous sediment input, autochthonous evaporitic and lake products were erased by chemical treatment. For the removal of gypsum, the sub-sample <2 mm was treated with sodium bicarbonate solution (210 g/l, 12 h at 60°C). This treatment converts the gypsum to calcium carbonate, which is subsequently dissolved by hydrochloric acid (HCl, 10 %). Prior to grain-size analysis, the samples were dispersed on a shaker for 12 h and underwent one minute of ultrasonic treatment. Sample aliquots were measured three times with a Beckman Coulter LS13320 laser particle sizer equipped with an autosampler, and the individual results were averaged. Grain-size data, including standard parameters, such as sorting (σ), skewness (SK), or kurtosis (K) were evaluated applying logarithmic graphic measures from Folk and Ward [8] and using GRADISTAT [9]. Grain-size fractions are given as percentages of the bulk sample (including gravel fraction).

1.4. Diatom Analysis

For diatom analyses, which were carried out on 28 samples sediment samples were treated following standard procedures of acid digestion with hydrochloric acid and hydrogen peroxide, and then washed repeatedly with distilled water [10]. A small fraction of each sample was then evaporated onto glass coverslips and mounted onto permanent slides using the high refractive index medium Naphrax. The diatoms on the slides were counted along parallel transects at X1000 magnification using a Nikon E600 microscope

equipped with differential interference contrast optics. Diatom concentration was extremely low, but at least 100 valves were counted per sample (average of 228 valves per sample). Taxonomic identification was based upon the available diatom floras from the region and elsewhere[11-17].

1.5. Age-Depth Model

Due to the absence of organic remains in the core, excluding radiocarbon dating, we used a combination of Optically Stimulated Luminescence (OSL) and paleomagnetic dating to obtain a reliable age-depth model. The composite core chronology was derived using AnalySeries V. 2.0 [18] for a preliminary age-depth model. Final age-depth modelling was performed using the Bayesian age-depth modelling software 'rBacon' of Blaauw and Christen [19]. Periods of non-deposition or erosion are included into the model as hiatuses.

1.5.1. Optical stimulated luminescence (OSL) dating

OSL dating was carried out at the Cologne Luminescence Laboratory (CLL) on twelve fine-grained sediment samples from the uppermost 6 m of cores PAG 1 and 6. Samples for burial dose determination were taken from closed cores opened under subdued red light conditions. They were pre-treated following standard procedures to extract the polymineral 4-11 µm grain-size fraction [20]. Aliquots of this grain-size fraction were mounted from suspension onto 9.8 mm diameter stainless steel discs. Measurements were done using conventional Risø TL/OSL readers with $^{90}Sr/^{90}Y$ beta sources delivering between 0.10 and 0.13 Gy/s at the sample position. Signals were stimulated using infrared diodes (870±40 nm), and detected through a 410 nm interference filter. Equivalent dose measurements were performed using the post-infrared infrared protocol measured at 225 °C, pIRIR225.

Aliquots bleached for 24 hours in a solar simulator were used to determine residual signals and to test the reproducibility of the protocol by means of a dose-recovery test. Experiments were conducted following Auclair, et al. [21] to measure rates of anomalous fading. For each sample 6-30 aliquots were measured. Derived dose values, De, were accepted if the recycling ratio was between 0.9 and 1.1 and recuperation was <5 % of the measured De. Over-dispersion of the dose distributions, OD, were <8% in all cases. Measurement of fine-grained aliquots containing thousands of grains provides an average dose to which well and incompletely bleached grains contribute, i.e. grains with

insufficient exposure to light during transport prior to deposition. This effect is widespread in fluvial settings, especially in arid regions, where high sediment load and rapid transport during short intense rain events may lead to incomplete bleaching [22]. It is therefore expected that if the sediment is affected by incomplete bleaching, the average De values of fine-grained aliquots, which average the luminescence signal of up to 1 x 10^6 grains, might overestimate the true burial dose and the derived age. Incomplete bleaching of polymineral fine-grained samples can be evaluated through comparison between the pIR225 signal and the more easily bleached IR50 signal (e.g. [23-25]). This has been checked for all samples deriving in an IR50 to pIR225 average ratio of ~0.7, suggesting that the sediments are not affected by incomplete bleaching.

The central age model [26] was used for burial-dose calculation. Dose rate and age calculation was done using DRAC v1.2 [27]. Dose rates are based on radionuclide concentrations (U, Th, K) in the surrounding sediment derived from high-resolution gamma spectrometry. In situ water contents (the modern aridity is assumed to be representative for most of the burial period), geographical position and sediment overburden were taken into account in the calculation. An internal K content of 12.5±0.5 %, adopted from Huntley and Baril [28], and an a-value of 0.11±0.02 [29] to account for the contribution of alpha radiation, have been assumed.

1.5.2. Paleomagnetic – paleo-inclination & paleo-intensity reconstruction

The acquisition of magnetostratigraphic data, i.e., inclination, declination, and paleo-intensity was performed on whole-core samples running through a pass-through cryogenic magnetometer from 2-G Enterprises [30] with an embedded AF demagnetizer (max. 30 mT) at the Leibniz Institute for Applied Geophysics (LIAG) in Grubenhagen, Germany. The natural remanent magnetization (NRM) was determined after stepwise demagnetization (0, 10, 20, 30 mT) following the procedure after Rolf [30] and Rolf, et al. [31]. The relative paleo-intensity of the sediments was calculated using the ratio between the Natural Remanent Magnetization (NRM) at 30 mT to the magnetic susceptibility (MS) with the MS acquired in 2-cm resolution with a Bartington MS2E sensor on a multi-sensor core logger (MSCL-S; Geotek Ltd.).

2. Results

2.1. Lithological Characterisation

Grain Size Distributions

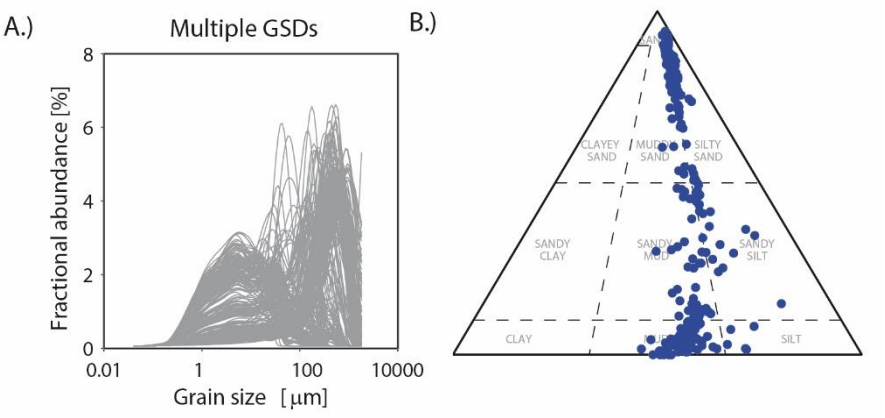

Figure S2: A.) Multi-Specimen grain size spectra plot B.) Sample distribution in a clay-silt-sand diagram with sediment classification according to after Folk Folk [32] and Shepard Shepard [33]. Plots created by AnalySize [34].

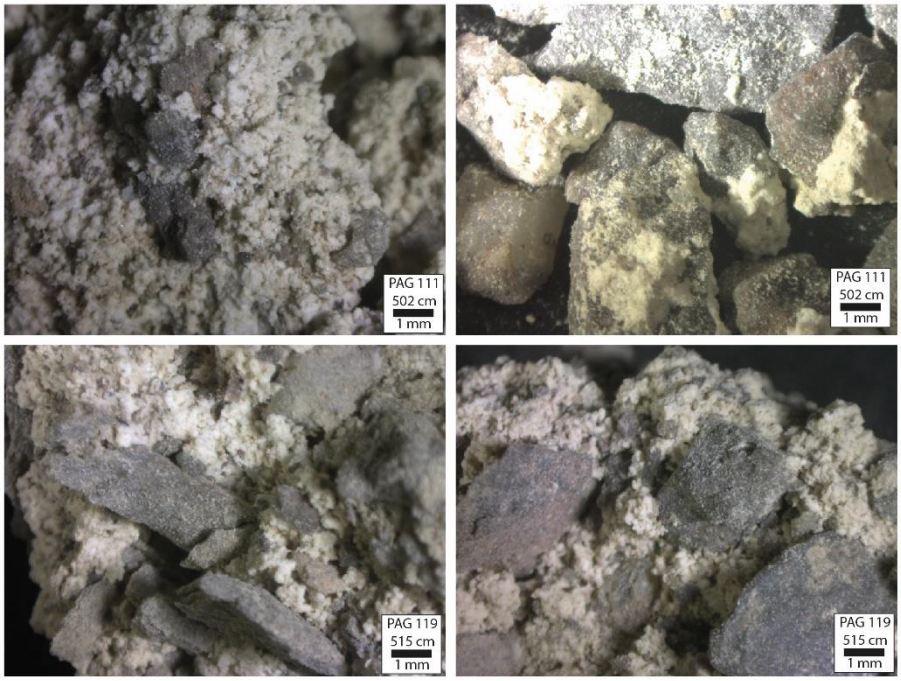

Figure S3: Photographs of some sediment samples from the gypsum crust sequence (~500-525 cm). Clasts are surrounded and cemented by calcium-sulphate, finer grain-sizes are mostly vanished. Gypsum partly appears as nodules.

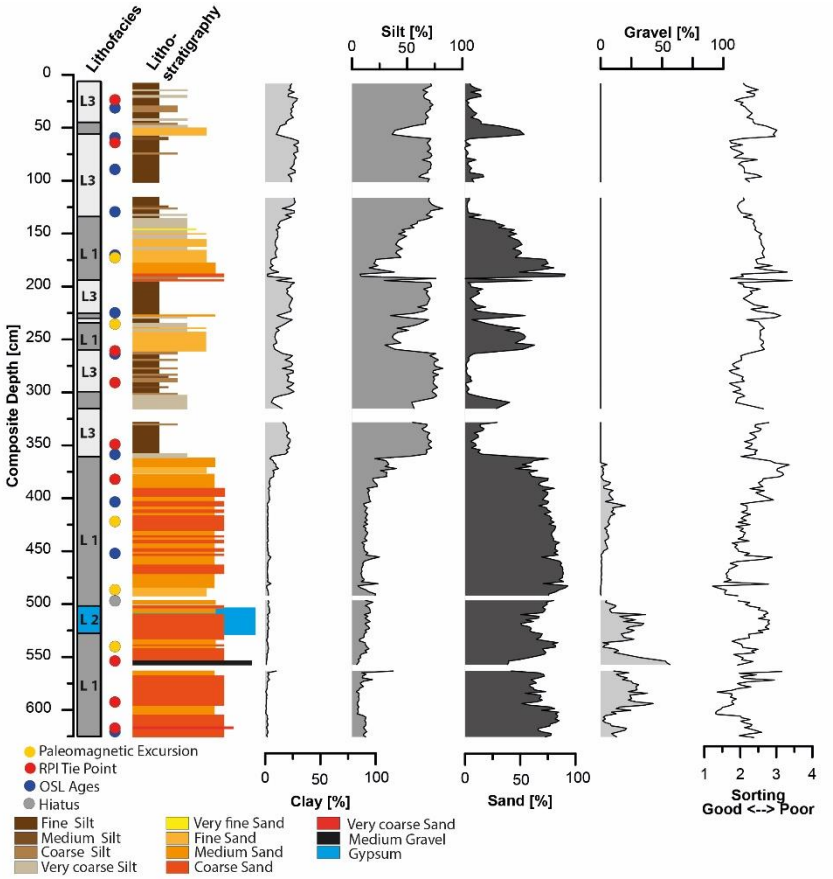

Figure S4: Lithofacies and lithology based on grain-size distributions (0->6.3 mm). Grain-size plots based on Beckman Coulter data (0-2 mm) and weighted gravel fraction (>2 mm). Sorting of the <2 mm fraction is based on laser particle size data. Coloured dots mark age tie points, see age-depth model (Fig. S6).

2.2. Biostratigraphical Characterisation

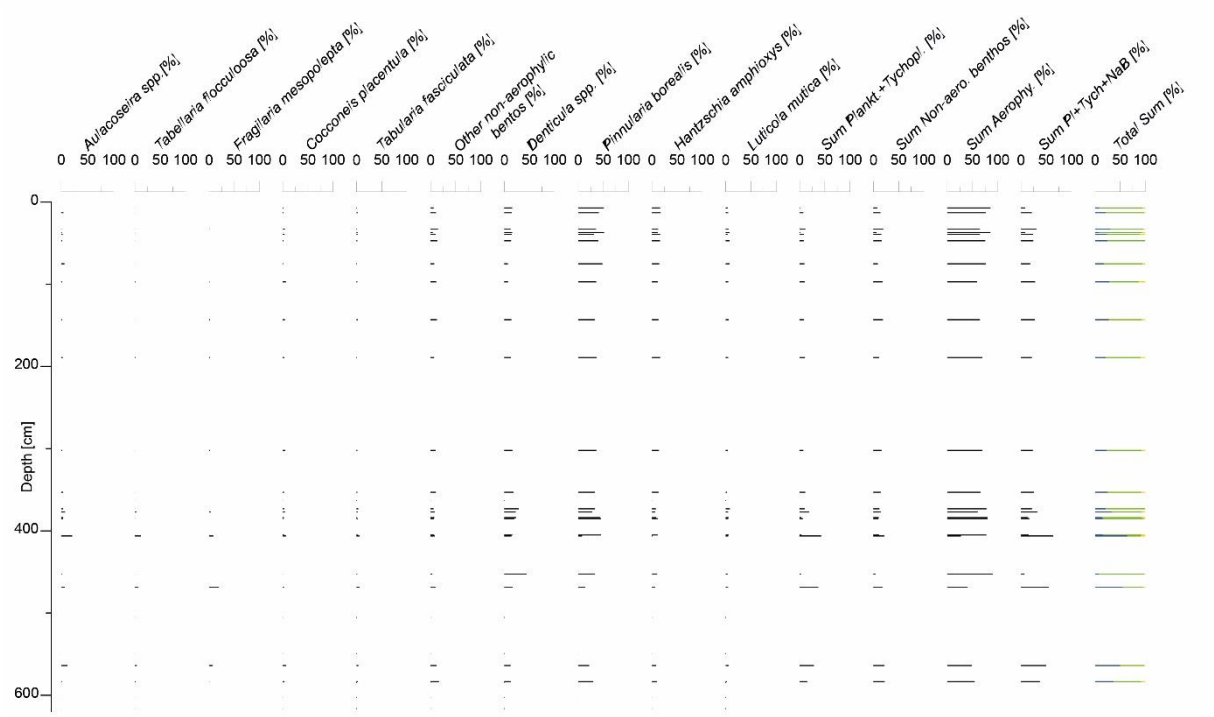

Figure S5: Simplified diatom percentage diagram for PAG5, 6.

2.3 Core Chronology

Table S1: Radionuclide data and total environmental dose rate. Water content 0 ±3 %, depth uncertainty ±0.05 m.

Sample	Depth (m)	U (ppm)	Th (ppm)	K (%)	Total environmental dose rate (Gy/ka)
PAG I-2	0.32	*2.45 ± 0.13*	*9.73 ± 0.60*	*2.08 ± 0.02*	5.26 ± 0.23
PAG I-3	0.6	*2.49 ± 0.14*	*9.62 ± 0.58*	*2.02 ± 0.02*	5.17 ± 0.23
PAG I-4	0.9	*2.46 ± 0.14*	*9.65 ± 0.58*	*2.14 ± 0.03*	5.27 ± 0.23
PAG I-5	1.3	*2.50 ± 0.20*	*9.50 ± 0.60*	*2.10 ± 0.10*	5.22 ± 0.24
PAG 6-2	1.7	*2.14 ± 0.12*	*8.14 ± 0.49*	*1.68 ± 0.02*	4.38 ± 0.20
PAG 6-3a	2.25	*2.23 ± 0.12*	*9.04 ± 0.54*	*1.97 ± 0.02*	4.85 ± 0.21
PAG 6-3b	2.64	*2.23 ± 0.12*	*9.04 ± 0.54*	*1.97 ± 0.02*	4.85 ± 0.21
PAG 6-4b	3.59	*2.40 ± 0.40*	*7.40 ± 0.50*	*1.78 ± 0.14*	4.47 ± 0.24
PAG 6-5a	4.03	*2.20 ± 0.30*	*6.50 ± 0.40*	*1.46 ± 0.09*	3.89 ± 0.20
PAG 6-5b	4.52	*1.53 ± 0.26*	*6.60 ± 0.40*	*1.43 ± 0.12*	3.50 ± 0.17
PAG 6-6b	5.40	*1.90 ± 0.09*	*7.22 ± 0.37*	*1.54 ± 0.03*	3.90 ± 0.17
PAG 6-7b	6.20	*1.66 ± 0.08*	*6.30 ± 0.32*	*1.48 ± 0.03*	3.55 ± 0.15

Table S2: Age estimates for geomagnetic excursion covering the last 215 ka. Given depths and ages are used to calculate an age model. Ages are given related to the occurrence of each geomagnetic excursion in the PISO1500 stack [35].

References for Paleomagnetic Excursions				**PISO1500**	**This Study**
	Age [ka]	**Uncertainty [ka]**	**Reference**	**Age [ka]**	**Depth[cm]**
Mono Lake / 3α	33	1	Lund, et al. [36]	**34**	**174**
	33	1	Channell [37]		
Laschamp / 3β	41	1	Lund, et al. [36]	**41**	**236**
	41	1	Channell [37]		
	40.9	1	Channell, et al. [38]		
	41.3	0.6	Laj, et al. [39]		
Post Blake Event 5α	~100		Lund, et al. [36]	**99**	**422**
	98	**2**	Channell, et al. [35]		
Blake / 5β	123	3	Lund, et al. [36]	**120**	**487**
	120.5	**1.5**	Channell, et al. [35]		
	120	12	Singer, et al. [40]		
Iceland Basin / 7α	~190		Lund, et al. [36]	**194**	**554**
	184	4	Channell [37]		
	188	3.5	Channell, et al. [38]		
	190.2	**1.77**	Channell [41]		
Pringle Falls	~211		Laj & Channell[42]		
	211	**1.5**	Roberts et al. [43]		

Age-Depth Models

1. Age-Depth Model Input Parameter:

This chronology includes geomagnetic excursions indicated in Fig. S6a (including Post-Blake Event), the uppermost seven OSL ages and additionally eight RPI tie points (Fig. S6b). OSL ages (PAG 6-4b, PAG 6-5a, and PAG 6-5b) were not used/included in the age-depth modelling using a Bayesian statistic approach ('rBacon' [19]). The OSL signals of these samples may not have been fully reset during transport of the coarser sediments found below 360 cm. Two high sedimentation rate episodes (according to OSL and geomagnetic data) between 131-191 cm and 236-264 cm (coarse layers) were treated as event layers. The pedogenic gypsum layer (500-525 cm) was treated as a hiatus at the top of Lithofacies 2. The applied models were modified using following parameters acc.mean=500, acc.shape=1.5, mem.mean=0.4 and mem.strength=6. Age-depth models were merged (transition hiatus at 500 cm) as the combination of event layers and a hiatus resulted in

anomalous non-realistic age models and/or one of the features were not included into the Bayesian statistics. Accumulation time plot was calculated using a model without event-layers.

2. Age-Depth Model Input Parameter:

Following the suggestion of one reviewer we developed an alternative age-depth model. This alternative chronology assumes that the Post-Blake Event at 420 cm is assigned to the Blake Event (~120 ka) instead. This results in a shift of assigned geomagnetic excursion and to the inclusion of the Pringle Falls event at ~211 ka. All OSL ages (except of the stratigraphically lowest two OSL ages, PAG 6-6b, PAG 6-7b; which are saturated) were included into the age-depth model. Additionally, we identified four potential RPI tie points to this chronology. Identical to the first age model, the two episodes of higher sedimentation were included as event layers into the model. Applied models were modified using following parameters acc.mean=500, acc.shape=1.5, mem.mean=0.3 and mem.strength=7. Age-depth models using assumed hiata at either 454 or 484 cm, had to be calculated and merged (with the model without hiatus). Age-depth modelling of all features failed in one run due to anomalous age-depth model results. The age-depth model assuming no hiatus indicates an episode of high accumulation time, which coincide with high probability to the occurrence of a hiatus between 454-484 cm. Due to this finding, two models with a minimum hiatus at 454 cm and a maximum hiatus at 484 cm were included in the modelling processes to account for the effects of potential hiata. Accumulation time plot was calculated using a model without event-layers.

The alternative assignment of one geomagnetic excursions at 422 cm to the Blake Event (120.5 +/-1.7 ka) and a subsequently shift of geomagnetic excursions would fit the measured OSL ages (Fig. S6D). The corresponding switch of the geomagnetic excursions at 487 cm (Iceland Basin 190 ± 5 ka) and at 554 cm (Pringle Falls 211 ± 1.5 ka) would slightly change the age-depth model to older modelled ages. This scenario indicates, compared to the first age-depth model, an episode of reduced accumulation into the basin between 454-484 cm (~150-190 ka). However, this modelled hiatus or episode of low accumulation is not reflected in the observed sedimentology. We modelled a younger hiatus at 454 cm (hiatus ~150-174 ka) and an older hiatus at 484 cm (hiatus ~163-189 ka) to indicate the potential chronological effects of non-sedimentation (Fig. S6D). The potential occurrence of a hiatus partly coincides with the assumed hiatus of our

chronology (total potential duration ~150-180 ka). However, this age chronology indicates certain disagreements with sedimentological data. The occurrence of the gypsum crust, as indicator for surface stagnancy would be shifted into a time of higher more stable sedimentation, which clearly contradicts the paleo-environmental reconstruction and evolution of a gypsum crust. Additionally, this period of low to non-sedimentation would coincide with the highest planktonic diatoms occurrence we could identify in the record, which would contradict the paleo-environmental reconstruction related to the presence of planktonic diatoms and lacustrine conditions.

Both age-depth models indicate an occurrence of a hiatus between ~135-190 ka, covering large parts of the MIS 6 glacial. The preferred age-depth model (including Post-Blake) indicates a maximum age at the bottom of ~215 ka. Sedimentation of coarser sediments during ~215-180 ka and ~135-70 ka with the occurrence of a gypsum-crust and concomitantly hiatus from ~180-135 ka (Fig. S6C). Accumulation of finer grain sizes take place between ~70-6 ka. The age-depth model indicates a maximum age of ~242 ka at the bottom, and phases of coarser sedimentation between ~242-205 ka and ~194-90 ka, with the occurrence of the gypsum crust between ~205-194 ka (Fig. S6D). Calculated sedimentation rates between ~189-150 ka are very low and point to the occurrence of an untraceable hiatus. Sedimentation of finer grain sizes into the basin would have occurred between ~90-6 ka. Both age-depth models have either discrepancy with the OSL ages or the sedimentological record. We place our confidence in the sedimentary record. The age differences between both models is approximately/maximum 10-30 ka between ~300-500 cm and 10-20 ka between 500-624 cm, respectively. We note that irrespective of which age-depth model is applied the main conclusion of our study, asynchonicity of wet/dry phases in the Altiplano and Coastal Cordillera remains.

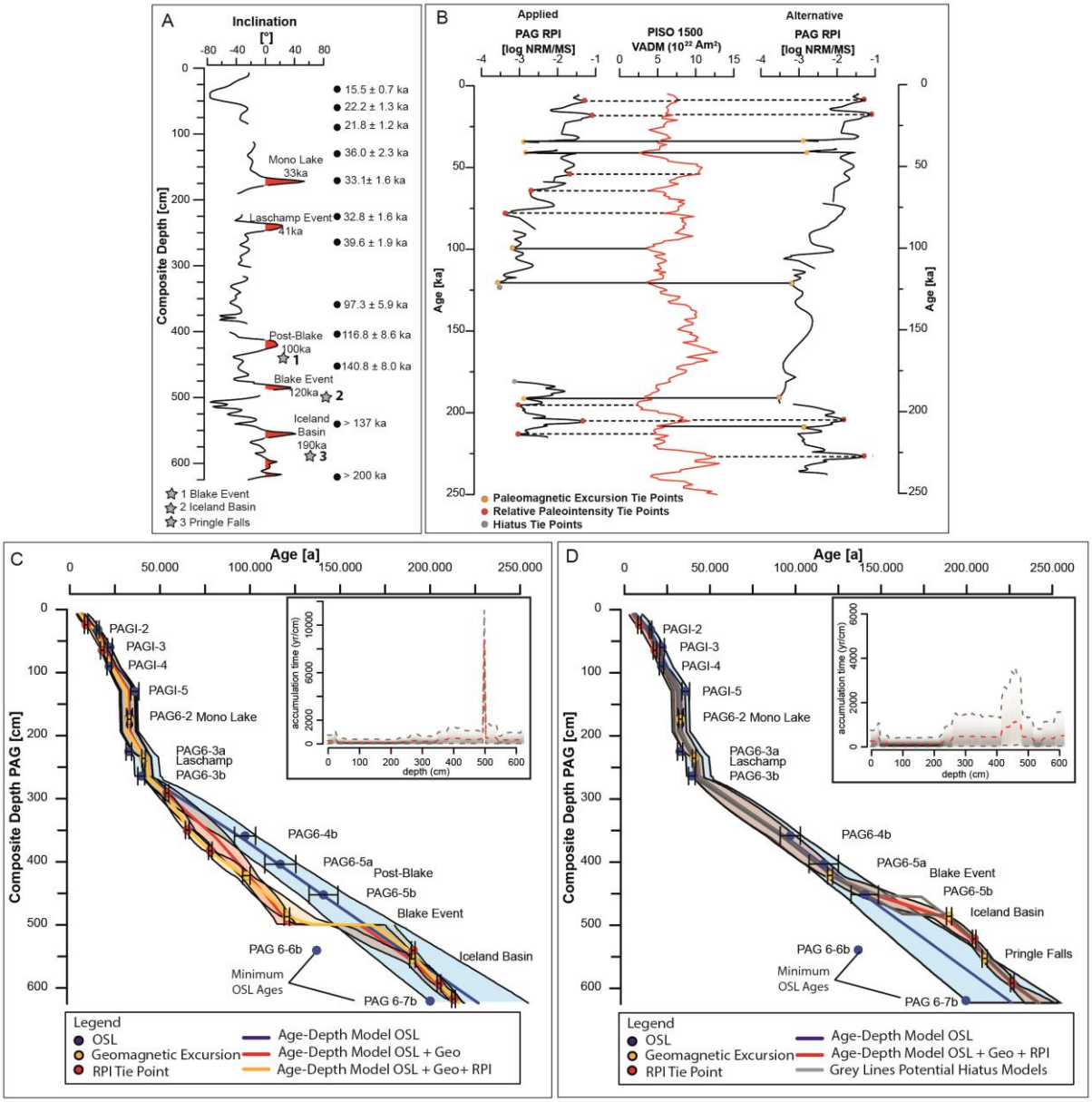

Figure S6 (A) Paleomagnetic inclination record of core PAG6. Geomagnetic inclination excursion recorded in the sediment record are marked in red with proposed geomagnetic events. Grey stars indicate an alternative assignment of potential geomagnetic excursion. Black dots display measured OSL ages. (B) Relative paleointensity (RPI) record (applied chronology and alternative chronology) vs. used RPI stacks PISO1500 [40]. Orange dots and solid lines indicate geomagnetic excursion tie points, red dots and dashed lines mark RPI tie points. Grey dots mark tie points for resembling phases of sedimentation stagnancy (hiatus). (C) and (D) derived Bayesian age-depth models using 'Bacon' from Blaauw and Christen [48]. Orange dots indicate geomagnetic excursion tie points, red dots RPI tie points and blue OSL ages. Accumulation time is given in yr/cm (calculated using 'Bacon'[48] without event-layers). Note that abrupt changes in the sedimentation rate is tightly linked to used tie points and do not reflect the likely smooth natural transitions. The lowest OSL ages (PAG 6-6b, PAG 6-7b) represent minimum ages. The alternative age-depth model (D) indicates an episode of relatively low sedimentation/high accumulation time around 454-484 cm, however a direct assignment of a hiatus, based on sedimentology is not possible. To accommodate the potential episode of non-sedimentation, two additional age-depth models were modelled for a minimum hiatus at 454 cm and a maximum hiatus at 484 cm (grey lines between 454-484 cm).

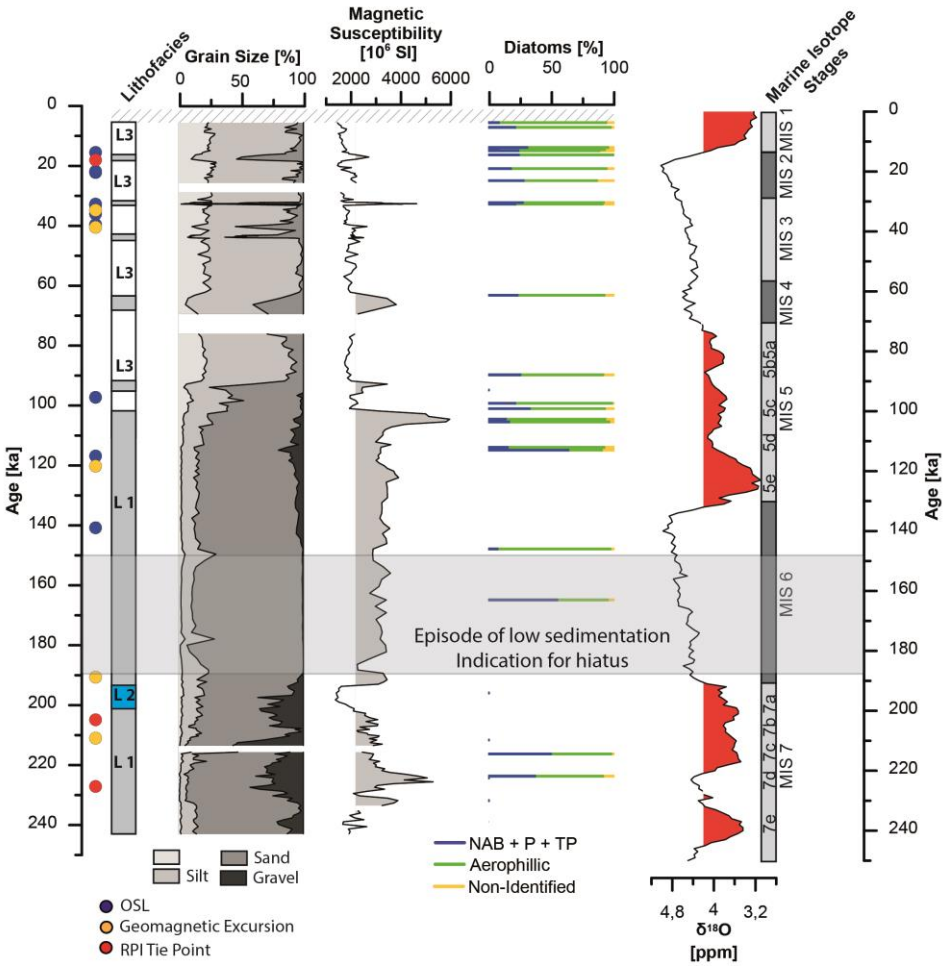

Fig. S7: Figure with identical format to figure 6 in manuscript, however, applying the alternative chronology. Note that interglacials are (MIS 7 and 5) are characterized by coarse (gravel) sediment deposition. Based on the alternative age-depth model a potential hiatus has to be taken into account between 150-180 ka. The latter episode is characterized by very low sedimentation rates and high accumulation times, so that the record is stretched. Note that the assumed hiatus represented by the pedogenic gypsum is placed in a period of higher sedimentation, when using the alternative chronology.

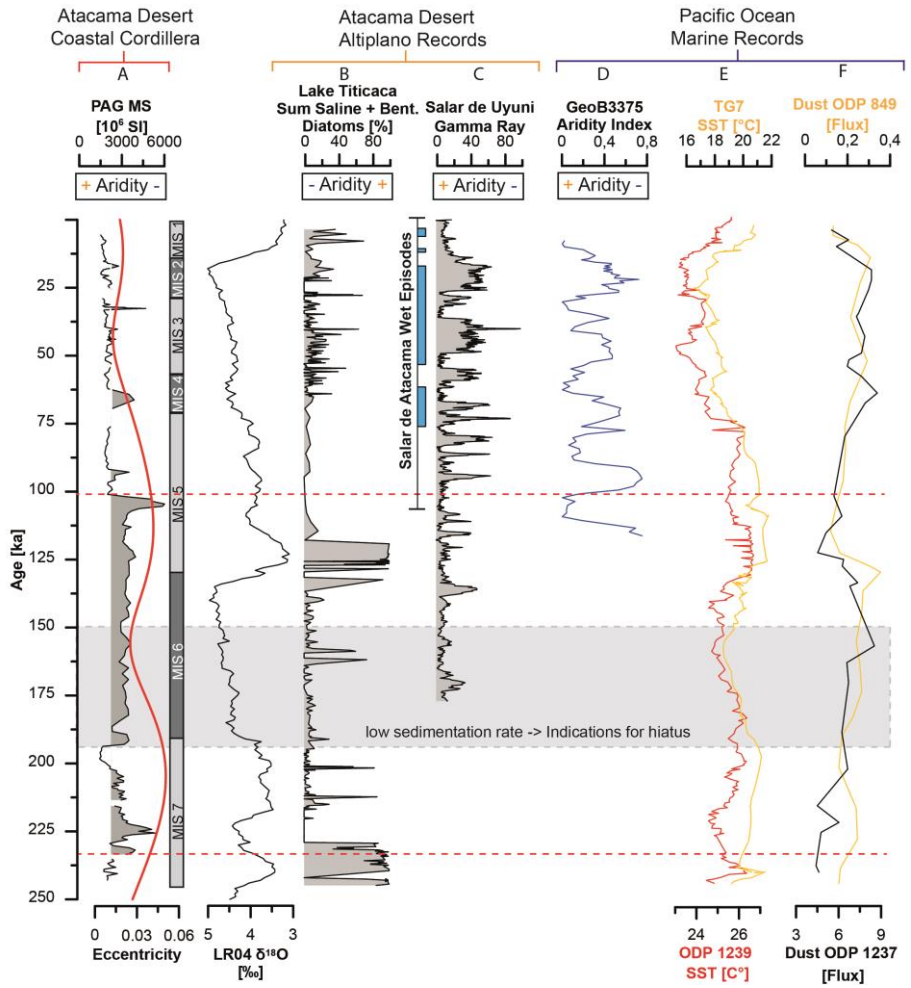

Fig. S8: Discussion figure 7 using the proposed alternative age-depth model. Note the grey marked area for an episode of low sedimentation rate / high accumulation time, indicative for the presence of hiatus between 454-484 cm.

References

1 Sandmeier, K. ReflexW v7. 5 Manual. from avaliable: http://www. sandmeiergeo. de/reflexw. html (2015).

2 Nogoshi, M. & Igarashi, T. On the amplitude characteristics of microtremor (part 2). Jour. Seism. Soc. Japan 24, 26-40 (1971).

3 Nakamura, Y. A method for dynamic characteristics estimation of subsurface using microtremor on the ground surface. Railway Technical Research Institute, Quarterly Reports 30 (1989).

4 Acerra, C. et al. Guidelines for the implementation of the H/V spectral ratio technique on ambient vibrations measurements, processing and interpretation. (2004).

5 Bravo, R. Estudio geofisico de los suelos de fundación para un zonificacion sísmica del area urbana de Santiago Norte. Memoria de título de Ingeniero Civil, Fac. Cs. Fis. y Mat., Universidad de Chile (1992).

6 Guéguen, P. Microzonage de santiago du Chile (technique de Nakamura). Master Thesis. Joseph Fourier University, Grenoble, France (1994).

7 Croudace, I. W., Rindby, A. & Rothwell, R. G. ITRAX: description and evaluation of a new multi-function X-ray core scanner. Geological Society, London, Special Publications 267, 51-63 (2006).

8 Folk, R. L. & Ward, W. C. Brazos River bar: a study in the significance of grain size parameters. Journal of Sedimentary Research 27 (1957).

9 Blott, S. J. & Pye, K. GRADISTAT: a grain size distribution and statistics package for the analysis of unconsolidated sediments. Earth surface processes and Landforms 26, 1237-1248 (2001).

10 Battarbee, R. W. et al. Diatoms. (Springer, 2002).

11 Frenguelli, J. Diatomee fossili delle conche saline del deserto cileno-boliviano. (1928).

12 Frenguelli, J. Diatomeas de la caliza de la cuenca de Calama en el desierto de Atacama Chile: Univ. nac. de la Plata. Inst. del Museo. (Coni, 1936).

13 Rumrich, U. & Rumrich, M. Diatomeen der Anden: von Venezuela bis Patagonien/Feuerland: und zwei weitere Beiträge. Vol. 9 (ARG Gantner Verlag KG, 2000).

14 Servant Vildary, S. Les Diatomées des Sédiments superficiels d'un lac salé, Chloruré, sulfaté sodique de L'Altiplano Bolivien, le lac Poopó. Cahiers ORSTOM. Série Géologie 10, 79-90 (1978).

15 Servant Vildary, S. & e Sousa, S. M. Palaeohydrology of the Quaternary saline Lake Ballivian (southern Bolivian Altiplano) based on diatom studies. International Journal of Salt Lake Research 2, 69-85 (1993).

16 Krammer, K. Bacillariophyceae 1. Susswasserflora von mitteleuropa (1986).

17 Krammer, K. & Lange-Bertalot, H. 1991. Süsswasserflora von Mitteleuropa. Bacillariophyceae 1–4. Stuttgart: Gustav Fisher (1986).

18 Paillard, D., Labeyrie, L. & Yiou, P. AnalySeries 1.0: a Macintosh software for the analysis of geophysical time-series. Eos 77, 379 (1996).

19 Zander, A. & Hilgers, A. Potential and limits of OSL, TT-OSL, IRSL and pIRIR(290) dating methods applied on a Middle Pleistocene sediment record of Lake El'gygytgyn, Russia. Climate of the Past 9, 719-733, doi:10.5194/cp-9-719-2013 (2013).

20 Auclair, M., Lamothe, M. & Huot, S. Measurement of anomalous fading for feldspar IRSL using SAR. Radiation measurements 37, 487-492 (2003).

21 Galbraith, R. F., Roberts, R. G., Laslett, G. M., Yoshida, H. & Olley, J. M. Optical dating of single and multiple grains of quartz from Jinmium rock shelter, northern Australia: Part I, experimental design and statistical models. Archaeometry 41, 339-364 (1999).

22 Durcan, J. A., King, G. E. & Duller, G. A. DRAC: Dose Rate and Age Calculator for trapped charge dating. Quaternary Geochronology 28, 54-61 (2015).

23 Huntley, D. J. & Baril, M. The K content of the K-feldspars being measured in optical dating or in thermoluminescence dating. Ancient TL 15, 11-13 (1997).

24 Kreutzer, S., Schmidt, C., DeWitt, R. & Fuchs, M. The a-value of polymineral fine grain samples measured with the post-IR IRSL protocol. Radiation Measurements 69, 18-29 (2014).

25 Rolf, C. Das Kryogenmagnetometer im Magnetiklabor Grubenhagen. Geologisches Jahrbuch E52, 161-188 (2000).

26 Rolf, C., Hambach, U., Novothny, Á., Horváth, E. & Schnepp, E. Dating of a Last Glacial loess sequence by relative geomagnetic palaeointensity: a case study from the Middle Danube Basin (Süttő, Hungary). Quaternary International 319, 99-108 (2014).

27 Folk, R. L. The distinction between grain size and mineral composition in sedimentary-rock nomenclature. The Journal of Geology 62, 344-359 (1954).

28 Shepard, F. P. Nomenclature based on sand-silt-clay ratios. Journal of Sedimentary Research 24 (1954).

29 Paterson, G. A. & Heslop, D. New methods for unmixing sediment grain size data. Geochemistry, Geophysics, Geosystems 16, 4494-4506 (2015).

30 Channell, J., Xuan, C. & Hodell, D. Stacking paleointensity and oxygen isotope data for the last 1.5 Myr (PISO-1500). Earth and Planetary Science Letters 283, 14-23 (2009).

31 Lund, S., Stoner, J. S., Channell, J. E. & Acton, G. A summary of Brunhes paleomagnetic field variability recorded in Ocean Drilling Program cores. Physics of the Earth and Planetary Interiors 156, 194-204 (2006).

32 Channell, J. Late brunhes polarity excursions (mono lake, laschamp, iceland basin and pringle falls) recorded at odp site 919 (Irminger basin). Earth and Planetary Science Letters 244, 378-393 (2006).

33 Channell, J., Riveiros, N. V., Gottschalk, J., Waelbroeck, C. & Skinner, L. Age and duration of Laschamp and Iceland Basin geomagnetic excursions in the South Atlantic Ocean. Quaternary science reviews 167, 1-13 (2017).

34 Laj, C., Guillou, H. & Kissel, C. Dynamics of the Earth magnetic field in the 10–75 kyr period comprising the Laschamp and Mono Lake excursions: New results from the French Chaîne des Puys in a global perspective. Earth and Planetary Science Letters 387, 184-197 (2014).

35 Singer, B. S., Guillou, H., Jicha, B. R., Zanella, E. & Camps, P. Refining the Quaternary geomagnetic instability time scale (GITS): Lava flow recordings of the Blake and Post-Blake excursions. Quaternary Geochronology 21, 16-28 (2014).

36 Channell, J. The Iceland Basin excursion: Age, duration, and excursion field geometry. Geochemistry, Geophysics, Geosystems 15, 4920-4935 (2014).

7. Discussion

7.1. Synthesis

The publications presented in this thesis emphasize the spatial and temporal heterogeneity of landscape and climate evolution in the Atacama Desert. Evidences of surface remnants of Miocene age can be found in the hyperarid core of the Atacama Desert (mostly Coastal Cordillera and parts of the Central Depression). Younger evidence for later onsets of aridity can be found proceeding from the hyperarid core outward to the north, east and south.

Tectonic activity is one of the factors responsible for the preservation of ancient surfaces in the Central Depression and also partly in the Coastal Cordillera (Jordan et al., 2014; Evenstar et al., 2017). However, climate variability is the main driver and agent for precipitation and is responsible for geomorphological processes that control landscape evolution. Climate change and landscape evolution since the Eocene/Oligocene are governed by global and local processes, such as the uplift of the Andes, the tectonic separation of the Coastal Cordillera and the establishment of the cold Humboldt Current. In order to identify potential forcing factors for landscape modification, derived data can be compared to global Cenozoic climate trends recorded by $\delta^{18}O$ variations in marine sediment records and key tectonic events (Zachos et al., 2001).

Onset of aridity

Along with published studies (Dunai et al., 2005; Carrizo et al., 2008; Evenstar et al., 2017) and new data (this thesis and publications), the Coastal Cordillera between 19° and 23°S appears to be notable in terms of the onset and duration of aridity, the preservation of old surfaces, sedimentation and impact of climate variation compared to other regions of the Atacama Desert. The preservation of ancient landscape surfaces illustrates the permanency of aridity in this part of the Atacama Desert. Aridity here appears to have been established earlier (Eocene/Oligocene, Dunai et al., 2005; Ritter et al., 2018b) when compared to the rest of the Atacama Desert (Sillitoe and McKee, 1996; Sáez et al., 1999; Hartley and Chong, 2002; Rech et al., 2003; Nishiizumi et al., 2005; Latorre et al., 2006; Rech et al., 2006; Kober et al., 2007; Nester et al., 2007; Evenstar et al., 2009; Placzek et al., 2010; Gayo et al., 2012b; Sáez et al., 2012; Jordan et al., 2014), with one of the studies

presented here (Publication 2 – Chapter 5, Ritter et al., 2018b) arguing that the timing determined for the onset of hyperaridity depends fundamentally on the location of an archive. Regarding modern precipitation patterns and gradients of the Atacama Desert, a hyperarid core with less than 2 mm/yr precipitation (Houston, 2006b) can be defined in the Coastal Cordillera between 19 and 23°S (Fig. 2). Assuming that similar climate gradients prevailed in the past, the Coastal Cordillera may have experienced the earliest onset of hyperaridity of the entire Atacama Desert. The existence of clasts with an Eocene/Oligocene exposure age at the southern fringe of the hyperarid core (Ritter et al., 2018b) and in the northern part (Pisagua, Dunai et al., 2005) implies an earlier onset of hyperaridity than has been otherwise determined (Fig. 7). These old clasts point to the existence of ancient Eocene/Oligocene surfaces and/or remnants (clasts in transit) in the Costal Cordillera (Dunai et al., 2005; Ritter et al., 2018b). This earlier onset of aridity and preservation of old clasts coincides with a global cooling at the Eocene/Oligocene boundary (Fig. 7, Zachos et al., 2001). Global climate changes are supposed to be the result of the opening of the Tasmanian-Antarctic passage occurring around the Eocene/Oligocene boundary and along with the opening of the Drake passage (deep-water connection) at approximately 34-30 Ma (Livermore et al., 2005). Both events led to the establishment of the Antarctic-Circumpolar current, the growth of the extensive Antarctic ice sheets, the evolution of a proto Humboldt current and the resulting abrupt Eocene/Oligocene climate deterioration (Zachos et al., 2001; Livermore et al., 2005).

However, the sparse preservation of clasts of Eocene/Oligocene age indicates that the climate reverted back to less arid conditions, which were responsible for the erosion and decay of surfaces of Eocene/Oligocene age, though this interlude of less arid conditions was not able to erode the entirety of ancient surfaces. Still, there is the potential for the preservation of Eocene/Oligocene surfaces that have not yet been identified as such.

According to Evenstar et al. (2017), the establishment of large parts of the Tarapaca paleosurface in the Coastal Cordillera is caused by the cessation of sediment deposition derived from the emerging Andes to the east (Fig. 5). Tectonic isolation caused the separation of the Coastal Cordillera from the Central Depression, which remained as the main depo-center for sediments from the uplifting Andes to the east (Evenstar et al., 2017). The deposited *Azapa* sediments (product of erosion of the emerging Andes, Garcia and Herail, 2005) display an allochthonous signal, as fluvial energy was derived by

precipitation in the Andes. This emphasizes that the Coastal Cordillera might be hyperarid since the Eocene/Oligocene, but was shaped (evolution of the Tarapaca paleosurface) from sediments and water originating in the emerging Andes. This relationship would suggest that the occurrence of ancient surfaces is dependent on the isolation from Andean influences. An autochthonous hyperarid climate is not sufficient enough to preserve surfaces, if allochthonous climate signals are influencing and modifying those sedimentation systems, for example due to large catchments, that experience several orders higher precipitation (Fig. 6). Therefore, the synchronous evolution of the Tarapaca paleosurface around ~23 Ma (Evenstar et al., 2017) with the onset of hyperarid conditions needs to be reconsidered. Potentially older surfaces and/or remnants might be preserved and point to an earlier onset of hyperaridity (Fig. 7). The discrimination of autochthonous climate and allochthonous signals and depositional signals is one of the main challenges for reconstructing landscape and climate evolution in the Atacama Desert.

Interspersed 'wetter' episodes

Comparable connectivity between an autochthonous climate and allochthonous sedimentation/precipitation influence led to the deposition of sediments and preservation of paleo-surfaces within the Central Depression (Fig. 5, 6, 7, e.g. Sáez et al., 2012; Jordan et al., 2014; Evenstar et al., 2017; Ritter et al., 2018a) and Coastal Cordillera (Dunai et al., 2005; Carrizo et al., 2008; Ritter et al., 2018b). Though the impact (surface modification) of somewhat 'wetter' episodes differs significantly between both regions (Ritter et al., 2018b), as well as their potential moisture source (Ritter et al., 2018b; Ritter et al., in review).

The autochthonous climate in the Central Depression (2-5 mm/yr, Houston, 2006b) allows the preservation of ancient surfaces (Carrizo et al., 2008; Jordan et al., 2014; Evenstar et al., 2017) and indicates that surface processes operate at very slow rates. However, catchments proximal to the rising Precordillera and Western Cordillera to the east with headwaters deep in the high Andes, where precipitation is 1-2 orders of magnitude higher than the Central Depression depo-centers, experience heterogeneous surface modification and sediment transport (Fig. 5, 6).

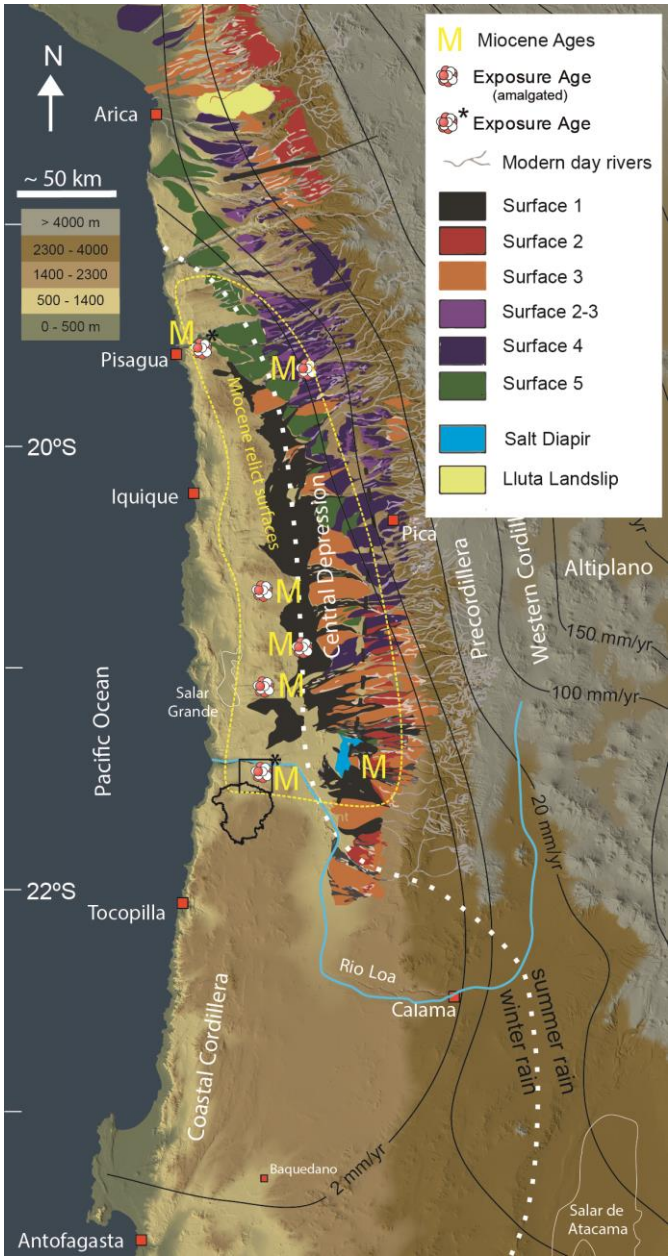

Figure 5: Colour shaded digital elevation model (derived from SRTM-data, created using ArcGIS 10.5.1) with isohyets (Houston, 2006b), modified after Ritter et al. (2018b). Dashed white line indicates the border between winter- and summer-rain dominated areas (Houston, 2006b). Note the zone of extreme hyperaridity in the Coastal Cordillera and parts of the Central Depression (19-23°S). Precipitation increase towards the Andean flanks with magnitudes that are up to 1-2 higher compared to the hyperarid zone. Various colours indicate the spatial extent of the five paleo-surfaces described by Evenstar et al. (2017). The stippled yellow outline for Miocene relict surfaces is derived from studies yielding Miocene exposure ages (M) for sediment surfaces (Dunai et al., 2005; Carrizo et al., 2008; Evenstar et al., 2009; Evenstar et al., 2017; Ritter et al., 2018b) and sedimentological studies (Jordan et al., 2014). Study site of Ritter et al. (2018b) is marked with a black rectangle and drainage catchment in black.

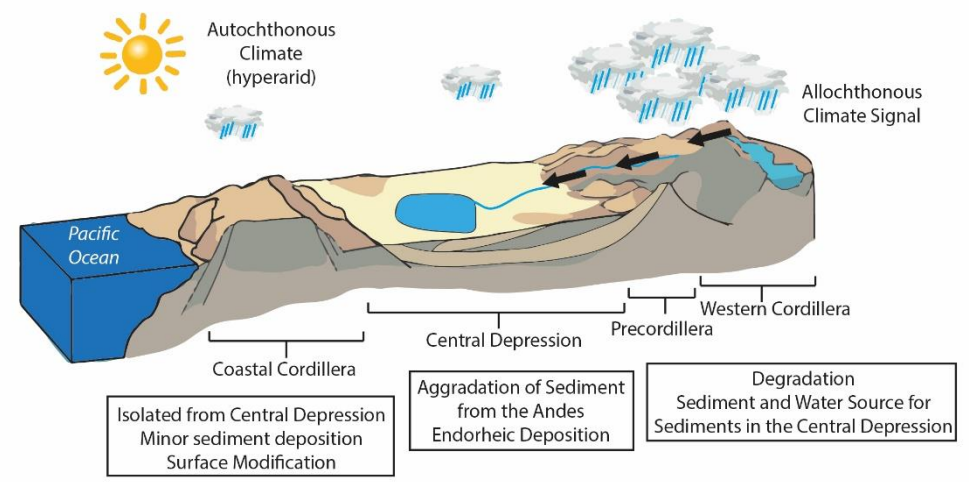

Figure 6: Sketch profile through the Atacama Desert (modified after Perez-Fodich et al. (2014)), emphasizing the influence of allochthonous climate signals from precipitation fallen in the high Andes to the east. Although the Central Depression experiences only minor amounts of precipitation (2-5 mm/yr, Houston, 2006b), reflecting a hyperarid climate, the allochthonous precipitation signal led to aggradation in the Central Depression which witnesses thick sediment depositions. In some parts the existing and previously existing long-lasting endorheic systems of the Central Depression led to the deposition of lacustrine-evaporitic sediments, which indicate a climate signal from precipitation originating in the Andes (Pfeiffer et al., 2018). The isolated Coastal Cordillera experienced only minor amounts of precipitation/moisture, which only led to subtle surface modification, such as exhumation.

'Wetter' episodes in the Central Depression are marked by the aggradation of scree material originating from the emerging Andes to the east, and/or endorheic sedimentation (e.g. lacustrine, evaporitic). In high-elevated areas with steep base-level gradients, degradational processes (Evenstar et al., 2017), such as erosion, incision and truncation into and from older sediments, occurred (Fig. 6). In relatively low-relief areas, such as the Central Depression (western part predominantly), deposition-dominated (Jordan et al., 2014; Evenstar et al., 2017). Both processes led to a large-scale relief reduction (Jordan et al., 2014; Evenstar et al., 2017). In the Coastal Cordillera 'wetter' events are identified based on cosmogenic nuclide exposure dating, by younger exposure ages of clasts on old surfaces (Dunai et al., 2005; Ritter et al., 2018b). Minor surface modification driven by more moist conditions, for example, regolith turbation and subsequent exhumation of clasts from beneath a layer of relatively thin (e.g. dm scale) sediment cover, can lead to some clasts with apparently younger ages on an old surface (Dunai et al., 2005; Evenstar et al., 2017; Ritter et al., 2018b; Binnie et al., submitted). The

difference between deposits and modification in the Central Depression compared to the Coastal Cordillera illustrates the spatial variability in quantity and impact of wetter episodes in the Atacama Desert.

As mentioned earlier, clasts of Eocene/Oligocene age point to aridification of the Coastal Cordillera at around ~35 Ma (Dunai et al., 2005; Ritter et al., 2018b). Subsequent to this, climate reverted back to more humid conditions (Fig. 7D), which led to the deposition of the *Azapa* sediments (~35-23 Ma, Hartley and Evenstar, 2010, Fig. 7B), whereby scree material from the emerging Andes to the east was transported and deposited in the Central Depression/Coastal Cordillera and offshore in the Pacific (Noble et al., 1985; Dunai et al., 2005; Garcia and Herail, 2005; Evenstar et al., 2017). The establishment of the regional Tarapaca paleosurface (Mortimer and Saric, 1972) exhibits a major hiatus in sedimentation at ~23 Ma (Fig. 7B, Dunai et al., 2005; Evenstar et al., 2017). The evolution of the Tarapaca paleosurface, according to the description of Evenstar et al. (2017), can be connected to tectonic isolation of the Costal Cordillera (Fig. 7, Delouis et al., 1998; Hartley et al., 2000; Wörner et al., 2002; Armijo et al., 2015) and to global cooling due to intensification of the Antarctic Circumpolar Current (ACC), which additionally reinforced the proto Humboldt Current (Zachos et al., 2001). Recent paleo-elevation reconstructions (Fig. 7C) point to an earlier uplift of the central Andes (Scott et al., 2018) than previously published (Ghosh et al., 2006; Garzione et al., 2008; Hoke and Garzione, 2008; Barnes and Ehlers, 2009; Leier et al., 2013; Garzione et al., 2014; Kar et al., 2016), which probably intensified the severity of the Andean rain shadow. Based on Sr and Nd isotopes from arc lavas, Scott et al. (2018) reconstructed elevations of the Western Cordillera, to suggest they had already reached ~4200 ± 516 m.a.s.l. at ~23 Ma. This is in a clear contrast to previously published paleo-altimetry data, which reconstructed a Mid- to Late Miocene rapid uplift of the Andes (Barnes and Ehlers, 2009; Garzione et al., 2014; Garzione et al., 2017). Strong positive feedbacks between Andean uplift, strengthening of the SE Pacific anticyclone and the establishment of a pronounced rain-shadow effect (Lamb and Davis, 2003) probably strengthened already arid conditions in the Atacama Desert and made it more vulnerable to global climate changes (Lamb and Davis, 2003).

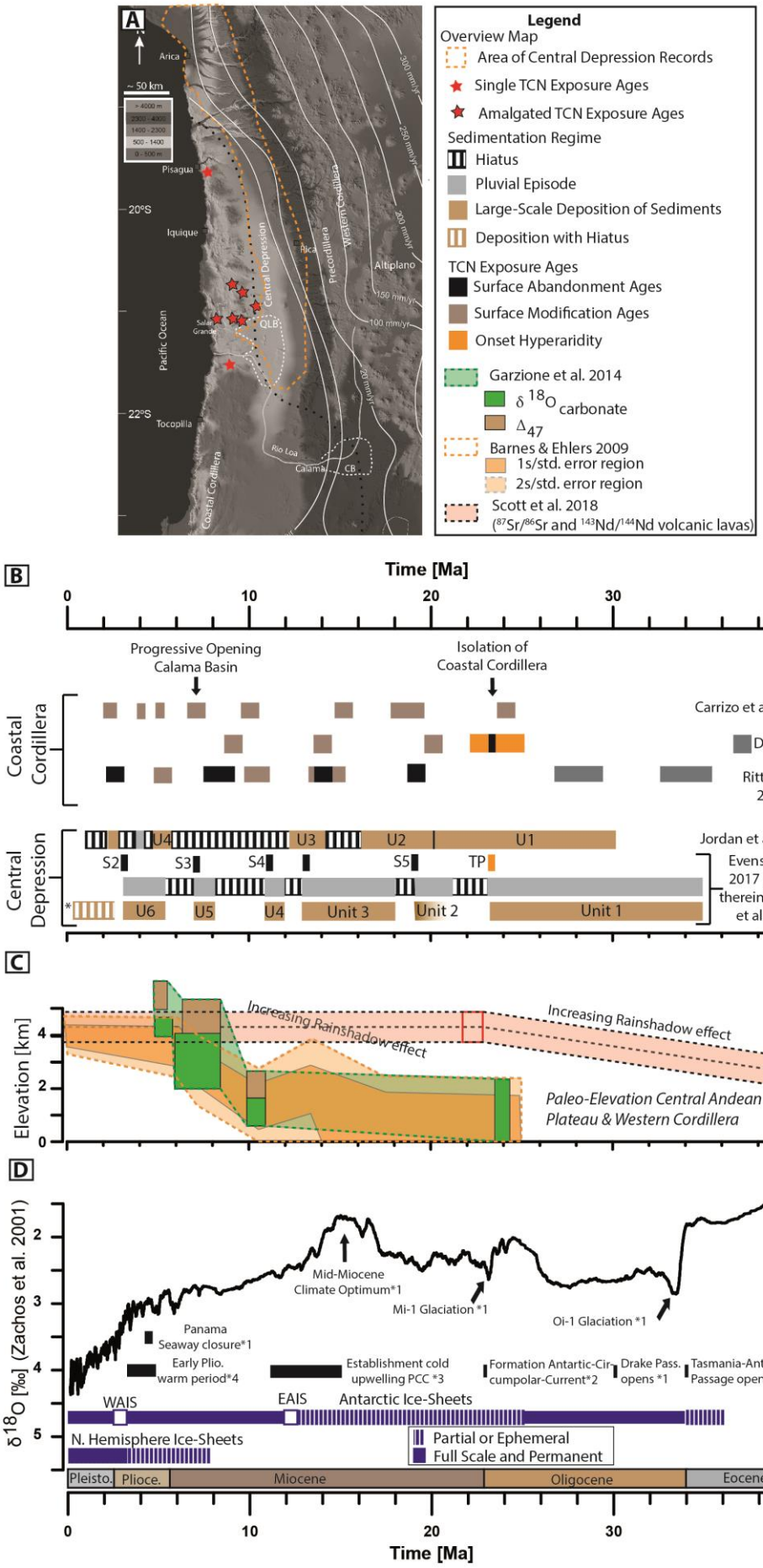
A
Arica
~ 50 km
Pisagua
20°S
Iquique
Pacific Ocean
Central Depression
Precordillera
Western Cordillera
Altiplano
Salar Grande
QLB
Tocopilla
22°S
Rio Loa
Calama
CB
Coastal Cordillera
300 mm/yr
250 mm/yr
200 mm/yr
150 mm/yr
100 mm/yr
20 mm/yr
Legend
Overview Map
Area of Central Depression Records
Single TCN Exposure Ages
Amalgated TCN Exposure Ages
Sedimentation Regime
Hiatus
Pluvial Episode
Large-Scale Deposition of Sediments
Deposition with Hiatus
TCN Exposure Ages
Surface Abandonment Ages
Surface Modification Ages
Onset Hyperaridity
Garzione et al. 2014
δ 18O carbonate
Δ47
Barnes & Ehlers 2009
1s/std. error region
2s/std. error region
Scott et al. 2018
(87Sr/86Sr and 143Nd/144Nd volcanic lavas)
B
Time [Ma]
0
10
20
30
40
Progressive Opening Calama Basin
Isolation of Coastal Cordillera
Coastal Cordillera
Carrizo et al. 2008
Dunai et al. 2005
Ritter et al. 2018b
Central Depression
U4
U3
U2
U1
Jordan et al. 2014
S2
S3
S4
S5
TP
Evenstar et al. 2017 (citation therein) + *Ritter et al. 2018a
*
U6
U5
U4
Unit 3
Unit 2
Unit 1
C
Elevation [km]
4
2
0
Increasing Rainshadow effect
Increasing Rainshadow effect
Paleo-Elevation Central Andean Plateau & Western Cordillera
D
δ18O [‰] (Zachos et al. 2001)
2
3
4
5
Mid-Miocene Climate Optimum*1
Mi-1 Glaciation *1
Oi-1 Glaciation *1
Panama Seaway closure*1
Early Plio. warm period*4
Establishment cold upwelling PCC *3
Formation Antartic-Circumpolar-Current*2
Drake Pass. opens *1
Tasmania-Antartic Passage opens *1
WAIS
EAIS
Antarctic Ice-Sheets
N. Hemisphere Ice-Sheets
Partial or Ephemeral
Full Scale and Permanent
Pleisto.
Plioce.
Miocene
Oligocene
Eocene
0
10
20
30
40
Time [Ma]

*Figure 7: A) Black/white shaded digital elevation model (derived from SRTM-data, created using ArcGIS 10.5.1) with isohyets (Houston, 2006b). Dashed black line indicates the border between winter- and summer-rain dominated areas (Houston, 2006b). Study area (Central Depression) investigated by Evenstar et al. (2017) and Jordan et al. (2014) is marked with the stippled orange line. Terrestrial cosmogenic nuclide exposure ages from the Costal Cordillera are marked with a red star (Dunai et al., 2005; Carrizo et al., 2008; Ritter et al., 2018b). Exposure ages from Carrizo et al. (2008) are amalgamated samples (red star with black frame). B) Compilation of exposure ages from the Coastal Cordillera identifying major surface evolution and surface modification episodes (Dunai et al., 2005; Carrizo et al., 2008; Ritter et al., 2018b). Combination of exposure ages and sedimentological investigation of deposited sediments from the Central Depression summarized and published by Evenstar et al. (2017) and Jordan et al. (2014). For detailed information about dating of sediments in the Central Depression, the reader is referred to Evenstar et al. (2017) and citations therein. Youngest age information for the infill of the Central Depression is given by Ritter et al. (2018a). C) Surface uplift of the Central Andes from the Eocene to present. Paleo-altimetry reconstructions from Scott et al. (2018) represent an early uplift of the Andes, compared to late Mid- to Late Miocene uplift reconstructions from Garzione et al. (2014); (2017) and Barnes and Ehlers (2009). Uplift of the Andes resulted in an enhanced rain-shadow effect and probably additionally increased the aridification of the Atacama Desert. D) Global deep-sea oxygen isotope stack based on data from Zachos et al. (2001). Vertical blue bars indicate a qualitative representation of ice volume in each hemisphere relative to the LGM, dashed parts indicate episodes of minimal ice cover (<50%), full bars represent close to maximum ice coverage (>50% of present) from Zachos et al. (2001). Major global tectonic and climatic periods/events are marked (*2 Kennett, 1982; *1 Zachos et al., 2001; *3 Houston and Hartley, 2003; *4 Wara et al., 2005).*

An earlier uplift could have additionally established the Tarapaca paleosurface at ~23 Ma (Fig. 7C, D). Still, there is a debate about the uplift chronology of the Andes based on various methods and proxy data (e.g. Barnes and Ehlers, 2009; Garzione et al., 2017; Scott et al., 2018). An earlier than previously assumed uplift, would have a significant impact on the ongoing discussion about climate controls on tectonic processes, or vice versa, in the Atacama Desert and the Andes. Lamb and Davis (2003) hypothesized that the onset of aridity is the cause, rather than the result of the uplift of the Andes (Lamb and Davis, 2003).

A 'wetter' episode prevailed prior to ~19 Ma, followed by a regionally widespread paleosurface that evolved around ~19 Ma (Fig. 7) and can be observed in the Coastal Cordillera (Dunai et al., 2005; Ritter et al., 2018b) and Central Depression (Fig. 5

paleosurface S5, Evenstar et al., 2017). During the Mid-Miocene climatic optimum (~14-17 Ma, Zachos et al., 2001) the El Diablo Fm was deposited (Unit 2, Jordan et al., 2014; or upper Altos de Pica Fm (Unit 3) Fig. 7B, Evenstar et al., 2017). The cessation of sediment deposition in the Central Depression (Evenstar et al., 2017) and surface modification and/or deposition in the Coastal Cordillera (Dunai et al., 2005; Ritter et al., 2018b) can be related to the permanent build-up of the East-Antarctic-Ice-Shield (EAIS) and the establishment of the cold Humboldt Current (Fig. 7D, Zachos et al., 2001; Houston and Hartley, 2003). A brief episode of sedimentation occurred in the Central Depression by the deposition of the upper El Diablo Fm (~11-12 Ma, Farías et al., 2005). However, this 'wetter' episode is not recorded in any archive from the isolated hyperarid Coastal Cordillera (19-23°S) so far (Dunai et al., 2005; Ritter et al., 2018b). This suggests that this brief humid episode was limited to the easternmost areas of the Atacama Desert. The rollback to a more arid climate is preserved by paleosurface S4 in large parts of the Central Depression (Fig. 5, 7B, Hoke et al., 2007; Evenstar et al., 2017). Evaporitic sedimentation (Hilaricos Fm, Sáez et al., 2012) in the southern Central Depression (Quillagua-Llamara basin) indicates 'wetter' conditions around ~8-7 Ma (Sáez et al., 1999; Sáez et al., 2012). Evaporitic-lacustrine sedimentation occurred due to the progressive opening of the Calama Basin and enlargement of the drainage catchment of the QLB (Sáez et al., 1999; May et al., 2005; Sáez et al., 2012). Contemporaneously, surface modification and fluvial erosion can be reconstructed for the southern fringe of the hyperarid Atacama Desert (Ritter et al., 2018b) and minor surface modification at the northern fringe (Dunai et al., 2005). A cooling of the Southern Ocean upper circum-polar and intermediate water masses (Billups et al., 2002) reinforced arid conditions and led to the evolution of paleosurface S3 in the Central Depression (Fig. 5, 7B, Evenstar et al., 2017).

The Early Pliocene warm period (Wara et al., 2005), characterized by an ice sheet retreat in Antarctica (Haywood et al., 2008) and the weakening of the Antarctic-Circumpolar Current, along with the closure of the Panama seaway (Fig. 7D, re-organization of oceanic currents and reinforcement of the Peru-Chile Counter Current, Haug and Tidemann, 1998) caused the formation of lacustrine depositional environments in the QLB (Quillagua Fm, Sáez et al., 1999; Sáez et al., 2012). Weakening of the Humboldt current during the Early Pliocene warm period is supposed to have triggered higher precipitation in the Atacama region (Garreaud et al., 2010). Sáez et al. (2012) interpret these conditions

as to resemble 'El Niño-like' conditions. Precipitation was most likely restricted to the Pre- and Western Cordillera, with subsequent drainage into the hyperarid Central Depression. Only rare evidences for this brief 'wetter' episode is found in the hyperarid Coastal Cordillera (Ritter et al., 2018b, ~2-3 Ma). Global climate deterioration towards the Quaternary commenced established widespread hyperarid conditions in the entire Atacama Desert. Minor fluctuations in climate were brief and exhibited only smaller magnitudes (Jordan et al., 2014; Evenstar et al., 2017).

Still, there are discrepancies about the age and formation of Plio-Pleistocene 'wetter' episodes in the Central Depression. Chapter 4 (Publication 1) reveals new ages for the youngest evaporitic Soledad Fm in the QLB. Cosmogenic nuclide exposure ages of shoreline terraces around Cerro Soledad point to repeated episodes of shoreline formation and the existence of a larger lake surface from the late Pliocene to the early Pleistocene (Ritter et al., 2018a). Due to dating uncertainty a direct and confident assignment to either glacial or interglacial time cannot be obtained. These new ages give insights about the age and formation of the last evaporitic-lacustrine episode within the QLB, along many other age constraints (Chong et al., 1999; Sáez et al., 2012; Quezada et al., 2013; Jordan et al., 2018). Mostly all of the water required for the existence of lacustrine systems originated from precipitation in the high Andes and was introduced into the QLB by the Río Loa or groundwater sources (Sáez et al., 2012; Ritter et al., 2018a). This study illustrates the connectivity between autochthonous climate and the allochthonous precipitation signal that was mentioned earlier (Fig. 6). The end of endorheic deposition in the QLB was heralded by overtopping water masses and groundwater sapping (Hoke et al., 2004; May et al., 2005), leading to the incision of the Río Loa and the formation of a canyon reaching up to 800 m deep through the Coastal Cordillera (Ritter et al., 2018a). Sáez et al. (2012) related those periods of enhanced water income into the QLB to prevailing '*La Niña-like'* conditions, with enhanced moisture flow from the interior of South America ('Atlantic moisture source'). Hence, this opens the discussion about where does the moisture come from?

Wetter episodes in the Coastal Cordillera are evident by exposure ages of clasts on old surfaces, which were probably exhumed during 'wetter' phases. However, these episodes were not capable of eroding and destroying an entire surface. Comparing wetter episodes recorded in the Central Depression, with pronounced influences of large drainage

catchments (1-2 magnitudes higher precipitation), to wetter episodes in the Coastal Cordillera, we can identify certain discrepancies in the spatial and temporal occurrence of these episodes (Fig. 7B). Interludes of 'wetter' (still arid) climate conditions, modifying ancient surfaces and allowing surface activity in the Atacama Desert caused something similar to a 'waxing and waning' of the spatial extents of arid areas, with different impact on the landscape. Since continuous paleo-records are scarce in the Coastal Cordillera, a better understanding of the impact and spatial distribution of 'wetter' episodes is challenging.

The first attempts to harmonise paleoclimate archives from the hyperarid Atacama Desert are presented in Chapter 6 (Publication 3). A climate record spanning the last ~215 ka (Ritter et al., in review) from the hyperarid Coastal Cordillera indicates that different moisture sources and atmospheric convections are responsible for precipitation and surface activity in the hyperarid desert interior. Antithetic occurrence of somewhat 'wetter' episodes in the Coastal Cordillera compared to the Altiplano records, indicate that different moisture sources and thus different atmospheric systems are operating (Fig. 8). For instance, during *'El Niño-like'* episodes higher moisture income into parts of the low-lying hyperarid Coastal Cordillera can be reconstructed, which leads to contemporaneous arid conditions and reduced discharge from drainages with headwaters in the high Andes, due to impeding Atlantic moisture income by weakening the flow of Atlantic air masses (Baker and Fritz, 2015). By contrast, during *'La Niña-like'* conditions, enhanced atmospheric flow of Atlantic air masses over the South American continent increases precipitation in the high Andes, recharging large drainage systems with water (e.g. Fritz et al., 2007; Baker and Fritz, 2015), thus enabling significant sediment transport to the lower depositional centres of the Central Depression (e.g. Sáez et al., 1999; Hartley and Chong, 2002; Sáez et al., 2012; Kirk-Lawlor et al., 2013; Jordan et al., 2014; Evenstar et al., 2017; Pfeiffer et al., 2018). Large catchment areas (with headwaters in the high Andes) cause and transfer an allochthonous climate signal into otherwise hyperarid areas of the Atacama Desert, as the Andes receive 1-2 magnitude higher rates of precipitation (Fig. 6). Whether these differences are also operating on longer time scales (Myr) is unknown due to the lack of adequate climate archives. Nevertheless, this study indicates that the Atacama Desert can be influenced by different moisture sources, and that 'wetter' episodes recorded in the Central Depression can be controlled by precipitation from the

Andes that does not necessarily have an influence on drainage systems in the Coastal Cordillera.

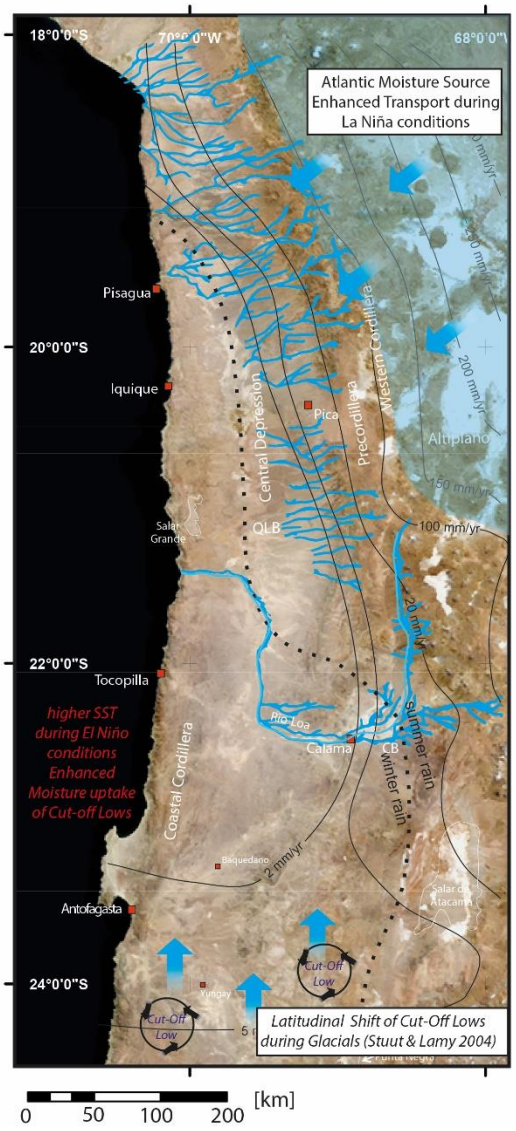

Figure 8: Natural-colour satellite image of Atacama Desert (NASA composite satellite image for March from Visible Earth - NASA's Earth Observatory). Significant hydrological channels, which receive their water from precipitation that has fallen in the high Andes, are marked in light blue. Major moisture sources are indicated with blue arrows. NE moisture originates from Atlantic air masses, passing the interior of South America and raining out in the Andes. This precipitation recharges groundwater systems of large drainage catchments, that discharges into the Central Depression and enables surface transport of sediments to the lower-lying Atacama Desert. Southerly precipitation occurs due to cut-off low systems migrating to the north, leading to enhanced precipitation south of Antofagasta. During glacial times, a northward migration of cut-off lows has been reconstructed (Lamy et al., 2000; Stuut and Lamy, 2004). Recent reconstructions from a closed

basin within the hyperarid Coastal Cordillera (Ritter et al., in review) indicate increasing surface activity and transport during interglacials, which can be connected to elevated SST offshore of Chile (Contreras et al., 2010; Rincón-Martínez et al., 2010) and enhanced moisture uptake of cut-off low systems, resembling behaviour similar to the flood of 2015 (Bozkurt et al., 2016).

The spatial and temporal pattern of 'wetter' episodes in the Atacama can be compared to a 'waxing and waning' of aridity of the desert. This behaviour of contraction and expansion of arid areas within the Atacama Desert is controlled by several forcing factors. Recent climate gradients can explain most of the variation, which we can observe in the distribution of relict surfaces and deposited sediments. These gradients are largely controlled by several atmospheric systems providing moisture income into northern Chile and have spatial antithetic effects (Fig. 8). A few studies connected deposition and moisture availability in the Atacama Desert during the Eocene/Oligocene to transport of humidity from the Amazon basin to the Atacama Desert (Houston and Hartley, 2003; Dunai et al., 2005). This trans-Andean transfer is believed to have been the main source of precipitation in the Atacama Desert since the evolution and manifestation of a proto Humboldt current (Zachos et al., 2001; Garreaud et al., 2010). Along with the uplift of the Andes, an enhanced rain-shadow effect increased aridity in the Atacama by blocking moisture-bearing systems. Due to the establishment of the Humboldt current and the existence of the high Andes, atmospheric systems significantly changed in northern Chile. Potential new processes, such as ENSO (El Niño Southern Oscillation), modified moisture transport to the Atacama Desert. If these atmospheric moisture sources are responsible for the spatial and temporal difference of recorded 'wetter' episodes on longer time scales (Myr) needs to be investigated. Still, depending on the spatial occurrence and extension of drainage systems, different moisture sources can be responsible for certain landscape modifications.

7.2. Limitations for climate and landscape reconstruction

In order to reconstruct paleo-climate and paleo-geomorphological processes in arid to hyperarid environments, scientists can choose between different approaches and archives. In arid environments the choice of a perfect archive is limited as well as the dating method. Using sediment archives, such as lake sediments, clay pans, alluvial and fluvial sediments, open the possibility to reconstruct past climate and landscape processes. Depositional surfaces and erosive geomorphological features, such as abandoned fluvial channels or shorelines, can be used to date major landscape modifying events connected to climate or tectonic activity. However, not all archives and methods are suitable to adequately resolve specific problems. Applied methods might be limited due the material used, such as the absence of organic remains for radiocarbon ^{14}C dating or by age/saturation limitations of radiogenic cosmogenic isotopes. Moreover, adequate archives may be lacking in the studied area and provide only partial or ambiguous records. The strengths, weaknesses and limits of the obtained data from sediment archives and cosmogenic exposure ages are briefly discussed below.

Terrestrial cosmogenic nuclide dating (TCN)

Using terrestrial cosmogenic nuclides is a widely applied tool to date landscape features, such as moraines (e.g. Gromig et al., 2018), fluvial/marine terraces (e.g. Binnie et al., 2016) or abandoned ancient depositional surfaces (e.g. Dunai et al., 2005). Applying cosmogenic nuclide dating requires adequate knowledge of the processes producing and shaping a certain kind of landscape feature. Dating of depositional surfaces might be affected by inheritance from previous exposure, postdepositional erosion and exhumation. Dating of surfaces can be biased by erosion, which should be independently quantified, or by pre-exposure due to depth-dependent production of cosmogenic nuclides, especially the muogenic component (Dunai, 2010). The application, furthermore, is restricted in terms of radionuclides to the half-life of the isotopes used (e.g. ^{10}Be, ^{26}Al, ^{36}Cl, ^{14}C). This age restriction can be managed by using non-radiogenic cosmogenic nuclides, such as ^{3}He or ^{21}Ne. ^{21}Ne was widely used in the Atacama Desert to date ancient surfaces (e.g. Dunai et al., 2005; González et al., 2006; Carrizo et al., 2008; Evenstar et al., 2017), beyond the age restriction of commonly used radionuclides (e.g. around 4-5 Myr for ^{10}Be). However, aside from the benefit that it does not reach a 'saturated' concentration, there are some disadvantages and problems in applying ^{21}Ne

exposure dating. The accumulation of cosmogenic nuclides during transport and temporary storage can cause major discrepancies (this applies to all cosmogenic nuclides). However, radionuclides are able to 'forget' previously collected cosmogenic signals by radioactive decay. Pre-exposure leads to erroneously high deposition ages (Dunai, 2010). In principle, multiple single clast ages from a depositional surface may yield clear age signals, i.e. tight clusters of ages, if the process delivering the clasts is capable of excavating previously unexposed material. Subsequent exhumation disperses age clusters towards younger ages, as the resulting deposits will contain material from various depths of shielding. In the absence of pre-exposure, the highest ages obtained on such a surface are the best estimates for the minimum deposition age (Evenstar et al., 2017; Binnie et al., submitted), since post-depositional erosion or intervening periods of burial, lower the assumed age of deposition. Pre-exposure, however, can be significant, particularly in hyperarid environments like the Atacama Desert, containing ancient landscapes and surfaces (Dunai et al., 2005; Carrizo et al., 2008; Evenstar et al., 2009; Jordan et al., 2014; Evenstar et al., 2017) and thus needs special consideration.

Parts of the Atacama Desert, especially the hyperarid core, are prone to significant atmospheric deposition of calcium sulphate (Rech et al., 2003; Michalski et al., 2004; Wang et al., 2015), which might raise the question of postdepositional burial of clasts. Following the 'born at the surface model' of Wells et al. (1995), clasts remain at the surface due to vertical inflation caused by deposition of atmospheric dust and its subsequent pedogenic modification. Any modification of the soil surface, either by deflation or marginal fluvial erosion, would keep clasts at the surface.

In-situ cosmogenic nuclide production rates are, in part, a function of altitude and latitude. Several scaling factors are published, which attempt to describe the variability of the cosmic-ray flux for a specific site on Earth, and allow the normalisation of the production rate, from sea-level and high latitude (SLHL) to a localised position (e.g., Lal, 1991; Dunai, 2001; Desilets and Zreda, 2003; Lifton et al., 2014). The surface sampled might have experienced uplift or subsidence since the time of deposition. Uplift reduces the atmospheric travel distance (atmospheric depth), whereas subsidence of a sampling site increases the atmospheric depth, i.e. atmospheric mass-shielding (Dunai, 2010). Applying local uplift/subsidence reconstructions can be applied to correct for altitude changes through time (e.g. Dunai et al., 2005; Evenstar et al., 2015). However, this requires a

detailed knowledge about past tectonic movement of the land surface, which is currently a matter of debate (e.g. Victor et al., 2004; Rech et al., 2006; Hoke et al., 2007; Garzione et al., 2008; Ehlers and Poulsen, 2009; Jordan et al., 2010; Evenstar et al., 2015; Cosentino and Jordan, 2017; Scott et al., 2018).

Sediment Archives in arid environments

Identifying continuous climate archives that are specific to the region's climate (autochthonous signal) in the Atacama Desert is complicated and challenging. Arid environments often lack targets for paleoclimate reconstructions which meet the desired requirements and expectations of a continuous archive. Published studies reveal rather discontinuous records from the Atacama Desert, such as soils, cave and fluvial deposits (e.g. Betancourt et al., 2000; Dunai et al., 2005; Maldonado et al., 2005; Nishiizumi et al., 2005; Quade et al., 2008; Evenstar et al., 2009; Maldonado et al., 2010; Amundson et al., 2012; Díaz et al., 2012; Gayo et al., 2012a; Jungers et al., 2013; Latorre et al., 2013; Jordan et al., 2014; Wang et al., 2015; Evenstar et al., 2017), or records which integrate over large drainage catchments that cover several climate gradients (with 1-2 orders of magnitude regional variation in precipitation) reflecting an allochthone climate signal (e.g. Bao et al., 1999; Sáez et al., 2012; Kirk-Lawlor et al., 2013; Pfeiffer et al., 2018).

Our study (Chapter 6, Publication 3) shows that there are endorheic basins available within the Coastal Cordillera, which record an autochthonous climate signal. Due to the arid to hyperarid climate with modern precipitation well below 2 mm/yr (Houston, 2006b), surface processes that deliver sediments to the pans investigated are slow. Sediment transport and deposition is mostly restricted to episodes with enhanced surface activity and fluvial transport. Therefore, climate archives in arid environments have to be interpreted as discontinuous records. Subsampling of these records implies the integration of climatic conditions over the sampling interval and might render the temporarily resolved reconstruction of climate variability. Arid to semi-arid environments are capable with even minor amounts of precipitation to produce significant surface runoff (exceptions are gypsum covered surfaces). Rare but efficiently localised precipitation can lead to high discharge events, transporting and mobilizing a lot of sediment in a short amount of time. The temporal absence of any precipitation, thereby of surface transport and deposition, combined with rare but dramatic precipitation events, make potential paleoclimate archives prone to only discontinuously record past

climate conditions. Moreover, closed basins or topographic lows can accumulate aeolian transported sediment in arid environments. Fortunately, the studied area within the Atacama Desert accommodates only minor aeolian transportable sediments, which is mostly gypsum. Applying grain-size analysis can significantly support the discrimination between aeolian, fluvial and lacustrine/evaporitic sedimentation and additionally contributes to the temporal resolution and identification of episodes of sedimentation quiescence. Grain size transport and sedimentation is directly connected to fluvial activity, except for aeolian input, and can give crucial insights about surface processes and climate conditions during deposition. Nevertheless, in arid environments aeolian erosion, evaporitic precipitation as well as soil activity and atmospheric deposition can alter the primary sedimentary signal. Additional use of standard sedimentological proxies, such as inorganic geochemistry (XRF), organic geochemistry (CNS, TOC, TN) or mineralogy (XRD) can significantly contribute to the understanding of sedimentological processes. Arid environments lack or are scarce in organic remains; such as plants or other organic remnants due to their hostile environment. However, short episodes of lacustrine environments exhibit the possibility for diatom existence/metabolism and their preservation in the sediments. Their taxa and distribution can give crucial insights about potential lacustrine phases, their duration, lake depths and water conditions (Battarbee et al., 2002).

Archive Chronology

One of the major challenges to interpret past sedimentary processes is the establishment of a robust chronology of a sedimentary archive. Due to the lack of preservation of organic plant remains in arid sediments, the commonly used radiocarbon (^{14}C) dating is usually not applicable. Volcanoclastic deposits are a widespread feature in the Atacama Desert, because of the active volcanoes in the Andes. They can be identified in sediment records by conspicuous colour and composition. However, the preservation of such fine-grained and easily erodible material in clay pans or temporary lakes is not always a given. During dry periods, volcanoclastic deposits cannot be protected against aeolian erosion and might not be preserved in the sedimentary sequence. Remnants of former volcanoclastic deposits, such as cryptotephra layers, might be preserved; though, they are difficult to detect and might be the product of secondary aeolian transport and sedimentation.

Due to the absence of any organic remains, we used a combination of Optically Stimulated Luminescence (OSL) and paleomagnetic dating to obtain a reliable age-depth model from the sediment record of the endorheic basin in the Coastal Cordillera (Publication 3). Using OSL dating to obtain ages from a sediment record requires certain assumptions, such as dose rates or water content. OSL ages can be overestimated by insufficient partial bleaching and/or anomalous fading. In arid environments, partial bleaching can be a major issue affecting the OSL signal. High sediment load and rapid transport, e.g. flood events during short rain events, can lead to an incomplete bleaching (Porat et al., 2010). This will lead to an overestimation of the calculated OSL age. Sediments may be deposited and stored in the catchment during hyperarid episodes and gain a certain amount of inherited signal, which then contributes to the total luminescence signal (incomplete bleaching). Partial bleaching tests, such as measuring the pIR225 and the IR50 signal can give insights about the potential of a previously gained OSL signal. Similar to radiogenic cosmogenic nuclide dating, OSL dating has age limitations due to saturation limits. Our study (Publication 3) indicates that we reached the OSL saturation in the lowest part of our record, thus only minimum ages can be estimated.

Geomagnetic field excursions are short periods of anomalous geomagnetic directional behaviour that emerge from the mean 'background' of normal secular variability of the Earth's magnetic field (Lund et al., 2006). Those brief geomagnetic 'events' are a valuable tool to date sediment archives beyond restrictions related to ^{14}C and OSL. The identification and cross calibration to other archives allows the establishment of a more detailed age-model for a sediment record. Such geomagnetic events are not tied to climate variability and therefore independent in contrast to cross-calibration/wiggle-matching using for example $\delta^{18}O$. The additional use of a relative paleo-intensity (RPI) proxy to define age tie points helps to establish a robust age model. The main weakness of paleomagnetic dating is its dependency on a certain sedimentation rate to record the Earth's magnetic field. In arid environments, slow surface activity can lead to low sedimentation rates or even hiatuses. This, in combination with only brief episodes of geomagnetic field polarity, implies that some geomagnetic excursions are reliably recorded while others may not be recorded at all (Roberts and Winklhofer, 2004). Using a combination of OSL and paleomagnetic dating minimizes potential method-dependent

uncertainties and allows the establishment of a robust age model for otherwise non-datable sediment archives.

8. Outstanding questions

Mainly as a consequence of the new findings presented in this thesis, some issues and outstanding questions emerged or could not be answered yet. In this context, some future projects/studies that may address the upcoming and still existing questions are mentioned in the following section.

As outlined in Chapter 7.1, substantial knowledge about the Coastal Cordillera representing the hyperarid core (between 19-22°S) is scarce. This thesis already indicated that the Atacama Desert is nothing more than a heterogeneous fabric of different landscapes, shaped and influenced by several climate gradients and sources. A more detailed study about the landscape-forming processes as well as dating of major surface modification can significantly contribute to the understanding of climate variability, even under persistent arid conditions. To date, there are only three major studies (Dunai et al., 2005; Carrizo et al., 2008; Ritter et al., 2018b) investigating the age of surfaces in the Coastal Cordillera between 19-22°S. However, these studies are distributed at the outer borders of the 'hyperarid core', allowing only a two-point interpolation (Dunai et al., 2005 - northern fringe; Ritter et al., 2018b - southern fringe) and/or exhibiting analysis of amalgated samples (Carrizo et al., 2008). Amalgated samples prohibit detailed information about multiple surface modification and reveal only a concentration average, and therefore a loss of age information. A detailed mapping of old surfaces over the Coastal Cordillera would contribute significantly to the spatial resolution of aridity and would furthermore help to define potential 'waxing and waning' of the Atacama hyperarid core.

Past studies (Dunai et al., 2005; Hartley et al., 2005) already hypothesized that aridity in the Atacama Desert might have been present earlier than recently expected, though a quantitative and robust proof of this theory is lacking. Combining the results of Dunai et al. (2005) and the new results of Ritter et al. (2018b), there are strong evidences for an earlier onset of aridification (Eocene/Oligocene). However, it is questionable if two exposure ages are sufficient for a valid proof of an Eocene/Oligocene onset of aridity.

Mapping and dating ancient surfaces in the hyperarid core could further test this hypothesis. A quantitative determination of the preservation of such old clasts would emphasize that erosion rates in the hyperarid Atacama were so small, that they were not able to entirely erode all 'old' material and reset the landscape signal to zero. The complete preservation of such old surfaces may be not possible and existing, however, parts of their entity might still be preserved. The existence of old clasts of Eocene/Oligocene age (Dunai et al., 2005; Ritter et al., 2018b) are concordant to the proposed early onset of aridity, that is required for the theory, stating that the onset of aridity in the Atacama Desert is the cause rather than the consequence of uplift of the Andes (Lamb and Davis, 2003). Stronger evidence could be reached by evaluating a robust amount of clasts of Eocene/Oligocene age.

Profound knowledge about the onset of aridity, its retreat and advance in the past, would significantly contribute to the major discussion about forcing factors controlling aridity. Moreover, in conjunction with studies about major tectonic events of global scale (e.g. opening of the Drake passage, establishment of the Antarctic Circumpolar Current, closure of the Panama Gateway) and climate variability/change, a fundamental understanding of the '*rate of aridification'* could be obtained.

Occasionally 'wetter' events led to the existence and deposition of lacustrine and salar sediments in the southern Central Depression. The paleoclimate reconstruction for the earlier lacustrine episodes (Quillagua and Hilaricos Fm) is more or less signed and sealed. Earliest deposition of lacustrine and deltaic sediments within the southern Central Depression (Quillagua-Llamara basin) are caused by climate variability and enhanced due to the tectonic opening of the Calama basin and the resulting drainage catchment expansion into the high Andes (Sáez et al., 1999; Sáez et al., 2012). However, the deposition of the youngest sediments (Soledad Fm) and their denudation are part of diverse interpretations and are built upon a series of many different data bases (Chong et al., 1999; Sáez et al., 1999; Quezada et al., 2012; Sáez et al., 2012; Jordan et al., 2018; Ritter et al., 2018a). There are several alternatives about the age of the Soledad Fm as well as about its depositional origin. The nature of climate's role differs between interpretations of Ritter et al. (2018a) and Jordan et al. (2018). Additional studies about the age and formation of the Soledad Fm and about the onset of basin-wide denudation due to the Río

Loa incision would significantly contribute to our understanding of this basin and about interspersed 'wetter' episodes, which extensively modified the Quillagua-Llamara basin.

One of the major targets should be the age determination of the Río Loa incision. The Río Loa is the only drainage to the Pacific for 600 km between south of Arica in the north (Pisagua- Quebrada Tana) and Taltal in the South. The drainage catchment comprises an area of up to 43,000 km^2 (Starke et al., 2017). Incision ages vary between 6 Ma and 260 ka (Chong et al., 1999; Sáez et al., 1999; Quezada et al., 2012; Sáez et al., 2012; Ritter et al., 2018a). However, direct evidence is missing. Reconstruction of the incision history of the Río Loa would contribute to the discussion about the age of the Soledad Fm and subsequent basin-wide denudation of former lacustrine and evaporitic sediments. Moreover, the question arises if the Río Loa incision, accompanied by opening of the basin towards the Pacific and subsequent large-scale denudation, was tectonic or climate induced. The Río Loa canyon incision created one of the major biological borders, which potentially induced genetic diversification and endemism. Potential approaches to determine the onset of incision, would be direct dating of Río Loa sediments (fluvial), for example depositional river terraces (tephra dating, cosmogenic nuclides) and/or erosive terraces (bedrock) with cosmogenic nuclides. First attempts, however, indicate that due to the denudation of old previously exposed material within and onto depositional terraces, a straightforward dating by applying cosmogenic nuclide exposure dating is hampered (Personal communication T. Jordan). Other potential approaches could be, considering the 'source to sink' model, marine sediment archives off the Río Loa mouth, which should indicate a major change of detrital clastic input at the onset of incision.

The first sediment core from the hyperarid Coastal Cordillera (Chapter 6, Publication 3) already indicates that the establishment of a robust chronostratigraphy is complex and difficult for such a hostile environment. We already reached with this 6 m core the limit of standard OSL technique in terms of saturation limit. New dating techniques (e.g. U-Series, Lu-Hf geochronology, see CRC1211) and standard ones (e.g. Electron-Spin-Resonanz ESR, burial dating using TCN, see CRC 1211, crypto-tephrochonology) should be developed and applied.

This study already reveals significant information about timing and source of somewhat 'wetter' episodes within the hyperarid Atacama Desert during the last 215 ka. The recovered sediments represent very clearly the difference in humidity sources between

the hyperarid Atacama Desert (Coastal Cordillera, Pacific moisture source) bordering the summer and winter rain region and the humidity source of the Altiplano-Puna Plateau (Atlantic moisture source). It indicates potential north-south differences in precipitation patterns and a possible association with warmer sea-surface temperatures off northern Chile and El Niño-like conditions. Unfortunately, our record covers only the last glacial-interglacial cycle. Whether this pattern is representative for all interglacial/glacial times has to be tested with longer paleoclimate records (PAG Deep Drilling, see CRC 1211). If this record is representative for the entire hyperarid Atacama Desert needs to be validated with other sediment archives from the Coastal Cordillera.

9. Conclusion

Landscape and climate evolution in the arid to hyperarid Atacama Desert have been analysed by using terrestrial cosmogenic nuclides, tephra dating and sedimentary archives. The target of the specific studies presented in chapters 4-6 was to contribute to the ongoing debate about the onset of arid conditions, the spatial and temporal dependencies, and the origin, influence and duration of interspersed 'wetter' climate episodes within the Atacama Desert. Conclusions drawn from the individual studies are presented in the associated chapters (chapters 4-6). A brief synthesis of recent juvenile data, as well as an evaluation of used methods and archives was conducted in chapter 7. Chapter 8 elucidates major unsolved questions regarding paleoclimate and landscape evolution and provides scientific approaches and ideas to answer these questions or to contribute to their solution.

The main conclusions of the thesis are as follows:

- The preservation of Miocene surfaces in the recent hyperarid core of the Atacama Desert point to an early onset of aridity in the Coastal Cordillera.
- The occurrence of clasts of Eocene/Oligocene age (Dunai et al., 2005; Ritter et al., 2018b) indicates an even earlier desertification time of the Atacama Desert.
- There is a clear spatial and temporal difference in the determination for the onset of aridity in the Atacama Desert. However, considering climatic gradients, the apparent conflict with different interpretations can be reconciled.
- Dating interspersed 'wetter' (still arid) episodes in the Central Depression and Coastal Cordillera remain challenging and needs further consideration (e.g. Soledad Fm).
- A climate record from the Coastal Cordillera indicates that moisture sources significantly differ within the Atacama Desert and exhibit a potential antithetic appearance and behaviour compared to high Andean records.

In summary, various archives and methods were used to contribute to the understanding of landscape and climate evolution of the Atacama Desert. In order to reconstruct the ancient history of the Atacama Desert, the use of various dating techniques and archives is one of the major keys to reconstruct and understand climate and landscape evolution.

It has been demonstrated that each dating method and each archive has its own potential, but also its own limits and uncertainties. A synthesis of various archives and methods is the key to reconstruct the heterogeneous paleoclimate of the Atacama Desert.

10. References

Aceituno, P., 1988, On the functioning of the Southern Oscillation in the South American sector. Part I: Surface climate: Monthly Weather Review, v. 116, no. 3, p. 505-524

Allmendinger, R. W., and González, G., 2010, Invited review paper: Neogene to Quaternary tectonics of the coastal Cordillera, northern Chile: Tectonophysics, v. 495, no. 1-2, p. 93-110.DOI 10.1016/j.tecto.2009.04.019

Allmendinger, R. W., Gonzalez, G., Yu, J., Hoke, G., and Isacks, B., 2005, Trench-parallel shortening in the Northern Chilean Forearc: Tectonic and climatic implications: Geological Society of America Bulletin, v. 117, no. 1-2, p. 89-104.Doi 10.1130/B25505.1

Alpers, C. N., and Brimhall, G. H., 1988, Middle Miocene climatic change in the Atacama Desert, northern Chile: Evidence from supergene mineralization at La Escondia: Geol. Soc. Am. Bull., v. 100, p. 1640-1656

Amundson, R., Dietrich, W., Bellugi, D., Ewing, S., Nishiizumi, K., Chong, G., Owen, J., Finkel, R., Heimsath, A., Stewart, B., and Caffee, M., 2012, Geomorphologic evidence for the late Pliocene onset of hyperaridity in the Atacama Desert: Geological Society of America Bulletin, v. 124, no. 7-8, p. 1048-1070.10.1130/b30445.1

Armijo, R., Lacassin, R., Coudurier-Curveur, A., and Carrizo, D., 2015, Coupled tectonic evolution of Andean orogeny and global climate: Earth-Science Reviews, v. 143, p. 1-35

Baker, A., Allmendinger, R. W., Owen, L. A., and Rech, J. A., 2013, Permanent deformation caused by subduction earthquakes in northern Chile: Nature Geoscience, v. 6, no. 6, p. 492-496.10.1038/ngeo1789

Baker, P. A., and Fritz, S. C., 2015, Nature and causes of Quaternary climate variation of tropical South America: Quaternary Science Reviews, v. 124, p. 31-47

Bao, R., Sáez, A., Servant-Vildary, S., and Cabrera, L. s., 1999, Lake-level and salinity reconstruction from diatom analyses in Quillagua formation (late Neogene, Central Andean forearc, northern Chile): Palaeogeography, Palaeoclimatology, Palaeoecology, v. 153, no. 1, p. 309-335

Barnes, J., and Ehlers, T., 2009, End member models for Andean Plateau uplift: Earth-Science Reviews, v. 97, no. 1-4, p. 105-132

Battarbee, R. W., Jones, V. J., Flower, R. J., Cameron, N. G., Bennion, H., Carvalho, L., and Juggins, S., 2002, Diatoms, Springer.

Betancourt, J. L., Latorre, C., Rech, J. A., Quade, J., and Rylander, K. A., 2000, A 22,000-year record of Monsoonal precipitation from Northern Chile's Atacama Desert: Science, v. 289, p. 1542-1546

Billups, K., Channell, J. E. T., and Zachos, J., 2002, Late oligocene to early Miocene geoghronology and paleoceanography from the subantarctic South Atlantic: Paleoceaongraphy, v. 17, no. 1, p. 10.1029/2000PA000568

Binnie, A., Binnie, S. A., Parteli, E. J. R., and Dunai, T. J., submitted, The implications of sampling approach and geomorphological processes for cosmogenic 10Be exposure dating of marine terraces: Nuclear Instruments and Methods- B: Beam Interactions with Materials and Atoms

Binnie, A., Dunai, T. J., Binnie, S. A., Victor, P., González, G., and Bolten, A., 2016, Accelerated late quaternary uplift revealed by 10 Be exposure dating of marine terraces, Mejillones Peninsula, northern Chile: Quaternary Geochronology, v. 36, p. 12-27

Bobst, A. L., Lowenstein, T. K., Jordan, T. E., Godfrey, L. V., Ku, T.-L., and Luo, S., 2001, A 106ka paleoclimate record from drill core of the Salar de Atacama, northern Chile: Palaeogeography, Palaeoclimatology, Palaeoecology, v. 173, no. 1, p. 21-42

Bouzari, F., and Clark, A. H., 2002, Anatomy, evolution, and metallogenic significance of teh supergene orebody of the Cerro Colorado porphyry copper deposit, I region, northern Chile: Economic Geology and the Bulletins of the Society of Economic Geologists, v. 97, no. 8, p. 1701-1740

Bozkurt, D., Rondanelli, R., Garreaud, R., and Arriagada, A., 2016, Impact of Warmer Eastern Tropical Pacific SST on the March 2015 Atacama Floods: Monthly Weather Review, v. 144, no. 11, p. 4441-4460

Cáceres, L., Gómez-Silva, B., Garró, X., Rodríguez, V., Monardes, V., and McKay, C. P., 2007, Relative humidity patterns and fog water precipitation in the Atacama Desert and biological implications: Journal of Geophysical Research, v. 112, no. G4.10.1029/2006jg000344

Carrizo, D., Gonzalez, G., and Dunai, T., 2008, Neogene constriction in the northern Chilean Coastal Cordillera: Neotectonics and surface dating using cosmogenic 21Ne: Revista Geologica De Chile, v. 35, no. 1, p. 1-38

Cereceda, P., Larrain, H., Osses, P., Farías, M., and Egaña, I., 2008, The spatial and temporal variability of fog and its relation to fog oases in the Atacama Desert, Chile: Atmospheric Research, v. 87, no. 3–4, p. 312-323.http://dx.doi.org/10.1016/j.atmosres.2007.11.012

Cereceda, P., Osses, P., Larrain, H., Farías, M., Lagos, M., Pinto, R., and Schemenauer, R. S., 2002, Advective, orographic and radiation fog in the Tarapacá region, Chile: Atmospheric Research, v. 64, no. 1–4, p. 261-271.http://dx.doi.org/10.1016/S0169-8095(02)00097-2

Charrier, R., Herail, G., Pinto, L., Garcia, M., Riquelme, R., Farias, M., and Munoz, N., 2013, Cenozoic tectonic evolution in the Central Andes in northern Chile and west central Bolivia: implications for paleogeographic, magmatic and mountain building evolution: International Journal of Earth Sciences, v. 102, no. 1, p. 235-264.10.1007/s00531-012-0801-4

Chong, G., Mendoza, M., García-Veigas, J., Pueyo, J. J., and Turner, P., 1999, Evolution and geochemical signatures in a Neogene forearc evaporitic basin: the Salar Grande (Central Andes of Chile): Palaeogeography, Palaeoclimatology, Palaeoecology, v. 151, no. 1, p. 39-54

Clarke, J. D. A., 2006, Antiquity of aridity in the Chilean Atacama Desert: Geomorphology, v. 73, no. 1-2, p. 101-114.10.1016/j.geomorph.2005.06.008

Contreras, S., Lange, C. B., Pantoja, S., Lavik, G., Rincón-Martínez, D., and Kuypers, M. M., 2010, A rainy northern Atacama Desert during the last interglacial: Geophysical Research Letters, v. 37, no. 23

Cosentino, N. J., and Jordan, T. E., 2017, 87Sr/86Sr of calcium sulfate in ancient soils of hyperarid settings as a paleoaltitude proxy: Pliocene to Quaternary constraints for northern Chile (19.5–21.7° S): Tectonics, v. 36, no. 1, p. 137-162

Cristini, L., Grosfeld, K., Butzin, M., and Lohmann, G., 2012, Influence of the opening of the Drake Passage on the Cenozoic Antarctic Ice Sheet: a modeling approach: Palaeogeography, Palaeoclimatology, Palaeoecology, v. 339, p. 66-73

Croudace, I. W., Rindby, A., and Rothwell, R. G., 2006, ITRAX: description and evaluation of a new multi-function X-ray core scanner: Geological Society, London, Special Publications, v. 267, no. 1, p. 51-63

del Río, C., Garcia, J.-L., Osses, P., Zanetta, N., Lambert, F., Rivera, D., Siegmund, A., Wolf, N., Cereceda, P., and Larraín, H., 2017, ENSO influence on coastal fog-water yield in the Atacama Desert, Chile: Aerosol and Air Quality Research, v. 18, p. 127-144

Delouis, B., Philip, H., Dorbath, L., and Cisternas, A., 1998, Recent crustal deformation in the Antofogasta region (northern Chile) and the subduction process: Geophys. J. Int., v. 132, p. 302-338

Desilets, D., and Zreda, M., 2003, Spatial and temporal distribution of secondary cosmic-ray nucleon intensities and applications to in situ cosmogenic dating: Earth and Planetary Science Letters, v. 206, p. 21-42

Díaz, F. P., Latorre, C., Maldonado, A., Quade, J., and Betancourt, J. L., 2012, Rodent middens reveal episodic, long-distance plant colonizations across the hyperarid Atacama Desert over the last 34,000 years: Journal of Biogeography, v. 39, no. 3, p. 510-525.10.1111/j.1365-2699.2011.02617.x

Dunai, T. J., 2001, Influence of secular variation of the geomagnetic field on production rates of in situ produced cosmogenic nuclides: Earth and Planetary Science Letters, v. 193, no. 1-2, p. 197-212.10.1016/s0012-821x(01)00503-9

Dunai, T. J., 2010, Cosmogenic Nuclides: Principles, concepts and applications in the Earth surface sciences, Cambridge University Press.

Dunai, T. J., González López, G. A., and Juez-Larré, J., 2005, Oligocene–Miocene age of aridity in the Atacama Desert revealed by exposure dating of erosion-sensitive landforms: Geology, v. 33, no. 4, p. 321.10.1130/g21184.1

Ehlers, T. A., and Poulsen, C. J., 2009, Influence of Andean uplift on climate and paleoaltimetry estimates: Earth and Planetary Science Letters, v. 281, no. 3-4, p. 238-248.10.1016/j.epsl.2009.02.026

Evenstar, L., Mather, A., Hartley, A., Stuart, F., Sparks, R., and Cooper, F., 2017, Geomorphology on geologic timescales: Evolution of the late Cenozoic Pacific paleosurface in Northern Chile and Southern Peru: Earth-Science Reviews

Evenstar, L. A., Hartley, A. J., Stuart, F. M., Mather, A. E., Rice, C. M., and Chong, G., 2009, Multiphase development of the Atacama Planation Surface recorded by cosmogenic 3He exposure ages: Implications for uplift and Cenozoic climate change in western South America: Geology, v. 37, no. 1, p. 27-30.10.1130/g25437a.1

Evenstar, L. A., Stuart, F. M., Hartley, A. J., and Tattitch, B., 2015, Slow Cenozoic uplift of the western Andean Cordillera indicated by cosmogenic 3He in alluvial boulders from the Pacific Planation Surface: Geophysical Research Letters, v. 42, no. 20, p. 8448-8455

Farías, M., Charrier, R., Comte, D., Martinod, J., and Hérail, G., 2005, Late Cenozoic deformation and uplift of the western flank of the Altiplano: Evidence from the depositional, tectonic, and geomorphologic evolution and shallow seismic activity (northern Chile at 19°30'S): Tectonics, v. 24, no. 4, p. TC4001.10.1029/2004tc001667

Fontugne, M., Usselmann, P., Lavallée, D., Julien, M., and Hatté, C., 1999, El Niño variability in the coastal desert of southern Peru during the mid-Holocene: Quaternary research, v. 52, no. 2, p. 171-179

Fritz, S. C., Baker, P. A., Lowenstein, T. K., Seltzer, G. O., Rigsby, C. A., Dwyer, G. S., Tapia, P. M., Arnold, K. K., Ku, T.-L., and Luo, S., 2004, Hydrologic variation during the last 170,000 years in the southern hemisphere tropics of South America: Quaternary Research, v. 61, no. 1, p. 95-104

Fritz, S. C., Baker, P. A., Seltzer, G. O., Ballantyne, A., Tapia, P., Cheng, H., and Edwards, R. L., 2007, Quaternary glaciation and hydrologic variation in the South American tropics as reconstructed from the Lake Titicaca drilling project: Quaternary Research, v. 68, no. 3, p. 410-420.10.1016/j.yqres.2007.07.008

Garcia, M., and Herail, G., 2005, Fault-related folding, drainage network evolution and valley incision during the Neogene in the Andean Precordillera of Northern Chile: Geomorphology, v. 65, no. 3-4, p. 279-300.10.1016/j.geomorph.2004.09.007

Garreaud, R. D., Molina, A., and Farias, M., 2010, Andean uplift, ocean cooling and Atacama hyperaridity: A climate modeling perspective: Earth and Planetary Science Letters, v. 292, no. 1-2, p. 39-50.10.1016/j.epsl.2010.01.017

Garreaud, R. D., Vuille, M., and Clement, A. C., 2003, The climate of the Altiplano: observed current conditions and mechanisms of past changes: Palaeogeography Palaeoclimatology Palaeoecology, v. 194, no. 1-3, p. 5-22.10.1016/s0031-0182(03)00269-4

Garreaud, R. D., Vuille, M., Compagnucci, R., and Marengo, J., 2009, Present-day South American climate: Palaeogeography Palaeoclimatology Palaeoecology, v. 281, no. 3-4, p. 180-195.10.1016/j.palaeo.2007.10.032

Garzione, C. N., Auerbach, D. J., Smith, J. J.-S., Rosario, J. J., Passey, B. H., Jordan, T. E., and Eiler, J. M., 2014, Clumped isotope evidence for diachronous surface cooling of the Altiplano and pulsed surface uplift of the Central Andes: Earth and Planetary Science Letters, v. 393, p. 173-181

Garzione, C. N., Hoke, G. D., Libarkin, J. C., Withers, S., MacFadden, B., Eiler, J., Ghosh, P., and Mulch, A., 2008, Rise of the Andes: Science, v. 320, no. 5881, p. 1304-1307.10.1126/science.1148615

Garzione, C. N., McQuarrie, N., Perez, N. D., Ehlers, T. A., Beck, S. L., Kar, N., Eichelberger, N., Chapman, A. D., Ward, K. M., and Ducea, M. N., 2017, Tectonic evolution of the Central Andean plateau and implications for the growth of plateaus: Annual Review of Earth and Planetary Sciences, v. 45, p. 529-559

Gayo, E. M., Latorre, C., Jordan, T. E., Nester, P. L., Estay, S. A., Ojeda, K. F., and Santoro, C. M., 2012a, Late Quaternary hydrological and ecological changes in the hyperarid core of the northern Atacama Desert (~21°S): Earth-Science Reviews, v. 113, no. 3-4, p. 120-140.10.1016/j.earscirev.2012.04.003

Gayo, E. M., Latorre, C., Santoro, C. M., Maldonado, A., and De Pol-Holz, R., 2012b, Hydroclimate variability in the low-elevation Atacama Desert over the last 2500 yr: Climate of the Past, v. 8, no. 1, p. 287-306.10.5194/cp-8-287-2012

Ghosh, P., Garzione, C. N., and Eiler, J. M., 2006, Rapid uplift of the Altiplano revealed through 13C-18O bonds in paleosol carbonates: Science, v. 311, no. 5760, p. 511-515

González, G., Dunai, T. J., Carrizo, D., and Allmendinger, R., 2006, Young displacements on the Atacama Fault System, northern Chile from field observations and cosmogenic Ne-21 concentrations: Tectonics, v. 25, p. doi:10.1029/2005TC001846.doi:10.1029/2005TC001846

González, G., Gerbault, M., Martinod, J., Cembrano, J., Carrizo, D., Allmendinger, R., and Espina, J., 2008, Crack formation on top of propagating reverse faults of the Chuculay Fault System, northern Chile: Insights from field data and numerical modelling: Journal of Structural Geology, v. 30, no. 6, p. 791-808.10.1016/j.jsg.2008.02.008

Gromig, R., Mechernich, S., Ribolini, A., Wagner, B., Zanchetta, G., Isola, I., Bini, M., and Dunai, T. J., 2018, Evidence for a Younger Dryas deglaciation in the Galicica Mountains (FYROM) from cosmogenic 36Cl: Quaternary International, v. 464, p. 352-363

Hartley, A., and Jolley, E., 1995, Tectonic implications of Late Cenozoic sedimentation from the Coastal Cordillera of northern Chile (22–24ºS): Journal of the Geological Society, v. 152, no. 1, p. 51-63

Hartley, A. J., 2003, Andean uplift and climate change: Journal Geol. Soc. Lond., v. 160, p. 7-10

Hartley, A. J., and Chong, G., 2002, Late Pliocene age for the Atacama Desert: Implications for the desertification of western South America: Geology, v. 30, p. 43-46

Hartley, A. J., Chong, G., Houston, J., and Mather, A. E., 2005, 150 million years of climatic stability: evidence from the Atacama Desert, northern Chile: J. Geol. Soc., v. 162, p. 421-424

Hartley, A. J., and Evenstar, L., 2010, Cenozoic stratigraphic development in the north Chilean forearc: Implications for basin development and uplift history of the Central Andean margin: Tectonophysics, v. 495, no. 1-2, p. 67-77.10.1016/j.tecto.2009.05.013

Hartley, A. J., May, G., Chong, G., Turner, P., Kape, S. J., and Jolley, E. J., 2000, Development of a continental forearc: A Cenozoic example from the Central Andes, northern Chile: Geology, v. 28, no. 4, p. 331-334

Haschke, M., Scheuber, E., Günther, A., and Reutter, K. J., 2002, Evolutionary cycles during the Andean orogeny: repeated slab breakoff and flat subduction?: Terra nova, v. 14, no. 1, p. 49-55

Haug, G. H., and Tidemann, R., 1998, Effect of the formation of the Isthmus of Panama on the Atlantic thermohaline circulation: Nature, v. 393, p. 673-676

Haywood, A. M., Smellie, J. L., Ashworth, A. C., Cantrill, D. J., Florindo, F., Hambrey, M. J., Hill, D., Hillenbrand, C.-D., Hunter, S. J., and Larter, R. D., 2008, Middle Miocene to Pliocene history of Antarctica and the Southern Ocean: Developments in Earth and Environmental Sciences, v. 8, p. 401-463

Hoke, G. D., and Garzione, C. N., 2008, Paleosurfaces, paleoelevation, and the mechanisms for the late Miocene topographic development of the Altiplano plateau: Earth and Planetary Science Letters, v. 271, no. 1-4, p. 192-201.10.1016/j.epsl.2008.04.008

Hoke, G. D., Isacks, B. L., Jordan, T. E., Blanco, N., Tomlinson, A. J., and Ramezani, J., 2007, Geomorphic evidence for post-10 Ma uplift of the western flank of the central Andes 18 degrees 30'-22 degrees S: Tectonics, v. 26, no. 5.Tc5021 10.1029/2006tc002082

Hoke, G. D., Isacks, B. L., Jordan, T. E., and Jennifer, S. Y., 2004, Groundwater-sapping origin for the giant quebradas of northern Chile: Geology, v. 32, no. 7, p. 605-608

Houston, J., 2006a, Evaporation in the Atacama Desert: An empirical study of spatio-temporal variations and their causes: Journal of Hydrology, v. 330, no. 3-4, p. 402-412.10.1016/j.jhydrol.2006.03.036

Houston, J., 2006b, Variability of precipitation in the Atacama Desert: its causes and hydrological impact: International Journal of Climatology, v. 26, no. 15, p. 2181-2198.10.1002/joc.1359

Houston, J., and Hartley, A. J., 2003, The Central Andean west-slope rainshadow and its potential contribution to the origin of hyper-aridity in the Atacama desert: International Journal of Climatology, v. 23, p. 1453-1464

Jordan, T., Blanco, N., Quezada, A., Jensen, A., Vásquez, P., and Sepúlveda, F., 2018, Comment on paper by Ritter et al.(2018), Evidence for multiple Plio-Pleistocene lake episodes in the hyperarid Atacama Desert, published in Quaternary Geochronology: v. 44, p. 1–12: Quaternary Geochronology

Jordan, T. E., Kirk-Lawlor, N. E., Blanco P., N., Rech, J. A., and Cosentino, N. J., 2014, Landscape modification in response to repeated onset of hyperarid paleoclimate states since 14 Ma, Atacama Desert, Chile: Geological Society of America Bulletin.10.1130/b30978.1

Jordan, T. E., Nester, P. L., Blanco, N., Hoke, G. D., Dávila, F., and Tomlinson, A. J., 2010, Uplift of the Altiplano-Puna plateau: A view from the west: Tectonics, v. 29, no. 5, p. n/a-n/a.10.1029/2010tc002661

Jungers, M. C., Heimsath, A. M., Amundson, R., Balco, G., Shuster, D., and Chong, G., 2013, Active erosion–deposition cycles in the hyperarid Atacama Desert of Northern Chile: Earth and Planetary Science Letters, v. 371-372, p. 125-133.10.1016/j.epsl.2013.04.005

Kar, N., Garzione, C. N., Jaramillo, C., Shanahan, T., Carlotto, V., Pullen, A., Moreno, F., Anderson, V., Moreno, E., and Eiler, J., 2016, Rapid regional surface uplift of the northern Altiplano plateau revealed by multiproxy paleoclimate reconstruction: Earth and Planetary Science Letters, v. 447, p. 33-47

Kennett, J. P., 1982, Marine geology, Englewood Cliffs, N.J., Prentice-Hall.

Kirk-Lawlor, N., Jordan, T. L., Rech, J. A., and Lehman, S. B., 2013, Late Miocene to Early Pliocene paleohydrology and landscape evolution of Northern Chile, 19° to 20° S: Palaegeography Palaeoclimatology Palaeoecology, v. 387, p. 76-90

Kober, F., Ivy-Ochs, S., Schlunegger, F., Baur, H., Kubik, P. W., and Wieler, R., 2007, Denudation rates and a topography-driven rainfall threshold in northern Chile: Multiple cosmogenic nuclide data and sediment yield budgets: Geomorphology, v. 83, p. 97-120

Lagabrielle, Y., Godderis, Y., Donnadieu, Y., Malavieille, J., and Suarez, M., 2009, The tectonic history of Drake Passage and its possible impacts on global climate: Earth and Planetary Science Letters, v. 279, no. 3-4, p. 197-211.10.1016/j.epsl.2008.12.037

Lal, D., 1991, Cosmic ray labeling of erosion surfaces: in situ nuclide production rates and erosion models: Earth Planet. Sci. Lett., v. 104, p. 424-439

Lamb, S., and Davis, P., 2003, Cenozoic climate change as a possible cause for the rise of the Andes: Nature, v. 425, p. 792-797

Lamy, F., Hebbeln, D., and Wefer, G., 1998, Late Quaternary precessional cycles of terrigenous sediment input off the Norte Chico, Chile (27.5ºS) and palaeoclimatic implications: Palaeogeography, Palaeoclimatology, Palaeoecology, v. 141, p. 233-251

Lamy, F., Klump, J., Hebbeln, D., and Wefer, G., 2000, Late Quaternary rapid climate change in northern Chile: Terra Nova, v. 12, p. 8-13

Latorre, C., Betancourt, J. L., and Arroyo, M. T. K., 2006, Late Quaternary vegetation and climate history of a perennial river canyon in the Río Salado basin (22°S) of Northern Chile: Quaternary Research, v. 65, no. 3, p. 450-466.10.1016/j.yqres.2006.02.002

Latorre, C., Santoro, C. M., Ugalde, P. C., Gayo, E. M., Osorio, D., Salas-Egana, C., De Pol-Holz, R., Joly, D., and Rech, J. A., 2013, Late Pleistocene human occupation of the hyperarid core in the Atacama Desert, northern Chile: Quaternary Science Reviews, v. 77, p. 19-30.10.1016/j.quascirev.2013.06.008

Leier, A., McQuarrie, N., Garzione, C., and Eiler, J., 2013, Stable isotope evidence for multiple pulses of rapid surface uplift in the Central Andes, Bolivia: Earth and Planetary Science Letters, v. 371, p. 49-58.10.1016/j.epsl.2013.04.025

Lifton, N., Sato, T., and Dunai, T. J., 2014, Scaling in situ cosmogenic nuclide production rates using analytical approximations to atmospheric cosmic-ray fluxes: Earth and Planetary Science Letters, v. 386, p. 149-160.10.1016/j.epsl.2013.10.052

Livermore, R., Nankivell, A., Eagles, G., and Morris, P., 2005, Paleogene opening of Drake Passage: Earth and Planetary Science Letters, v. 236, no. 1-2, p. 459-470.10.1016/j.epsl.2005.03.027

Lund, S., Stoner, J. S., Channell, J. E., and Acton, G., 2006, A summary of Brunhes paleomagnetic field variability recorded in Ocean Drilling Program cores: Physics of the Earth and Planetary Interiors, v. 156, no. 3-4, p. 194-204

Maldonado, A., Betancourt, J. L., Latorre, C., and Villagran, C., 2005, Pollen analyses from a 50 000-yr rodent midden series in the southern Atacama Desert (25° 30′ S): Journal of Quaternary Science, v. 20, no. 5, p. 493-507.10.1002/jqs.936

Maldonado, A., Mendez, C., Ugalde, P., Jackson, D., Seguel, R., and Latorre, C., 2010, Early Holocene climate change and human occupation along the semiarid coast of north-central Chile: Journal of Quaternary Science, v. 25, no. 6, p. 985-988.10.1002/jqs.1385

Martin, T., Erasmo, C. M., Enzo, A. a., Wolf, E. A., Horacio, B., Katherina, B., Patricio, A. C., JuanCarlos, C., Leonardo, R. C., Maritza, C. s., Clement, P. D., Ruben, E., Miriam, F., Jhon, A. G., Carlos, F. G., Ivan, G., AndrV?s, E. G. l., Humberto, E. G. l., Pilar, A. H., Juan-Enrique, I., JoseLuis, I., Domingo, A. L., Guillermo, L.-J., Carolina, L., Patricio, H. M., VV?ctor, M. n., Praxedes, M. o., Sergio, A. N., Eduardo, P., Elie, P., Javier, S., HectorHito, S. l., Wolfgang, S., Fadia, T., Andrew, T., Cristian, A. V., Julio, A. V., and Alonso, V., 2007, The Humboldt Current System of Northern and Central Chile, Oceanography and Marine Biology, CRC Press, p. 195-344.

May, G., Hartley, A., Stuart, F., and Chong, G., 1999, Tectonic signatures in arid continental basins: an example from the Upper Miocene–Pleistocene, Calama Basin, Andean forearc, northern Chile: Palaeogeography, Palaeoclimatology, Palaeoecology, v. 151, no. 1, p. 55-77

May, G., Hartley, A. J., Chong, G., Stuart, F., Turner, P., and Kape, S. J., 2005, Eocene to Pleistocene lithostratigraphy, chronostratigraphy and tectono-sedimentary evolution of the Calama Basin, northern Chile: Revista Geologica de Chile, v. 32, no. 1, p. 33-58

McKay, C. P., Friedmann, E. I., Gómez-Silva, B., Cáceres-Villanueva, L., Andersen, D. T., and Landheim, R., 2003, Temperature and moisture conditions for life in the extreme arid region of the Atacama Desert: four years of observations including the El Niño of 1997-1998: Astrobiology, v. 3, no. 2, p. 393-406

Michalski, G., Bohlke, J. K., and Thiemens, M., 2004, Long term atmospheric deposition as the source of nitrate and other salts in the Atacama Desert, Chile: New evidence from mass-independent oxygen isotopic compositions: Geochimica et Cosmochimica Acta, v. 68, no. 20, p. 4023-4038.10.1016/j.gca.2004.04.009

Mortimer, C., 1973, The Cenozoic history of the southern Atacama Desert, Chile: Journal Geol. Soc. Lond., v. 129, p. 505-526

Mortimer, C., and Saric, N., 1972, Landform evolution in the coastal region of Tarapacá Province, Chile: Revue de géomorphologie dynamique, v. 21, no. 4, p. 162-170

Mortimer, C., and Saric, N., 1975, Cenozoic studies in northernmost Chile: Geologische Rundschau, v. 64, p. 395-420

Nester, P. L., Gayo, E., Latorre, C., Jordan, T. E., and Blanco, N., 2007, Perennial stream discharge in the hyperarid Atacama Desert of northern Chile during the latest Pleistocene: Proceedings of the National Academy of Sciences of the United States of America, v. 104, no. 50, p. 19724-19729.10.1073/pnas.0705373104

Nishiizumi, K., Caffee, M. W., Finkel, R. C., Brimhall, G., and Mote, G., 2005, Remnants of a fossil alluvial fan landscape of Miocene age in the Atacama desert of northern Chile using cosmogenic nuclide exposure age dating: Earth Planet. Sci. Lett., v. 237, p. 499-507

Noble, D. C., Sebrier, M., Megard, F., and McKee, E. H., 1985, Demonstration of two pulses of Paleogene deformation in the Andes of Peru: Earth Planet. Sci. Lett., v. 73, p. 345-349

Okada, A., 1971, On the neotectonics of the Atacama fault zone region. Preliminary notes on late Cenozoic faulting and geomorphic development of the Coast Range of northern Chile: Bulletin of the Department of Geography, University of Tokyo, v. 3, p. 47-65

Ortlieb, L., Zazo, C., Goy, J. L., Hillaire-Marcel, C., Ghaleb, B., and Cournoyer, L., 1996, Coastal deformation and sea-level changes in the northern Chile subduction area (23ºS) during the last 330 ky: Quaternary Sci. Rev., v. 15, p. 819-831

Perez-Fodich, A., Reich, M., Alvarez, F., Snyder, G. T., Schoenberg, R., Vargas, G., Muramatsu, Y., and Fehn, U., 2014, Climate change and tectonic uplift triggered the formation of the Atacama Desert's giant nitrate deposits: Geology, v. 42, no. 3, p. 251-254.10.1130/g34969.1

Pfeiffer, M., Latorre, C., Santoro, C. M., Gayo, E. M., Rojas, R., Carrevedo, M. L., McRostie, V. B., Finstad, K. M., Heimsath, A., and Jungers, M. C., 2018, Chronology, stratigraphy and hydrological modelling of extensive wetlands and paleolakes in the hyperarid core of the Atacama Desert during the late quaternary: Quaternary Science Reviews, v. 197, p. 224-245

Placzek, C. J., Matmon, A., Granger, D. E., Quade, J., and Niedermann, S., 2010, Evidence for active landscape evolution in the hyperarid Atacama from multiple terrestrial cosmogenic nuclides: Earth and Planetary Science Letters, v. 295, no. 1-2, p. 12-20.10.1016/j.epsl.2010.03.006

Porat, N., Amit, R., Enzel, Y., Zilberman, E., Avni, Y., Ginat, H., and Gluck, D., 2010, Abandonment ages of alluvial landforms in the hyperarid Negev determined by luminescence dating: Journal of Arid Environments, v. 74, no. 7, p. 861-869

Quade, J., Rech, J. A., Betancourt, J. L., Latorre, C., Quade, B., Rylander, K. A., and Fisher, T., 2008, Paleowetlands and regional climate change in the central Atacama Desert, northern Chile: Quaternary Research, v. 69, no. 3, p. 343-360.10.1016/j.yqres.2008.01.003

Quezada, A., Vásquez, P., and Sepúlveda, F., 2013, Soledad Formation: mapping and radiometric ages, Atacama Desert, I Region, Chile: GEOSUR.

Quezada, A., Vasquez, P., Sepúlveda, F., Blanco, N., and Tomlinson, A. J., 2012, Mapa Compilación Geológica Área Quillagua - Salar Grande 1:100.000: Servicio Nacional de Geologica y Mineria Gobierno Regional de Tarapacá.

Radtke, U., 1989, Marine Terrassen und Korallenriffe. Das Probleem der Quartären Meeresspiegelschwankungen erläutert an Fallstudien aus Chile, Argentinien und Barbados., Diisseldorfer Geographische Schriften, 245 p.:

Rech, J. A., Currie, B. S., Michalski, G., and Cowan, A. M., 2006, Neogene climate change and uplift in the Atacama Desert, Chile: Geology, v. 34, no. 9, p. 761-764.10.1130/g22444.1

Rech, J. A., Quade, J., and Hart, W. S., 2003, Isotopic evidence for the source of Ca and S in soil gypsum, anhydrite and calcite in the Atacama Desert, Chile: Geochim. Cosmochim. Acta, v. 67, p. 575-586

Regard, V., Saillard, M., Martinod, J., Audin, L., Carretier, S., Pedoja, K., Riquelme, R., Paredes, P., and Herail, G., 2010, Renewed uplift of the Central Andes Forearc revealed by coastal evolution during the Quaternary: Earth and Planetary Science Letters, v. 297, no. 1-2, p. 199-210.10.1016/j.epsl.2010.06.020

Rincón-Martínez, D., Lamy, F., Contreras, S., Leduc, G., Bard, E., Saukel, C., Blanz, T., Mackensen, A., and Tiedemann, R., 2010, More humid interglacials in Ecuador during the past 500 kyr linked

to latitudinal shifts of the equatorial front and the Intertropical Convergence Zone in the eastern tropical Pacific: Paleoceanography, v. 25, no. 2

Ritter, B., Binnie, S. A., Stuart, F. M., Wennrich, V., and Dunai, T. J., 2018a, Evidence for multiple Plio-Pleistocene lake episodes in the hyperarid Atacama Desert: Quaternary Geochronology, v. 44, p. 1-12.doi.org/10.1016/j.quageo.2017.11.002

Ritter, B., Stuart, F. M., Binnie, S. A., Gerdes, A., Wennrich, V., and Dunai, T. J., 2018b, Neogene fluvial landscape evolution in the hyperarid core of the Atacama Desert: Scientific Reports, v. 8, no. 1, p. 13952.10.1038/s41598-018-32339-9

Ritter, B., Wennrich, V., Medialdea, A., Brill, D., King, G. E., Schneiderwind, S., Niemann, K., Fernandez-Galego, E., Diederich, J., Rolf, C., Melles, M., and Dunai, T. J., in review, Climate reconstruction of the hyperarid core of the Atacama Desert during the past 215 ka: Nature Scientific Reports

Roberts, A. P., and Winklhofer, M., 2004, Why are geomagnetic excursions not always recorded in sediments? Constraints from post-depositional remanent magnetization lock-in modelling: Earth and Planetary Science Letters, v. 227, no. 3-4, p. 345-359

Rojas, M., Moreno, P. I., Kageyama, M., Crucifix, M., Hewitt, C., Abe-Ouchi, A., Ohgaito, R., Brady, E. C., and Hope, P., 2009, The Southern Westerlies during the last glacial maximum in PMIP2 simulations: Climate Dynamics, v. 32, no. 4, p. 525-548.10.1007/s00382-008-0421-7

Sáez, A., Cabrera, L., Garcés, M., Bogaard, P. v. d., Jensen, A., and Gimeno, D., 2012, The stratigraphic record of changing hyperaridity in the Atacama desert over the last 10Ma: Earth and Planetary Science Letters, v. 355-356, p. 32-38.10.1016/j.epsl.2012.08.029

Sáez, A., Cabrera, L., Jensen, A., and Chong, G., 1999, Late Neogene lacustrine record and palaeogeography in the Quillagua–Llamara basin, Central Andean fore-arc (northern Chile): Palaeogeography, Palaeoclimatology, Palaeoecology, v. 151, no. 1, p. 5-37

Scheihing, K. W., Moya, C. E., Struck, U., Lictevout, E., and Tröger, U., 2017, Reassessing Hydrological Processes That Control Stable Isotope Tracers in Groundwater of the Atacama Desert (Northern Chile): Hydrology, v. 5, no. 1, p. 3

Scher, H. D., and Martin, E. E., 2006, Timing and climatic consequences of the opening of Drake Passage: Science, v. 312, no. 5772, p. 428-430.10.1126/science.1120044

Scheuber, E., and Andriessen, P. A., 1990, The kinematic and geodynamic significance of the Atacama fault zone, northern Chile: Journal of Structural Geology, v. 12, no. 2, p. 243-257

Scheuber, E., and Gonzalez, G., 1999, Tectonics of the Jurassic-Early Cretaceous magmatic arc of the north Chilean Coastal Cordillera (22°–26° S): A story of crustal deformation along a convergent plate boundary: Tectonics, v. 18, no. 5, p. 895-910

Scott, E. M., Allen, M. B., Macpherson, C. G., McCaffrey, K. J., Davidson, J. P., Saville, C., and Ducea, M. N., 2018, Andean surface uplift constrained by radiogenic isotopes of arc lavas: Nature communications, v. 9, no. 1, p. 969

Sillitoe, R. H., and McKee, E. H., 1996, Age of supergene oxidation and enrichment in the Chilean porphyry copper province: Economic Geology, v. 91, no. 1, p. 164-179

Starke, J., Ehlers, T., and Schaller, M., 2017, Tectonic and Climatic Controls on the Spatial Distribution of Denudation Rates in Northern Chile (18° S to 23° S) Determined From Cosmogenic Nuclides: Journal of Geophysical Research: Earth Surface, v. 122, no. 10, p. 1949-1971

Stuut, J. B. W., and Lamy, F., 2004, Climate variability at the southern boundaries of the Namib (Southwestern Africa) and Atacama (northern Chile) coastal deserts during the last 120,000 yr: Quaternary Research, v. 62, no. 3, p. 301-309.10.1016/j.yqres.2004.08.001

Surma, J., Assonov, S., Herwartz, D., Voigt, C., and Staubwasser, M., 2018, The evolution of 17 O-excess in surface water of the arid environment during recharge and evaporation: Scientific reports, v. 8, no. 1, p. 4972

Takahashi, K., and Battisti, D. S., 2007, Processes controlling the mean tropical Pacific precipitation pattern. Part II: The SPCZ and the southeast Pacific dry zone: Journal of Climate, v. 20, no. 23, p. 5696-5706

Tosdal, R. M., Clark, A. H., and Ferrar, E., 1984, Cenozoic polyphase landscape and tectonic evolution of the Cordillera Occidental, southernmost Peru: Geol. Soc. Am. Bull., v. 95, p. 1318-1332

Vargas, G., Rutllant, J., and Ortlieb, L., 2006, ENSO tropical–extratropical climate teleconnections and mechanisms for Holocene debris flows along the hyperarid coast of western South America (17°–24°S): Earth and Planetary Science Letters, v. 249, no. 3-4, p. 467-483.10.1016/j.epsl.2006.07.022

Victor, P., Oncken, O., and Glodny, J., 2004, Uplift of the western Altiplano plateau: Evidence from the Precordillera between 20° and 21°S (northern Chile): Tectonics, v. 23, no. 4, p. n/a-n/a.10.1029/2003tc001519

Vuille, M., 1999, Atmospheric circulation over the Bolivian Altiplano during dry and wet periods and extreme phases of the Southern Oscillation: International Journal of Climatology, v. 19, no. 14, p. 1579-1600

Vuille, M., and Ammann, C., 1997, Regional snowfall patterns in the high, arid Andes, Climatic Change at High Elevation Sites, Springer, p. 181-191.

Vuille, M., Bradley, R. S., and Keimig, F., 2000, Interannual climate variability in the Central Andes and its relation to tropical Pacific and Atlantic forcing: Journal of Geophysical Research-Atmostpheres, v. 105, no. D10, p. 12447-12460

Vuille, M., and Keimig, F., 2004, Interannual variability of summertime convective cloudiness and precipitation in the central Andes derived from ISCCP-B3 data: Journal of Climate, v. 17, no. 17, p. 3334-3348

Wang, F., Michalski, G., Seo, J.-H., Granger, D. E., Lifton, N., and Caffee, M., 2015, Beryllium-10 concentrations in the hyper-arid soils in the Atacama Desert, Chile: Implications for arid soil formation rates and El Niño driven changes in Pliocene precipitation: Geochimica et Cosmochimica Acta, v. 160, p. 227-242.http://dx.doi.org/10.1016/j.gca.2015.03.008

Wara, M. W., Ravelo, A. C., and Delaney, M. L., 2005, Permanent El Niño-like conditions during the Pliocene warm period: Science, v. 309, no. 5735, p. 758-761

Wells, S. G., McFadden, L. D., Poths, J., and Olinger, C. T., 1995, Cosmogenic 3He surface-exposure dating of stone pavements: Implications for landscape evolution in deserts: Geology, v. 23, no. 7, p. 613-616

Wörner, G., Uhlig, D., Kohler, I., and Seyfried, H., 2002, Evolution of the West Andean Escarpment at 18ºS (N.Chile) during the last 25 Ma: uplift, erosion and collapse through time: Tectonophysics, v. 345, p. 183-198

Zachos, J., Pagani, M., Sloan, L., Thomas, E., and Billups, K., 2001, Trends, rhythms and abberrations in Global Climate 65 Ma to present: Science, v. 292, p. 686-693

11. Paper Contributions

Ritter, B., Binnie, S. A., Stuart, F. M., Wennrich, V., & Dunai, T. J. (2018). Evidence for multiple Plio-Pleistocene lake episodes in the hyperarid Atacama Desert. Quaternary Geochronology, 44, 1-12.

B. Ritter participated in the fieldwork (Atacama Desert – Chile) and conducted the laboratory work on the geochemical preparation for cosmogenic nuclides samples in Cologne. The isotope analysis was carried out in Cologne (for ^{10}Be and ^{26}Al at CologneAMS under guidance of Prof. T. Dunai and Dr. Steven A. Binnie) and in Glasgow (for ^{21}Ne at SUERC under the guidance of Prof. F. Stuart). B. Ritter wrote the text with contributions from all co-authors. Overall, B. Ritter contributed 85% to the paper.

Fieldwork: 100%
Data Acquisition (field, laboratory): 90%
Analysis & Interpretation: 90%
Writing of the publication: 75%

Ritter, B., Stuart, F.M., Binnie, S.A., Gerdes, A., Wennrich, V., Dunai, T.J. (2018). Neogene fluvial landscape evolution in the hyperarid core of the Atacama Desert. Scientific Reports Vol. 8 doi: 10.1038/s41598-018-32339-9

B. Ritter participated during two field campaigns in the Atacama Desert for cosmogenic nuclide exposure sampling and collecting geological field observations. Sample preparation was conducted in Cologne by B. Ritter. Isotope analysis for ^{21}Ne were conducted at Scottish University Environmental Research Centre (SUER) in Glasgow under the supervision of Prof. F. Stuart by B. Ritter. ^{10}Be isotope analysis was carried out in Cologne (at CologneAMS) under the guidance of Prof. T. Dunai and Dr. S. Binnie by B. Ritter. Data processing and analysis were done by B. Ritter and Co-Authors. Manuscript writing was done by B. Ritter with contributions by the Co-Authors. B. Ritter contributed 85% to the paper.

Fieldwork: 100%
Data Acquisition (field, laboratory): 90%
Analysis & Interpretation: 90%
Writing of the publication: 75%

Ritter, B., Wennrich, V., Medialdea, A., Brill, D., King, G., Schneiderwind, S., Niemann, K., Fernandez-Galego, E., Diederich, J., Rolf, C., Bao, R., Melles, M., Dunai, T.J., (2019) – Climatic fluctuations in the hyperarid core of the Atacama Desert during the past 215 ka. Scientific reports, 9(1), 5270.

Field work and coring was done by B. Ritter, V. Wennrich, J. Diederich and Prof. T. Dunai during three field campaigns. Sub-sampling and standard sedimentological analysis (grain-size, XRF, magnetic susceptibility) was done by B. Ritter and contributions by V. Wennrich and J. Diederich. Diatom and Phytolith analysis was done by E. Fernández-Galegao and R. Bao. Paleomagnetic data acquisition was conducted by V. Wennrich and C. Rolf, interpretation by B. Ritter. OSL dating was performed by D. Brill, A. Medialdea and G. King. Age-depth modelling was executed by B. Ritter. Interpretation and writing was done by B. Ritter and significant contributions by all Co-Authors.

Fieldwork: 70%
Data Acquisition (field, laboratory): 60%
Analysis & Interpretation: 75%
Writing of the publication: 75%

12. Erklärung

Ich versichere, dass ich die von mir vorgelegte Dissertation selbständig angefertigt, die benutzten Quellen und Hilfsmittel vollständig angegeben und die Stellen der Arbeit – einschließlich Tabellen, Karten und Abbildungen –, die anderen Werken im Wortlaut oder dem Sinn nach entnommen sind, in jedem Einzelfall als Entlehnung kenntlich gemacht habe; dass diese Dissertation noch keiner anderen Fakultät oder Universität zur Prüfung vorgelegen hat; dass sie – abgesehen von unten angegebenen Teilpublikationen – noch nicht veröffentlicht worden ist, sowie, dass ich eine solche Veröffentlichung vor Abschluss des Promotionsverfahrens nicht vornehmen werde. Die Bestimmungen der Promotionsordnung sind mir bekannt. Die von mir vorgelegte Dissertation ist von Prof. Tibor J. Dunai betreut worden.

Folgende Teilpublikationen liegen vor:

Ritter, B., Binnie, S. A., Stuart, F. M., Wennrich, V., & Dunai, T. J. (2018). Evidence for multiple Plio-Pleistocene lake episodes in the hyperarid Atacama Desert. Quaternary Geochronology, 44, 1-12.

Ritter, B., Stuart, F.M., Binnie, S.A., Gerdes, A., Wennrich, V., Dunai, T.J. (2018). Neogene fluvial landscape evolution in the hyperarid core of the Atacama Desert. Scientific Reports Vol. 8 doi: 10.1038/s41598-018-32339-9

Ritter, B., Wennrich, V., Medialdea, A., Brill, D., King, G., Schneiderwind, S., Niemann, K., Fernandez-Galego, E., Diederich, J., Rolf, C., Bao, R., Melles, M., Dunai, T.J., (2019) – Climatic fluctuations in the hyperarid core of the Atacama Desert during the past 215 ka. Scientific reports, 9(1), 5270.

Köln, den 24.06.2019